Resonant Wave-Particle Manipulation Techniques

Andrey I. Zhmoginov

A DISSERTATION

PRESENTED TO THE FACULTY

OF PRINCETON UNIVERSITY

IN CANDIDACY FOR THE DEGREE

OF DOCTOR OF PHILOSOPHY

RECOMMENDED FOR ACCEPTANCE

BY THE DEPARTMENT OF

ASTROPHYSICAL SCIENCES

PROGRAM IN PLASMA PHYICS

January 2012

Abstract

Charged particle dynamics can be altered considerably even by weak electromagnetic waves if some of the particles are in resonance. Depending on the wave parameters, the resonances in the phase space can either be well separated, in which case the particle dynamics is regular almost everywhere, or they can overlap leading to stochastic particle motion in a large volume of the phase space. Although different, both of these regimes allow one to manipulate particle ensembles by arranging resonant interactions with appropriate waves.

This thesis is devoted to studying two wave-particle manipulation techniques having potential applications in fusion and laser-plasma interaction research. Specifically, we study the α-channeling effect (which relies on stochastic diffusion of resonant particles) and the so-called negative-mass effect (NME) (which involves the conservation of the adiabatic invariant).

The α-channeling effect entails the use of radio-frequency waves to expel and cool high-energetic α particles born in a fusion reactor; the device reactivity can then be increased even further by redirecting the extracted energy to fuel ions. Recently, the α-channeling technique, originally proposed for tokamaks, was shown to be suitable for application in mirror machines as well. In the first part of this thesis, we deepen the understanding of issues and possibilities of the α-channeling implementation in open-ended reactors. We verify the feasibility of this technique and identify specific

waves and supplementary techniques, which can potentially be used for implementing the α-channeling in realistic mirror devices. We also propose a new technique for using the α-channeling wave energy to catalyze fusion reaction by employing minority ions as a mediator species.

In the second part of this thesis, the NME manifesting itself as an unusual response of a resonant particle to external adiabatic perturbations mimicking the behavior of a particle with a negative mass, is discussed. Using the Hamiltonian perturbation theory, the calculation of the effective parallel mass is extended to the non-vacuum waves and the NME is shown to be robust. Also, the consequences of radiation friction and collisions with the background particles on the NME are studied and new collective phenomena emerging in plasmas with negative-mass particles are considered.

Dedication

To my wife Elena,

my parents, and sister

for their love and support.

Acknowledgements

Like with virtually any intellectual work, this thesis would never exist without people who guided and supported me during the years in Princeton and long before that. The most important contribution is, of course, that of my scientific adviser Prof. Nathaniel Fisch, whose guidance and expertise were the main driving forces behind this work. I am obliged to him for a wonderful opportunity to work on many exciting problems covering a wide range of questions in theoretical plasma physics. My growth in the course of these years would surely be impossible without his expert advice and prudent instruction. I would also like to thank Prof. Fisch for his understanding, trust and support during the times when my scientific inquiries deviated from the stipulated direction of the thesis. Most of these distractions proved not only fruitful, but also immensely interesting to work on.

The second person who played an extremely important role in this work is my friend and co-author Ilya Dodin, who was also a wonderful teacher to me. Aside from sharing his vision and knowledge of the theoretical plasma physics, he taught me numerous important skills necessary at different stages of the scientific research from literature search to reporting one's results. Working with Ilya was a very interesting and rewarding experience.

I thank the readers of this thesis, Hong Qin and Nikolai Gorelenkov, for their speedy and thorough review of the manuscript.

I would like to express my gratitude to the faculty of the Graduate Program in Plasma Physics. Much of my knowledge about plasma physics, including both the fundamental concepts and the present state of the scientific research, was acquired during their classes. My special thanks go to Barbara Sarfaty, the Graduate Program Administrator, whose invaluable help was so crucial for dealing with numerous bureaucratic routines including those necessary to finalize this thesis. Thanks to her efforts the profoundly intellectual environment created for students at the PPPL by the Program faculty was complemented by a comfortable friendly atmosphere that made studying and working at Princeton a real pleasure.

Studying in Princeton was not easy, but thanks to my classmates Mikhail Dorf, Brendan McGeehan, Jong-Kyu Park, Laura Berzak, Sterling Smith and Xiaoyan Ma, numerous examinations and assignments were much simpler to endure. I would also like to thank other students in the Program, who livened the intellectual atmosphere of the PPPL, including Jessica Baumgaertel, Joshua Burby, John Rhoads, Martin Griswold, Clayton Myers, Katy Ghantous, Zeev Toroker and my officemate Jeffrey Parker.

Being extremely grateful to the Princeton University as an incredible place to study and work, I cannot dismiss the education and support I received from Nizhegorodsky State University (NNSU) and the Institute of Applied Physics of Russian Academy of Science (IAP RAS). The faculty of the Advanced School of General and Applied Physics has given me the fundamental knowledge I needed to succeed at my studies in Princeton and for that I am very grateful. My special gratitude goes to my research co-advisor Professor Gennady Fraiman and my other advisors Vladimir Bratman and Alexander Shalashov. I would also like to thank other people of IAP

RAS including Mikhail Tokman, Vyacheslav Mironov, Alexander Litvak, Yevgeniy Suvorov, and many others for their guidance and advice.

After many years together, I cannot even imagine life in Princeton without my wife Elena. Her presence gave my life a sense of meaning and many of my accomplishments including this work would be impossible without her love and support. It is also impossible to overestimate the importance of moral support and encouragement that my parents and my sister gave me. Thanks to them, I chose this career path and was able to retain my focus on it.

Finally, living and working in Princeton would not be such a pleasant experience if my friends were not around. I would like to thank Zaur Agayev, Vladimir Martyanov, Maxim Kuznetsov, Paul Schmit, Mikhail Dorf, Mikhail Ivanov, Mikhail Bautin, Timur Yusupov, Vasily Geyko, Konstantin Kravtsov, Troy Mestler, William Holloway, Alexander Zharov, Segrey Antipov, Viktor Shevtsov, Anna Gorbunova, Anastasia Ryzhova, Alexander Pikulin, Artem Smirnov, Grigory Kagan, Alexander Likhanskii, Anton Stepanov, Yury and Olga Polyansky, Jenya Ilyunina, Irina Yampolsky, Dasha Smirnova, Nikolay Yampolsky, Andrei Rachkov, Elena Zayarkina, Tatyana Medvedeva, Mikhail and Tatyana Shilovy, Polina Stepanova, Maria Martynovsky, Nabieva, Andrey Sokolov, Olga Antipova, Andrey Belkin, Vasily Pestun, and many others for their help and support and for a wonderful time we had together.

Contents

List of Figures

List of Tables

Chapter 1

Introduction

Many practical techniques and exotic phenomena appearing in a wide variety of physical contexts are based on a resonant interaction between different degrees of freedom of a physical system. In plasma and beam physics, which are focused on studying the dynamics of charged particles and electromagnetic fields, resonant interaction between the two provides the basis for numerous wave-particle manipulation techniques and resonant phenomena including among many others: particle heating [Stix, 1958; Kesner, 1978; Stix, 1975; Suvorov and Tokman, 1983; Bernstein and Baxter, 1981; Stix, 1992] and cooling [Busnardo-Neto et al., 1976; Arunasalam, 1976; Fisch and Rax, 1992; Uleysky et al., 2010; Tumanian, 2003; Berk et al., 1997], current drive and particle acceleration [Fisch, 1987; Davydovskii, 1963; Kolomenskii and Lebedev, 1963; Karimabadi et al., 1990; Friedland, 1994; Friedland et al., 2006], particle ejection [Baldwin et al., 1976; Turner et al., 1977] and injection [Kesner, 1979; Breun et al., 1981], controllable excitation of cold plasmas [Barth et al., 2009; Andresen et al., 2011], isotope separation [Rax et al., 2007] and generation of coherent electromagnetic radiation [Petelin, 1974; Bratman et al., 1979; Brau, 1990].

Depending on the parameters of the dynamical system[1], the resonant system trajectories can either be stochastic (the case of overlapping resonances leading to stochastic diffusion in a large phase space volume), or regular almost everywhere (with exception for motion near the island separatrices) [Lichtenberg and Lieberman, 1992]. In this thesis, two different particle manipulation techniques relying on the resonance between the particles and the external wave are considered.

The first thesis subject is a technique called α-channeling, which belongs to the class of phenomena relying on a strong stochasticity within a resonance region. By a careful choice of the wave parameters, the regions of strong diffusion are designed to cause quick extraction and cooling of α particles born through the D-T fusion reaction. This technique could potentially improve fusion reactors by ejecting the fusion ash and converting the energy extracted from α particles (accounting for about 20% of the total released energy) to plasma heating and fuel injection. In this thesis, applications of this technique to the open-ended fusion devices are identified and considered.

The second subject concerns a phenomenon called the negative-mass effect (NME) emerging in the systems with non-overlapping resonance islands. Sticking to the resonance with the wave, the particle response to external electromagnetic fields (or forces of different nature) can be shown to differ from that of the free particle. As a result, the particle behaves as if it has an effective mass different from the rest mass. Interestingly, in some physical systems, the effective mass is shown to be negative, causing, for example, particle acceleration in the direction opposite to that of the applied force. Besides studying this single particle effect (and the influence of

[1]See Appendix A for a more detailed discussion.

different dissipative mechanisms on it), numerous exotic examples of this effect are also discussed.

1.1 Historical Background and Motivation

1.1.1 Alpha-Channeling in Mirror Machine

The α-channeling technique was originally proposed for tokamaks [Fisch and Rax, 1992]. Expelling α particles while extracting their energy and redirecting it to plasma heating or current drive [Fisch, 1987], the effective fusion reactivity of a reactor might be more than doubled [Fisch and Herrmann, 1994]. As a result, the cost of electricity by tokamak fusion could be reduced significantly [Emmert et al., 1994].

Realizing that the α-channeling might prove even more promising if applied to other magnetic fusion concepts, Fisch proposed an approach for implementing the α-channeling technique in mirror machines [Fisch, 2006, 2007]. [2] The open-ended systems have several advantages over tokamaks, such as simplicity, high-β, and steady-state operation. Unfortunately, the prospects for fusion based on these concepts are dimmed by their low Q-factor, the ratio of fusion power produced to circulating power [Post, 1962; Fowler and Rankin, 1966]. However, employing α-channeling together with other approaches for increasing the Q-factor [Baldwin and Logan, 1979; Post, 2007] could indeed significantly enhance the prospects of mirror fusion. In more advanced mirror geometry, such as in a tandem mirror, the reactor prospects are marginally promising, but might be indeed ... with α-channeling techniques. Even

[2] Later this idea was also extended to rotating plasmas [Fetterman and Fisch, 2008, 2010a, 2011b, 2010c, 2011a].

in a simple mirror, the effect of expelling the fusion ash taking up a valuable electric potential and preventing the fuel ions from being injected into the device is alone expected to increase the effective fusion reactivity of a mirror machine by a factor of 2.8 [Fisch, 2006]. Using the energy extracted from α particles to inject and heat fuel ions, creating a temperature disparity between the ions and electrons, could improve the device operation even further.

In the following, we outline the main idea of the α-channeling in mirror machines as introduced in Ref. [Fisch, 2006]. Consider first the wave-particle interaction in a homogeneous magnetic field $\boldsymbol{B} = |\boldsymbol{B}|\hat{\boldsymbol{b}}$. In the presence of rf waves in the ion-cyclotron frequency range, α particles with velocities $\boldsymbol{v}$ satisfying $\omega - k_z v_z - \ell\Omega_\alpha \approx 0$ for some integer $\ell \neq 0$ are expected to be in resonance with wave. Here ω is the wave frequency, $\boldsymbol{k}$ is the wavevector, Ω_α is the α particle gyrofrequency and the axis z is chosen to be directed along $\hat{\boldsymbol{b}}$. If the wave amplitude is sufficiently large, the resonant particle trajectory becomes stochastic and exhibits a random walk in the full configuration-velocity phase space.

The direction and extent of the particle diffusion can be calculated using the canonical perturbation theory [Lichtenberg and Lieberman, 1992]. Let H_0 be the unperturbed particle Hamiltonian. For simplicity, consider a slab geometry with coordinates (x, y, z) and express the vector potential as $\boldsymbol{A} = -By\hat{\boldsymbol{x}}$. The unperturbed Hamiltonian H_0 can then be represented as follows [Smith and Kaufman, 1978]:

$$H_0(\boldsymbol{J}, \boldsymbol{\phi}) = \mu\Omega_\alpha + \frac{p_z^2}{2}, \tag{1.1}$$

where the particle action-angle variables read $\boldsymbol{J} = (p_z, \mu, m_\alpha\Omega_\alpha X)$ and $\boldsymbol{\phi} = (z, \theta, Y)$. Here m_α is the α particle mass, $\boldsymbol{p}$ is the kinetic momentum, $\boldsymbol{P} = \boldsymbol{p} - q\boldsymbol{A}/c$ is the canonical momentum, $\mu = p_\perp^2/(2m_\alpha\Omega_\alpha)$ is the gyromoment, $\boldsymbol{p}_\perp = \boldsymbol{p} - p_z\hat{\boldsymbol{z}}$, θ is the gyroangle, $X = x + P_y/m_\alpha\Omega_\alpha$ and $Y = -P_x/m_\alpha\Omega_\alpha$ are the gyrocenter coordinates.

The wave field can then be treated as a perturbation $\varepsilon H_1(\boldsymbol{J}, \boldsymbol{\theta})$, where ε is a small parameter proportional to the wave amplitude. Choosing $k_x = 0$, the wave phase multiplier $e^{i\varphi}$ entering H_1 can be expanded as follows:

$$e^{i\varphi} = e^{ik_z z + ik_y Y + ik_y \rho \cos\theta - i\omega t} \approx \sum_{\ell \in \mathbb{Z}} J_\ell(k_y \rho) e^{ik_z z + ik_y Y + i\ell\theta - i\omega t}, \tag{1.2}$$

where J_ℓ is the Bessel functions of the first kind and ρ is the particle gyroradius. Therefore, one confirms that the resonant wave-particle interaction occurs when $\omega - \ell\Omega_\alpha - k_z v_z = 0$. Furthermore, writing the Manley-Rowe relations for the resonant term, one obtains:

$$\frac{\dot{\mu}}{\dot{H}} \approx \frac{\ell}{\omega}, \qquad \frac{\dot{p}_z}{\dot{H}} \approx \frac{k_z}{\omega}, \qquad \frac{\dot{X}}{\dot{H}} \approx \frac{k_y}{m_\alpha \Omega_\alpha \omega}. \tag{1.3}$$

These relations define the direction of particle diffusion and show that the particle spatial excursion ΔX is proportional to the particle energy change. As a result, particles losing energy are expected to drift in a direction opposite to that of particles gaining energy.

Recall that the resonance condition has the form $v_z = v_{\text{res}} = (\omega - \ell\Omega)/k_z$ and assume that the characteristic resonance width Δv_z is much smaller than the resonant v_z. Using Eq. (1.3), one observes that $\dot{v}_z/\dot{v}_\perp \ll 1$ only if $v_\perp \ll \omega/k_z - v_z$, where $v_\perp = \sqrt{v_x^2 + v_y^2}$. Therefore, unless k_z is much smaller than ω/v, the resonant particle goes out of the resonance with the wave losing or gaining only a fraction of its initial energy. This can also be seen by noticing that the wave-particle interaction Hamiltonian in the case of an electrostatic wave reading

$$H = \frac{p^2}{2m_\alpha} + \Phi \exp(-i\omega t + ik_z z + ik_y y) \tag{1.4}$$

has an exact integral of motion [Smith and Kaufman, 1978]:

$$I = \frac{m_\alpha(v_x^2 + v_y^2)}{2} + \frac{m_\alpha(v_z - \omega/k_z)^2}{2} + \Phi \exp(-i\omega t + ik_z z + ik_y y). \tag{1.5}$$

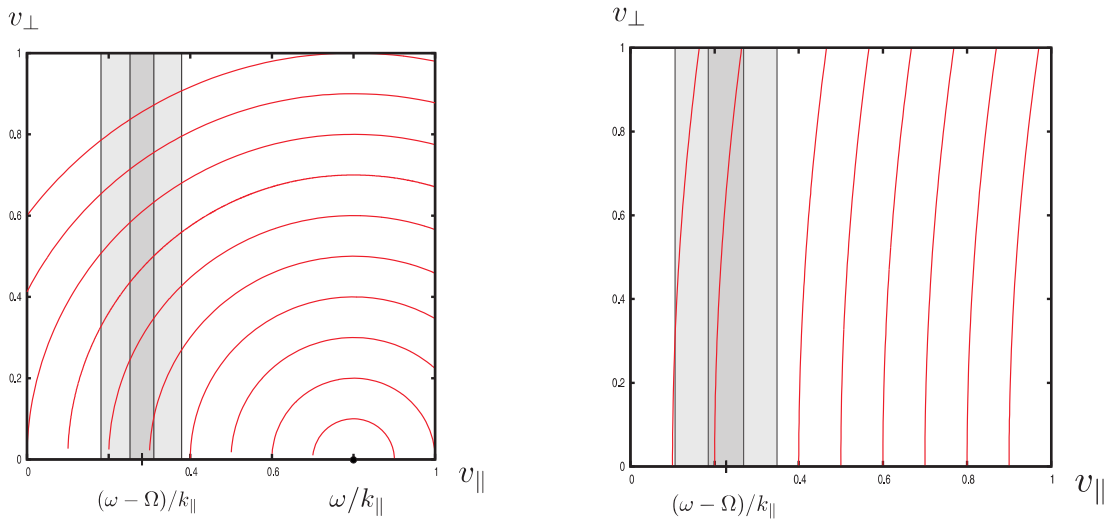

Figure 1.1: The velocity space $(v_\perp, v_\parallel)$ showing a resonance region (gray) and integral curves $I \approx m_\alpha[v_x^2 + v_y^2 + (v_z - \omega/k_z)^2] = \text{const}$ (red): (a) $v \sim \omega/k_z$, (b) $v \ll \omega/k_z$.

The resonant particle velocity change is then directed along the circles centered at $v_z = v_0 = \omega/k_z$ and $v_\perp = 0$; and hence $\dot{v}_z/\dot{v}_\perp \ll 1$ requires that $v_0 \gg v$ (Fig. 1.1). Note that if the particle leaves the resonance with the wave, it can, in principle, be captured by another wave. In the following, however, we consider phase-space manipulation with a finite number of paths, requiring that $k_z \ll \omega/v$ for each rf region.

Now consider the resonant wave-particle interaction in an inhomogeneous magnetic field. Specifically, consider a particle trapped in a simple mirror machine[3] interacting with an rf region located at $z = z_{\text{rf}}$. The particle state can be characterized by the particle magnetic moment μ and particle energy E, which are conserved outside of the rf wave. In the following, we will also use an alternative description of the

[3]The presence of the electrostatic potential can be included later by modifying the shape of the loss cone.

particle state, specifying parallel and perpendicular midplane particle energies reading $W_{\perp 0} = \Omega_{\alpha 0}\mu$ and $W_{\parallel 0} = E - W_{\perp 0}$ correspondingly, where $\Omega_{\alpha 0}$ is the α particle gyrofrequency in the device midplane. If the particle is in resonance with the rf region having $k_z \ll \omega/v$, the local (at $z = z_{\rm rf}$) particle parallel velocity $v_\parallel = \boldsymbol{v}\cdot\hat{\boldsymbol{b}}$ is conserved during the interaction. Introducing the change of the perpendicular particle velocity $\Delta v_\perp$, one can see that:

$$\Delta\mu \approx \frac{m_\alpha v_\perp \Delta v_\perp}{\Omega_{\rm rf}}, \qquad \Delta E \approx m_\alpha v_\perp \Delta v_\perp, \tag{1.6}$$

where $\Omega_{\rm rf}$ is Ω_α calculated for $B = B_{\rm rf} = B(z_{\rm rf})$. Substituting Eqs. (1.6) in the expressions for $W_{\perp 0}$ and $W_{\parallel 0}$, one obtains:

$$\frac{\Delta W_{\parallel 0}}{\Delta W_{\perp 0}} \approx R_{\rm rf} - 1, \tag{1.7}$$

where $R_{\rm rf} = B(z_{\rm rf})/B(0)$ and $z = 0$ is the midplane location. Therefore, one concludes that the particle interacting resonantly with an rf region located at $z = z_{\rm rf}$ will exhibit a random walk along effectively a one-dimensional curve $W_{\parallel 0} \approx \Delta W_{\perp 0}(R_{\rm rf} - 1) + mv_{\rm res}^2/2$, which we will further call a *diffusion path*. Note that any diffusion path intersects the device loss cone $\Delta W_{\parallel 0} = \Delta W_{\perp 0}(R - 1)$, crossing which particles leave the mirror machine through one of its ends. Here $R = \max_z B(z)/B(0)$ is the device mirror ratio.

Consider a mirror machine with an rf region with $v_{\rm res} < v_\alpha$, where v_α is a velocity of a 3.5 MeV alpha particle born in the D-T fusion reaction. Alpha particles born near the corresponding diffusion path will exhibit a random walk moving both in velocity and configuration space. If the diffusion induced along the path is suppressed at high energy, whereas at low-energy there is an effective particle "sink" attributed to the particle loss through the mirror loss cone, the interaction with the waves will result in the ejection of the cold α particles and the simultaneous transfer of their initial energy

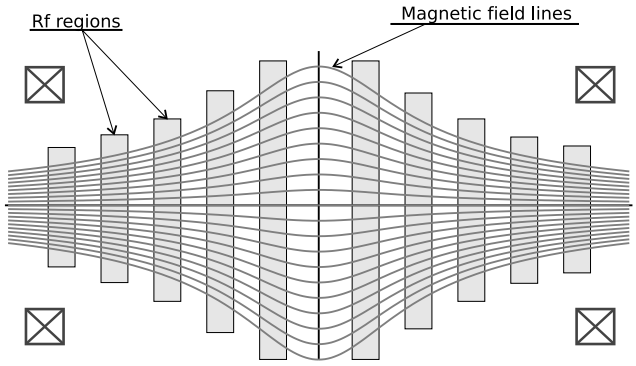

Figure 1.2: Arrangement of regions (shown with grey bars) with high-n azimuthally propagating radially-localized electrostatic waves in the ion cyclotron range of frequencies.

to the waves, thereby accomplishing the α-channeling effect [Fisch and Rax, 1992]. To capture α particles within a wide range of pitch angles, it was suggested [Fisch, 2006] that numerous rf regions with the same $v_{\rm res}$, but different values of $R_{\rm rf}$ (and consequently different $z_{\rm rf}$) should be employed (Fig. 1.2). Note that these diffusion paths (Fig. 1.3) do not intersect with each other above the loss cone[4], otherwise there would be regions in the phase space, where the diffusion tensor would be nearly isotropic and the correspondence between $\Delta\mu$, $\Delta p_{\|}$ and Δr would be lost.

Fast α particle extraction and cooling require that the diffusion paths are limited at high energies above the α birth energy. Superadiabaticity [Aamodt, 1971; Rosenbluth, 1972] characteristic for sufficiently high-energetic particles was suggested [Fisch, 2006] as one of the possible mechanisms for supressing α particle diffusion at high energies. Another proposed mechanism is a consequence of the particle radial drift, which accompanies particle heating and cooling. Specifically, recall that according to Eq. (1.3), for a wave with a finite azimuthal wave number m, the radial

[4]The diffusion paths intersect in a single point $W_{\perp\,0} = 0$, $W_{\|\,0} = mv_{\rm res}^2/2$, which is located below the loss cone.

particle excursion Δr is proportional to the energy change ΔE. If the wave is such that $\Delta r/\Delta E < 0$, the α particle located close the device axis at some $r = r_0$ will move closer to the device center when gaining energy. Therefore, the maximum possible energy increase of the particle is equal to $m_\alpha \omega \Omega_{\rm rf} r_0^2/(2m)$ and for sufficiently large m, this mechanism could be used to limit α particle heating.

The approach to the α-channeling implementation in a mirror machine discussed in Ref. [Fisch, 2006] relied on an idealized model of the wave-particle interaction and did not consider various non-ideal effects which could potentially limit the applicability of the method. Particularly, the following issues and questions were not fully addressed: (a) a finite width of the diffusion paths caused by the magnetic field inhomogeneity, (b) a possibility of intersecting diffusion paths, (c) perturbation of the background plasma by the wave, (d) identification of specific plasma modes capable of extracting α particle energy, (e) a possibility of arranging rf regions in the device to extract a substantial fraction of the trapped α particle energy. In the first part of the thesis, we address these and other questions important for providing a practical scenario of α-channeling in mirror machines. Specifically, using analytical estimates and numerical codes, we optimize the α-channeling efficiency with respect to the rf region parameters and discuss the effect of intersecting diffusion paths. Furthermore, we identify localized plasma modes which can potentially be used for α-channeling implementation[5] and propose a novel method for depositing the extracted energy to the fuel ion heating. Finally, we outline several possible experiments, which could

[5]Excitation of similar localized weakly-damped modes is believed to be the explanation for a stronger than expected α-channeling effect in tokamaks [Fisch, 1997; Clark and Fisch, 2000; Fisch, 2000; Gorelenkov et al., 2010].

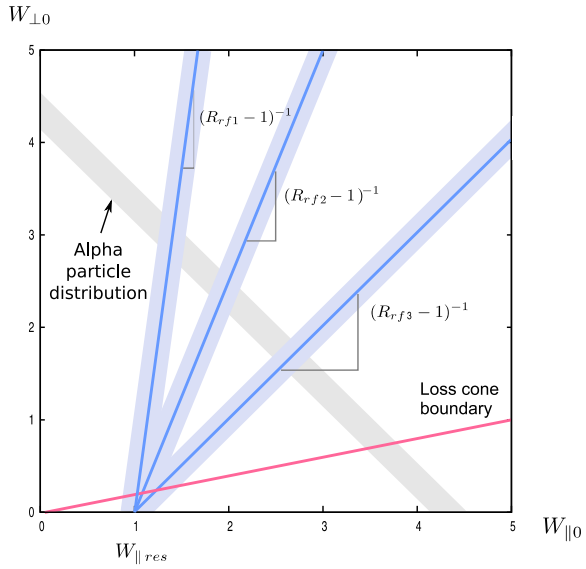

Figure 1.3: Implementation of α-channeling in mirror machines. Configuration of diffusion paths in the midplane energy space $W_{\| 0}$–$W_{\perp 0}$ used for α particle cooling; finite widths of diffusion paths affect exit energy uncertainty and lead to an intersection of paths what isotropizes diffusion tensor in a vicinity of a loss cone.

be conducted on one of the existing mirror machines to verify the core ideas of the α-channeling technique.

1.1.2 Negative-Mass Effect

Although the main focus of this thesis is the α-channeling technique, being interested in particle manipulation with waves, we also considered another phase-space engineering technique called the negative-mass effect (NME), which unlike α-channeling relies on regular particle motion near the resonance.

Analytical treatment of many physical phenomena exhibiting a separation of temporal and spatial scales can be dramatically simplified by considering a hierarchy of adiabatic invariants corresponding to different degrees of freedom [Lichtenberg and Lieberman, 1992]. For example, motion of a classical particle in a high-frequency wave

and slowly-changing weakly-inhomogeneous fields can be studied using the guiding-center approach, which allows one to separate the fast oscillatory particle motion from the slow translational motion [Northrop, 1963; Dewar, 1973; Brizard and Hahm, 2007]. Following this approach, the slow particle motion is viewed as a motion of a "quasiparticle" associated with the particle guiding center. The response of such a quasiparticle to applied external fields is affected by the fast particle oscillations, which can be accounted for in the equations of the guiding center motion by introducing the *effective quasiparticle mass*.

The effective particle mass was previously found for specific physical systems like an electron interacting with an intense laser wave [Rax, 1992; Moore and Fisch, 1994; Bauer et al., 1995; Mora and Antonsen, 1997; Tokman, 1999]. A general approach for calculating the effective particle mass for relativistic particles in arbitrary electromagnetic fields was developed [Dodin and Fisch, 2008c], where it was shown that the effective particle mass $m_{\rm eff}$ is proportional to the gauge-independent part of the averaged Routhian [Landau and Lifshitz, 1976, §41]. Specifically, it was shown that:

$$m_{\rm eff}(\boldsymbol{Q},\dot{\boldsymbol{Q}}) = \frac{1}{c^2}\left[\boldsymbol{J}\cdot\boldsymbol{\nu}(\boldsymbol{Q},\dot{\boldsymbol{Q}}) - \langle L\rangle\right]_{\bar{v}=0}, \tag{1.8}$$

where $\boldsymbol{Q}$ are the coordinates of the slow guiding center motion, $\boldsymbol{J}$ are the conserved actions of the fast oscillations, $\boldsymbol{\nu}(\boldsymbol{Q},\dot{\boldsymbol{Q}})$ are the oscillation frequencies, L is the particle Lagrangian and $\bar{\boldsymbol{v}} = \langle \boldsymbol{v}\rangle$ is the guiding center velocity. The guiding center dynamics in slow and smooth external fields can then be derived from the following Lagrangian:

$$\mathcal{L} = -m_{\rm eff}c^2\sqrt{1-\bar{v}^2/c^2} + \frac{e}{c}(\bar{\boldsymbol{v}}\cdot\tilde{\boldsymbol{A}}) - e\tilde{\varphi}, \tag{1.9}$$

where $\tilde{\boldsymbol{A}}$ and $\tilde{\varphi}$ are the vector and scalar potentials of the external field.

The general formalism can then be applied to a variety of physical problems including an interaction of a relativistic particle with a circularly-polarized vacuum wave

propagating along a static magnetic field [Dodin and Fisch, 2008c]. Integrating the particle motion equations analytically, the expression for the particle effective mass was obtained and two intriguing properties of the system dynamics were observed. Specifically, separating free particle gyromotion from the wave-induced oscillations, the existence of up to *three stable* energy states with identical average velocities $\bar{\boldsymbol{v}}$ and magnetic momenta μ (associated with the free gyromotion) was demonstrated. The stability of all three states is generally impossible for a one-dimensional nonlinear oscillator [Bogoliubov and Mitropolskii, 1961, §15] as well as for many other systems involving a resonant wave-particle interaction in the presence of the background magnetic field. The second intriguing phenomena was associated with the sign of the particle effective mass. Introducing the effective parallel mass $m_{\parallel}$, characterizing the response of the oscillating particle to external adiabatic forces directed along the background magnetic field, it was observed that under certain circumstances, this mass can become negative. As a result, unlike a particle with a positive mass, the particle with $m_{\parallel} < 0$ was shown to accelerate in the direction opposite to that of the applied force.

The expressions for m_{eff} and $m_{\parallel}$ derived in Ref. [Dodin and Fisch, 2008c] were obtained for a vacuum wave with a refraction index n_0 exactly equal to 1. The particle motion in such a wave is exactly integrable, allowing one to derive NME from the least action principle directly. However, of practical interest are wave interactions with particle ensembles (*e.g.,* finite-density plasmas), in which case the wave dispersion differs from that in vacuum. As a rule, the corresponding particle trajectories cannot be found explicitly then, so the analytical approach [Dodin and Fisch, 2008c] becomes virtually inapplicable. In the second part of this thesis, we develop a different approach to the NME based on the Hamiltonian perturbation theory, showing that

this phenomenon persists robustly in realistic environments. The developed formalism is then extended to include non-Hamiltonian and stochastic forces, what allows us to verify that the radiation friction and collisions with the background particles do not invalidate the negative-mass effect or make it unpractical. Along with showing the feasibility of the NME, we also demonstrate that the radiation friction can transport a fraction of particle energy to the wave and that the collisions with the background particles can, in principle, be used to bring the particle to the negative-mass state. Finally, we discuss possible applications of the NME including: frequency doubling, plasma wave group velocity manipulation and coherent amplification of waves.

1.2 Thesis Emphasis and Objectives

The present dissertation is focused on two phase-space manipulation techniques involving the resonant wave-particle interaction: the α-channeling and the negative-mass effect. Even though the core idea of both techniques is the resonance between the external force and the particle degrees of freedom, they represent two extreme cases of a single phenomenon. Particularly, while the α-channeling is an example of the phase space manipulation technique based on a strongly *chaotic* behavior of the wave-particle dynamical system, the negative-mass effect is the facilitation of the nonlinear *regular* system dynamics.

The first part of the thesis (Chapters 2-6) is devoted to α-channeling in open-ended systems. Specifically, we discuss the feasibility of the α-channeling implementation in mirror machines [Fisch, 2006]. The objectives of this research are to use numerical simulations and analytical models to verify and optimize the α-channeling effect in

open-ended devices, and propose specific plasma waves and practical device configurations, for which this effect could potentially be demonstrated and utilized. The detailed list of research objectives of the first part of the thesis is:

- Numerical and analytical investigation of the α-channeling technique implementation in mirror machines;
- Investigation of particle flows in complex diffusion domains, specifically in networks of diffusion paths;
- Identification of plasma waves suitable for implementing α-channeling in mirror machines;
- Investigation of techniques capable of redirecting energy extracted from α particles to the background plasma heating;
- Investigation of a possibility to use present-day experimental devices for demonstrating the α-channeling effect.

In the second part of the thesis (Chapters 7-10), we discuss the negative-mass effect. Specifically, using the Hamiltonian approach to the wave-particle interaction problem, we generalize previous results [Dodin and Fisch, 2008c], considering also the effects of radiation friction and collisions with background plasmas and propose several potential applications of the NME. The detailed list of NME research objectives is:

- Investigation of different analytical approaches to the systems exhibiting the negative-mass effect;
- Generalization of the previous results [Dodin and Fisch, 2008c] to the particle interaction with waves characterized by the refraction index $n_0 \neq 1$;

- Investigation of the resonant particle and wave dynamics in the presence of friction forces, particularly the radiation friction;
- Analysis of the particle ensemble dynamics in the presence of external stochastic forces, specifically the effect of particle collisions on the NME;
- Investigation of phenomena related to the NME and possible applications of this effect.

1.3 Thesis Overview

In **Chapter 2**, a feasibility of the α-channeling technique in mirror machines is studied and a rough optimization of the α-channeling efficiency with respect to rf region parameters (without restricting them by the background plasma dispersion relation) is performed. Deriving the analytical expressions for the diffusion path width and shape, we propose systems of rf regions suitable for the α-channeling implementation in two mirror machine designs. In addition to choosing the proper rf region location and parallel resonant velocity [Fisch, 2006], we also estimate optimal rf region widths, perpendicular and parallel wavelengths and optimal wave amplitudes. In one of such optimized designs, the possibility of extracting more than 60% of the total trapped α particle energy on a time much smaller than the characteristic collisional time is simulated [Zhmoginov and Fisch, 2008b]. Also, we show that the waves proposed for α-channeling are not expected to perturb the background plasma significantly, but can be employed for injecting and heating of fuel ions.

In **Chapter 3**, a flux rearrangement problem in a network of diffusion paths is formulated and solved [Zhmoginov and Fisch, 2008a]. This optimization problem is motivated by the need to maximize the α particle energy extraction in the case

of intersecting diffusion paths. Showing that the steady-state particle diffusion in a rectangular network of thin intersecting paths can be approximately described using a finite number of algebraic equations, we demonstrate an analogy between the diffusion flux rearrangement problem and a similar problem of current rearrangement in an electrical network of one-dimensional conductors. We then proceed to the solution of the formulated problem, showing that the optimum can be reached in a system of paths with diffusion coefficients equal to 1, β, β^2, β^3 and β^4 as β goes to infinity. The algorithm of assigning these diffusion coefficients is also presented. Finally, noticing that the infinite diffusion coefficients are not physical, we discuss numerical methods for finding the optima in problems with more general optimization functionals and parameter limitations. The supplementary calculations necessary for implementing such methods are presented.

In **Chapter 4**, localized weakly-damped electromagnetic modes suitable for α-channeling implementation in mirror machines are identified [Zhmoginov and Fisch, 2009, 2010]. Studying the effect of wave damping on dynamics of the α-channeling mode, we show that excitation of localized weakly-damped modes can be more advantageous (particularly if the device fusion reactivity is not sufficiently high) for α-channeling implementation compared to the excitation of waves fully damped in a resonance region [Valeo and Fisch, 1994]. Using the geometrical optics approximation and assuming that the waves of interest propagate primarily along or across the magnetic field lines, we then develop an algorithm capable of searching the parameter space for weakly-damped modes localized in the device interior. This algorithm is then applied to two mirror machine designs to identify weakly-damped localized modes with properties similar to those proposed in Chapter 2. As a result, three waves, namely the shear and fast Alfvén waves (propagating along and across the

magnetic field) and the ion Bernstein wave (propagating along the magnetic field), are identified as suitable for α-channeling implementation.

In **Chapter 5**, two techniques capable of redirecting the extracted α particle energy to heating of the background plasma are proposed [Zhmoginov and Fisch, 2011b]. The localized modes identified in Chapter 4 damp most of their energy on electrons rather than fuel ions participating in the fusion reaction. However, we show that by injecting minorities resonant with the wave, a significant fraction of the wave energy can be redirected to heating of the minority ions, which act as a catalyst, eventually forwarding the energy to colder fuel ions through collisions. The proposed technique can, in principle, be used to heat the fuel ions in the device central cell. However, we also show that a fraction of the energy extracted from α particles in the central cell can be used to heat plasmas in the device plugs. Specifically, by a proper choice of the device plug parameters (bringing two device cavities in "resonances"), the α-channeling mode gaining energy in the central cell is shown to be stabilized by weak damping in the plug.

In **Chapter 6**, a possibility of using currently available experimental devices for studying the α-channeling modes and demonstrating the α-channeling effect is examined. Specifically, we discuss how some of the recent experiments on the Large Plasma Device (LAPD) [Gekelman et al., 1991] could be modified in order to show the existence of the localized fast Alfvén waves and demonstrate the core principles involved in the α-channeling technique.

In **Chapter 7**, a new approach [Zhmoginov et al., 2010] to the negative-mass effect studied previously by integrating the particle equations of motion exactly [Dodin and Fisch, 2008c] is discussed. For a classical particle undergoing nonlinear interaction with a wave in dielectric medium, a perturbation theory is developed, showing that

the particle motion can be described in terms of an effective parallel mass which can become negative. A relativistic particle interacting with a circularly polarized wave and a static magnetic field is studied as an example. For the three stationary orbits corresponding to the same velocity parallel to the magnetic field, the conditions are found under which all these equilibria are centerlike, or neutrally stable. It is shown that a negative parallel mass is realized in the vicinity of the intermediate-energy equilibrium, and a plasma collective instability of a new type is identified.

In **Chapter 8**, the effect of radiation friction is included [Zhmoginov et al., 2011b] in the Hamiltonian treatment of wave-particle interactions with autoresonant phase-locking, yielding a generalized canonical approach to the problem of dissipative dynamics near a nonlinear resonance. As an example, the negative-mass effect exhibited by a charged particle in a pump wave and a static magnetic field is studied in the presence of the friction force due to cyclotron radiation. Particles with negative parallel masses $m_{\|}$ are shown to transfer their kinetic energy to the pump wave, thus amplifying it. Counterintuitively, such particles also undergo stable dynamics, decreasing their transverse energy monotonically due to cyclotron cooling, whereas some of those with positive $m_{\|}$ undergo cyclotron heating instead, extracting energy from the pump wave.

In **Chapter 9**, we propose how stochastic perturbations can be included in the canonical formalism for a broad class of resonant Hamiltonian systems similar to those yielding NME [Zhmoginov et al., 2011c]. Specifically, modeling the stochastic system evolution with the Fokker-Planck equation, we express the equation coefficients through the statistical properties of the external noise. Considering a charged particle interacting with a pump wave in a static magnetic field, we then find the

diffusion coefficient and the drag terms caused by the particle collisions with the cold background plasmas.

In **Chapter 10**, we demonstrate several unexpected phenomena emerging in the physical systems exhibiting the NME. If a particle is initialized near the extremum of the $v(p)$ dependence, the particle response to the external wave with frequency ω_p is shown to occur at the second harmonic of this frequency. We also show that by slowly changing the laser wave frequency and amplitude, it might be possible to control the group velocity of electrostatic waves propagating in plasmas with negative-mass particles. Finally, we investigate a negative-mass particle dynamics in the field of a resonant low-frequency adiabatic electrostatic wave. It is demonstrated that depending on the peak wave amplitude and wave phase velocity, four different scenarios, each characterized by different final particle states, are possible. We then show that only two of these scenarios can be used to transport particles between the states with $v = 0$ and identify one scenario with the largest probability of such a transition.

In **Appendix B**, we derive equations of motion for a particle trapped in a mirror machine and interacting resonantly with an electrostatic wave. This subsidiary result is employed in Chapter 2 for simulating single particle motion and is also used to derive the diffusion path characteristics.

In **Appendix C**, we show that a spatial scale of the particle density distribution in a rectangular network of thin diffusion paths greatly exceeds a characteristic diffusion path width. This fact is employed in Chapter 3 to use one-dimensional equations for finding the particle distribution function.

In **Appendix D**, we show that the separation of fluxes between two intersecting diffusion paths in the non-steady-state problem is the same as the flux separation in a steady-state solution. Assuming arbitrary initial conditions "above" the intersection

point (no particles are placed in between the intersection point and the particle sinks), the fraction of particles escaping horizontal and vertical sinks over an infinite time is calculated. The obtained expression is shown to be identical to the ratio of fluxes in the steady-state problem.

Chapter 2

Simulations of Alpha-Channeling in Mirror Machines

The conceptual possibility of using rf waves to extract α particle energy and redirect it to fuel ions in a simple mirror machine was suggested in Refs. [Fisch, 2006, 2007]. There, an arrangment of rf regions (Fig. 1.2) in the ion-cyclotron frequency range capable of creating a population inversion along the advantageous configuration of diffusion paths similar to that shown in Fig. 1.3 was proposed. However, the analysis of the α particle diffusion along the paths assumed that the diffusion paths were of vanishing thickness and only the asymptotic time behaviour of the particles was considered. A finite width of the diffusion paths captures α particles within the full accessible range of pitch-angles, which is helpful, but it makes uncertain the exit energy, since diffusion paths can intersect. Besides depending on the average energy of the exiting α particles, the efficiency of α-channeling also depends on the particle extraction or channeling time. The extraction time needs to be much smaller than the collisional energy relaxation time for effective channeling.

In this chapter, the particle distribution function evolution in a mirror machine of finite length in the presence of multiple rf regions is studied numerically. Using the six-dimensional particle motion equation and the Fokker-Planck equation solvers, the non-ideal effects of finite diffusion path width and intersection of diffusion paths are addressed. Although a strict optimization is not performed, the possibility to extract more than 60% of energy of resonant α particles in a practical system design is simulated [Zhmoginov and Fisch, 2008b]. It is also shown that wave-particle interactions can be used to couple energy extraction from α particles with the plasma injection accompanied by heating of fuel ions.

This chapter is organized as follows. In Sec. 2.1, the exact and approximate single particle motion equations are discussed. Then, in Sec. 2.2, the equations describing the evolution of the particle distribution function are provided. Using the single particle motion equations, the diffusion path characteristics are estimated in Sec. 2.3 for the regime of interest. Section 2.4 then introduces the computational method used to solve the Fokker-Planck equation numerically. In Sec. 2.5, the results of the numerical simulations of α-channeling are discussed. Finally, in Sec. 2.6, the pump-out of the hot fuel ions by rf regions employed for α-channeling is estimated.

2.1 Single particle motion equations

The evolution of α particles trapped in a mirror machine in the presence of rf fields can be modelled by either solving equations of motion for each particle in the ensemble, or by using the Fokker-Planck equation in the configuration-velocity space in midplane coordinates [Fisch, 2006; Stix, 1992]. The Fokker-Planck equation coefficients can, in principle, be determined analytically using the quasilinear theory

[Grawe, 1969; Kesner, 1979; Bernstein and Baxter, 1981]. However, the analytical expressions for these coefficients can be very complicated if the magnetic field is strongly inhomogeneous and the wave profile is allowed to vary across the device. Another approach to calculating Fokker-Planck coefficients is based on numerical integration of the single particle motion equations for particles with various wave- and gyro-phases. In this section, we discuss, a fast yet sufficiently accurate particle tracing code, which can be used to find trajectories for large ensembles of particles.

Consider an axially symmetric magnetic mirror trap with a system of localized rf regions located along the device axis. Suppose that the radial size of the system is much smaller than its longitudinal scale length L, so that a paraxial approximation for the magnetic field can be used:

$$\boldsymbol{B} = \boldsymbol{r} B_z'(z)/2 + B_z(z)\hat{\boldsymbol{z}}. \tag{2.1}$$

Here we use a cylindrical system of coordinates with $r = 0$ on the device axis and $z = 0$ in the midplane. The rf fields are assumed to be electrostatic monochromatic waves localized in layers $z \in [z^i, z^i + l^i]$ of width $l^i \ll L$ specified by the following expression for the scalar potential φ:

$$\varphi^i \approx \varphi_0^i(r, z) \cos\left(-\omega^i t + \int k_z^i(z)\, dz + m^i \psi\right), \tag{2.2}$$

where the index i enumerates layers and ψ is an azimuthal angle. For simplicity, the radial wavelengths of all rf regions are assumed to be large compared to $2\pi/k_z^i$, $2\pi r/m^i$ and R and are thus omitted.

The motion of a charged particle in an rf region is governed by equation:

$$m\dot{\boldsymbol{v}} = ec^{-1}\, \boldsymbol{v} \times \boldsymbol{B} + q\varphi_0 \boldsymbol{k} \sin\left(-\omega_0 t + \int k_z\, dz + m\psi\right), \tag{2.3}$$

where $\boldsymbol{k}_\perp = \hat{\boldsymbol{\psi}} m/r$ with $\hat{\boldsymbol{\psi}}$ being an azimuthally-directed unit vector. Introducing new dimensionless time $\tau = t\Omega_0$, particle gyrofrequency $\Omega = eB/(mc\Omega_0)$ normalized to the

midplane gyrofrequency Ω_0 and dimensionless magnetic field $\boldsymbol{b} = \boldsymbol{B}/B_0$ normalized to the midplane magnetic field B_0, the equation on the dimensionless velocity $\boldsymbol{u} = \boldsymbol{v}/\Omega_0$ can be obtained:

$$\frac{d\boldsymbol{u}}{d\tau} = \boldsymbol{u} \times \boldsymbol{b} + \boldsymbol{k} f_0 \sin\left(-\omega\tau + \int k_z \, dz + m\psi\right), \tag{2.4}$$

where $\omega = \omega_0/\Omega_0$ and $f_0 = q\varphi_0/m\Omega_0^2$.

Recall that $r \ll L$, yet $r \gg \rho$ and assume that the particle experiences none or only one resonance on the whole length of any rf region. Following a derivation in Appendix B, the particle motion can then be approximately described by the following system of equations [Litvak et al., 1993; Shklyar, 1986; Albert, 1993]:

$$\frac{d\delta}{dz} \approx -\mathrm{Re}\left[\frac{i^\ell (i f_0 k_z - \partial f_0/\partial z) J_\ell(m\rho/r) e^{-i\phi}}{u_{\parallel 0}}\right], \tag{2.5}$$

$$\frac{d\phi}{dz} = (\omega - k_z u_{\parallel 0} - \ell\Omega)/u_{\parallel 0} - (\omega - \ell\Omega)\delta/u_{\parallel 0}^2, \tag{2.6}$$

$$\frac{dE}{d\delta} \approx \omega/k_z, \tag{2.7}$$

$$\frac{dr}{dE} \approx \frac{m}{r\omega\Omega}, \tag{2.8}$$

where $\delta = u_\parallel - u_{\parallel 0}$ is a small parallel velocity perturbation, $E = u^2/2$, $u_\perp^2 = u^2 - u_\parallel^2$, $\rho = u_\perp/b$, θ_0 is the initial gyroangle, ℓ is a resonance number and $u_{\parallel 0}$ is the unperturbed parallel particle velocity given by $\sqrt{2E - 2\mu b(z)}$. The system of equations (2.5)-(2.8) describes the evolution of the particle parallel velocity and particle energy instead of the three-dimensional particle velocity like in Eq. (2.4). This means that while for integrating Eq. (2.4), the time step should be much smaller than ω^{-1}, the characteristic time step necessary to integrate Eqs. (2.5)-(2.8) for the resonant particle is proportional to $(\omega - \ell\Omega - k_z u_{\parallel 0})^{-1} \gg \omega^{-1}$. Using Eqs. (2.5)-(2.8) to trace particle trajectories can, therefore, be more computationally efficient compared to the integration of Eq. (2.4).

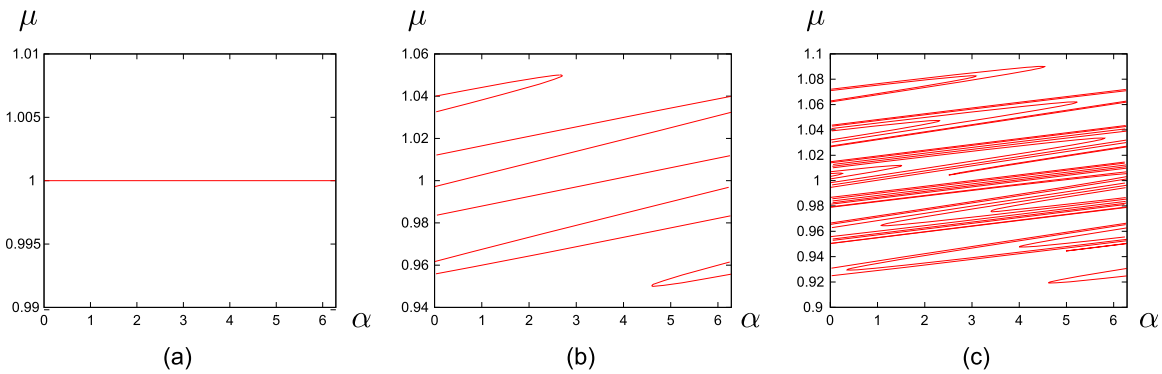

Figure 2.1: Two iterations of the mapping $\mu_{n+1} = \mu_n + M\cos\alpha_n$, $\alpha_{n+1} = \alpha_n + X\mu_{n+1}$ (modulo 2π) with $M = 0.05$ and $X = 200$: (a) initial particle distribution, (b) first iteration of the mapping, (c) second iteration of the mapping.

2.2 Particle distribution evolution

Let us now discuss the discrete dynamical system with parameters, which must be calculated only once for a given physical configuration, that can be used to trace large ensembles of particles. To develop this system, we first assume that the wave is sufficiently strong to make the particle trajectories in the considered region of phase space stochastic. Since the condition of stochasticity is not satisfied for particles with energy above a certain threshold [Timofeev, 1974; Smith et al., 1980; Lichtenberg et al., 1969], we assume that this threshold is much higher than the α particle birth energy. To illustrate the onset of stochasticity, consider a simple model of a particle moving in a mirror machine with a single rf region. Let τ_n, θ_n, and μ_n be the time, gyroangle and magnetic moment upon the n^{th} entrance of the particle into the region. Noticing that the magnetic moment is perturbed while the particle is within the rf region only and assuming that the region is sufficiently thin, one can approximate $\mu_{n+1} \approx \mu_n + M(\mu_n)\cos\alpha_n$, where $\alpha_n = \ell\theta_n + \omega\tau_n$. The change of α_n on a single particle bounce, on the other hand, contains contributions attributed to particle motion inside $[\Delta\alpha_n^i(\mu_n)]$ and outside $[\Delta\alpha_n^o(\mu_{n+1})]$ of the region. Consider a particle ensemble with

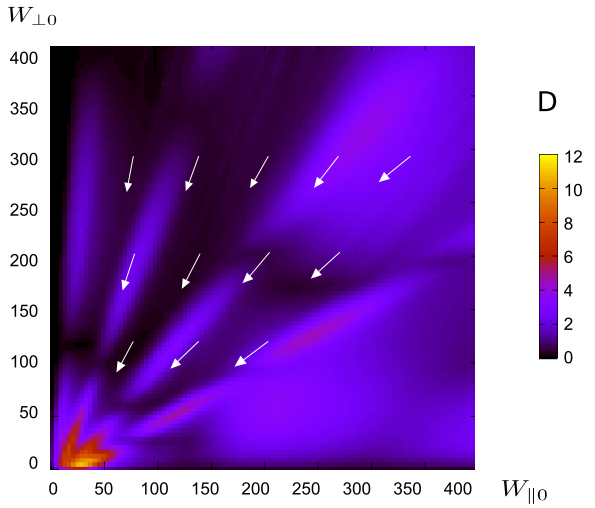

Figure 2.2: Diffusion diagram for the arrangement of paths shown on Fig. 1.3. Arrows indicate the direction of the strongest diffusion, colors show the magnitude of the diffusion coefficient. The area with the largest D is influenced by several diffusion paths.

$\mu_n = \mu_0$ and a homogeneous distribution in α_n and assume that $\Delta\alpha_n^i \ll \Delta\alpha_n^o$. The difference $\alpha_{n+1} - \alpha_n$ can then be expressed as $\Delta\alpha_n^o[\mu_n + M(\mu_n)\cos\alpha_n]$. Therefore, if the wave amplitude and the device length are sufficiently large and $(\partial\Delta\alpha_n^o/\partial\mu)M \gg 1$, the particle distribution will exhibit strong phase-mixing (Fig. 2.1) after just a single bounce.

Let $\boldsymbol{g} = (R, \theta, \Psi, u_\perp, u_\|, \tau)$ be a vector specifying the state of a particle upon crossing the device midplane, where R is the radial position of the particle gyrocenter and Ψ is it's azimuthal angle. The particle dynamics can then be studied by iterating $\boldsymbol{g}_{n+1} = \hat{G}\boldsymbol{g}_n$, where $\hat{G}$ maps a particle state to the state after a single longitudinal bounce. If the phase-mixing is sufficiently strong, one can choose random wave- and gyro-phase on each iteration, thus making it possible to consider a mapping of just a four-dimensional vector $(R, u_\perp, u_\|, \tau)$. Furthermore, assuming that all particles are localized in a thin ring $R \approx R_0$ and assuming that the particle radial excursion

ΔR is small, one can neglect the dependence of $k_\perp \approx (m/R_0)(1 - \Delta R/R_0)$ on ΔR and study the mapping of a three dimensional vector $\boldsymbol{h} = (u_\perp, u_\parallel, \tau)$. Generally speaking, if the wave phase is randomized on each particle bounce, the mapping $\hat{H} : \boldsymbol{h}_n \mapsto \boldsymbol{h}_{n+1}$ should be sampled from a probability distribution $\bar{H}(\boldsymbol{h}_{n+1}; \boldsymbol{h}_n)$, which can be determined by solving the single particle motion equations for various gyro- and wave-phases. However, if the particle excursion on a single bounce is small, one can use the central limit theorem to approximate $\bar{H}$ by the normal distribution, *i.e.,* the mapping $\hat{H}$ can be approximated by:

$$\boldsymbol{u}_{n+1} = \boldsymbol{u}_n + \boldsymbol{f} + \hat{\boldsymbol{d}}\,\boldsymbol{w}, \tag{2.9}$$

$$\tau_{n+1} = \tau_n + \Delta\tau(\boldsymbol{u}), \tag{2.10}$$

where $\boldsymbol{u} = (u_\perp, u_\parallel)$, $\boldsymbol{f} = \langle \Delta\boldsymbol{u} \rangle$, $\hat{\boldsymbol{d}} = \langle (\Delta\boldsymbol{u} - \langle \Delta\boldsymbol{u} \rangle)\,(\Delta\boldsymbol{u} - \langle \Delta\boldsymbol{u} \rangle) \rangle$, $\Delta\tau$ is the time between particle bounces and $\boldsymbol{w}$ is sampled from a two-dimensional normal distribution with $\langle w_i \rangle = 0$ and $\langle w_i w_j \rangle = \delta_{i,j}$ with $\delta_{i,j}$ being the Kronecker delta. The vector field $\boldsymbol{f}$ and tensor field $\hat{\boldsymbol{d}}$ can be calculated by integrating Eq. (2.4) or Eqs. (2.5) and (2.6) numerically and then visualized using the so-called diffusion diagrams showing the direction and the magnitude of the strongest diffusion (Fig. 2.2). (Note here that particles with regular orbits can, in principle, be accounted for by setting $\hat{\boldsymbol{d}}$ and $\boldsymbol{f}$ to 0.) Strictly speaking, the time increment $\Delta\tau$ entering Eq. (2.10) also contains a random component, which is proportional to $(\Delta u_\parallel / u_\parallel)(L_{\mathrm{wl}}/L_{\mathrm{sys}})$, where L_{w} is the total length of all rf regions and L_{sys} is the full mirror length. This component, however, is much smaller than the particle bounce time and it's contribution scaling as the square root of number of bounces can therefore be neglected on large times.

Assuming that the average velocity increments given by Eq. (2.9) are much smaller than the characteristic particle velocity and neglecting the random component of $\Delta\tau$,

one can rewrite Eq. (2.9) as a stochastic differential equation [Gardiner, 2004]

$$\dot{\boldsymbol{u}} = \frac{\boldsymbol{f}}{\Delta\tau} + \frac{\hat{\boldsymbol{d}}}{\sqrt{\Delta\tau}}\dot{\widetilde{\boldsymbol{w}}}, \tag{2.11}$$

where $\widetilde{\boldsymbol{w}}$ is a two-dimensional Wiener process. Consider an ensemble of particles following Eq. (2.11). The particle distribution function of such an ensemble can then be described by the Fokker-Planck equation:

$$\frac{\partial p}{\partial \tau} = -\sum_i \frac{\partial}{\partial u_i}\left(\frac{f_i p}{\Delta\tau}\right) + \frac{1}{2}\sum_{i,j}\frac{\partial^2}{\partial u_i \partial u_j}\left[\frac{p}{\Delta\tau}\left(\hat{\boldsymbol{d}}\hat{\boldsymbol{d}}^T\right)_{ij}\right], \tag{2.12}$$

where $p(\boldsymbol{u}, \tau)$ is the particle distribution function in the two-dimensional velocity space (usually chosen to be the *midplane velocity space*). Note, however, that this model does not include particle collisions. Our assumption is that collisions may be neglected since the collision frequency is much smaller than the characteristic inverse time scale in the regimes of interest.

2.3 Regimes of strong and weak magnetic field inhomogeneity

Equations (2.5)-(2.8) can be used to estimate various characteristics of the diffusion paths. For example, Eqs. (2.7) and (2.8) define the local shape of the diffusion path by connecting the parallel velocity perturbation δ to the perturbations of the particle energy and the particle radial position. Specifically, integrating Eqs. (2.7) and (2.8), one obtains:

$$\frac{\Delta E}{\omega} \approx \frac{\Delta u_\parallel}{k_z} \approx \frac{\Delta(\Omega r^2/2)}{m}, \tag{2.13}$$

where Δx stands for a small change of x over a given time interval. Note that the same result follows from the Manley-Rowe relations written for the wave-particle interaction Hamiltonian [Dodin and Fisch, 2008a; Dodin et al., 2008].

If $u_\perp \ll \omega/k_z$, Eq. (2.13) suggests that $\Delta u_\perp \gg \Delta u_\parallel$. As a result, since the parallel velocity is perturbed only weakly, the particle stays in resonance with the wave even if the change of particle energy is substantial. Rewriting $\Delta u_\perp \gg \Delta u_\parallel$ (expressed in local variables) in midplane energy coordinates reading $W_\perp^0 = u_\perp^2/2b$ and $W_\parallel^0 = u_\parallel^2/2 + u_\perp^2(1-b^{-1})/2$, one obtains:

$$\frac{\Delta W_\perp^0}{\Delta W_\parallel^0} \approx \frac{1+(1-\ell\Omega/\omega)}{(b-1)-(1-\ell\Omega/\omega)} \approx (b-1)^{-1} \tag{2.14}$$

in accordance with Ref. [Fisch, 2006].

Let us now simplify Eqs. (2.5) and (2.6), solving them analytically in two opposite regimes of strong and weak magnetic field inhomogeneity. First notice that Eqs. (2.5) and (2.6) can be rewritten in a Hamiltonian form:

$$H = \frac{\omega - k_z u_\parallel - \ell\Omega}{u_\parallel}\delta - \frac{\omega-\ell\Omega}{u_\parallel^2}\frac{\delta^2}{2} - \frac{f_0 k_z}{u_\parallel} J_\ell(m\rho/r)\mathrm{Re}\left(i^\ell e^{-i\phi}\right) - \\ - \frac{f_0'}{u_\parallel} J_\ell(m\rho/r)\mathrm{Re}\left(i^{\ell-1}e^{-i\phi}\right) = \bar{a}\delta^2 + \bar{b}\delta + \bar{c}\cos(\phi+\phi_0), \tag{2.15}$$

where δ, ϕ and z play the roles of the canonical momentum, canonical coordinate and canonical time correspondingly; $\Omega(z)$, $u_\parallel$, f_0 and f_0' are treated as independent slow-varying parameters. System dynamics governed by Hamiltonian (2.15) has two "time" scales: (a) scale z_{bnc} associated with a particle bounce motion in a homogeneous magnetic field and (b) scale z_{inhom} of explicit dependence of the Hamiltonian on z. The analytical solution of the Hamiltonian equations can then be simplified when a fraction of these two scales ν defined as

$$\nu = \frac{z_{\mathrm{bnc}}}{z_{\mathrm{inhom}}} = \frac{\ell\Omega' u_\parallel}{2\pi k_\parallel^2 f_0 J_\ell(m\rho/r)} \tag{2.16}$$

is much greater or much smaller than unity.

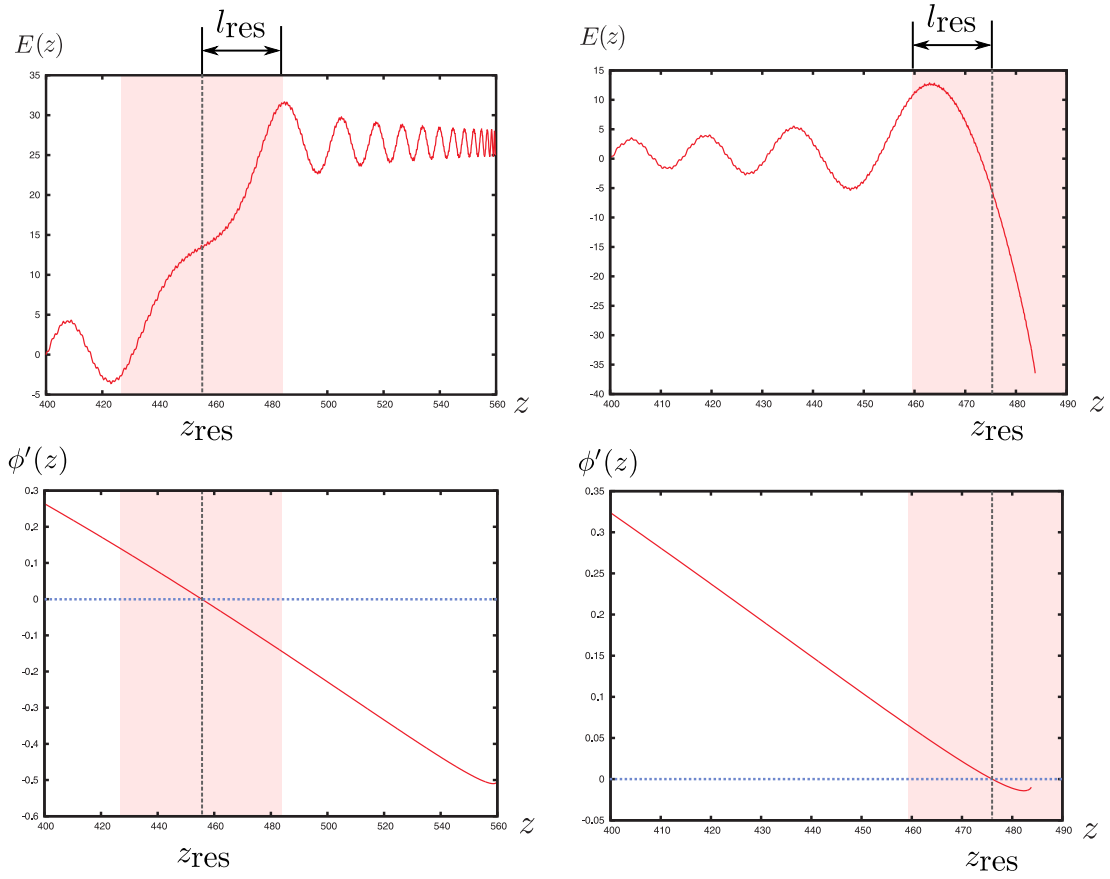

Figure 2.3: Dependencies $E(z)$ and $\phi'(z)$ calculated for two different physical systems using Eqs. (2.5) and (2.6). The resonance layer, in which the major contribution to ΔE occurs, is located in a vicinity of $z = z_{\rm res}$ defined as $\phi'(z_{\rm res}) = 0$. The characteristic size of the resonance layer $l_{\rm res}$ is such that $|\phi(z_{\rm res} \pm l_{\rm res}) - \phi(z_{\rm res})| = \pi$.

When $\nu \gg 1$ one can neglect the term proportional to δ in Eq. (2.6), omitting nonlinear phase corrections. Particle velocity perturbation change is then given by

$$\Delta\delta \approx -\int \frac{f_0(z)k_z J_\ell(m\rho/r)}{u_\parallel^0} \cdot \sin\left(\int \frac{\omega - k_z u_\parallel^0 - \ell\Omega}{u_\parallel^0}\, dz + \ell\theta_0\right) dz. \tag{2.17}$$

Consider a single rf region of width $l^i \ll L$. The wave-particle resonance occurs in this region near the point $z_{\rm res}$ solving $\phi'(z_{\rm res}) = \omega - k_z u_\parallel^0(z_{\rm res}) - \ell\Omega(z_{\rm res}) = 0$ (Fig. 2.3. The width $l_{\rm res}$ of the resonance layer in a configuration space can then be defined by setting $\phi(z_{\rm res} \pm l_{\rm res}) - \phi(z_{\rm res}) = \pi$. Using Eq. (2.17), one can obtain the following expression for $l_{\rm res}$:

$$l_{\rm res} \approx \sqrt{\frac{u_\parallel}{\Omega'|\chi|}}, \tag{2.18}$$

where $\chi = (\ell - \omega/\Omega)(u_\perp^2/2u_\parallel^2 - 1) - \ell$. Note here that choosing $l^i \gg l_{\rm res}$ does not result in stronger resonant particle diffusion compared to $l^i \sim l_{\rm res}$ (Fig. 2.3).

After calculating the resonance width in the configuration space, one can also estimate the resonance width (or the diffusion path width) in the midplane velocity space. A range of resonant parallel velocities is proportional to the difference of magnetic field magnitudes on both sides of the rf region:

$$\Delta u_{\rm res} \sim \frac{\ell\Omega'(l^i + l_{\rm res})}{k_z}, \tag{2.19}$$

where assuming that the wave profile is abrupt, we extended the rf region length l^i by $l_{\rm res}$. This expression and the definition of $l_{\rm res}$ suggest that the increase of rf region width over $l_{\rm res}$ increases the range of resonant velocities $\Delta u_{\rm res}$, but does not lead to an increase of a wave-particle energy exchange.

Now consider the case $\nu \ll 1$. If $l^i \ll z_{\rm bnc}$, one can use Eq. (2.17) to describe the dynamics of resonant particles. However, when $l^i \gtrsim z_{\rm bnc}$, trapping and detrapping effects become essential [Bruhwiler and Cary, 1992, 1994b,a]. In this case, the characteristic diffusion path width and diffusion coefficient are defined by the trapping

width[1] $\Delta u_{\rm trap} \sim \sqrt{f_0 J_\ell(k_\perp \rho)}$ and the coordinates, where the particle is trapped by the wave and where it is released. The particle velocity change after the passage of the rf region can be estimated by considering adiabatic invariant conservation [Landau and Lifshitz, 1976] in both trapped and passing areas of the phase space:

$$J_{\rm passing} = \frac{\pi \bar{b}}{\bar{a}} + \int\limits_0^{2\pi} \xi \, d\phi = \langle \delta \rangle_\phi \approx \text{const}, \tag{2.20}$$

$$J_{\rm trapped} = 2 \int\limits_{\phi_{\rm min}}^{\phi_{\rm max}} |\xi| \, d\phi \approx \text{const}, \tag{2.21}$$

where $\xi = \delta - \bar{b}/2\bar{a}$, $\phi_{\rm min}$ and $\phi_{\rm max}$ are the minimal and maximal phases for which the integrand turns to zero and $\langle \cdot \rangle_\phi$ stands for average over the wave phase.

The evolution of the particle velocity perturbation in the rf region with smooth profile can be broken into three stages during which adiabatic invariant is approximately conserved: before the trapping, trapping in the wave (if it occurs) and the passing motion after the trapping. If the particle is not trapped in the wave, the final value of δ is the same as the initial value because $\langle \delta \rangle_\phi$ changes when the particle is trapped only. As a result, the effective diffusion coefficient for such a particle would vanish. If the particle is trapped in the wave at some point z_t, depending on parameters and initial particle phase, it can either be reflected from the wave or pass it, untrapping at some z_u with $\delta_+ = -\bar{b}/2\bar{a} + \Xi$ or $\delta_- = -\bar{b}/2\bar{a} - \Xi$, where $\Xi = \langle |\xi| \rangle_\phi$, $\bar{a}$, $\bar{b}$ and E are calculated for the separatrix at z_u. The formalism discussed in Refs. [Bruhwiler and Cary, 1992, 1994b,a; Cary et al., 1986; Cary and Skodje, 1989] can, in principle, be used to estimate the ratio of particles detrapping with $\delta = \delta_+$ and $\delta = \delta_-$. This calculation, however, lies beyond the scope of this thesis.

---

[1] The discussion of this concept can be found, for example, in Ref. [Smith and Pereira, 1978].

In all our numerical simulations, the magnetic field profile was sufficiently steep to have $\nu \gg 1$, allowing us to use Eqs. (2.18) and (2.19) to estimate the characteristic diffusion path characteristics. Furthermore, using Eq. (2.17)) and assuming that for most particles, phase decorrelation occurs on a single bounce, one can also estimate the diffusion coefficient along the diffusion path [Grawe, 1969; Kesner, 1979; Bernstein and Baxter, 1981]:

$$D_E = \langle \Delta E^2 \rangle / \Delta\tau \sim f_0^2(r)\sqrt{bE}J_\ell^2(\rho bE/r), \tag{2.22}$$

where the particle bounce time $\Delta\tau$ was approximated by $2\pi L/u_\perp$. Note here that the diffusion coefficient D_E vanishes in an infinite number of points along the diffusion path. The zeroes of D_E turn out to be important because they can limit the stochastic particle heating at high or low energies.

2.4 Computational method

Describing the particle motion as a random walk process is a major computational simplification. To verify that a Monte-Carlo simulation of Eq. (2.12) based on Eqs. (2.9) and (2.10) describes the particle distribution function evolution adequately, even assuming wave coherence and even in the absence of collisions, we compared our Monte-Carlo results with the exact solution of Eq. (2.4). The number of particles which left the system n_{loss}, the average energy of all particles E (including those escaped), and the characteristic shape of the particle distribution were compared for different times t for resonant particles diffusing along a single path. The good agreement shown in Table 2.1 between dependencies obtained using Monte-Carlo and

Table 2.1: Dependencies $n_{\rm loss}(t)$ and $E(t)$ for resonant particles calculated using both random-walk equations and exact 6D particle motion Eq. (2.4).

t, ms	3	6	12	25	50
$n_{\rm loss\ walk/exact}$, %	7.5 / 9.0	25.6 / 29.4	48.3 / 49.7	69.2 / 74.3	83.3 / 86.3
$E_{\rm walk/exact}$, MeV	3.45 / 3.40	3.19 / 3.13	2.92 / 2.85	2.59 / 2.38	2.23 / 2.04

Eq. (2.4) suggests that the random walk can be used to describe the particle distribution evolution. Nonetheless, in order to verify our other results, exact solutions for small number of particles were tracked in all further simulations.

The approximate equations (2.5), (2.6) and (2.7) can be used to estimate resonant particle diffusion tensor $\hat{\boldsymbol{d}}$ and determine characteristic parameters of the diffusion paths. These approximations will be most precise for short times; large deviations in particle distribution evolution are expected when long-time dynamics in a system with several rf waves is considered.

The rf region parameters are chosen using estimates outlined in Sec. 2.3. First, the inner radial profile boundary r_0 and ion-cyclotron resonance number ℓ are picked. The designed diffusion path slope defines b at the rf region location and the azimuthal wave number m is chosen to optimize the diffusion coefficient distribution along the path $D_E \sim \sqrt{E} J_\ell^2(m\rho/r)$. The designed path width defines $k_\parallel$ through Eq. (2.19). Even though the diffusion path width should be smaller for more effective α-channeling, it cannot be chosen arbitrarily small, being limited by Eq. (2.19) and condition $k_\parallel \ll \omega/u_{\parallel\,\rm res}$ which is necessary for small particle parallel velocity perturbation. The wave frequency ω is chosen to select a certain resonant parallel velocity $u_{\parallel\,\rm res} = (\omega - \ell\Omega)/k_\parallel$ and the rf region length is picked to be smaller than $l_{\rm res}$ defined by Eq. (2.18) and smaller than $k_\parallel u_\parallel/(b'L)$ to avoid resonance with particles reflected inside the wave.

The optimal number of rf regions in the system is defined by the requirement to capture α particles within a whole accessable range of pitch angles and by the length of the system. The amplitudes of the rf regions determine the α particle diffusion rate. There are also limitations imposed on these amplitudes. The waves of course are derived under the condition that $e\varphi \ll kT$ so that the perturbation of plasma density is small, *i.e.,* $n \approx n_0 \exp(-e\varphi/kT)$. A more stringent limitation arises from the effect on the fuel ions; as discussed in Sec. 2.6, using high-amplitude rf waves can lead to fuel ion pump-out even if the interaction is non-resonant. Thus, for intersecting multiple waves, the fuel ion residence time may impose additional limitations on practical rf wave amplitudes.

2.5 Simulation results

In the following, the feasibility of cooling down 3.5 MeV α particles using rf waves was explored computationally by choosing an optimal arrangement of diffusion paths in the midplane energy space. The configuration consisted of thin diffusion paths with nearly identical resonant velocities, but different slopes in $W_\parallel - W_\perp$ space (see Fig. 1.3). Diffusion paths with various slopes were used to diffuse α particles within a wide range of pitch-angles. The wave resonant velocity was chosen to avoid expulsion of fuel ions and maximize the extracted α particle energy.

For efficient α-channeling, α particle heating along the diffusion path should be limited. The issue with unlimited heating is not that the particle gains unlimited energy; rather the issue that in the finite time scale associated with its collisional slowing down, the α particle is not extracted. A limitation can be imposed through the radial particle excursion $r_\Delta > 0$ coupled to the energy excursion ΔE. Suppose

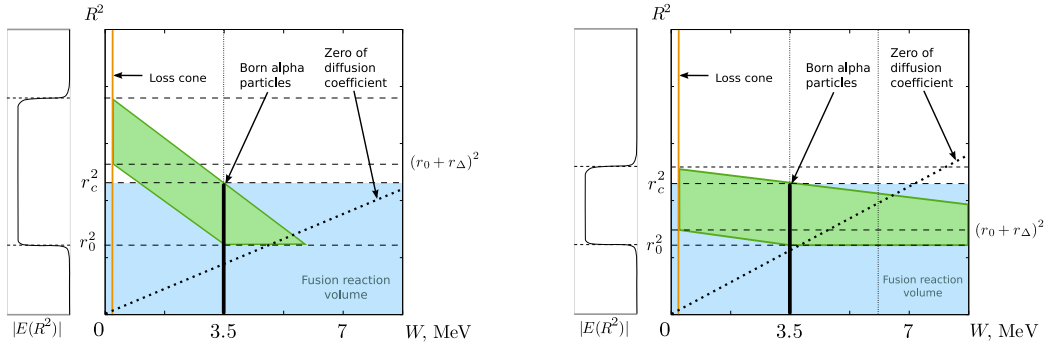

Figure 2.4: Diffusion paths in the coupled configuration-energy space in two regimes: (a) $r_\Delta \sim r_c$ with limitation at low wave radial profile boundary r_0 and (b) $r_\Delta \ll r_c$ with limitation at $k_\perp \rho \approx m\alpha\sqrt{E}/r = z_1$, where z_1 stands for first zero of $J_\ell(z)$ and α is a constant depending on $b(z)$.

the α particles are born in a hot device center of radius r_c. If $r_\Delta \gtrsim r_c$, the limitation of α particle penetration into the device core is caused by approaching the lower wave boundary r_0 (see Fig. 2.4a). When $r_\Delta \ll r_c$, the majority of α particles can be heated to very high energies while remaining in the rf region (see Fig. 2.4b). The effects which can limit heating in this case include: (a) the vanishing of the diffusion coefficient $D_E \sim \sqrt{E}J_\ell^2(m\rho/r)$; (b) leaving the resonance $\omega - k_\| u_\| - \ell\Omega \approx 0$ when a change of the particle energy ΔE leads to a significant parallel velocity change $\Delta u_\| \sim (k_\|/\omega)\Delta E$; (c) the boundary of the stochastic region occuring at high particle energies [Aamodt, 1971; Rosenbluth, 1972; Karney, 1979].

Stuyding the feasibility of the α-channeling technique, we simulated two device designs. In both designs, the magnetic field was 2 T at the midplane with parabolic axial profile $b = 1 + z^2/L^2$, and mirror ratio $R = 5$; in the longer design, $L = 20$ m and in the smaller design, $L = 10$ m. Eight waves with the longitudinal wave profile given by $|E(z)| \sim E_0 \sin[\pi(z - z^i)/l^i]$, $E_0 \sim 200$ to 300 kV/m, $r_0 \sim 1$ m, $m \sim 40$ to 70 and $k_\| \sim 0.04$ to 0.1 cm^{-1} were placed along the system axis. These waves perturbed the density of 20 keV plasma by less than 5%. Because the effective resonance layer

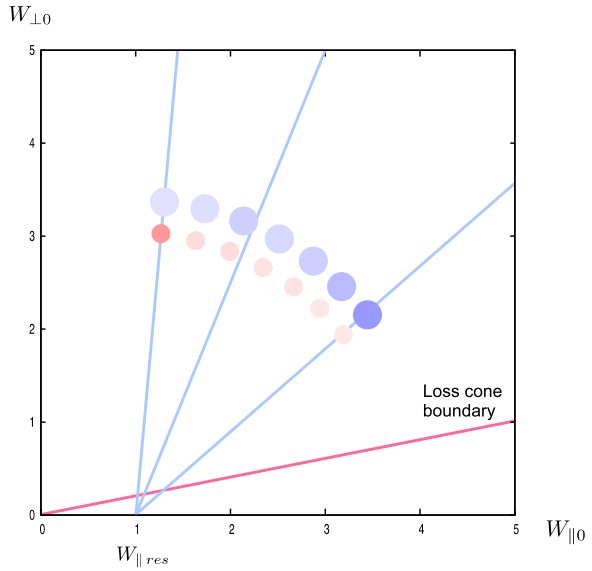

Figure 2.5: Dependence of the channeling time (small circle) and the average output energy (large circle) on the initial pitch angle of the α particle. Darker colors correspond to larger values.

length $l_{\rm res}$ defined by Eq. (2.18) is proportional to $\sqrt{L}$, increasing the length of the system and choosing $l^i \approx l_{\rm res}$, while keeping other wave parameters unchanged, results not only in enhanced particle diffusion, but also in smaller diffusion path widths (see Eq. (2.19)). Therefore, to avoid diffusion near $u = 0$, larger resonant velocities were chosen in the system with $L = 10\,\mathrm{m}$; this resulted in higher average output α particle energy and smaller α-channeling efficiency (see Table 2.2).

The numerical simulations in the longer device were conducted for two regimes (see Table 2.2): (a) $r_\Delta \ll r_c$ with limitation by a zero of a Bessel function and (b) "radially limited" paths when $r_\Delta \gtrsim r_c$. In the system with paths limited by zeros of Bessel functions, particles left the device slowly because the diffusion coefficient never vanishes exactly on the path. Some particles could pass the point with $D_E \approx 0$, becoming trapped above it. The average particle energy over long times was also found to be higher because particles trapped over $D_E \approx 0$ could be heated to rather

Table 2.2: Numerical simulation results for both device designs. Here n_{loss} is the amount of α particles initially resonant with waves (approximately 70% of all trapped α particles interacting with waves) that leave the system in time t, E is the average particle energy for both left particles and particles remaining in the system, E_{loss} is the average energy of all expelled particles.

t, ms	10	25	50	100	150	300
$L = 10$ m, Bessel zero limitation						
n_{loss}, %	22.0	32.2	42.2	51.4	56.6	65.1
E, MeV	3.0	2.9	2.9	2.8	2.6	2.5
E_{loss}, MeV	1.06	0.99	0.94	0.88	0.85	0.85
$L = 20$ m, Bessel zero limitation						
n_{loss}, %	24.1	35.6	46.7	56.7	62.3	72.0
E, MeV	2.7	2.6	2.4	2.3	2.2	2.1
E_{loss}, MeV	0.91	0.88	0.84	0.75	0.76	0.77
$L = 20$ m, radial limitation						
n_{loss}, %	31.1	53.3	66.7	71.1	75.5	80.2
E, MeV	2.7	2.3	2.1	1.9	1.8	1.6
E_{loss}, MeV	0.96	0.84	0.76	0.63	0.6	0.55

high energies. Further numerical simulations of α-channeling in the longer device confirmed the possibility to extract more than 60% of energy of resonant α particles in 300 ms. These simulations employed waves that perturb the plasma density by less than 5%.

Figure 2.5 shows the dependence of the average output energy and the number of particles leaving the system in a given time on the initial α particle pitch angle. Particles near the loss cone boundary were observed to leave the system quicker, but with higher energy compared to the more deeply trapped particles. Also, most of the α particles left the system on a time much smaller than the characteristic collisional

slowing down time [2], confirming that the collisionless equations describe the particle density evolution adequately.

Large radial particle excursions and mostly perpendicular velocity-space diffusion can be achieved by using waves with large azimuthal wave numbers. Low azimuthal wave number waves in ion-cyclotron range of frequencies have been coupled into mirrors [Intrator et al., 1989; Amagishi et al., 1982; Majeski et al., 1987; Yamaguchi et al., 2006; Yasaka et al., 1992; Yamaguchi et al., 2004; Yatsu et al., 2001]. The excitation of the higher azimuthal wave number waves required for effective α-channeling might be achieved through mode conversion.

For a system with several rf regions with amplitudes $E_0 \sim 250\,\mathrm{kV/m}$, α particles leave the system quickly. For lower wave amplitudes, many rf regions are needed to retain the short exit times. Thus, by decreasing wave amplitudes and increasing the number of rf regions and the device volume they affect, it is possible to retain the overall wave energy and α-channeling efficiency. Additional techniques for increasing α-channeling efficiency for fixed wave amplitudes include: use of higher cyclotron resonances, but lower resonant velocities; and waves with higher azimuthal wave numbers. The wave parallel resonant velocity, which determines the maximum possible energy extracted from α particles (see Fig. 1.3), must be chosen to avoid resonant interaction with fuel ions. As discussed in Sec. 2.6, higher ion-cyclotron resonances diminish the characteristic ion diffusion rate, allowing a smaller wave parallel resonant velocity, thus improving the α-channeling efficiency. A second technique is to decrease α-channeling time by improving α particle heating limitation along the diffusion path using waves with higher azimuthal wave numbers. If the azimuthal wave

[2]The characterstic α particle slowing down time is approximately equal to 1 s for plasmas with $T = 10\,\mathrm{keV}$ and $n_e = 3 \cdot 10^{13}\,\mathrm{cm}^{-3}$.

number is increased, the point where $D_E \approx 0$ moves towards the origin along the diffusion path. Once the zero of D_E passes $E_0 = 3.5\,\mathrm{MeV}$, the α particle extraction is nearly stopped. To avoid vanishing of D_E along the diffusion path, several almost identical decorrelated rf regions with large, but different azimuthal wave numbers might be employed.

Simulations for the system of 8 high-m rf regions with $\ell = 3$ and $E_0 \sim 150\,\mathrm{kV/m}$ showed that more than 60% of energy of all resonant α particles could be extracted in 300 ms. The same α-channeling efficiency was simulated for 16 waves with $E_0 \sim 100\,\mathrm{kV/m}$. Extrapolating these results, the same efficiency is expected for a system of 40 rf regions with $E_0 \sim 60\,\mathrm{kV/m}$ and 60 rf regions with $E_0 \sim 50\,\mathrm{kV/m}$. Any further increase of the number of rf regions is limited by the length of the device.

The injection of plasma in mirror machines for fueling can also be approached using rf waves [Kesner, 1979; Breun et al., 1981]. In simulating fuel injection and heating with the same waves used also for α particle energy extraction, two system designs were considered.

In the first configuration, a high-density ion source of cold fuel ions was located near the trapped-passing boundary. Since the diffusion paths connect particles on the loss cone near the cold device periphery with deeply trapped particles in the hot center (see Fig. 2.6a), this results in a population inversion along the path for both ions and α particles [Fisch, 2006]. An ion injected on the path passes through the whole device, interacting with all rf regions situated along its length. The velocity excursion, upon interaction with the resonant wave, can cause it to either become more deeply trapped, or to leave the device. If the ion stays in the device after a single pass, the process repeats until the particle leaves through the loss cone or until it gains substantial energy and fuses. The ion injection at the loss cone is most efficient

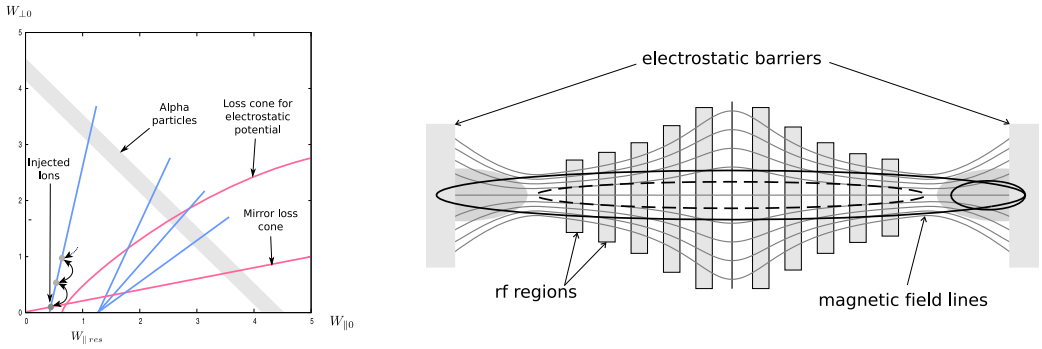

Figure 2.6: Configuration used for ion injection with the source located on the loss cone: (a) diffusion paths in the midplane energy space, ion velocity excursions are shown schematically with gray circles; (b) proposed device design; three ion trajectories are shown: (i) trajectories of the ion with velocity above the loss cone, trapped in the smaller volume between the mirror and the electrostatic barrier (smaller solid ellipse) and (ii) between the magnetic mirrors (dashed ellipse); (iii) trajectory of the ion below the loss cone, passing through the whole device and being reflected from the electrostatic barriers (larger solid ellipse).

if the source energy consumption is small compared to the energy of heated fuel ions. This is achievable when the energy of injected, but detrapped, particles is recycled. A possible method might be to use an electrostatic particle traps at both ends of the device (see Fig. 2.6b). A cold ion trapped in the smaller region between the magnetic mirror and electrostatic potential barrier may penetrate into the central plug with velocity slightly above the loss cone. If the low-energy particle is not trapped or if it detraps after some period of time, it gets reflected by the electrostatic potential, thus retaining its energy and having a chance to be trapped again.

In the second configuration, ions were injected above the loss cone and diffused along the path limited below the injection point (see Fig. 2.7a), in order to trap and heat the majority of the injected ions while still extracting α particles.

The possibility to heat fuel ions, transporting them deeper into the mirror machine, and yet cool α particles along the same diffusion path was demonstrated in

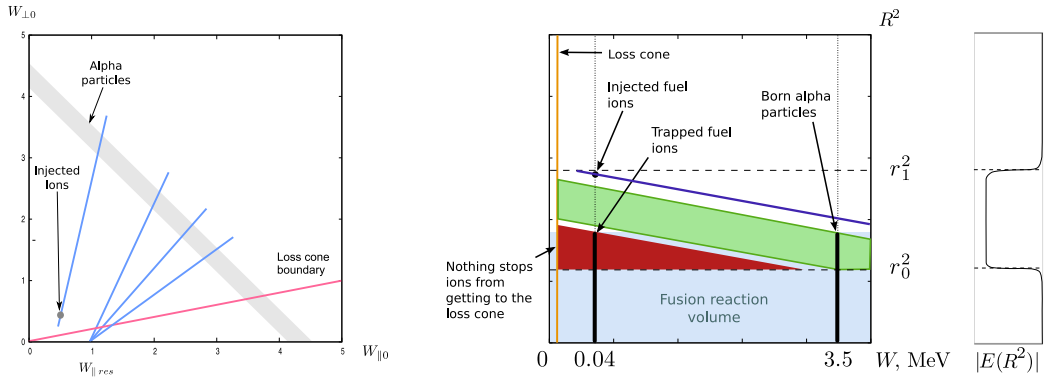

Figure 2.7: Arrangement of diffusion paths allowing to heat ions by the same wave which is used to cool down α particles: (a) diffusion paths in the midplane energy space; (b) diffusion paths in the coupled configuration-energy space, injected ions are limited at $r = r_1$, α particles and trapped fuel ions with $r > r_0$ escape the system through the loss cone.

simulations for both device designs. The characteristic time of ion diffusion along the path was found to be approximately equal to 300 ms. Numerical simulations for configuration with ion injection over the loss cone showed that the average energy of injected ions increased from 20 keV to 80 keV in 100 ms, while only approximately 3% of them escaped the device following other diffusion paths. The loss of the average α particle energy on the same time scale exceeded 400 keV. The time over which half of the injected ions left the device was found to exceed 1 s.

Despite these promising simulation results, both of the ion injection schemes have certain shortcomings. In both designs, the injected ions can be overheated, reaching energies up to 1.7 MeV. This would not only lower the effective DT fusion reaction cross section relative to its maximum value at $E \sim 70$ keV, but also not optimally employ the rf wave energy. Collisions and other collisionless effects not considered here might, however, limit the heating. Utilization of high-density ion source and trapping escaped ions in the first configuration also imposes additional engineering challenges. The shortcoming of the second injection scheme is the possible interaction

of employed rf waves with the trapped fuel ions (see Fig. 2.7b). However, a wave with $k_\parallel = k_\parallel(r)$ with a larger resonant parallel velocity near the center, might help to avoid this interaction.

2.6 Ion ejection by rf waves

One of the major concerns in coupling waves in the ion-cyclotron range of frequencies into mirror machine plasmas is the fuel ion pump-out [Baldwin et al., 1976; Turner et al., 1977; Baldwin, 1977; Goto et al., 2000]. In Ref. [Goto et al., 2000], for instance, an increase of ion loss rate was found to correlate with emergence of Alfvén ion cyclotron wave, whose diffusion path connected ions with large pitch angles with the loss cone boundary. Despite using non-resonant rf waves in the present study, the numerical simulations of the fuel ion distribution evolution in the first device design, discussed in Sec. 2.5 with $L = 20\,\mathrm{m}$, showed that the ion lifetime was approximately equal to 50 ms, corresponding to several hundred bounces in the device. Note that even though the number of bounces is close to those obtained in early works on rf plasma pump-out by DCLC instability [Turner et al., 1977], in our simulations waves with almost 100 times larger amplitudes were employed. This smaller pump-out is due to the fact that although nonresonant diffusion takes place, it is much less effective then diffusion by resonant waves.

The characteristic ion velocity excursion in a single pass through the rf region depends on the amplitude of the resonant longitudinal wave harmonic with $k_\parallel \approx (\omega - \ell\Omega)/u_\parallel$. The parallel resonance velocities of the diffusion paths were chosen to exceed the fuel ion thermal velocity, thereby avoiding such resonances. However, the longitudinal spectrum of the wave with profile $|E(z)| \sim E_0 \sin[\pi(z - z^i)/l^i]$ had long

$\sim 1/k_\parallel^2$ tails, resulting in a relatively low ion confinement time. To avoid the long tails, smooth wave profiles with an exponentially decaying spectrum were used and numerically verified to allow better ion confinement, reaching 200 ms. Any further increase of ion time of life by increasing $k_\parallel l^i$, thus making the wave spectrum narrower, is limited by the magnetic field gradients, which broaden the resonance. If at some point $z = z_0$ of the rf region, the resonance condition is satisfied for α particles, then $\omega - k_\parallel u_{\parallel\alpha} - \ell\Omega \approx 0$, and at the point $z = z_0 + \Delta z = z_0 + k_\parallel u_{\parallel\alpha}/(\ell\Omega')$, the resonance condition is satisfied for cold ions, thus limiting the rf region length by $l^i \ll \Delta z$.

Besides diminishing ion ejection by using non-resonant rf waves, ion ejection can also be avoided by making the diffusion coefficient for ions vanishingly small near the point where the ions would be ejected, *i.e.,* at low energy, where $k_\perp \rho_i < 1$. If $k_\perp \rho_i \lesssim 1$, where ρ_i is a characteristic ion gyroradius, ion energy diffusion coefficient $D_E \sim \sqrt{E} J_\ell^2(k_\perp \rho_i) \sim \sqrt{E}(k_\perp \rho_i)^{2\ell}$ can be diminished by using higher cyclotron resonances. The use of waves with $l = 3$ to 5 was shown numerically to further increase ion time of life to several seconds, while retaining the α-channeling efficiency.

The use of the rf waves for injecting the fuel ions and heating those ions is only one of the possible dual uses for the waves that accomplish the α-channeling. Other uses might be to create transport barriers [Cho et al., 2006] or to maintain a sloshing ion distribusion [Moiseenko and Ågren, 2005]. In either case, if the rf waves are amplified by cooling the α particles, the energy requirement to achieve these uses becomes small. It is anticipated that the effect would would best be accomplished by making use of a lightly damped mode in the ion cyclotron range of frequencies [Litwin and Hershkowitz, 1987; Hanson and Ott, 1984; Yamaguchi et al., 2006]. Identifaction of such waves in mirror geometry is discussed in Chapter 4.

Chapter 3

Flux Control in Networks of Diffusion Paths

One of the core ideas of the α-channeling technique is using external fields to cause particle diffusion in localized volumes of the phase space. Those particles that belong to the intersection of several such volumes corresponding to different rf regions are expected to interact resonantly with several waves simultaneously. As a result, particles exhibiting a random walk inside of one of the localized volumes can at some point make a transition to a different volume, then after encountering the same or different intersection region, they can make another transition, and so on. The resulting particle dynamics in this case can become very complex and the redistribution of fluxes of the outgoing particles (leaving the system through the loss boundary) may occur.

Consider, for example, an implementation of the α-channeling technique in a mirror machine, where rf regions can be placed at the minimum $B_{\min}$, or near the maximum $B_{\max}$ of the magnetic field only (Fig. 3.1). As follows from the discussions

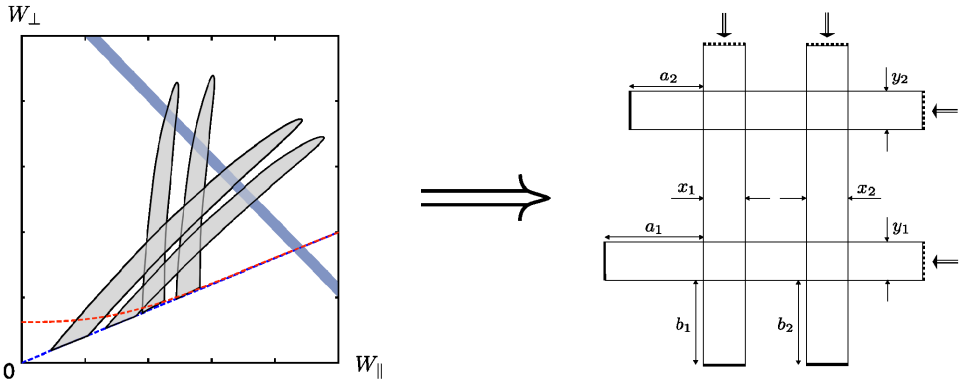

Figure 3.1: Diffusion paths in the midplane energy space W and the corresponding rectangular network R of intersecting diffusion paths. The rectangular network of diffusion paths modeling particle motion in the midplane energy space can be justified by assuming the diffusion equation on W and making a linear transformation on this space. The left and bottom boundaries of the diffusion paths in R correspond to the intersections of diffusion paths with the loss cone in W (shown with dashed lines: blue for magnetic field confinement only, red in the presence of an electrostatic potential). The particle flows entering the top and right diffusion path ends in R model an incoming flow of born α particles in W (blue area).

in Sec. 1, the corresponding diffusion paths are characterized by small and large inclinations in the midplane particle energy space $(W_{\perp 0}, W_{\parallel 0})$. Specifically, particles interacting with the rf region placed near $B = B_{\min}$ are exhibiting a random walk in $W_{\perp 0}$, while $W_{\parallel 0}$ remains nearly constant. Particles interacting with the rf region placed near $B = B_{\max}$, on the other hand, diffuse in the direction parallel to the loss cone boundary. If both types of waves (located at $B_{\min}$ and $B_{\max}$) are present in the system, a network of diffusion paths (see Fig. 3.1) is formed. Given the α particle birth rate distribution in the energy space, one should then optimize such a system of diffusion paths in order to minimize the energy with which α particles leave the device diffusing to the loss cone. In the following, we consider a problem of optimizing diffusion coefficients of the paths in a network with fixed geometry, *i.e.,* choosing proper rf region amplitudes to maximize the α particle energy extraction. Note

that the solution discussed in the remainder of this chapter is particularly useful for configurations with complex loss boundaries, when the conditions necessary for the simplest partial solution discussed in the beginning of Sec. 3.3 do not hold.

The networks of diffusion paths also emerge in the applications of the α-channeling technique to tokamaks [Fisch and Herrmann, 1995]. As it turns out, using a single wave to both extract and cool α particles can be difficult in tokamaks [Fisch and Herrmann, 1995]. Therefore, a combination of two different waves, each performing it's own task [1] and hence a network of corrisponding diffusion paths is proposed as a possible mechanism for α-channeling.

Note that besides the α-channeling applications, the networks of narrow one-dimensional diffusion paths are frequently used to model porous media [Scheidegger, 1974; Suchomel et al., 1998; Dunn and Bergman, 1995; Hizi and Bergman, 2000; Hellén et al., 2002] and fiber networks in brain white matter [Poupon et al., 2000]. Also, a discrete model of diffusion path network, in which particles exhibit random-walk steps between nodes of some graph [Costa and Travieso, 2007], is used to study computer and social networks [Kleinberg, 1998; Eriksen et al., 2003; Simonsen, 2005; Wasserman and Faust, 1994; Zhang et al., 2007; Costa and Travieso, 2007], as well as city traffic [Volchenkov and Blanchard, 2007].

Particle diffusion is, in principle, straightforwardly treated in any geometry including a network of diffusion paths described above. Consider, for instance, a rectangular network formed of vertical and horizontal intersecting diffusion paths (Fig. 3.2). The diffusion tensor on each path is assumed diagonal with the transverse diffusion being

---

[1] The mode converted ion-Berstein wave is expected to cool down α particles, while the TAE mode should transport them radially.

much weaker than the diffusion along the path. The diffusion tensor in each intersection region is set to be equal to the sum of tensors of intersecting paths. The particle distribution $f(x, y)$ can then be found by solving the diffusion equation:

$$\frac{\partial f}{\partial t} = -\nabla \cdot \left[\hat{D}(\boldsymbol{x}) \cdot \nabla f \right], \tag{3.1}$$

where $\hat{D}$ is a piecewise constant diffusion tensor, yielding a unique stationary solution of Eq. (3.1), assuming proper boundary conditions [Cranck, 1975].

Unfortunately, the straightfoward approach based on the analysis of the two-dimensional diffusion equation (3.1) proves to be very tedious particularly, when the goal is the solution of the optimization problem rather than finding a stationary or a time-dependent solution of a system with given parameters. As will be shown in Appendices C and Sec. 3.4, the stationary solution of Eq. (3.1) in a rectangular network of thin diffusion paths can be reduced to a set of linear equations, which can be solved for any particular configuration. However, the dependence of particle fluxes on diffusion coefficients is not linear; any change of the diffusion coefficient of a single path results in a redistribution of the flux in the whole network. In this chapter, the optimization problem of flux rearrangement in a network of diffusion paths is solved [Zhmoginov and Fisch, 2008a]. Specifically, we find the diffusion coefficients minimizing a weighted sum of the outgoing fluxes.

The solution of the optimization problem is shown to be a limit of a system with the diffusion coefficients equal to 1, β, ..., β^k, with $k < 5$ as β goes to infinity. As demonstrated in Ref. [Dunn and Bergman, 1995], the network of diffusion paths is equivalent to the network of intersecting one-dimensional conductors (wires). As a result, all theorems true for one of the systems can be immediately applied to the other. The equivalence of systems is demonstrated and the optimization problem in networks of diffusion paths is extended to specific electrical circuits.

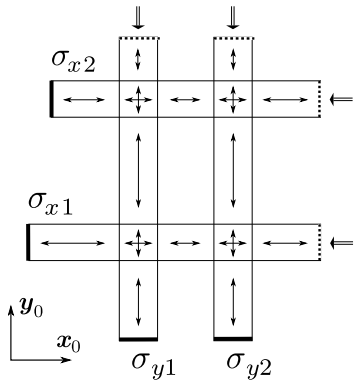

Figure 3.2: Diffusion domain comprised of four intersecting paths. The diffusion tensor $\hat{D}$ on a path σ_{dn} outside of the intersection regions is $\hat{D}_p(\sigma_{dn}) = D_{dn}\boldsymbol{d}_0 + \mu\boldsymbol{\tau}_0(d)$, and $\hat{D} = \hat{D}_p(\sigma_1) + \hat{D}_p(\sigma_2)$ in the volume formed by intersection of two paths σ_1 and σ_2, where μ is the coefficient of a weak transverse diffusion, $d \in \{x, y\}$, $n \in \{1, 2\}$, and $\boldsymbol{\tau}_0(d)$ is equal to $\boldsymbol{y}_0$, when d is equal to $\boldsymbol{x}_0$ and vice versa. Boundary conditions are: $f = 0$ at the thick boundaries; $f' = 0$ (i.e. no particle flux) at the thin boundaries; and the input particle flux density is given through the dashed boundaries.

This chapter is organized as follows. In Sec. 3.1, we reduce the original system of finite-size intersecting diffusion paths to an approximate system of one-dimensional equations and discuss the relation of the random-walk in networks of paths to the random-walk on oriented graphs. In Sec. 3.2, we show the equivalence between the network of diffusion paths and the network of intersecting conductors. The main result of the chapter, a solution of the general optimization problem, is given in Sec. 3.3. In Appendix C, we prove that a network of thin diffusion domains can be reduced to a system of intersecting one-dimensional paths. A local optimization of the weighted sum of outgoing fluxes by varying diffusion coefficients is considered in Sec. 3.4.

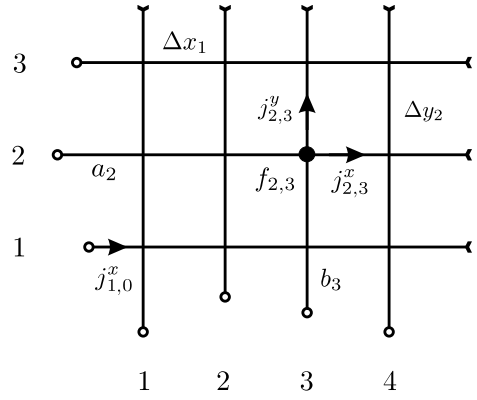

Figure 3.3: An example of a network comprised of one-dimensional paths. Circles show sinks, while arrows at the ends of diffusion paths correspond to given input fluxes.

3.1 Basic Equations

The optimization of a flux distribution in a rectangular network of diffusion paths can be performed analytically if each path can be approximated as a one-dimensional curve. As discussed in Appendix C, if the transverse diffusion is negligible, the path characteristic widths are much smaller than all distances between the paths, and the input flows are quasi-homogeneous, then Eq. (3.1) yields a stationary solution with a spatial scale much larger than the characteristic path width. Hence, particle flux distribution in a network of thin diffusion paths can be estimated by calculating fluxes in a network of one-dimensional paths (see Fig. 3.3). Particle density fluxes and particle densities in such network satisfy conditions: (a) particle conservation, reading

$$j^x_{i,j} - j^x_{i,j-1} + j^y_{i,j} - j^y_{i-1,j} = 0 \tag{3.2}$$

and (b) relation between the linear fall of particle density along the path, supporting the constant particle flux between two adjacent intersection volumes, and the flux

itself:

$$j^x_{i,j} = \frac{f_{i,j+1} - f_{i,j}}{D_{x,i}\Delta x_j}, \quad j^y_{i,j} = \frac{f_{i+1,j} - f_{i,j}}{D_{y,j}\Delta y_i}, \tag{3.3}$$

where $f_{i,j}$ is the particle density at the intersection of the horizontal and vertical diffusion paths with indices i and j correspondingly, further called the volume (i, j), Δx_i and Δy_i are the distances between horizontal and vertical paths with indices i and $i + 1$ respectively, and $j^x_{i,j}$, $j^y_{i,j}$ are density fluxes through the segments linking volume (i, j) with volumes $(i, j + 1)$ and $(i + 1, j)$ correspondingly. The outgoing fluxes are denoted by $j^x_{i,0}$ and $j^y_{0,j}$. The optimization problem of particular physical interest for such a network is to find $\boldsymbol{D}_x$ and $\boldsymbol{D}_y$ minimizing a linear combination of the outgoing fluxes:

$$\min_{\boldsymbol{D}_x, \boldsymbol{D}_y} \left(\sum_{i=1}^{\bar{n}} w_{xi} j^x_{i0} + \sum_{j=1}^{\bar{m}} w_{yj} j^y_{0j} \right), \tag{3.4}$$

where $\bar{m}$ and $\bar{n}$ are total numbers of horizontal and vertical paths correspondingly, weights w_{xi} and w_{yi} are constants, densities at the left and bottom sides of the network are zero $[j^x_{i,0} = f_{i,1}/(a_i D_{x,i})$ and $j^y_{0,j} = f_{1,j}/(b_j D_{y,j})]$ and input fluxes at the top $j^y_{n,j}$ and to the right $j^x_{i,k}$ are given.

Random-walk of particles in a network of diffusion paths can be represented as a random-walk on an oriented graph with nodes corresponding to the intersection volumes, sinks and sources and with edges corresponding to possible particle transitions between these nodes. A probability p_{ij} of a particle jump from the node i to the node j is defined by assigning weights to all graph edges according to $p_{ij} = \xi_{ij} / \sum\limits_k \xi_{ik}$, where ξ_{ij} is a weight of the edge connecting the node i with the node j, or zero if there is no such edge. One can show then that for every diffusion path network, there exists a weight distribution such, that the probabilities of particle jumps between the nodes are the same in both systems. Due to the fact that the inverse is not true, and some optimization problems of the form (3.4) for the graphs with variation over the

edge weights cannot be reformulated for the diffusion path networks, one can argue that the class of optimization problems on oriented graphs is wider. For instance, the problem of maximum extractable energy from plasmas under wave-induced diffusion [Fisch and Rax, 1993] can be reduced to an optimization of a random-walk on a certain graph. Another example is an optimization of outgoing fluxes (3.4) in a graph corresponding to the network of diffusion paths, in which jumps between two nodes are permitted in only one direction. Restricting all jumps to be directed towards the sinks, and the weights of the edges located on the same path to be equal, one defines a well posed optimization problem. The solution of this problem can be found using dynamic programming [Bellman, 2003] by successively adding horizontal and vertical paths to the system. It can be shown that the optimum is achieved for a system with path weights proportional to 1, β, ..., β^k with $k < 5$ as β goes to infinity. The same property holds for the system of diffusion paths, however the proof of this fact is different and will be given in Sec. 3.3.

3.2 Equivalence to Electrical Circuit

Replacing j by currents, f by potentials, and D by conductivities of a unit length ρ^{-1} in Eqs. (3.2) and (3.3), the optimization problem (3.4) becomes equivalent to an analogous optimization problem for electrical circuit comprised of intersecting homogeneous wires with grounded left and bottom ends ($f = 0$) and given currents through top and right ends. Equivalence between two systems allows to apply any knowledge about one system to another. For example, the distribution of currents in the circuit can be found as a solution of a variational problem:

$$\min_{\boldsymbol{I}\in S} \sum_{k=1}^{n} I_k^2 \Delta l_k \rho_k, \tag{3.5}$$

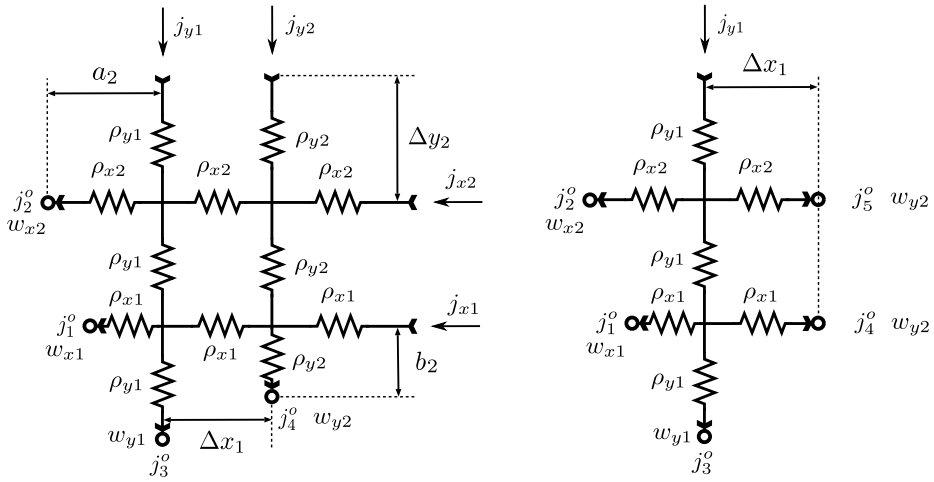

Figure 3.4: (a) Electrical circuit equivalent to the simplest diffusion network formed by four intersecting diffusion paths. (b) The same circuit when the resistivity of the second vertical diffusion path is much smaller than all the others.

where n is a number of the edges, $\boldsymbol{I}$ is an n-dimensional vector of the currents, ρ_k^{-1} is the conductivity of a unit length of the k-th edge, Δl_k is the length of this edge, and $S \subset \mathbb{R}^n$ is such that $\sum_{i \in e(v)} I_i = 0$ for every circuit node v, with $e(v)$ being a set of indices of edges adjacent to it. Thus reformulated, the variational problem in the network of intersecting diffusion paths reads:

$$\min_{\boldsymbol{j} \in S} \sum_{k=1}^{n} j_k^2 \Delta l_k / D_k, \tag{3.6}$$

where a vector of currents $\boldsymbol{I}$ is replaced by a vector of particle fluxes $\boldsymbol{j}$, and conductivities ρ_k^{-1} are replaced by diffusion coefficients D_k.

An example illustrating the transition from the optimization problem (3.4) to that for an electrical circuit is the optimization problem for the intersection of two pairs of parallel wires (Fig. 3.4a). Redirection of all input currents to the horizontal (vertical) exit with index x_1 (y_1) is possible in a limit $\beta \to 0$ of the configuration $\rho_{x1} = \beta\rho_{y1} = \beta^2\rho_{x2} = \beta^2\rho_{y2}$ ($\rho_{y1} = \beta\rho_{x1} = \beta^2\rho_{x2} = \beta^2\rho_{y2}$). This solves the optimization problem in the case when w_{x1} or w_{y1} are smaller than the other weights. The case when w_{x2}

(w_{y2}) is the smallest weight is more difficult because it is impossible to direct all input currents into the corresponding exit even if ρ_{x2} (ρ_{y2}) is much smaller than the other weights. However, as shown in Sec. 3.3, the minimum of the weighted sum is reached when the resistance ρ_{x2} (ρ_{y2}) is the smallest and the system is reduced to the circuit shown on Fig. 3.4b. The optimization problem is then reformulated as:

$$\min_{\boldsymbol{j}} w = \min_{\boldsymbol{j}} \Big[w_{x1} j_1 + w_{x2} j_2 + w_{y1} j_3 + w_{y2} j_4 + w_{y2} j_5 \Big], \tag{3.7}$$

where output currents are connected by $j_i = j_1 + j_2 + j_3 + j_4 + j_5$, $j_2/j_5 = \Delta x_1/a_2$, $j_1/j_4 = \Delta x_1/a_1$. Substituting these expressions into Eq. (3.7), the problem reduces to the minimization of a linear function

$$\begin{aligned} w = w_{x1} j_4 \Delta x_1/a_1 + w_{x2} j_5 \Delta x_1/a_2 + w_{y2} j_4 + w_{y2} j_5 + \\ + w_{y1}(j_i - j_4 \Delta x_1/a_1 - j_5 \Delta x_1/a_2 - j_4 - j_5) \end{aligned} \tag{3.8}$$

over a triangle in (j_4, j_5) space, formed by three inequalities: $j_4 \geq 0$, $j_5 \geq 0$, $j_i \geq j_4(\Delta x_1/a_1 + 1) + j_5(\Delta x_1/a_2 + 1)$. The minimum of a linear function is reached in one of the triangle's vertices [Luenberger, 1984], and thus three different solutions are possible:

$$\begin{aligned} &\text{(a)} \qquad \rho_{y2} = \beta \rho_{x2} = \beta^2 \rho_{x1} = \beta^2 \rho_{y1}, \\ &\text{(b)} \qquad \rho_{y2} = \beta \rho_{x1} = \beta^2 \rho_{x2} = \beta^2 \rho_{y1}, \\ &\text{(c)} \qquad \rho_{y2} = \beta \rho_{y1} = \beta^2 \rho_{x1} = \beta^2 \rho_{x2}. \end{aligned}$$

3.3 Solution for the Diffusion Path Network

In the general case of $n \times m$ rectangular network of diffusion paths, the minimum in Eq. (3.4) is reached in the limit $\beta \to \infty$ of a network with finite diffusion coefficients

equal to 1, β, ..., β^k with $k < 5$. This property, which is the main result of this chapter, is proved in this section in two steps. First, we note that the diffusion path with a minimum-weighted sink (we take this weight to be equal to 0 for distinctness) should have a diffusion coefficient much greater than the diffusion coefficients of the paths intersecting it. Then, using independence of the subnetworks obtained by partition of the original network by the minimum-weighted path, solutions in each subsystem is obtained separately.

When the sink of the leftmost (bottom) diffusion path has the smallest weight, the optimization problem has a trivial solution. In this case, all particles can be directed to the minimum-weighted path by making its diffusion coefficient large compared to the diffusion coefficient of the bottom horizontal (leftmost vertical) path, which should in turn be much larger than diffusion coefficients of other paths.

In a more general case, when the minimum-weighted sink is not on the leftmost or the bottom path, the optimum is also achieved when the diffusion coefficient $D_{\min}$ of the minimum-weighted path is much larger than the coefficients D_{int} of the paths intersecting it. This can be proved using a random-walk process analogy. Compare a configuration in which $D_{\min} \sim D_{\text{int}}$ with the same configuration having $D_{\min} \gg D_{\text{int}}$. For each particle trajectory which does not cross the minimum-weighted path in the large-$D_{\min}$ system, there is an identical particle trajectory in the finite-$D_{\min}$ system with the same realization probability and the same output weight. On the other hand, for each trajectory crossing the minimum-weighted path (and then leaving immediately) in the large-$D_{\min}$ system, there is a family of trajectories in the finite-$D_{\min}$ system with the same path before the crossing and the same overall probability, but larger or equal average output weight. Thus, averaging over all trajectories, one

concludes that the weight defined by Eq. (3.4) in the large-$D_{\min}$ system is smaller or equal to the weight in the finite-$D_{\min}$ system.

The minimum-weighted path divides the network into two subnetworks. An optimal solution to the right of this path (we choose vertical orientation of the minimum-weighted path for distinctness) is trivial: all vertical diffusion paths have diffusion coefficients much smaller than the diffusion coefficients of every horizontal path. In this case, all particles entering the system to the right of the minimum-weighted path are captured by it. On the other hand, the part of the network to the left of the minimum-weighted path, which we will call *enclosed*, can be treated as an isolated part in which points of intersection with the minimum-weighted path are replaced by particle sinks with zero weights (the minimum weight in the system). To specify the network geometry, the number of vertical and horizontal paths in the enclosed system are denoted by m and n correspondingly, fluxes entering the system from above are denoted by j_k^i, distances between horizontal or vertical diffusion paths with indices i and $i+1$ are denoted by Δx_i and Δy_i, and the distances from the leftmost vertical path to the left sinks and from the bottom horizontal path to the bottom sinks are denoted by a_i and b_i correspondingly.

To solve the optimization problem in a general case, we first analyze a horizontal path with fixed vertical input and output fluxes. Then we solve an optimization problem in a class of networks, in which the relations between vertical fluxes and corresponding differences of densities of adjacent intersection volumes are omitted. We prove that there are many optimal solutions, one of which can be asymptotically reached in a conventional diffusion path network.

Consider a single horizontal diffusion path with vertical fluxes j_k entering from the above, vertical outgoing fluxes i_k, and the left outgoing flux j_0. The equation for

j_0 then reads:

$$j_0 a_k + (j_0 - \Delta_1)\Delta x_1 + (j_0 - \Delta_1 - \Delta_2)\Delta x_2 + \cdots + \\ + (j_0 - \Delta_1 - \Delta_2 - \cdots - \Delta_m)\Delta x_m = 0, \quad (3.9)$$

where $\Delta_k = j_k - i_k$. This solution is correct when particle densities in all intersection volumes are nonnegative, which results in m conditions:

$$j_0 \geq 0, \quad j_0 a_k + (j_0 - \Delta_1)\Delta x_1 \geq 0, \quad (3.10)$$

$$\cdots$$

$$j_0 a_k + (j_0 - \Delta_1)\Delta x_1 + (j_0 - \Delta_1 - \Delta_2)\Delta x_2 + \cdots + \\ + (j_0 - \Delta_1 - \Delta_2 - \cdots - \Delta_{m-1})\Delta x_{m-1} \geq 0. \quad (3.11)$$

Consider the optimization problem in a network of diffusion paths, in which vertical fluxes and corresponding differences of densities are not related. In such a network, the fluxes on all segments of vertical diffusion paths, or $\Delta_{ij} = j^y_{i,j} - j^y_{i-1,j}$, can be defined independently. Limiting all particle densities and outgoing vertical fluxes to be positive, $nm + m$ linear conditions are imposed on the system:

$$j_0 = \frac{\sum_{i=1}^{m} \sum_{j=1}^{i} \Delta_{kj} \Delta x_i}{a_k + \Delta x_1 + \ldots \Delta x_m} \geq 0, \quad (3.12)$$

$$j_0 a_k + (j_0 - \Delta_{k1})\Delta x_1 \geq 0, \quad \ldots, \quad (3.13)$$

$$j_0 a_k + \sum_{i=1}^{m-1} \Delta x_i \left(j_0 - \sum_{j=1}^{i} \Delta_{kj} \right) \geq 0 \quad (3.14)$$

for $1 \leq k \leq n$, and

$$\sum_{k=1}^{n} \Delta_{kl} \leq j^i_l \quad \text{for} \quad 1 \leq l \leq m. \quad (3.15)$$

Under these conditions, the minimum weight of the enclosed system is nonnegative and the expression for the linear weight function w reads:

$$w = \sum_{k=1}^{n} w_{xk} \frac{\sum_{i=1}^{m} \sum_{j=1}^{i} \Delta_{kj} \Delta x_i}{a_k + \Delta x_1 + \ldots \Delta x_m} + \sum_{k=1}^{m} w_{yk} \left(j_k^i - \sum_{l=1}^{n} \Delta_{lk} \right). \tag{3.16}$$

The solution of a linear optimization problem is reached in the vertex of nm-dimensional manifold defined by Eqs. (3.12)–(3.15). This vertex corresponds to the intersection of nm hyperplanes (out of $nm + m$ conditions), limiting it. In terms of conditions (3.12)–(3.15), this means that $0 \leq s \leq m$ vertical output fluxes are zero and there are at least $nm - s$ intersection volumes with vanishing f. Due to the fact that the horizontal flux cannot emerge from the intersection volume with zero density, there should be exactly s volumes with nonzero densities in the system with all input fluxes greater than zero. Furthermore, every vertical path with vertical output flux equal to zero should contain just one such volume; henceforth we call such configurations *primitive*.

The found optimum cannot necessarily be realized in an ordinary network of intersecting horizontal *and vertical* diffusion paths. However, we show here that any such optimum can be transformed to another configuration with exactly the same weight, which can be represented as a network of both horizontal and vertical diffusion paths. We use a convenient notation, characterizing each primitive configuration by $(m + 1)$-dimensional vector $(\alpha_1, \ldots, \alpha_m, 0)$, where α_k is equal to l if the nonzero density volume is situated on the intersection of the vertical path with index k and the horizontal diffusion path with index l, and α_k is equal to zero if there is no such intersection volume on this vertical path. Considering a primitive solution of the minimization problem corresponding to a vector $(\alpha_1, \ldots, \alpha_m, 0)$, we can construct other primitive configurations with the same weight applying a following lemma.

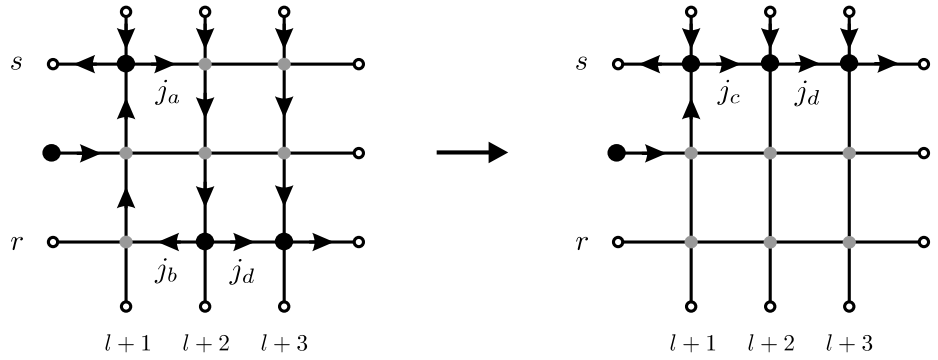

Figure 3.5: Construction of a primitive configuration described by vector $(\dots, s, s, s, \dots, s, 0, \dots)$ from a primitive solution defined by vector $(\dots, s, r, r, \dots, r, 0, \dots)$. Denoting by f^{II} particle densities in the constructed system and by f^{I} particle densities in the original system, the construction is defined by relation $f^{II}_{sj} = D_{xr} f^{I}_{rj} / D_{xs}$ for indices $j \geq l+2$. As a result, all flows except for j_a, j_b and j_c are left unchanged. All segments without arrows indicate the segments with zero fluxes. Relation $j_c = j_a - j_b$ proves that all outgoing flows are the same in both systems.

Lemma 1 *For every primitive configuration of the form* $(\alpha_1, \dots, \alpha_l,\ s,\ r, \dots, r,\ 0,\ \alpha_q, \dots, \alpha_m, 0)$ *[or* $(\alpha_1, \dots, \alpha_l,\ s,\ r, \dots, r, 0)$*], where* $s > 0$, $r > 0$ *and* $s \neq r$, *there exists another primitive configuration corresponding to the vector* $(\alpha_1, \dots, \alpha_l,\ s, s, \dots, s,\ 0,\ \alpha_q, \dots, \alpha_m, 0)$ *[or* $(\alpha_1, \dots, \alpha_l,\ s, s, \dots, s, 0)$*], which has the same weight.* □

Proof Consider a primitive configuration defined by:

$$f^{II}_{ij} = 0, \quad i \neq s, \tag{3.17}$$

$$f^{II}_{sj} = \frac{D_{xr} f^{I}_{rj}}{D_{xs}}, \quad l+2 \leq j \leq q-2, \tag{3.18}$$

where f^{I}_{ij} and f^{II}_{ij} are particle densities in the original and constructed solutions correspondingly (Fig. 3.5). In the considered configuration all horizontal fluxes between nonzero density volumes are left the same as in the original system, except for the volumes on vertical paths with indices $l+1$ and $l+2$. This, in turn, means that all outgoing fluxes for vertical paths with indices ranging from $l+3$ to $q-2$ are left equal to zero. Noting that $j_c = j_a - j_b$, we also see that $\sum_k \Delta^{I}_{k,l+1} = \sum_k \Delta^{II}_{k,l+1} = j^{i}_{l+1}$

and $\sum_k \Delta^I_{k,l+2} = \sum_k \Delta^{II}_{k,l+2} = j^i_{l+2}$, which suggests that outgoing fluxes for vertical paths with indices $l+1$ and $l+2$ are equal to zero, too. This proves that the weight of constructed system is equal to the weight of the original configuration because all outgoing fluxes are the same in both configurations. ■

Applying the lemma repeatedly, one can prove that for any primitive configuration there exists a configuration with the same weight, which is described by either a vector $(s_1, \ldots, s_1, 0, \ldots, 0, s_2, \ldots, s_2, 0, \ldots, 0, s_k, \ldots, s_k, 0)$, or a vector $(0, \ldots, 0, s_1, \ldots, s_1, 0, \ldots, 0, s_2, \ldots, s_2, 0, \ldots, 0, s_k, \ldots, s_k, 0)$ with $s_i > 0$. Noticing then that for every primitive configuration of the form $(\ldots, 0, r, \ldots, r, 0, \ldots, 0)$ with $r > 0$, there exists another primitive configuration having the same weight and described by the vector $(\ldots, 0, s, \ldots, s, 0, \ldots, 0)$ with $s > 0$, one can state that an arbitrary primitive optimum is equivalent to another primitive configuration with all nonzero density volumes situated on a single horizontal diffusion path with index denoted further by s. Interestingly, such configurations can be asymptotically reached as $\beta \to \infty$ in a conventional network of intersecting horizontal *and vertical* diffusion paths. The diffusion coefficients in the diffusion path network are to be set as follows (if there is at least one nonzero intersection volume in the system): the diffusion coefficient of the horizontal path with index s is to be much larger ($\sim \beta^3$) than the diffusion coefficients of the rest of horizontal paths ($\sim \beta$) and vertical paths with nonzero density volumes ($\sim \beta^2$); remaining vertical paths are to have $D_y \sim \beta^4$.

Having determined the form of the optimal solution, Eq. (3.16) can be rewritten as

$$w = w_{xs} \frac{\sum\limits_{i=1}^{m} \sum\limits_{j=1}^{i} \Delta_{sj} \Delta x_i}{a_s + \Delta x_1 + \ldots \Delta x_m} + \sum_{l=1}^{m} w_{yl} \left(j^i_l - \Delta_{sl} \right), \tag{3.19}$$

where $\Delta_{sl} \leq j_l^i$; then the value of s can be then found by minimizing

$$\frac{w_{xs}}{a_s + \Delta x_1 + \cdots + \Delta x_m}. \tag{3.20}$$

By substituting the corresponding values to Eq. (3.19), the optimization problem is reformulated as a minimization of

$$\min \sum_{j=1}^{m} \mu_j \Delta_{sj} \tag{3.21}$$

over a manifold limited by Eqs. (3.12)-(3.14) and m conditions $\Delta_{sl} \leq j_l^i$. The solution of this optimization problem defines which of vertical diffusion paths are to have diffusion coefficients proportional to β^4 and which are to be proportional to β^2.

3.4 Derivative Calculation

In practical applications, the optimal solution obtained in Sec. 3.3 might be impossible to achieve. In α-channeling implementation, for instance, infinitely large diffusion coefficient would imply an infinitely large wave amplitude. One can resolve this by introducing additional limitations on the parameter space or adding terms depending on $\boldsymbol{D}_x$ and $\boldsymbol{D}_y$ into the optimized functional. Numerical algorithms suitable for solution of such extended optimization problem, like gradient descent method, might require calculation of derivatives of the weight function w with respect to the diffusion coefficients. In this section we outline such calculation for an isolated system enclosed by the minimum-weighted diffusion path.

Denote by $\boldsymbol{x}_i$ a vector of particle densities and their derivatives down the path for the intersection volumes situated on a horizontal path with index i:

$$\boldsymbol{x}_i = (f_{i1}, f_{i2}, \ldots, f_{im}, f'_{i1}, \ldots, f'_{im}), \tag{3.22}$$

where f'_{ij} is a y-derivative of f down the vertical path with index j. To solve for particle densities given incoming fluxes, two $2m \times 2m$ linear operators $\hat{t}_i$ and $\hat{T}_k$ are introduced:

$$\boldsymbol{x}_{i+1} = \hat{t}_i(D_{xi})\boldsymbol{x}_i, \tag{3.23}$$

$$\hat{T}_k = \hat{t}_k\hat{t}_{k-1}\ldots\hat{t}_1 = \begin{pmatrix} \hat{A}_k & \hat{B}_k \\ \hat{C}_k & \hat{D}_k \end{pmatrix}, \qquad \hat{T}_0 = \hat{I}, \tag{3.24}$$

where $\hat{I}$ is an identity operator. Given the m-dimensional vector of input fluxes $\boldsymbol{I}_0$ entering the system from above, the state vector at the bottom diffusion path is calculated:

$$\begin{aligned} \boldsymbol{x}_1 = \hat{\kappa}^{-1}(\boldsymbol{D}_x) \begin{pmatrix} \hat{\Lambda}_y^{-1}\boldsymbol{I}_0 \\ \hat{\Lambda}_b^{-1}\hat{\Lambda}_y^{-1}\boldsymbol{I}_0 \end{pmatrix} = \\ = \begin{pmatrix} \hat{C}_n + \hat{D}_n\hat{\Lambda}_b^{-1} & 0 \\ 0 & \hat{C}_n + \hat{D}_n\hat{\Lambda}_b^{-1} \end{pmatrix}^{-1} \begin{pmatrix} \hat{\Lambda}_y^{-1}\boldsymbol{I}_0 \\ \hat{\Lambda}_b^{-1}\hat{\Lambda}_y^{-1}\boldsymbol{I}_0 \end{pmatrix}, \end{aligned} \tag{3.25}$$

where $(\hat{\Lambda}_b)_{ij} = \delta_{ij}b_j$ and $(\hat{\Lambda}_y)_{ij} = \delta_{ij}D_{yj}$ are $m \times m$ matrices and $\hat{t}_n$ is constructed by introducing a virtual horizontal path with index $n+1$ having vanishing $D_{x,n+1}$ and situated arbitrary distance Δy_n apart from the adjacent path. The value of the weight function can then be calculated:

$$w = \left[\boldsymbol{w}_y^T\hat{\Lambda}_y\hat{\Lambda}_b^{-1} + \left(\frac{w_{x1}D_{x1}}{a_1}\hat{I} + \frac{w_{x2}D_{x2}}{a_2}\hat{T}_1 + \cdots + \frac{w_{xn}D_{xn}}{a_n}\hat{T}_{n-1}\right)_1\right]\boldsymbol{x}_1, \tag{3.26}$$

where $(\hat{S})_1$ denotes the first row of the matrix $\hat{S}$, and $\boldsymbol{w}_x$, $\boldsymbol{w}_y$ are vectors of positive weights of the leftmost horizontal and vertical sinks relative to the weight w_0 of the

rightmost horizontal sinks. Using $(\hat{S}^{-1})' = -\hat{S}^{-1}\hat{S}'\hat{S}^{-1}$, and

$$\partial \hat{t}_i / \partial D_{xk} = \delta_{k,i} \begin{pmatrix} \Delta y_i \hat{c}_i' & 0 \\ \hat{c}_i' & 0 \end{pmatrix} = \\ = \delta_{k,i} D_{xi}^{-1} \left(\hat{t}_i - \hat{I} - \Delta y \begin{pmatrix} 0 & \hat{I} \\ 0 & 0 \end{pmatrix} \right) = \delta_{k,i} D_{xi}^{-1} \left(\hat{t}_i(D_{xi}) - \hat{t}_i(0) \right), \quad (3.27)$$

one can differentiate Eq. (3.26) with respect to D_{xk} to obtain:

$$\frac{\partial w}{\partial D_{xk}} = \left[\frac{w_{xk}}{a_k} \hat{I} + \hat{A} \left(\hat{t}_k - \hat{t}_k(D_{xk} = 0) \right) \right]_1 \hat{T}_{k-1} \boldsymbol{x}_1 - \\ - \left[\boldsymbol{w}_y^T \hat{\Lambda}_y \hat{\Lambda}_b^{-1} + \left(\hat{B} \right)_1 \right] \cdot \hat{\kappa}^{-1} \frac{\hat{\kappa} - \hat{\kappa}(D_{xk} = 0)}{D_{xk}} \boldsymbol{x}_1, \quad (3.28)$$

where

$$\hat{A} = \left(\frac{w_{x,k+1} D_{x,k+1}}{a_{k+1} D_{xk}} \hat{I} + \frac{w_{x,k+2} D_{x,k+2}}{a_{k+2} D_{xk}} \hat{t}_{k+1} + \frac{w_{x,k+3} D_{x,k+3}}{a_{k+3} D_{xk}} \hat{t}_{k+2} \hat{t}_{k+1} + \dots \right), \quad (3.29)$$

$$\hat{B} = \frac{w_{x1} D_{x1}}{a_1} \hat{I} + \frac{w_{x2} D_{x2}}{a_2} \hat{T}_1 + \dots + \frac{w_{xn} D_{xn}}{a_n} \hat{T}_{n-1}, \quad (3.30)$$

and where we used $D_{xk}\hat{\kappa}' = \hat{\kappa}(\boldsymbol{D}_x) - \hat{\kappa}(D_{xk} = 0)$. Consider a network formed from the original by removing k-th horizontal path, or equivalently by taking $D_{xk} = 0$; henceforth we call such network *reduced*. Denote by $\boldsymbol{I}_r$ such vector of input fluxes entering the reduced system, that the values of f at its bottom horizontal path are equal to $\boldsymbol{x}_1$:

$$\begin{pmatrix} \hat{\Lambda}_y^{-1} \boldsymbol{I}_r \\ \hat{\Lambda}_b^{-1} \hat{\Lambda}_y^{-1} \boldsymbol{I}_r \end{pmatrix} = \hat{\kappa}(D_{xk} = 0) \boldsymbol{x}_1, \quad (3.31)$$

the last term in the right-hand side of Eq. (3.28), multiplied by D_{xk}, can be interpreted as the difference of weights of the original system with $\boldsymbol{I} = \boldsymbol{I}_0$ and the same system with $\boldsymbol{I} = \boldsymbol{I}_r$. The first term in the right-hand side of Eq. (3.28), multiplied by D_{xk}, is equal to the sum of weights of horizontal paths with indices $k, k+1, \dots, n$ in the

original system minus the sum of weights of paths with indices $k+1,\ldots,n$ in the reduced system with $\boldsymbol{I}=\boldsymbol{I}_r$. Noticing that all outgoing vertical fluxes and horizontal fluxes leaving through sinks with indices $1,\ldots,k-1$ of the reduced system with $\boldsymbol{I}=\boldsymbol{I}_r$ are equal to the same fluxes of the original system with $\boldsymbol{I}=\boldsymbol{I}_0$ (because $\boldsymbol{f}_1$ is the same in both systems), Eq. (3.28) finally takes the form:

$$D_{xk}\frac{\partial w}{\partial D_{xk}} = \left[\boldsymbol{w}_y^T\hat{\Lambda}_y\hat{\Lambda}_b^{-1}+\sum_{i=1}^{n}\frac{w_{x,i}D_{x,i}}{a_i}\hat{T}_{i-1}\right]_1\cdot\hat{\kappa}^{-1}\hat{\kappa}(D_{xk}=0)\boldsymbol{x}_1- \\ -\left(\boldsymbol{w}_y^T\hat{\Lambda}_y\hat{\Lambda}_b^{-1}+\sum_{i=1,\,i\neq k}^{n}\frac{w_{x,i}D_{x,i}}{a_i}\hat{T}_{i-1}(D_{xk}=0)\right)_1\boldsymbol{x}_1. \quad (3.32)$$

According to this relation, the derivative of the system weight with respect to D_{xk} is simply equal to the difference of weights of the original system with $\boldsymbol{I}=\boldsymbol{I}_r$ and the reduced system with $\boldsymbol{I}=\boldsymbol{I}_r$.

Chapter 4

Alpha-Channeling Modes in Mirror Machines

Numerical simulations of α-channeling discussed in Chapter 2 were carried out for systems of rf regions which were not restricted by the background plasma dispersion relation. As a result, studying a vast parameter space of the problem, limitations on the wave properties, not necessarily realistic, required for reaching high α-channeling efficiency were identified. In particular, the frequency ω of the optimized α-channeling mode was shown to be close to the α particle cyclotron frequency Ω_α, the longitudinal wave number $k_\parallel$ was limited by the designed resonance width through Eq. (2.19) and the transverse component of the wave vector $k_\perp$ was shown to satisfy $k_\perp \rho_\alpha \geq 1$, where ρ_α is the α particle gyroradius.

In this chapter, we address the feasibility of exciting plasma waves with parameters close to the optimal [Zhmoginov and Fisch, 2010, 2009]. First, we study the implications of the mode damping[1] on the feasibility of α-channeling and present a simple dynamical model of the α-channeling in the presence of dissipations. We then assume that the fusion reactivity is not sufficiently high to make excitation of a travelling wave, which damps all its energy in a single pass, practical. In this case, excitation of a marginally-stable mode is necessary and we proceed to finding a method of identifying weakly-damped modes localized in the device core and satisfying conditions necessary for efficient α-channeling. The proposed method relies on the geometrical optics approximation previously employed to study α-channeling wave propagation and damping in tokamaks [Valeo and Fisch, 1994]. The application of this method to practical and hypothetical mirror machines is then discussed. As a result, several candidate modes suitable for α-channeling are identified. Note that some of these modes could also be used in rotating plasmas [Fetterman and Fisch, 2008, 2010b,a, 2011b].

4.1 Effect of Wave Damping on α-Channeling

4.1.1 Limitations on the Mode Damping Rate

The main goal of the α-channeling technique is to quickly eject α particles from the fusion reactor, while transferring their energy to the channeling wave. The wave energy can later be damped on the plasma species, preferably on the fuel ions, which

[1]Wave energy can be dissipated through wave damping on the background plasma species or by scattering energy outside of the mirror machine.

are directly involved in the fusion reaction. As a result, since the characteristic particle extraction time $\tau_{\rm extr}$ is much smaller than the collisional α-electron energy relaxation time $\tau_{\alpha e}$, the electron heating by the fusion reaction by-products can be avoided.

However, even if $\tau_{\rm extr} \gg \tau_{\alpha e}$, electrons can gain more energy from α particles than ions if the wave damping on electrons is stronger than the wave damping on ions. Therefore, we will further focus our attention on waves with $\tau_e \gg \tau_i$, where τ_s is a characteristic Landau or ion-cyclotron wave damping time on species s. If for some wave $\tau_i \geq \tau_e$, we will assume that there exist another mechanism (like through minority ion heating discussed in Sec. 5.1) which can transport wave energy to ions on a time scale much smaller than τ_e. This energy transport time scale is further denoted by the same τ_i.

Another limitation on τ_i follows from the fact that the α-channeling technique is practical only if the energy extracted from α particles exceeds the energy necessary to excite the channeling wave. Assuming that the geometrical optics approximation is valid, one can consider two wave launching schemes: (a) excitation of a weakly-damped mode trapped in the device core, and (b) excitation of a traveling wave which first extracts energy from α particles and then dissipates it on ions.

The choice of a particular scheme depends on a dimensionless parameter $\xi = \tau_{\rm amp}/\tau_L$, where τ_L is the time it takes the wave packet to travel a distance comparable to the device length L and $\tau_{\rm amp}$ is the characteristic wave amplification time, on which the wave energy is increased by a factor of 2. If the α particle production rate is so large that $\xi \ll 1$, the α-channeling technique can be implemented by launching traveling waves which first encounter the α particle resonance region (passing which

they are amplified by at least a factor of 2) and then encounter the wave-damping region, dissipating most of their energy on the background plasma species.

In devices with smaller fusion reactivity, for which $\xi \gg 1$, excitation of a weakly-damped mode localized in the device core might be necessary. This mode should be marginally stable to require as little external energy as possible to sustain itself. Assume that the equation on the mode energy $\mathcal{E}$ can be approximated by $\dot{\mathcal{E}} = \gamma_\Sigma(\mathcal{E})\mathcal{E}$, where $\gamma_\Sigma = 1/\tau_i - 1/\tau_{\rm amp}$ is the characteristic wave growth rate and $\tau_{\rm amp}$ is the characteristic wave energy amplification time attributed to interaction with α particles. The mode saturation level $\mathcal{E}_*$ can be found as a solution of $\gamma_\Sigma(\mathcal{E}_*) = 0$. Assume first that the α-channeling mode amplitude is far from the saturation level and $\gamma_\Sigma \approx$ const. If $\gamma_\Sigma < 0$ and $|\gamma_\Sigma|\tau_i \ll 1$, the wave energy will decrease, but slowly enough to channel much more energy than was used to excite the channeling wave. In a vicinity of a saturation energy $\mathcal{E}_*$, γ_Σ can be expanded in $\delta\mathcal{E} = \mathcal{E} - \mathcal{E}_*$ to yield $\delta\mathcal{E} \sim e^{\mathcal{E}_*\gamma' t}$. Therefore, if $\gamma'(\mathcal{E}_*) < 0$, the dynamics in a vicinity of the saturation level is stable and is unstable otherwise.

4.1.2 Dynamics of the α-Channeling Mode

In the abscence of wave dissipation, the amplitude of the α-channeling mode gaining energy from the α particle population would grow indefinitely. Therefore, accounting for the wave damping is necessary to identify the stationary state of the system. Furthermore, the wave dissipation is responsible for plasma heating, which itself results in an increase of fusion reaction rate and thus, the α particle production. In the following, we study a simple model of the α-channeling and discuss the effect of wave damping on the system dynamics.

One of the most accurate models of α-channeling is the system of Vlasov equations [Stix, 1992, §8.4]. Unfortunately, this approach can prove very difficult for analytical treatment and thus simple, yet less accurate, models of the process should be developed. For instance, the α-channeling process can be modelled using a two-dimensional system of ordinary differential equations, in which the wave and the plasma are characterized by only two parameters: the density of α particles n_α and the energy of the α-channeling mode $\mathcal{E}$.

To derive equations on these characteristics, assume that the dynamics of the α particle distribution $f_\alpha(E)$ can be described by a one-dimensional Fokker-Planck equation

$$\frac{\partial f_\alpha}{\partial t} = (Df)'' - (Ff)' + g(E), \tag{4.1}$$

where $D(E)$ and $F(E)$ are the diffusion and drift coefficients correspondingly, the derivatives are taken with respect to the α particle energy E and $g(E)$ is the α particle source. Integrating this equation by E, one obtains:

$$\frac{\partial n_\alpha}{\partial t} = D(E_{\text{loss}})f'(E_{\text{loss}}) + \mathcal{N}_\alpha, \tag{4.2}$$

where $\mathcal{N}_\alpha = \int g(E)\,dE$ is the α particle birth rate. We assumed here that f vanishes at the loss cone $E = E_{\text{loss}}$ (where the particles leave the mirror machine) and for $E \to \infty$. The α particle diffusion coefficient D has two contributions: D_w from the wave-induced diffusion and D_c from the collisional slowing-down on electrons. Noticing that D_w is proportional to the wave energy $\mathcal{E}$, assuming that D_c is a constant and approximating f' by ϱn_α, where ϱ is a constant, one may rewrite Eq. (4.2) as:

$$\dot{n}_\alpha = -n_\alpha(\varsigma_w\mathcal{E} + \nu_c) + \mathcal{N}_\alpha, \tag{4.3}$$

where ς_w and ν_c are some positive constants.

The equation on the mode energy $\mathcal{E}$ should contain energy gain from α particles and energy dissipation terms due to damping on other plasma species:

$$\dot{\mathcal{E}} = \varsigma_\alpha n_\alpha \mathcal{E} - \nu_d \mathcal{E}, \tag{4.4}$$

where ς_α is constant and we assumed that the wave damping is linear with a constant rate ν_d and that the energy inflow from α particles can be approximated by the term $\varsigma_\alpha n_\alpha \mathcal{E}$ proportional to both $\mathcal{E}$ and n_α.

The dynamical system described by Eqs. (4.3) and (4.4) has two stationary points $(n_\alpha, \mathcal{E}) = (n_1, \mathcal{E}_1)$ and $(n_2, \mathcal{E}_2)$:

$$n_1 = \mathcal{N}_\alpha/\nu_c, \qquad \mathcal{E}_1 = 0, \tag{4.5}$$

$$n_2 = \nu_d/\varsigma_\alpha, \qquad \mathcal{E}_2 = \frac{\mathcal{N}_\alpha \varsigma_\alpha - \nu_c \nu_d}{\varsigma_w \nu_d}. \tag{4.6}$$

In the first stationary state $(n_1, \mathcal{E}_1)$, the α particle evolution is dominated by the collisional slowing down on electrons. In this regime, there is no α-channeling wave in the system and all α particle energy is transfered to electrons. The second stationary state $(n_2, \mathcal{E}_2)$ corresponds to the α-channeling regime. In this case, the collisional particle loss proportional to ν_c does not influence the stationary α particle density and enters the expression for $\mathcal{E}_2$ as an additive term disappearing as $\nu_c \to 0$.

The behavior of the dynamical system in a vicinity of some stationary point $(n_0, \mathcal{E}_0)$ is characterized by the eigenvalues λ_i of the linearized system, which are calculated as follows:

$$\begin{Vmatrix} -\varsigma_w \mathcal{E}_0 - \nu_c - \lambda & -\varsigma_w n_0 \\ \varsigma_\alpha \mathcal{E}_0 & \varsigma_\alpha n_0 - \nu_d - \lambda \end{Vmatrix} = 0. \tag{4.7}$$

Rewrite Eq. (4.7) as:

$$\lambda^2 + b\lambda + c = 0, \tag{4.8}$$

where $b = \varsigma_w \mathcal{E}_0 + \nu_c - \varsigma_\alpha n_0 + \nu_d$ and $c = \varsigma_w \mathcal{E}_0 \nu_d - \nu_c \varsigma_\alpha n_0 + \nu_c \nu_d$. Using Eqs. (4.5) and (4.6), the expressions for coefficients b and c can be rewritten for two stationary states 1 and 2 as follows:

$$b_1 = \nu_c + \varsigma_\alpha (n_2 - n_1), \qquad c_1 = \nu_c \varsigma_\alpha (n_2 - n_1), \tag{4.9}$$

$$b_2 = \frac{n_1}{n_2} \nu_c, \qquad c_2 = \nu_c \varsigma_\alpha (n_1 - n_2). \tag{4.10}$$

Noticing that $c_1 = -c_2$, one concludes that one of the stationary states 1 or 2 is unstable.

The efficient α-channeling is possible if the α particle energy redirected to the wave is much larger than the energy damped on electrons. This condition can be written as $\nu_c n_2 \ll \mathcal{N}_\alpha$, or after using the expressions for n_1 and n_2:

$$n_2 \ll n_1. \tag{4.11}$$

Equation (4.11) can then be used to simplify the expressions for b and c:

$$b_1 = \nu_c - \varsigma_\alpha n_1, \qquad c_1 = -\nu_c \varsigma_\alpha n_1, \tag{4.12}$$

$$b_2 = \frac{n_1}{n_2} \nu_c, \qquad c_2 = \nu_c \varsigma_\alpha n_1. \tag{4.13}$$

Recalling that $\nu_c > 0$ and $\varsigma_\alpha > 0$, one can immediately see that the first stationary state is unstable. Another stationary state $(n_2, \mathcal{E}_2)$ is then either a stable focus if $b_2^2 < 4c_2$, or a stable knot otherwise.

In conclusion, we described a simplified model of the α-channeling technique. The analysis of this dynamical system shows that there is only one stable stationary state, corresponding to a saturated α-channeling mode. The characteristic time scale of attraction towards this stable state can be roughly estimated as $\nu_d/(\varsigma_\alpha \mathcal{N}_\alpha)$. Also, the system without an electromagnetic wave is shown to be unstable. As a result

of this instability, the α-channeling mode is excited and then saturated at the level corresponding to the stable stationary state. The characteristic mode excitation time is of order of $\nu_c/(\varsigma_\alpha \mathcal{N}_\alpha)$.

4.2 Ray-Tracing and the Search for the α-Channeling Modes

The choice of the wave, which can be used to extract α particle energy and redirect it to the plasma species depends on the value of the parameter ξ introduced in Sec. 4.1.1. The energy necessary to excite and sustain the α-channeling mode should be much smaller than the energy extracted from α particles, otherwise the utility of the α particle energy is small. If the fusion reaction rate is so large that $\xi \ll 1$, it is practical to radiate the α-channeling wave into the device core continuously. In this scenario, the wave excited by an external source is amplified by a large factor while traveling through the mirror machine and is then damped inside the device before leaving it. If $\xi \gg 1$, however, excitation of a marginally-stable α-channeling mode, requiring only very little external energy to sustain itself, is necessary. In this section, we consider a feasibility of exciting such weakly-damped waves and propose an algorithm for consistently searching for these modes in an arbitrary mirror device.

The electromagnetic mode existing in the central cell of a mirror machine can have a large time of life or a large *quality factor* (Q-factor) if the mode damping on plasma species is small and if the mode energy does not scatter outside of the device. While the wave damping can be controlled by a proper choice of wave parameters, the energy scattering can be avoided by either arranging perfect wall reflections, or by picking a mode reflecting inside the plasma before reaching the plasma exterior.

Consider a stationary inhomogeneous medium parametrized by an n-dimensional vector $\boldsymbol{r}$. The equations describing linear monochromatic modes in this medium can be put in the following general form:

$$\sum_{\mu} \hat{K}^{(\omega)}_{\mu\,\nu} \mathcal{A}^{\mu} = 0, \tag{4.14}$$

where $\boldsymbol{\mathcal{A}}(\boldsymbol{r})$ is the complex electromagnetic 4-potential related to the scalar potential φ and the vector potential $\boldsymbol{A}$ through $(\varphi, \boldsymbol{A}) = \mathrm{Re}\,(e^{i\omega t}\boldsymbol{\mathcal{A}})$, ω is the complex mode frequency, and $\hat{K}^{(\omega)}_{\mu\,\nu}$ is a linear integro-differential operator. The operator $\hat{K}^{(\omega)}_{\mu\,\nu}$ can be derived once the plasma model is specified. For instance, the medium can be modelled with the Maxwell's equations supplied with the following relations between the electric displacement field $\boldsymbol{D}$, the magnetic field $\boldsymbol{B}$, the electric field $\boldsymbol{E}$ and the magnetizing field $\boldsymbol{H}$:

$$\boldsymbol{D}(\boldsymbol{r}, t) = \int \hat{\boldsymbol{\varepsilon}}(\boldsymbol{\delta}, \tau; \boldsymbol{r}) \boldsymbol{E}(\boldsymbol{r} + \boldsymbol{\delta}, t - \tau)\, d^3\delta\, d\tau, \tag{4.15}$$

$$\boldsymbol{B}(\boldsymbol{r}, t) = \int \hat{\boldsymbol{\mu}}(\boldsymbol{\delta}, \tau; \boldsymbol{r}) \boldsymbol{H}(\boldsymbol{r} + \boldsymbol{\delta}, t - \tau)\, d^3\delta\, d\tau. \tag{4.16}$$

In this case, the expressions for permittivity $\hat{\boldsymbol{\varepsilon}}(\boldsymbol{\delta}, \tau; \boldsymbol{r})$ and magnetic permeability $\hat{\boldsymbol{\mu}}(\boldsymbol{\delta}, \tau; \boldsymbol{r})$ containing all information about the medium, should be specified as a plasma model.

Assuming some realistic boundary conditions, Eq. (4.14) can be solved providing a discrete set of frequencies ω_σ, for which this equation has non-trivial solutions, and corresponding eigenmodes $\boldsymbol{\mathcal{A}}_\sigma(\boldsymbol{r})$. The modes suitable for the α-channeling implementation can then be picked as those localized in the device, having small damping rate and posessing properties necessary for the optimal α-channeling efficiency (see Chapter 2).

The analysis of Eq. (4.14) can be simplified when the geometrical optics approximation is valid. Assuming that the characteristic inhomogeneity scale L is much

larger than both the radiation wavelength λ and the characteristic medium correlation scale length ρ_c [2], the wave field $\boldsymbol{\mathcal{A}}_\sigma$ can be represented as a superposition of propagating waves $\boldsymbol{\mathcal{A}}_{\sigma\varkappa}$, each of which looks locally like a plane wave:

$$\boldsymbol{\mathcal{A}}_{\sigma\varkappa} \approx \boldsymbol{a}_{\sigma\varkappa} e^{iS_{\sigma\varkappa}(\boldsymbol{r})}, \tag{4.17}$$

where the amplitude $\boldsymbol{a}_{\sigma\varkappa}(\boldsymbol{r})$ and the wavevector $\boldsymbol{k}_{\sigma\varkappa}(\boldsymbol{r}) \equiv \nabla S_{\sigma\varkappa}$ are slow functions with a characteristic scale of order of L. In the following, we will omit indices $\sigma\varkappa$. Substituting Eq. (4.17) in the mode equation (4.14), one obtains in the zeroth order in a small parameter $\varepsilon_\lambda = \max\{\lambda/L, \rho_c/L\}$:

$$\sum_\mu \hat{\boldsymbol{\mathcal{K}}}^{(\omega)}_{\mu\nu}(\nabla S, \boldsymbol{r}) a^\mu = 0, \tag{4.18}$$

which has a non-zero solution for $\boldsymbol{a}$ when $\boldsymbol{k}(\boldsymbol{r})$ satisfies a *local dispersion relation*:

$$\det \hat{\boldsymbol{\mathcal{K}}}^{(\omega)}(\boldsymbol{k}, \boldsymbol{r}) = 0, \tag{4.19}$$

where $\hat{\boldsymbol{\mathcal{K}}}^{(\omega)}$ is some matrix calculated once the original kernel $\hat{K}^{(\omega)}_{\mu\nu}$ and the wave phase $S(\boldsymbol{r})$ are provided. For instance, if $\hat{K}^{(\omega)}_{\mu\nu}$ is a differential operator, $\hat{\boldsymbol{\mathcal{K}}}^{(\omega)}$ is obtained from $\hat{\boldsymbol{K}}^{(\omega)}$ by replacing each partial derivative ∂_{x_i} with $\partial S/\partial x_i$ [3].

Equation (4.19) can be solved for $S(\boldsymbol{r})$ using the method of characteristics. The characteristics corresponding to this equation turn out to be identical to the trajectories of the Hamiltonian system with $H(\boldsymbol{k}, \boldsymbol{r}; \omega) = \det \hat{\boldsymbol{\mathcal{K}}}^{(\omega)}$, where $\boldsymbol{k}$ plays a role of a canonical momentum and $\boldsymbol{r}$ is a canonical coordinate. These characteristics are called the *ray trajectories* and the Hamiltonian equations describing them and reading [Stix,

---

[2] For the medium model given by Maxwell's equations and Eqs. (4.15) and (4.16), this length is proportional to the characteristic scale of $\hat{\boldsymbol{\varepsilon}}(\boldsymbol{\delta})$ and $\hat{\boldsymbol{\mu}}(\boldsymbol{\delta})$.

[3] Each term of the form $\prod_i \partial^{n_i}_{x_i}$ is then replaced with $\prod_i (\partial S/\partial x_i)^{n_i}$.

1992, §4.7]

$$\frac{d\boldsymbol{r}}{d\tau} = \frac{\partial H}{\partial \boldsymbol{k}}, \qquad \frac{d\boldsymbol{k}}{d\tau} = -\frac{\partial H}{\partial \boldsymbol{r}} \tag{4.20}$$

are a special case of the *ray-tracing equations* written for the stationary medium. Here τ is a coordinate parameterizing the trajectories.

Another approach to solving Eq. (4.19) is separation of variables. The idea of this method is to identify such a set of new coordinates $(\xi_1, \ldots, \xi_n)$ that all solutions of Eq. (4.19) can be found in the following form:

$$S(\boldsymbol{r}) = S_1(\xi_1) + S_2(\xi_2) + \cdots + S_n(\xi_n), \tag{4.21}$$

where S_i are functions of one variable. Noticing that Eq. (4.19) is identical to the stationary Hamilton-Jacobi equation for the system with the Hamiltonian $H(\boldsymbol{k}, \boldsymbol{r})$, the possibility to separate variables can be interpreted as integrability of the system.

Unfortunately, in the general case for $n \geq 2$, the separation of variables is possible for a very limited class of dynamical systems and even if the system is in fact integrable, finding proper integrals can be a very difficult task. However, for a small class of problems, in which the system dynamics can be represented as a combintation of n motions with different characteristic time scales τ_i^* such that $\tau_{i+1}^* \gg \tau_i^*$, approximate integrals of motion can be derived. In the following, we use this approach to find waves suitable for α-channeling. In particular, the ray trajectory (of the mode of interest) is assumed to be directed predominantly along the background magnetic field or transverse to it. This assumption is used to approximately integrate the ray tracing equations and find conditions under which the studied wave is localized in the device, avoiding damping on background plasma species.

4.2.1 Ray-Tracing Equations in Curvilinear Coordinates

In this section, we study wave propagation in a mirror machine and derive ray-tracing equations in cylindrical coordinates and in a system of coordinates adjusted to the magnetic field lines. Considering wave propagation outside of the regions of strong damping, we assume that the device is large enough to fit many wavelengths so that the geometrical optics approximation is valid[4]. Introducing a characteristic device length L, and a characteristic device diameter $d \ll L$, this condition can be rewritten as $k_{\|}L \gg 1$ and $k_{\perp}d \gg 1$.

The wave packet propagation in the 3-dimensional (3D) device interior can be described using the 3D ray-tracing equations (4.20):

$$\frac{d\boldsymbol{r}}{d\tau} = \frac{\partial \mathcal{D}}{\partial \boldsymbol{k}}, \qquad \frac{d\boldsymbol{k}}{d\tau} = -\frac{\partial \mathcal{D}}{\partial \boldsymbol{r}}, \tag{4.22}$$

where $\mathcal{D}(\boldsymbol{r}, \boldsymbol{k}; \omega) \equiv H(\boldsymbol{r}, \boldsymbol{k}; \omega) = 0$ is a wave dispersion relation, $\boldsymbol{r}$ and $\boldsymbol{k}$ are the wave packet position and the wave vector correspondingly, and τ is the new independent variable, or "time" defined through [Stix, 1992]

$$\frac{dt}{d\tau} = \frac{\partial \mathcal{D}}{\partial \omega}. \tag{4.23}$$

Recalling that Eqs. (4.22) are Hamiltonian equations of motion, one can introduce cylindrical coordinates (r, ϕ, z) through

$$x = r\cos\phi, \qquad y = r\sin\phi, \tag{4.24}$$

and define the corresponding canonical momenta (k_r, k_ϕ, k_z) as:

$$k_x = k_r\cos\phi - \frac{k_\phi}{r}\sin\phi, \qquad k_y = k_r\sin\phi + \frac{k_\phi}{r}\cos\phi, \tag{4.25}$$

---

[4]If this approximation fails, the mode structure can generally be calculated solving the integral equation [Ferraro et al., 1987; Burkhart et al., 1988, 1989; Zhmoginov and Fisch, 2011a]

Assume that the device is azimuthally-symmetric and therefore $\mathcal{D}$, written in the cylindrical coordines, does not depend on ϕ. In this case, since $\dot{k}_\phi = -\partial\mathcal{D}/\partial\phi$, the azimuthal wave vector component k_ϕ of any ray trajectory is constant. Therefore, in the following, looking for the eigenmodes of the wave equation (4.14), we fix the azimuthal wave number k_ϕ as some integer number M, defining the wave azimuthal structure $\varphi \sim e^{iM\phi}$ and thus eliminating one dimension from our further analysis.

Notice that the wave packet motions along and across the field lines can be decoupled by introducing new coordinates (R, η) such that R and η are constant along the magnetic field lines and along the curves orthogonal to them correspondingly. Requiring that $R(r, z = 0) = r$, $\eta(r = 0, z) = z$, $\partial R/\partial r = -\alpha b_z$, $\partial R/\partial z = \alpha b_r$, $\partial\eta/\partial r = \beta b_r$, and $\partial\eta/\partial z = \beta b_z$, where $\boldsymbol{b} = (b_r, b_z)$ is a unit vector field directed along the magnetic field lines, one can calculate functions α and β. In particular, considering a divergence-free magnetic field given by

$$B_r = -r\mathcal{B}(z)'/2, \qquad B_z(r, z) = \mathcal{B}(z), \tag{4.26}$$

where $\mathcal{B}(z)$ is a function defining magnetic field profile along the device axis, one obtains:

$$\alpha = \sqrt{\frac{\mathcal{B}(z)}{\mathcal{B}(0)}}\left(1 + \frac{r^2\mathcal{B}'^2}{8\mathcal{B}^2}\right) + O\left(\frac{r^4}{L^4}\right), \tag{4.27}$$

$$\beta = 1 - r^2\frac{\mathcal{B}''(z)}{\mathcal{B}(z)} + \frac{3r^2\mathcal{B}'^2(z)}{8\mathcal{B}^2(z)} + O\left(\frac{r^4}{L^4}\right), \tag{4.28}$$

where we assumed that the characteristic device radius is much smaller than the device length L. The important property of this coordinate transformation is that the basis vectors $\boldsymbol{e}_R$ and $\boldsymbol{e}_\eta$ are orthogonal when the original basis $(\boldsymbol{e}_r, \boldsymbol{e}_z)$ is orthonormal [5]. The

[5]Recall that the basis vectors $\boldsymbol{e}_R = \partial/\partial R$ and $\boldsymbol{e}_\eta = \partial/\partial\eta$ are such vectors that the derivative of any function f along them is equal to $\partial f/\partial R$ and $\partial f/\partial\eta$ correspondingly.

metric tensor $\bar{g}_{ij}$ in the new coordinates is diagonal and $\bar{g}_{RR} = \boldsymbol{e}_R \cdot \boldsymbol{e}_R = \alpha^{-2}$, $\bar{g}_{\eta\eta} = \boldsymbol{e}_\eta \cdot \boldsymbol{e}_\eta = \beta^{-2}$. Note here that $R = r\sqrt{\mathcal{B}(z)/\mathcal{B}(0)}$ and even though the lines of constant R coincide with the lines of constant magnetic flux, the new coordinates (R, η) are different from the flux coordinates (ψ, ζ) [Katanuma et al., 2000]. In particular, the magnetic flux ψ is a non-linear function of R and the linear coordinate along the magnetic field line ζ is equal to η only in the lowest order in r/L.

Making a canonical transformation in $\mathcal{D}$ from (r, z) to (R, η) using a generating function [Landau and Lifshitz, 1976, §45]

$$\Phi(r, z, k_R, k_\eta) = k_R R(r, z) + k_\eta \eta(r, z), \tag{4.29}$$

one obtains that $k_r = k_R\, \partial R/\partial r + k_\eta\, \partial\eta/\partial r$ and $k_z = k_R\, \partial R/\partial z + k_\eta\, \partial\eta/\partial z$. Substituting the expressions for $R(r, z)$ and $\eta(r, z)$ here, one finally obtains for k_R and k_η [6]:

$$k_R = \frac{b_r k_z - b_z k_r}{\alpha} = \frac{k_n}{\alpha}, \tag{4.30}$$

$$k_\eta = \frac{b_r k_r + b_z k_z}{\beta} = \frac{k_\parallel}{\beta}, \tag{4.31}$$

where $k_\parallel = \boldsymbol{b} \cdot \boldsymbol{k}$ and $k_n^2 = |\boldsymbol{k}|^2 - k_\parallel^2$. Here $\boldsymbol{k}$ is a two-dimensional vector with components (k_r, k_z) and k_n is the projection of this vector on a direction perpendicular to the magnetic field lines. The actual transverse component (orthogonal to the magnetic field lines) of the three-dimensional wave vector $\boldsymbol{k}$ reads $k_\perp = \sqrt{k_n^2 + M^2/r^2}$.

---

[6] Alternatively, k_R and k_η can be calculated by recalling that $k \in T_q^* M$ is a contravariant vector, where $q \in M$ is an element of the configuration space and therefore, $k_R = k_r\, \partial r/\partial R + k_z\, \partial z/\partial R$ and $k_\eta = k_r\, \partial r/\partial \eta + k_z\, \partial z/\partial \eta$.

The new coordinates (R, η) and the new momenta (k_R, k_η) form a canonical set of coordinates and therefore:

$$\dot{k}_R = -\partial\mathcal{D}/\partial R, \qquad \dot{R} = \partial\mathcal{D}/\partial k_R, \tag{4.32}$$

$$\dot{k}_\eta = -\partial\mathcal{D}/\partial \eta, \qquad \dot{\eta} = \partial\mathcal{D}/\partial k_\eta. \tag{4.33}$$

The dispersion relation $\mathcal{D}(k_\parallel, k_\perp, r, z; \omega)$ can be transformed to the new variables by replacing $k_\parallel$ with βk_η, k_n with αk_R, and by substituting the known expressions for $r(R, \eta)$ and $z(R, \eta)$. This finalizes the derivation of the ray-tracing equations in the curvilinear coordinates.

Albeit natural from the geometrical point of view, coordinates (R, η, k_R, k_η) contain non-Euclidean projections of the wave vector $\boldsymbol{k}$ and thus a more convenient set of coordinates $(r, z, k_\parallel, k_n)$ may be preferrable in certain cases. Considering $\mathcal{D}$ as a function of $k_\parallel$ and k_n, one can rewrite the ray-tracing equations (4.32) and (4.33) as:

$$\dot{r} = \frac{\partial\mathcal{D}}{\partial k_\parallel} b_r + \frac{\partial\mathcal{D}}{\partial k_n} b_z, \tag{4.34}$$

$$\dot{z} = \frac{\partial\mathcal{D}}{\partial k_\parallel} b_z - \frac{\partial\mathcal{D}}{\partial k_n} b_r \tag{4.35}$$

$$\dot{k}_\parallel = -b_r \left.\frac{\partial\mathcal{D}}{\partial r}\right|_{k_\parallel, k_n} - b_z \left.\frac{\partial\mathcal{D}}{\partial z}\right|_{k_\parallel, k_n} + \frac{\partial\mathcal{D}}{\partial k_n}\left[\frac{k_\parallel}{\rho_\parallel} + \frac{k_n}{\rho_\perp}\right], \tag{4.36}$$

$$\dot{k}_n = -b_z \left.\frac{\partial\mathcal{D}}{\partial r}\right|_{k_\parallel, k_n} + b_r \left.\frac{\partial\mathcal{D}}{\partial z}\right|_{k_\parallel, k_n} - \frac{\partial\mathcal{D}}{\partial k_\parallel}\left[\frac{k_\parallel}{\rho_\parallel} + \frac{k_n}{\rho_\perp}\right], \tag{4.37}$$

where $\rho_\parallel^{-1} = \boldsymbol{n} \cdot [(\boldsymbol{b}\nabla)\boldsymbol{b}]$ is the magnetic field curvature, $\rho_\perp^{-1} = \boldsymbol{n} \cdot [(\boldsymbol{n}\nabla)\boldsymbol{b}]$ is the curvature of lines in (r, z) plane transverse to the magnetic field lines and $\boldsymbol{n}$ is a two-dimensional unit vector perpendicular to $\boldsymbol{b}$ such that $n_r > 0$. These ray-tracing equations are more complicated than Eqs. (4.32) and (4.33), but they describe the dynamics of a more intuitive set of variables.

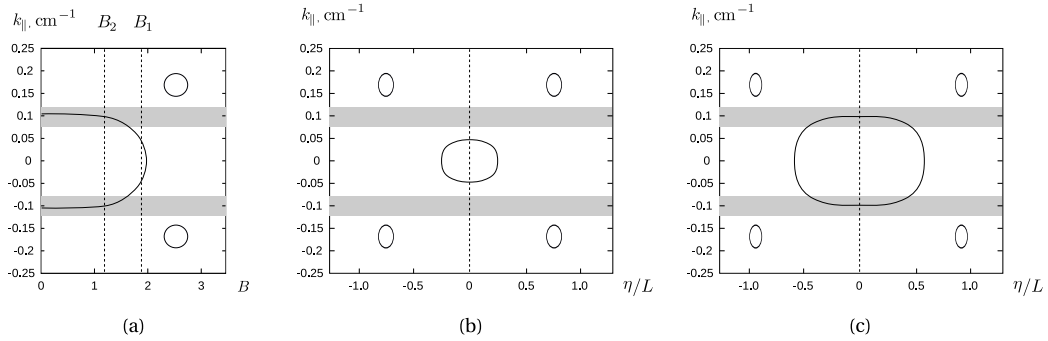

Figure 4.1: A conceptual plot of $k_\parallel(\mathcal{B})$ and $k_\parallel(\eta)$ dependencies plotted for different values of the midplane magnetic field $\mathcal{B}_0$: (a) the original $k_\parallel(B)$ dependence showing two closed loops and a half of a loop located in the vicinity of $\mathcal{B} = B_1$ (gray bars indicate areas of strong wave damping), (b) $k_\parallel(\eta)$ dependence plotted for the mirror machine with $\mathcal{B}_0 = B_1$, (c) $k_\parallel(\eta)$ dependence plotted for $\mathcal{B}_0 = B_2$. The choice of $\mathcal{B}_0 = B_1$ results in a weakly-damped mode trapped in the device core, while in the $\mathcal{B}_0 = B_2$ case, the corresponding wave might be strongly damped.

4.2.2 Quasi-Longitudinal Propagation

Consider a wave packet propagating in a mirror confined plasma. Assume that the group velocity of the wave packet is directed primarily along the magnetic field and that the radial gradients of the background medium can be neglected. More specifically, assume that the changes of R and k_R on a single longitudinal ray bounce (during which both η and k_η change substantially) are small. In this case, the approximate longitudinal ray dynamics can be established by treating k_R and R entering the wave dispersion relation $\mathcal{D}(k_\eta, \eta, k_R, R)$ as constant parameters. The $k_\eta(\eta; k_R, R)$ dependence is then found by solving $\mathcal{D}(k_\eta, \eta; k_R, R) = 0$. Note that according to Eqs. (4.27) and (4.30), the conservation of k_R is equivalent to the conservation of $k_n \mathcal{B}^{-1/2}$. Recalling that $r \sim \mathcal{B}^{-1/2}$, one may notice that $k_\perp = \sqrt{k_n^2 + M^2/r^2}$ is also proportional to $\mathcal{B}^{1/2}$.

The slow transverse dynamics in (k_R, R) variables can be calculated in two different ways. One approach to deriving $k_R(R)$ is using the conservation of the longitudinal

adiabatic invariant reading

$$I_{\parallel}(k_R, R) = \oint k_\eta \, d\eta, \tag{4.38}$$

where the integral is taken over the full longitudinal bounce period. Another approach is averaging the equations of the transverse ray dynamics over the fast longitudinal bounces:

$$\dot{k}_R = - \langle \partial \mathcal{D} / \partial R \rangle \,, \tag{4.39}$$

$$\dot{R} = \langle \partial \mathcal{D} / \partial k_R \rangle \,, \tag{4.40}$$

where $\langle \ldots \rangle$ denotes averaging over the quick bounce motion.

For a special case, in which $k_\eta \ll k_R$ and the wave of interest is localized near the midplane, *i.e.,* $|\eta| \ll L$, one can expand $\mathcal{D}$ in powers of k_η and η, assuming that the device is symmetric in η and that $\mathcal{D}$ is even in k_η:

$$\mathcal{D} \approx \mathcal{D}_0(k_R, R) + \varkappa_k(k_R, R) k_\eta^2/2 + \varkappa_\eta(k_R, R) \eta^{2g}/2g, \tag{4.41}$$

where g is some integer number. Neglecting first order corrections with respect to k_η and η, the slow motion in k_R and R can be found by solving $\mathcal{D}_0(k_R, R) \approx 0$. Substituting the solution for $k_R(R)$ in the expressions for $\varkappa_k(k_R, R)$ and $\varkappa_\eta(k_R, R)$, the fast longitudinal ray dynamics in (k_η, η) space can then be calculated.

If the magnetic field profile $\mathcal{B}(\eta)$ is fixed as well as all plasma parameters and the wave frequency ω, all ray trajectories localized axially while passing $R = R_0$ can be found by solving $\mathcal{D}(k_\eta, \eta; k_R, R_0) = 0$ for $k_\eta(\eta; k_R)$. The localized weakly-damped modes may correspond to such *candidate* values of k_R, for which the plots of $k_\eta(\eta)$ contain closed loops that avoid the regions of resonant wave-particle interactions. The resonance regions include the Landau resonance at $\omega/k_\parallel \sim w_{e\backslash i}$ and cyclotron resonances at $(\omega - n\Omega_i)/k_\parallel \sim w_i$, where w_s is a thermal velocity of species s. After

several candidate waves (localized and weakly-damped at the given radial position R_0) are identified, one should calculate their transverse dynamics $k_R(R)$ and ensure that the radial wave packet motion is indeed slow and limited and that the ray avoids resonance regions and remains localized longitudinally as it's readial components (k_R, R) drift.

Assume now that the magnetic field profile $\mathcal{B}(\eta)$ is also allowed to vary during the search for the localized weakly-damped modes. Noticing that in the lowest order, α and β depend on $\mathcal{B}$ but not on its higher derivatives and assuming that the plasma temperature and the line density of the plasma are constant along the device [7], one can see that $\mathcal{D}(k_\eta, \eta; k_R, R)$ depends on η only through $\mathcal{B}(\eta)$. Therefore, all axially localized ray trajectories passing $R = R_0$ can be identified by studying the dependence $k_\eta(\mathcal{B}; k_R)$ that solves $\mathcal{D}(k_\eta, \mathcal{B}; k_R, R_0) = 0$.

If the magnetic field profile $\mathcal{B}(\eta)$ is fixed, the candidate waves can be identified on the graphs $k_\eta(\eta; k_R)$ as closed loops further called *candidate loops*. However, if $\mathcal{B}(\eta)$ can be varied along with k_R, the function $k_\eta(\mathcal{B}; k_R)$ should be analyzed instead. Assume that $\mathcal{B}(\eta)$ is even and that it has only three extrema: one at the midplane ($\eta = 0$) and two at the locations of the magnetic mirrors ($|\eta| = \eta_R$ with $\eta_R \approx L$). Then, given $k_\eta(\mathcal{B})$, the topological properties of $k_\eta(\eta)$ can be established once the midplane magnetic field $\mathcal{B}_0$ and the mirror ratio $R_\mathcal{B}$ are provided. Assume that a candidate loop can be identified on the resulting graph $k_\eta(\eta)$. Plotted as a function of $\mathcal{B}$, this loop can be located either (a) in the middle of the segment $[\mathcal{B}_0, R_\mathcal{B}\mathcal{B}_0]$, or (b) be "wrapped" around one of its ends, in which case the $k_\parallel(\mathcal{B})$ graph, restricted to $\mathcal{B}_0 \leq \mathcal{B} \leq R_\mathcal{B}\mathcal{B}_0$, shows just a half loop (see Fig. 4.1). Therefore, in order to

[7] We assume that temperatures of the plasma species $T_{e\backslash i}$ are functions of R only and that the plasma density $n_{e\backslash i}$ is given by $n_{e\backslash i} \approx n^0_{e\backslash i}(R)\sqrt{\mathcal{B}(\eta)/\mathcal{B}(0)}$.

find a candidate system allowing a propagation of a slowly-damped contained mode trapped near the device core, one needs to study $k_{\|}(\mathcal{B})$ dependencies plotted for different values of ω, M, k_R, n^0, R_0, and T^0. The features indicating the existence of the mode include either the presence of a candidate loop, or a half loop, located at $\mathcal{B} = \mathcal{B}_0$ for some $\mathcal{B}_0$. For the modes contained near the device mirrors, a half loop should be localized near $\mathcal{B} = R_{\mathcal{B}}\mathcal{B}_0$ for some $\mathcal{B}_0$ and $R_{\mathcal{B}}$.

4.2.3 Quasi-Transverse Propagation

Consider a case of a transverse wave propagation when the ray trajectories are nearly orthogonal to the magnetic field lines. In contrast to the quasi-longitudinal propagation scenario, assume that the dynamics in (k_R, R) variables is much faster than the dynamics in (k_η, η) variables. In this case, by analogy with the quasi-longitudinal wave propagation analysis, one can establish the transverse ray dynamics by treating k_η and η as constant parameters. The $k_R(R)$ dependence can then be found by solving $\mathcal{D}(k_R, R; k_\eta, \eta) = 0$.

The slow longitudinal dynamics in (k_η, η) variables can be calculated either from conservation of the transverse adiabatic invariant

$$I_\perp(k_\eta, \eta) = \oint k_R \, dR, \tag{4.42}$$

or by averaging Eqs. (4.33) over the fast oscillations in (k_R, R) space:

$$\dot{k}_\eta = - \langle \partial \mathcal{D} / \partial \eta \rangle \,, \tag{4.43}$$

$$\dot{\eta} = \langle \partial \mathcal{D} / \partial k_\eta \rangle \,, \tag{4.44}$$

where $\langle \ldots \rangle$ denotes averaging over the fast motion in (k_R, R) variables. These averaged equations can also be rewritten in terms of $(k_\parallel, k_n)$ variables:

$$\dot{k}_\parallel \approx - \left\langle \frac{\partial \mathcal{D}}{\partial l} \right\rangle + \left\langle k_n \frac{\partial \mathcal{D}}{\partial k_n} \right\rangle \frac{1}{\rho_\perp}, \tag{4.45}$$

$$\dot{l} \approx \left\langle \frac{\partial \mathcal{D}}{\partial k_\parallel} \right\rangle, \tag{4.46}$$

where l is a linear coordinate along the magnetic field line such that Δl for any segment of the line is equal to the length of the curve segment.

If the magnetic field profile $\mathcal{B}(z)$ is fixed, the axially-localized modes can be identified by studying a "phase portrait" in (k_η, η) coordinates for certain prescribed

plasma parameters and wave frequency ω. This portrait can be calculated by solving $I_\perp(k_\eta, \eta) = I$ for different values of I. The contained weakly-damped modes are then identified by finding values of I corresponding to closed contours avoiding regions of strong wave damping and characterized by ray trajectories limited in (k_R, R) space. Assume now that the magnetic field profile $\mathcal{B}(z)$ is also allowed to vary during the search for the localized weakly-damped modes. By analogy with a quasi-longitudinal case, substitute the lowest-order expressions for α and β given by Eqs. (4.27) and (4.28) in $\mathcal{D}$ and assume that the plasma temperature and the line density are constant along the device axis. In this case, the dispersion relation depends on η through $\mathcal{B}(\eta)$. Therefore, the search for axially localized ray trajectories can be performed in a manner similar to that used in the quasi-longitudinal case, by studying dependence $k_\eta(\mathcal{B}; I)$, obtained as a solution of $I_\perp(k_\eta, \mathcal{B}) = I$ [8].

Instead of applying a general method described above, in the following, we will consider a special case of a transversely-propagating wave with $k_\parallel \ll k_n$ localized near the midplane at $|\eta| \ll L$. Assuming that the device is symmetric in η and that $\mathcal{D}$ is even in $k_\parallel$, one can expand the dispersion relation with respect to k_η and η:

$$\mathcal{D} \approx \mathcal{D}_0(k_R, R) + \varkappa_k(k_R, R)k_\eta^2/2 + \varkappa_\eta(k_R, R)\eta^{2g}/2g, \tag{4.47}$$

where g is some integer number. The fast transverse ray dynamics is then approximately given by $\mathcal{D}_0(k_R, R) = 0$, while the longitudinal wave packet motion is found by substituting Eq. (4.47) in Eqs. (4.33):

$$\dot{k}_\eta \approx -\langle \varkappa_\eta \rangle \eta^{2g-1}, \tag{4.48}$$

$$\dot{\eta} \approx \langle \varkappa_k \rangle k_\eta. \tag{4.49}$$

[8] Alternatively, one may use averaged ray tracing equations written in $(k_\eta, \mathcal{B})$ variables.

If $\langle \varkappa_k \rangle \langle \varkappa_\eta \rangle > 0$, Eqs. (4.48) and (4.49) describe particle motion in an attractive potential $U(\eta) = \langle \varkappa_k \rangle \langle \varkappa_\eta \rangle \eta^{2g}/2g$. Therefore, if $\langle \varkappa_k \rangle \langle \varkappa_\eta \rangle > 0$, the ray trajectories are bounded in (k_η, η) space, and under a proper choice of initial parameters they will be weakly damped on electrons due to $k_\parallel \ll \omega/w_e$. By studying $k_\eta(\mathcal{B})$ dependence and by looking for waves with $k_\parallel \approx 0$, the transversely-propagating waves suitable for α-channeling can thus be identified.

4.3 Numerical Results of the α-Channeling Mode Search

To illustrate the methods discussed in Sec. 4.2 and to show that weakly-damped modes can exist in a practical fusion device, consider two mirror machine designs: a proof-of-principle facility and a fusion reactor prototype with parameters similar to those used in Refs. [Pratt and Horton, 2006; Pratt et al., 2008]. Assume that the magnetic field $\boldsymbol{B}$ is given by $B_\phi = 0$ and Eqs. (4.26) with

$$\mathcal{B}(z) = B_{\min} + \frac{1}{2}(B_{\max} - B_{\min})\left[1 - \cos\left(\pi\left|2\zeta_* z/L\right|^g\right)\right], \tag{4.50}$$

where g is an integer, $\zeta_* \geq 1$ is a constant close to 1, $B_{\min}$ and $B_{\max}$ are the minimum and the maximum values of $\mathcal{B}$ correspondingly. Assume also that (a) the densities n_s of all plasma species s have a Gaussian radial profile and the linear density does not depend on the axial position, *i.e.,* $n_s(\boldsymbol{r}, z) = n_s^0\sqrt{\mathcal{B}(z)/\mathcal{B}(0)}\exp(-R^2/a^2)$, and (b) that radial plasma temperature T profile is given by $T(\boldsymbol{r}) = T^0[\kappa + (1-\kappa)\exp(-R^2/a^2)]$, where $\kappa \leq 1$ is a constant, and a is a characteristic plasma radius. The dispersion relation $\mathcal{D} = 0$ is modelled by the plasma kinetic dispersion relation reading $\mathcal{D} = \det(\hat{\boldsymbol{\varepsilon}} - n^2\hat{\mathbf{1}} + \boldsymbol{nn})$, where $\boldsymbol{n} = \boldsymbol{k}c/\omega$, $\hat{\boldsymbol{\varepsilon}} = \hat{\mathbf{1}} + \sum_s \hat{\boldsymbol{\chi}}_s$, $\hat{\boldsymbol{\chi}}_s = \omega_{ps}^2/\omega \cdot \sum_\ell e^{-\lambda}\hat{\boldsymbol{Y}}_\ell^s(\lambda)$, and tensor $\hat{\boldsymbol{Y}}_\ell^s(\lambda)$ is given by the following expression [Stix, 1992]:

$$\hat{\boldsymbol{Y}}_\ell^s = \begin{pmatrix} \dfrac{\ell^2 I_\ell}{\lambda_s}A_\ell & -i\ell\Delta I_\ell A_\ell & \dfrac{k_\perp}{\Omega_s}\dfrac{\ell I_\ell}{\lambda_s}G_\ell \\ i\ell\Delta I_\ell A_\ell & \left(\ell^2 I_\ell\lambda_s^{-1} + 2\lambda_s\Delta I_\ell\right)A_\ell & \dfrac{ik_\perp}{\Omega_s}\Delta I_\ell G_\ell \\ \dfrac{k_\perp}{\Omega_s}\dfrac{\ell I_\ell}{\lambda_s}G_\ell & -\dfrac{ik_\perp}{\Omega_s}\Delta I_\ell G_\ell & \dfrac{2(\omega - \ell\Omega_s)}{k_\parallel w_{s\perp}^2}I_\ell G_\ell \end{pmatrix}. \tag{4.51}$$

Here ω_{ps}^2 is the plasma frequency for species s, $\Delta I_\ell = I_\ell(\lambda_s) - I_\ell'(\lambda_s)$, $A_\ell = (k_\parallel w_{s\parallel})^{-1}Z_0(\xi_\ell^s)$, $G_\ell = k_\parallel^{-1}[1 + \xi_\ell^s Z_0(\xi_\ell^s)]$, $\xi_\ell^s = (\omega - \ell\Omega_s)(k_\parallel w_{s\parallel})^{-1}$, $\lambda_s = k_\perp^2\rho_s^2/2$, Z_0 is the real part of

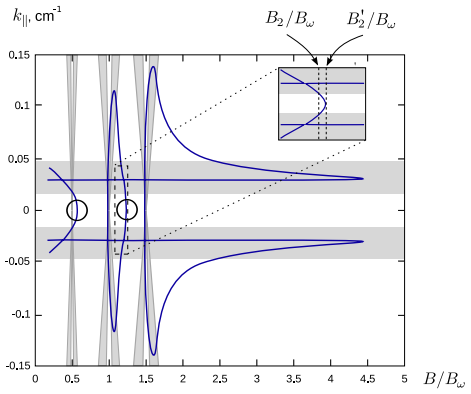

Figure 4.2: Dependence of $k_{\|} \approx k_\eta$ on B/B_ω for $\omega \approx 5.8 \times 10^7\,\mathrm{s}^{-1}$, $R = 18.3\,\mathrm{cm}$, $n_D^0 = n_T^0 = 6.67 \times 10^{12}\,\mathrm{cm}^{-3}$, $M = 1$, and $k_R = 0.045\,\mathrm{cm}^{-1}$. Parts of the dispersion curve inside the gray areas do not satisfy the applicability conditions of the employed dispersion relation and correspond to waves strongly damped through electron Landau resonance, or ion cyclotron resonance. Circles indicate the parts of the dispersion curve in the regions $[B_{1\backslash 2}/B_\omega, B'_{1\backslash 2}/B_\omega]$ corresponding to the weakly-damped mode candidates. The inset shows zoomed in band $[B_2/B_\omega, B_2'/B_\omega]$ in better resolution.

the plasma dispersion function, $w_{s\,\|}$ and $w_{s\,\perp}$ are parallel and perpendicular thermal particle velocities correspondingly, $\rho_s = w_{s\,\perp}/\Omega_s$, and Ω_s is the gyrofrequency.

4.3.1 Proof-of-Principle Facility

For a proof-of-principle facility [Pratt and Horton, 2006; Pratt et al., 2008] consider an open system with characteristic diameter $d = 6a = 1.2\,\mathrm{m}$, central cell length $L = 12\,\mathrm{m}$, ion and electron temperatures on the axis $T_e^0 = T_i^0 = 4\,\mathrm{keV}$, $\kappa = 0.15$, $B \sim 1\,\mathrm{T}$, and electron and ion densities on axis at the midplane $n_e^0 = n_D^0 + n_T^0$ being of order of $10^{13}\,\mathrm{cm}^{-3}$, with n_D^0 and n_T^0 being the deuterium and tritium densities correspondingly.

Consider first the case $k_\perp \rho_\alpha \sim 1$, which implies $k_\perp \rho_i \ll 1$. Calculating the dependence $k_{\|}(\mathcal{B})$ numerically for $R = 18.3\,\mathrm{cm}$, $n_D^0 = n_T^0 = 6.67 \times 10^{12}\,\mathrm{cm}^{-3}$, $M = 1$, $k_R = 0.045\,\mathrm{cm}^{-1}$, and $\omega \approx 5.8 \times 10^7\,\mathrm{s}^{-1}$ approximately equal to the deuterium

gyrofrequency in the magnetic field $B_\omega = 1.2\,\mathrm{T}$, several loop candidates were identified (Fig. 4.2). Two parts of the plot indicated by circles lie outside of the areas susceptible to strong Landau and ion cyclotron damping and have reflection points at the higher values of the magnetic field. Both curve segments can be described by an approximate dispersion relation

$$a = n_\parallel^2 + \frac{d^2}{b - n^2}, \tag{4.52}$$

where

$$a \approx 1 - \sum_i \frac{\omega_{pi}^2}{\omega} \sum_\ell e^{-\lambda_i} \frac{\ell^2 I_\ell(\lambda_i)}{\lambda_i(\omega - \ell\Omega_i)}, \tag{4.53}$$

$$b \approx 1 - \sum_i \frac{\omega_{pi}^2}{\omega} \sum_\ell \frac{e^{-\lambda_i}}{\omega - \ell\Omega_i} \left[\frac{\ell^2 I_\ell(\lambda_i)}{\lambda_i} + 2\lambda_i \left(I_\ell - I_\ell' \right) \right], \tag{4.54}$$

$$d \approx \sum_i \frac{\omega_{pi}^2}{\omega} \sum_\ell \frac{\ell e^{-\lambda_i} \left(I_\ell - I_\ell' \right)}{\omega - \ell\Omega_i} + \frac{\omega_{pe}^2}{\omega\Omega_e}, \tag{4.55}$$

might correspond to weakly-damped modes trapped near the midplane. This dispersion relation was derived from $\|\hat{\boldsymbol{\varepsilon}} - n^2\hat{\mathbf{1}} + \boldsymbol{nn}\| = 0$ neglecting $n_\perp^2$ compared to ε_{zz}, neglecting ε_{xz}, ε_{zx}, ε_{xy}, ε_{yx}, and assuming that $\Omega_e \gg \omega$. The dispersion relation (4.52) is the finite-$k_\perp\rho$ version of the fast/shear Alfvén wave dispersion relation for cold plasmas obeying

$$(S - n_\parallel^2)(S - n^2) = D^2, \tag{4.56}$$

where

$$S = 1 + \sum_s \frac{\omega_{ps}^2}{\Omega_s^2 - \omega^2}, \tag{4.57}$$

$$D = \sum_s \frac{\omega_{ps}^2 \Omega_i}{\omega(\Omega_s^2 - \omega^2)}. \tag{4.58}$$

However, while Eq. (4.52) describes all of the predicted waves with $k_\parallel \approx 0$ shown in Fig. 4.2, the cold plasma dispersion relation holds only at $\omega \approx \Omega_D$.

Both candidate loops shown in Fig. 4.2 are expected to be localized near the local minimum of the magnetic field and have $k_\parallel \ll k_n$. Numerical calculations of

$k_\parallel(\mathcal{B})$ for other wave and plasma parameters (different from those used in Fig. 4.2 by no more than one order of magnitude) did not reveal any candidate waves which either had $k_\parallel \gtrsim k_n$, or were represented by closed loops in $k_\parallel(\mathcal{B})$ plot. Hence, for $k_\perp \rho_i \ll 1$, the observed candidate waves can be studied assuming quasi-longitudinal, or quasi-transverse propagation for the approximate dispersion relation $\mathcal{D}$ given by Eq. (4.41). Furthermore, numerically calculating $k_\parallel(\mathcal{B})$ for $k_\perp \rho_i \gtrsim 1$ for plasma and wave parameters similar to those used in the $k_\perp \rho_i \ll 1$ case, we also did not observe candidate waves with $k_\parallel \gtrsim k_n$, or closed loops in the $(k_\parallel, \mathcal{B})$ space. This suggests that the candidate waves with $k_\perp \rho_i \gtrsim 1$ can also be studied using the approximate dispersion relation (4.41).

Consider candidates loops similar to those shown in Fig. 4.2. Assume that the corresponding waves propagate either quasi-longitudinally, or quasi-transversely and that for such waves the expansion (4.41) is valid. Using this expansion, the wave packet trajectory in (k_n, R) space can be approximated by:

$$\mathcal{D}_0(k_n, R) \approx 0. \tag{4.59}$$

The numerical solution of this equation for $\omega \approx 5.8 \times 10^7\,\mathrm{s}^{-1}$, $T_e^0 = T_i^0 = 4\,\mathrm{keV}$, $n_e^0 \approx 7.4 \times 10^{12}\,\mathrm{cm}^{-3}$, $n_D^0/n_T^0 = 1$, $\kappa = 0.15$, $M = 1$, and $B \approx 1.5\,\mathrm{T}$ is shown on Fig. 4.3. According to this figure, there are two distinct trajectories in (k_n, R) space, for one of which, marked with "s", the characteristic period of motion T_s is of order of $10\,T_l$, while for another, marked with "f", the period of motion T_f is of order of $0.02\,T_l$. Here T_l is a characteristic period of the longitudinal motion calculated for the ray trajectory with $k_\parallel \sim 0.004\,\mathrm{cm}^{-1}$. Since $T_f \ll T_l \ll T_s$, the trajectory marked with s corresponds to the longitudinal wave propagation, while the trajectory marked with f corresponds to the transverse case. An example of a ray trajectory plotted for the longitudinal case is shown on Fig. 4.4. According to this figure, which captures one

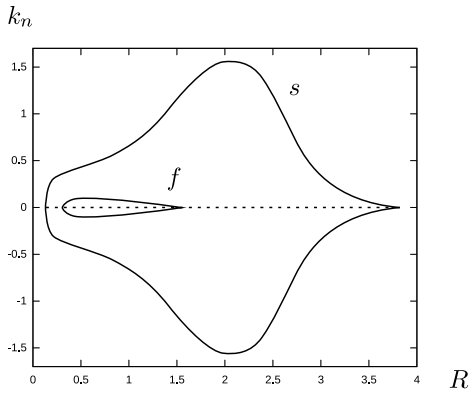

Figure 4.3: Solution of equation $\mathcal{D}_0(k_n, R) = 0$ for $\omega \approx 5.8 \times 10^7\,\mathrm{s}^{-1}$, $T_e^0 = T_i^0 = 4\,\mathrm{keV}$, $n_e^0 \approx 7.4 \times 10^{12}\,\mathrm{cm}^{-3}$, $\kappa = 0.15$, $n_D^0/n_T^0 = 1$, $M = 1$, and $B \approx 1.5\,\mathrm{T}$. The slow trajectory, period of motion along which is much larger than the characteristic period of the longitudinal oscillations, is marked with letter "s". The fast trajectory is marked with letter "f". The period of oscillations along this trajectory is much smaller than the characteristic period of the longitudinal motion.

period of slow motion in (k_n, R), the parallel adiabatic invariant $I_\parallel$ is nearly conserved. Due to $I_\parallel$ conservation, the maximum value of $k_\parallel \approx k_\eta$ is reached near the point of the curve $\mathcal{D}_0(k_n, R) = 0$, where $\varkappa_\eta/\varkappa_k$ reaches its maximum. For the parameter values used in Fig. 4.4, the minimum of $v_{\mathrm{ph}}/w_e = \omega/(k_\parallel w_e)$ is approximately equal to 3 and the corresponding wave is therefore weakly damped on electrons.

Unlike in the quasi-longitudinal case, the longitudinal dynamics of a transversely-propagating wave can exhibit chaotic behaviour. If the characteristic reflection time, on which $k_\parallel$ changes sign, is of order of T_f, the longitudinal ray dynamics cannot be accurately described by Eqs. (4.48) and (4.49). In this case, $k_\parallel$ performs a jump with a significant random component on each longitudinal reflection. As a result, the wave packet can approach Landau resonance characterized by $k_\parallel \sim \omega/w_e$ and become strongly damped on electrons (see Fig. 4.5). If the characteristic reflection time is much larger than T_f, the wave follows the equations of motion in the potential

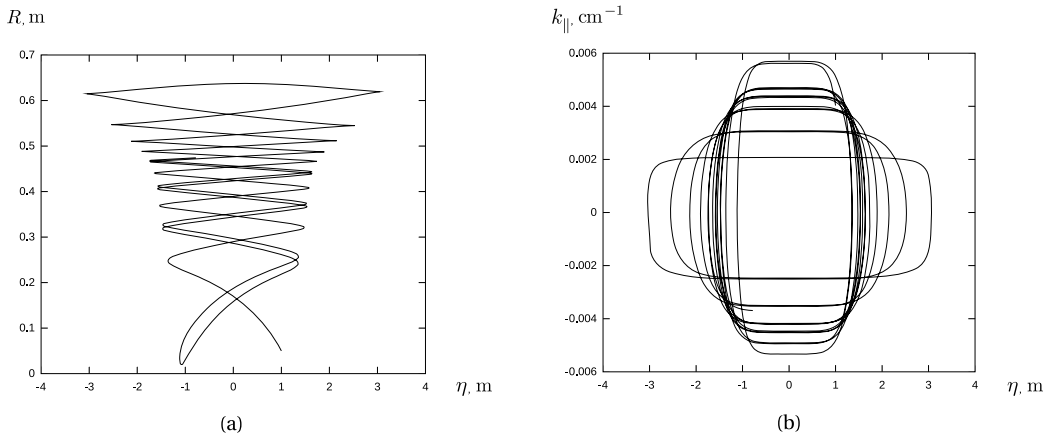

Figure 4.4: Ray trajectory plotted for the longitudinally propagating wave: (a) ray trajectory in $(k_\parallel, \eta)$ space, (b) ray trajectory in (r, z) coordinates. The system parameters are $\omega \approx 5.8 \times 10^7\,\mathrm{s}^{-1}$, $T_e^0 = T_i^0 = 4\,\mathrm{keV}$, $n_e^0 \approx 7.4 \times 10^{12}\,\mathrm{cm}^{-3}$, $n_D^0/n_T^0 = 1$, $\kappa = 0.15$, $M = 1$, $B_{\min} \approx 1.5\,\mathrm{T}$, $B_{\max} = 5B_{\min}$. The ray is launched from the point with $k_\parallel^0 = 0.004\,\mathrm{cm}^{-1}$ and $\eta = 1\,\mathrm{m}$.

$U(\eta) = \langle \varkappa_k \rangle \langle \varkappa_\eta \rangle \eta^{2g}$ (see Fig. 4.5). Under a proper choice of parameters, such wave can be made weakly-damped by avoiding resonant regions.

The α-channeling mode should not be resonant with electrons or plasma ions, but it must interact resonantly with trapped α particles. The mode satisfying these requirements and characterized by $k_\perp \rho_i \ll 1$ was identified in the system with $\omega \approx 5.8 \times 10^7\,\mathrm{s}^{-1}$, $T_e^0 = T_i^0 = 4\,\mathrm{keV}$, $n_e^0 \approx 4.2 \times 10^{12}\,\mathrm{cm}^{-3}$, $n_D^0/n_T^0 = 1$, $M = 1$, and $B \approx 0.6\,\mathrm{T}$. In this configuration, $\omega \approx 2\Omega_D$ and the interaction with α particles occurs through the second cyclotron resonance. The quasi-transverse wave launched near the midplane at $R = 20\,\mathrm{cm}$ with initial $k_\parallel \sim 0.005\,\mathrm{cm}^{-1}$ was shown to be weakly damped on electrons since $\min v_{\mathrm{ph}}/w_e \approx 3.5$. On the other hand, the same wave reaches the resonance with α particles since $\min v_{\mathrm{res}}/w_\alpha \approx 0.34$, where v_{res} is a resonance parallel velocity calculated for $\ell = 2$. The mode was also shown to be contained both radially and longitudinally, being localized in a region with $\Delta R \sim 30\,\mathrm{cm}$ and $\Delta\eta \sim 4\,\mathrm{m}$.

The present analysis of the wave propagation relies on the geometrical optics approximation. However, even if the characteristic values of $k_n\Delta R$ and $k_\parallel\Delta\eta$ are of order of π, the α-channeling mode with similar properties and the frequency close to that given by the WKB quantization condition is still expected to exist in a device of a comparable size. A full wave simulation would be, of course, necessary to find the corresponding mode frequency as well as the mode structure. One of the ways to increase both $k_n\Delta R$ and $k_\parallel\Delta\eta$ for a fixed device size and fixed $\mathcal{B}_0$ is to consider higher-order cyclotron resonances. Numerical simulations confirmed that after doubling ω (so that $\omega \approx 4\Omega_D$), the characteristic value of $k_\parallel$ can be doubled while leaving $\omega/(k_\parallel w_e)$ the same as for the $\omega \approx 2\Omega_D$ case. Furthermore, the maximum of k_n achieved for the quasi-transverse wave is also nearly doubled for $\omega \approx 4\Omega_D$. As a result, $k_n\Delta R$ increased nearly three times (due to both k_n and ΔR increase), while $k_\parallel\Delta\eta$ increased more than twice.

For the $k_\perp\rho_i \gg 1$ case, quasi-longitudinal modes in the system with $\omega \approx 5.8 \times 10^7\,\mathrm{s}^{-1}$, $T_e^0 = T_i^0 = 4\,\mathrm{keV}$, $n_e^0 \approx 7.6\times10^{12}\,\mathrm{cm}^{-3}$, $n_D^0/n_T^0 = 1$, $M = 20$, and $B \approx 1.15\,\mathrm{T}$ were considered. The ray trajectory was launched near the device periphery at $R = 55\,\mathrm{cm}$ with initial $k_\parallel \sim 0.006\,\mathrm{cm}^{-1}$. This wave was shown to be in resonance with α particles (since $\min v_{\mathrm{res}}/w_\alpha \approx 0.42$), while avoiding other resonances ($\min v_{\mathrm{ph}}/w_e \approx 3.5$). The mode was bounded both radially with $\Delta R \sim 60\,\mathrm{cm}$ and longitudinally with $\Delta\eta \sim 6\,\mathrm{m}$. The characteristic value of k_n was shown to reach 15.0 along the ray trajectory, hence the radial wave number of the mode was very large and $k_\perp\rho_\alpha$ reached the value of 300. At the same time, the characteristic value $k_\parallel\Delta\eta$ was approximately equal to 4. Therefore, such a mode can, in principle, be excited in the proof-of-principle facility.

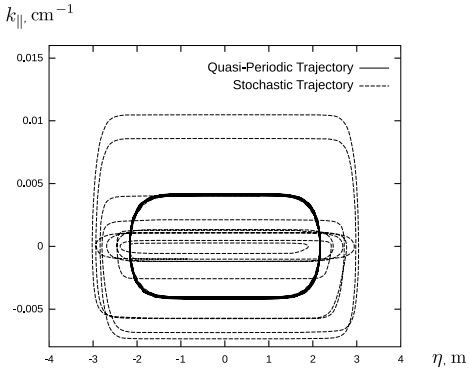

Figure 4.5: Ray trajectories in $(k_{\|}, \eta)$ space for two quasi-transverse waves: (a) chaotic trajectory plotted for the case $T_f \sim T_r$ (dashed), where T_r is a characteristic $k_{\|}$ reflection time, (b) quasi-periodic trajectory for $T_f \ll T_r$ (solid). Both trajectories are simulated for the system with $\omega \approx 5.8 \times 10^7\,\mathrm{s}^{-1}$, $M = 1$, $\kappa = 0.15$, $n_e^0 \approx 9.8 \times 10^{12}\,\mathrm{cm}^{-3}$, $B_{\min} \approx 1.5\,\mathrm{T}$, and $B_{\max} = 5B_{\min}$. The random walk occurs in a system with $T_e^0 = T_i^0 = 4\,\mathrm{keV}$ and $n_T^0/n_D^0 = 1$, while the quasi-periodic trajectory is plotted for the case $T_e^0 = T_i^0 = 2\,\mathrm{keV}$ and $n_T^0/n_D^0 = 1.5$.

As a conclusion of this section, two qualitatively different weakly-damped modes (one with $k_\perp \rho_D \ll 1$ and another with $k_\perp \rho_D \gg 1$) capable of resonant interaction with deeply-trapped α particles and characterized by $\tau_i \gg \tau_e$ were identified in a proof-of-principle facility.

4.3.2 Fusion Reactor Prototype

For a fusion reactor prototype, following Ref. [Pratt and Horton, 2006], we consider a mirror machine with the following parameters: $d = 6\,\mathrm{m}$, $L = 15\,\mathrm{m}$, $B_0 = 3\,\mathrm{T}$, $n_e^0 = n_D^0 + n_T^0 \approx 10^{14}\,\mathrm{cm}^{-3}$, $T_e = 60\,\mathrm{keV}$, and $T_i = 15\,\mathrm{keV}$. Even though $w_e \approx 0.2c$, we neglected relativistic effects and used the same dispersion relation as in Sec. 4.3.1. Similarly to the proof-of-principle facility, the dependencies of $k_{\|}$ on $\mathcal{B}$ did not show any candidate waves, which either had $k_{\|} \gtrsim k_n$, or were represented by closed loops on $k_{\|}(\mathcal{B})$ plot. Numerical simulations confirmed that two weakly-damped modes

capable of resonant interaction with deeply-trapped α particles exist in the fusion reactor prototype. Both waves are characterized by $\tau_i \gg \tau_e$ and for one of them $k_\perp \rho_D \ll 1$ (quasi-transverse wave), while for another $k_\perp \rho_D \gg 1$ (quasi-longitudinal wave). Since in the fusion reactor prototype, $\omega L/w_e$ is 1.3 times smaller compared to the proof-of-principle facility, higher ion cyclotron resonances were employed to satisfy both $k_\parallel \Delta\eta \gtrsim \pi$ and $k_n \Delta R \gtrsim \pi$.

4.3.3 Multiple Wave Regions

The system of rf regions with high α-channeling efficiency, proposed in Refs. [Fisch, 2006, 2007], consisted of several waves located at different axial positions. Unfortunately, the weakly-damped mode described by the dispersion relation (4.52) was shown to exist only in a small vicinity of the local magnetic field minimum and hence could not be employed anywhere except at the midplane. In order to use the mode described by Eq. (4.52) for α-channeling at an arbitrary axial position, a magnetic field profile with several minimum-$\mathcal{B}$ wells is proposed. To provide an example, two waves with equal values of $k_\perp$, but different values of ω, with the magnetic field profile illustrated in Fig. 4.6a were considered. The $k_\parallel(\eta)$ dependencies plotted for both waves are shown in Fig. 4.6b. As can be seen from this figure, three weakly-damped contained ion-cyclotron modes, one at the midplane, and two others at $|z| = z_m$ exist in such a configuration.

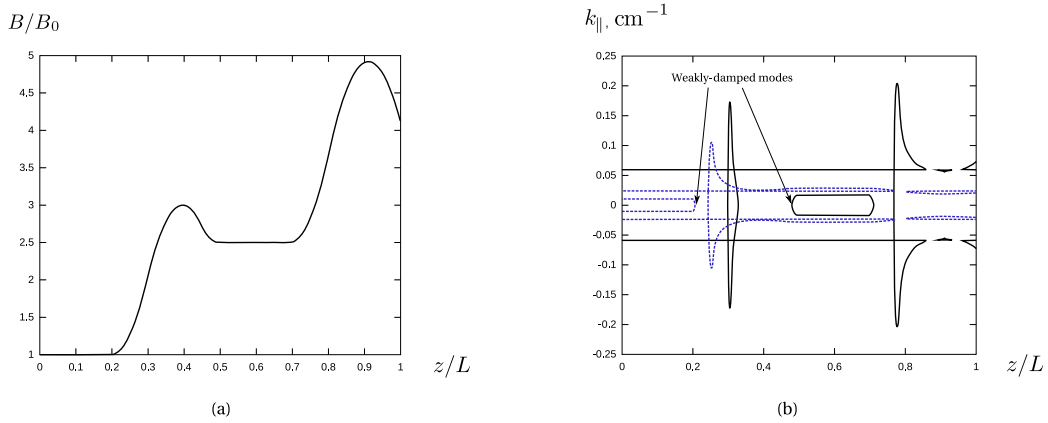

Figure 4.6: (a) The magnetic field profile in a system with three magnetic field wells. One well is near the midplane at $z = 0$ and the other two are at $|z| = z_m \approx 0.6L$. (b) The dependence $k_{\|}(z/L)$ for two waves with $\omega_1 \approx 0.8\Omega_D^0$ (dashed) and $\omega_2 \approx 2\Omega_D^0$ (solid), where Ω_D^0 is a deuterium gyrofrequency at the midplane. Three weakly-damped modes located near $z = 0$ and $|z| = z_m$ are indicated with arrows.

Chapter 5

Redirection of the Alpha Particle Energy to Ions

The α-channeling technique was originally developed to address two issues limiting the reactivity of a fusion reactor: an accumulation of fusion ash and collisional heating of electrons rather than fuel ions by energetic α particles. Unfortunately, finding appropriate modes that could interact vigorously enough with both α particles and fuel ions in a practical device proved to be challenging [Valeo and Fisch, 1994; Fisch and Herrmann, 1995; amd S. C. Chapman and Dendy, 2010; Kuley et al., 2011]. (For example, as discussed in Chapter 4, no such marginally-stable modes have been identified in mirror machines yet.) Therefore, it is highly advantageous to find other means of redirecting the α-channeling wave energy to fuel ions or other practical needs, thus expanding the parameter range of devices upon which α-channeling concept can be practiced.

In this chapter, we propose [Zhmoginov and Fisch, 2011b; Zhmoginov et al., 2011a] two ways of utilizing the α particle energy even if the channeling wave does not interact

resonantly with the background fuel ions. First, in Sec. 5.1, the minority ion injection technique capable of redirecting a fraction of the energy extracted from α particles to the fuel ions is proposed. Then, in Sec. 5.2, we demonstrate a possibility of an efficient energy transfer between two localized modes separated by an evanescent region: the α-channeling mode in the central cell and the mode heating background plasmas in the device plug. As a result of the mode coupling, the wave growth in the central cell can be balanced by the wave damping in the plugs, utilizing the fusion energy for supporting the device operation.

5.1 Minority Ion Heating with the Alpha-Channeling Wave

In this section, a new technique capable of redirecting the energy extracted from α particles to heating of the fuel ions is proposed [Zhmoginov and Fisch, 2011b]. This approach relaxes the requirements on suitable waves by combining the traditional α-channeling with minority ion heating [Yoshikawa et al., 1965; Stix, 1975; Andreson, 1983; Koch and Vaneester, 1993]. In Refs. [Koch and Vaneester, 1993; Riccitellia et al., 1999; Yamagiwa and Takizuka, 1988], the rf wave proposed for minority ion heating also heated α particles. Here, in contrast, the α particle energy flows in the opposite direction: we show that there exists a wave which can extract energy from hot α particles and transfer it to colder minority ions. The minority ions act as a catalyst, eventually forwarding the energy to colder fuel ions through collisions. By a proper choice of minority density, the wave can be made marginally-stable [Shklyar, 2011] requiring virtually no external power to sustain it. With the minority catalyst, the extracting waves no longer have to interact with α particles and fuel

ions simultaneously. We illustrate how this concept can broaden considerably the parameter space of useful waves by focusing on α-channeling in mirror geometry.

5.1.1 Choice of the Minority Species

Using minority species as a mediator species means that the operating wave is not required to interact resonantly with the fuel ions. However, the minority ion mediating species which must be in resonance with the wave cannot be chosen arbitrarily. In particular, it is required that $\omega \approx n\Omega_i$, where ω is the wave frequency, Ω_i is the gyrofrequency of the minority ions and n is an integer number. On the other hand, the wave frequency ω is restricted by the resonance condition with α particles satisfying $\omega \approx m\Omega_\alpha$ for some integer m, where Ω_α is the α particle gyrofrequency [1]. The choice of the low-energy minority ions is thus limited by the combination of these two conditions:

$$n\Omega_i \approx m\Omega_\alpha. \tag{5.1}$$

However, not all ion species that satisfy Eq. (5.1) are suitable for the technique. If Eq. (5.1) or $n\Omega_i = m\Omega_T$, where Ω_T is the tritium gyrofrequency, are satisfied exactly for some integer n and m, the resonant interaction of waves with minority ions will be accompanied by strong wave damping on the dense background ions. The optimal wave damping rate for steady-state device operation is equal to the wave growth rate due to the α particle energy extraction. Therefore, strong wave damping should be avoided if the fusion reaction rate is not sufficiently high.

---

[1] Note that even though the deuterium gyrofrequency Ω_D is equal to Ω_α, the resonant parallel velocity $v_{\rm res} = (\omega - m\Omega_\alpha)/k_\parallel$ is usually sufficiently large to avoid resonant interaction with deuterium ions, but smaller than the thermal α particle velocity.

To assess the choice of the minority ions quantitatively, we focus, for simplicity, on mirror geometry, where three candidate waves suitable for α-channeling were identified: the fast and shear Alfvén waves and the ion Bernstein wave. Two distinct regimes are then possible, depending on the parameter $k_\perp \rho_i$, where ρ_i is the minority ion gyroradius and $k_\perp$ is the perpendicular projection of the wave vector $\boldsymbol{k}$ with respect to the direction of the background magnetic field $\boldsymbol{B}$.

First, consider the perpendicularly-propagating fast Alfvén wave with $k_\perp \rho_i \ll 1$. In this case, the efficiency of the minority ion cyclotron heating is expected to decay quickly with the growth of the resonance number n. The choice of the first resonance $n = 1$ fixes $m = 1$ since hydrogen ions with $\Omega_H = 2\Omega_D$ cannot be chosen as the minority species. Therefore, all stable heavy ions with $Z = N - 1$ or $Z = N - 2$ (and hence $\Omega_i \approx \Omega_\alpha$), where Z is the number of protons and N is the number of neutrons, might be suitable for the minority ion heating technique implementation. The specific minority ion species can be chosen given the α-channeling wave frequency ω. The wave frequency can be determined by noticing that ω and $k_\parallel$ should satisfy:

$$\omega/k_\parallel = \xi_e v_e, \qquad (\omega - \Omega_\alpha)/k_\parallel = \xi_\alpha v_\alpha, \tag{5.2}$$

where $\xi_\alpha \lesssim 1/2$ to capture a large fraction of α particles and $\xi_e \gtrsim 3$ to avoid strong wave damping on electrons. Combining these two equations, one obtains:

$$\frac{\omega - \Omega_\alpha}{\omega} = \frac{\xi_\alpha}{\xi_e}\frac{v_\alpha}{v_e}. \tag{5.3}$$

For 10 keV plasmas, the frequency difference $\omega - \Omega_\alpha$ should be smaller or comparable to $0.05\,\Omega_\alpha$, which makes light stable ions (lighter than oxygen) unsuitable for the minority ion heating technique implementation. Notice here that the usability of heavy ions is also limited since their ionization energies can exceed the background plasma temperature, making their gyrofrequencies significantly smaller than Ω_α.

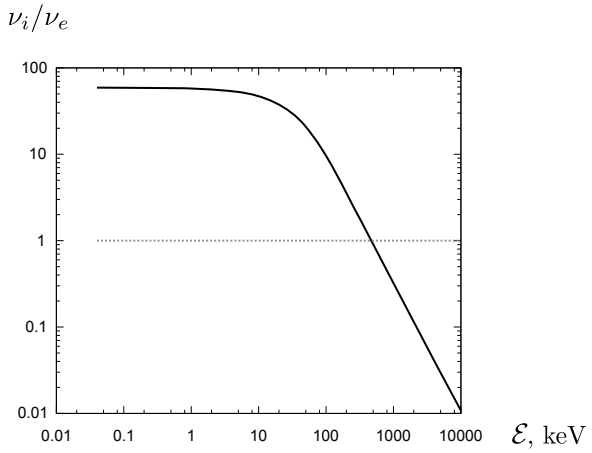

Figure 5.1: The dependence of $\nu_s^{m\backslash D}/\nu_s^{m\backslash e}$ on the minority ion energy $\mathcal{E}$ expressed in keV calculated for the Deuterium plasmas with the density $n_e = 3{\cdot}10^{13}\,\mathrm{cm}^{-3}$ and $T_D = T_e = 10\,\mathrm{keV}$. The quantities $\nu_s^{m\backslash D}$ and $\nu_s^{m\backslash e}$ denote the characteristic slowing-down rate for minority-deuterium and minority-electron collisions correspondingly. The slowing-down rates attributed to collisions with electrons and ions are approximately equal when $\mathcal{E} \approx 500\,\mathrm{keV}$.

Now consider perpendicularly-propagating waves with $k_\perp \rho_i \gtrsim 1$. In this case, higher cyclotron resonances can be employed, both for α particle energy extraction and minority ion heating. However, the extracting wave may need to have much larger intensity for α-channeling to remain efficient, because the quasilinear diffusion coefficient decays as $k_\perp \rho$ is growing [Stix, 1975; Karney, 1986, 1979]. It is for this reason that in the following we focus our attention on fast Alfvén waves.

5.1.2 Regimes of the Catalytic Effect

The requirement that minority ions must cool down preferentially on fuel ions imposes an upper bound on the extracting wave intensity. Specifically, the wave diffusion must be small enough such that the minority species remain at energies much lower than 1 MeV, for otherwise they would heat electrons instead (see Fig. 5.1). To avoid overheating, minority ions can be injected in regions where the wave energy

density is smaller than its peak value (say, where the wave is evanescent). Another way would be to detune the extracting wave from the exact resonant with the minority ions. The diffusion would then be determined by the tail of the wave spectrum.

On the other hand, a lower bound on the extracting wave intensity appears if the minority ion injection energy is lower than the majority ion thermal energy. In this case, if the wave intensity is not sufficiently high, the dominant energy transfer mechanism will be minority ion heating by the background plasmas. To avoid this, one should either use higher-intensity waves, or inject minority ions with the energy close to or even above the energy of the background species.

The final limitation on the scheme is connected with the fact that collisions result in loss of minority species through the loss cone. Since minority ions are energetic, the energy outflow associated with the particle escape must be arranged to be small compared to the total energy flow mediated by the minority population.

5.1.3 Numerical Model

Both minority ion overheating and large loss of energy with escaping ions can be critical for the implementation of the proposed technique. To address these effects quantitatively, we conducted numerical simulations of the minority ion and α particle dynamics by solving the Fokker-Planck equation [Stix, 1992]

$$\frac{\partial f}{\partial t} + \frac{1}{v_\perp}\frac{\partial}{\partial v_\perp}\left(v_\perp J_\perp\right) + \frac{\partial J_\parallel}{\partial v_\parallel} = S. \tag{5.4}$$

Here $f(v_\parallel, v_\perp, t)$ is the particle distribution function, $v_\parallel$ and $v_\perp$ are the parallel and the perpendicular particle velocities, S if the particle source and

$$J_\perp = -D_{\perp\perp}\frac{\partial f}{\partial v_\perp} - D_{\perp\parallel}\frac{\partial f}{\partial v_\parallel} + F_\perp f, \tag{5.5}$$

$$J_\parallel = -D_{\parallel\perp}\frac{\partial f}{\partial v_\perp} - D_{\parallel\parallel}\frac{\partial f}{\partial v_\parallel} + F_\parallel f, \tag{5.6}$$

where the diffusion tensor $\hat{D}$ and the particle drag $\boldsymbol{F}$ contain terms attributed to both collisions with the background plasma and quasilinear particle diffusion [Stix, 1992; Karney, 1986]. The particles are assumed to be trapped in a mirror cell with a homogeneous magnetic field while being subjected to an extracting wave. The mirror loss cone was simulated by using a boundary condition $f(v_\parallel, v_\parallel/\sqrt{R-1}, t) = 0$, where R is the mirror ratio.

The α particle extraction time, the steady-state minority ion energy and the energy loss with escaping ions were calculated in our simulations by finding the stationary solutions of Eq. (5.4). These solutions were obtained using the Monte-Carlo method: starting with no particles in the system ($f = 0$), new particles sampling the distribution S were injected and traced until the particle distribution was saturated reaching a steady state.

While accurate solutions of minority ion distribution function can be found by solving Eq. (5.4), the steady-state minority ion energy and collisional energy flows can be estimated using a simpler approach exploiting the fact that for sufficiently large wave amplitudes, the minority ion distribution function is highly anisotropic ($v_\perp \gg v_\parallel$ for most particles). The steady-state version of Eq. (5.4) can then be put in the form of the one-dimensional (1D) Fokker-Planck equation by integrating it over $v_\parallel$ [Fisch and Rax, 1992]:

$$F_\perp g - D_{\perp\perp}\frac{\partial g}{\partial v_\perp} = \frac{1}{v_\perp}\int_0^{v_\perp} v'_\perp \mathcal{S}\, dv'_\perp, \tag{5.7}$$

where $\mathcal{S} = \int_{-\infty}^{\infty} S\, dv_\parallel$ and $g(v_\perp, t) = \int_{-\infty}^{\infty} f\, dv_\parallel$. To simplify the boundary conditions, we consider the point particle source $S = \dot{N}\delta(v_\parallel - v_{\parallel 0})\delta(v_\perp - v_{\perp 0})/(2\pi v_{\perp 0})$ with $v_{\perp 0} \gtrsim v_{\parallel 0}$ and assume that the particle motion is dominated by the transverse diffusion and drag. In this case, most particles escape the device with $v_\parallel \approx v_{\parallel 0}$, corresponding to the boundary condition $g(v_{\parallel 0}/\sqrt{R-1}, t) = 0$ and Eq. (5.7) may be rewritten as:

$$F_\perp g - D_{\perp\perp}\frac{\partial g}{\partial v_\perp} = -\frac{\dot{N}}{2\pi v_\perp}, \qquad \text{for} \quad v_\perp < v_{\perp 0}, \tag{5.8}$$

$$F_\perp g - D_{\perp\perp}\frac{\partial g}{\partial v_\perp} = 0, \qquad \text{for} \quad v_\perp > v_{\perp 0}. \tag{5.9}$$

Notice that the exact location of the loss boundary does not affect the shape of the particle distribution function above $v_{\perp 0}$.

Given the solution of Eq. (5.7), one can estimate the wave energy absorbed by the minority ions and the energy flows to the majority ions and electrons. Multiplying Eq. (5.4) by $\pi v_\perp^3$ and integrating it over $v_\perp$ and $v_\parallel$, one obtains:

$$\frac{dW}{dt} = \frac{\dot{N}\left[v_{\perp 0}^2 - v_{\parallel 0}^2/(R-1)\right]}{2} + \int_{v_{\perp 0}}^{\infty} 2\pi v_\perp \left(v_\perp F_\perp + 2D_{\perp\perp} + v_\perp \frac{\partial D_{\perp\perp}}{\partial v_\perp}\right) g\, dv_\perp, \tag{5.10}$$

where W is the total minority ion energy. The energy fluxes attributed to wave energy absorption and collisions with the background plasma particles can be estimated by substituting the corresponding Fokker-Planck equation coefficients in Eq. (5.10).

5.1.4 Fokker-Planck Equation Coefficients and Plasma Parameters

The coefficients of the Fokker-Plank equation contain contributions from both particle collisions with the background plasma species and wave-particle interaction. The collisional components of the diffusion tensor and the particle drag denoted by

$\hat{D}^c$ and $\boldsymbol{F}^c$ correspondingly can be calculated for Maxwellian background plasmas and expressed in spherical coordinates (v, θ, ϕ) [Karney, 1986]:

$$D^c_{vv} = \sum_s \frac{\Gamma^{m\backslash s}}{2v_m}\left[\frac{\mathrm{erf}\,(u_s)}{u_s^2} - \frac{\mathrm{erf}\,'(u_s)}{u_s}\right], \tag{5.11}$$

$$D^c_{\theta\theta} = \sum_s \frac{\Gamma^{m\backslash s}}{4v_m}\left[\left(2 - \frac{1}{u_s^2}\right)\mathrm{erf}\,(u_s) + \frac{\mathrm{erf}\,'(u_s)}{u_s}\right], \tag{5.12}$$

$$F^c_v = -\sum_s \frac{\Gamma^{m\backslash s}}{v_m^2}\frac{m_m}{m_s}\left[\mathrm{erf}\,(u_s) - u_s\,\mathrm{erf}\,'(u_s)\right]. \tag{5.13}$$

Here $u_s = v_m/\sqrt{2}v_{\mathrm{th}\,s}$, $v_{\mathrm{th}\,s} = \sqrt{T_s/m_s}$, $\Gamma^{m\backslash s} = \nu_0^{m\backslash s} v_m^3$,

$$\nu_0^{m\backslash s} = \frac{4\pi q_m^2 q_s^2 n_s \ln\Lambda^{m\backslash s}}{m_m^2 v_m^3}, \tag{5.14}$$

$\mathrm{erf}\,(x)$ is the error function, $\ln\Lambda^{m\backslash s}$ is the Coulomb logarithm, v_m is the minority ion velocity and T_s, m_s, q_s, ρ_s are the temperature, mass, charge and gyroradius of the particles of species s correspondingly.

The wave-particle interaction contribution to the Fokker-Planck coefficients depends on the α-channeling wave properties. We assume that the chosen fast Alfvén wave is characterized by $|k_\parallel| \ll |k_\perp|$ and that it is in exact cyclotron resonance with the minority ions. At the same time, the wave cannot interact with α particles having velocity smaller than $\xi_\alpha v_\alpha$. Assuming that $k_\parallel v_\perp \ll \omega$, the general expression for the quasilinear diffusion tensor $\hat{D}^w$ can be expressed as follows for both α particles and minority ions [Karney, 1986; Kennel and Engelmann, 1966]:

$$\hat{D}^w \approx \lim_{V\to\infty}\frac{1}{V}\frac{q_i^2}{m_i^2}\sum_n \int \frac{d^3k}{(2\pi)^3}\left(\frac{n\Omega_i}{\omega}\right)^2 \pi\delta[\omega(\boldsymbol{k}) - n\Omega_i - k_\parallel v_\parallel](\xi_n^*\xi_n)\boldsymbol{v}_\perp\boldsymbol{v}_\perp, \tag{5.15}$$

where

$$\xi_n = \frac{E_{\boldsymbol{k}+}J_{n-1} + E_{\boldsymbol{k}-}J_{n+1}}{\sqrt{2}} + \frac{v_\parallel}{v_\perp}E_{\boldsymbol{k}\parallel}J_n, \tag{5.16}$$

V is the plasma volume, J_n is the Bessel function of the first kind with an argument $k_\perp \rho_i$ and

$$E_{\boldsymbol{k}+} = \frac{E_{\boldsymbol{k}x} + iE_{\boldsymbol{k}y}}{\sqrt{2}}, \tag{5.17}$$

$$E_{\boldsymbol{k}-} = \frac{E_{\boldsymbol{k}x} - iE_{\boldsymbol{k}y}}{\sqrt{2}}, \tag{5.18}$$

$$E_{\boldsymbol{k}\parallel} = E_{\boldsymbol{k}z} \tag{5.19}$$

are the components of the electric field spectral density assumed to be nearly constant for the considered range of particle velocities. The local coordinate system (x, y, z) is chosen here in such way that the unit vector $\hat{\boldsymbol{z}}$ is directed along $\boldsymbol{B}$ and $\boldsymbol{k}$ lies in the (x, z) subspace. Focusing on minority heating with the fast wave having $\omega \approx \Omega_D$, one observes that it is expected to have a right-hand circular polarization, whats makes it disadvantageous for minority ion heating. Specifically, since $E_{\boldsymbol{k}+} \approx (R/L)E_{\boldsymbol{k}\perp}$ and $E_{\boldsymbol{k}-} \approx -E_{\boldsymbol{k}\perp}$, where $E^2_{\boldsymbol{k}\perp} = |E_{\boldsymbol{k}x}|^2 + |E_{\boldsymbol{k}y}|^2$, one concludes that $|E_{\boldsymbol{k}+}/E_{\boldsymbol{k}-}| \approx |\omega - \Omega_D|/\Omega_D$.

Choosing $\omega \approx \Omega_\alpha$ and recalling that the wave interacts resonantly with all minority ions, but does not interact with α particles having $|v_\parallel| < \xi_\alpha v_\alpha$, one can approximate:

$$\hat{D}^{w\,i} \approx D_0 \widetilde{\xi}^*_1 \widetilde{\xi}_1 \boldsymbol{v}_\perp \boldsymbol{v}_\perp, \tag{5.20}$$

$$\hat{D}^{w\,\alpha} \approx D_0 \left(\frac{\Omega_\alpha}{\Omega_i}\right)^3 \widetilde{\xi}^*_1 \widetilde{\xi}_1 St(v_\parallel/v_\alpha\xi_\alpha) \boldsymbol{v}_\perp \boldsymbol{v}_\perp, \tag{5.21}$$

where $\widetilde{\xi}_n = f_+ J_{n-1} + f_- J_{n+1}$, $f_+ = E_{\boldsymbol{k}+}/E_{\boldsymbol{k}\perp}$, $f_- = E_{\boldsymbol{k}-}/E_{\boldsymbol{k}\perp}$, D_0 is proportional to the wave intensity, $\hat{D}^{w\,i}$ is the diffusion tensor for minority ions, $\hat{D}^{w\,\alpha}$ is the diffusion tensor for α particles and $St(x) = 0$ for $|x| < 1$ and is equal to 1 otherwise. For convenience, we also introduced a parameter $\gamma = I/I_0$ characterizing the operating wave intensity I. The wave intensity I_0 is such that $D_0(I_0)\,(\Omega_\alpha/\Omega_i)^3 = v^2_\alpha/\tau_\alpha$, where v_α is the α particle velocity and τ_α is the α particle collisional slowing down time.

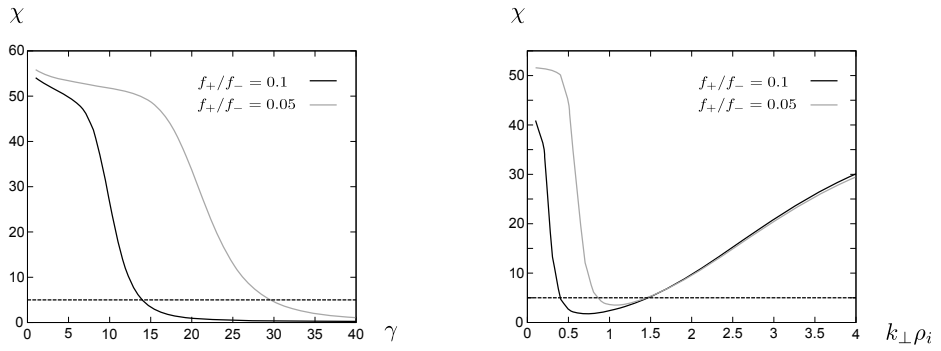

Figure 5.2: $\chi(\gamma)$ and $\chi(k_\perp\rho_i)$ for $E_+/E_- = 0.05$ and $E_+/E_- = 0.1$, from 1D Fokker-Planck simulation for ^{22}Ne and ^{21}Ne minority ions with injection energy 1.1 keV and loss energy 300 eV. The dependence $\chi(\gamma)$ is calculated for $k_\perp\rho_i = 0.45$, while $\chi(k_\perp\rho_i)$ is plotted for $\gamma = 15$. Here ρ_i is the gyroradius of 100 keV ions and $\gamma = I/I_0$, where I is the wave intensity. The quasilinear diffusion tensor was approximated by $D_{\perp\perp}(I) \approx (I/I_0)(\Omega_i/\Omega_\alpha)^4(v_\alpha^2/\tau_\alpha)(J_0 f_+ + J_2 f_-)^2/2$, where J_n is the Bessel function of order n with an argument $k_\perp v_\perp/\Omega_i$, v_α is the velocity of 3.5 MeV α particles and τ_α is a characteristic α particle collisional relaxation time.

5.1.5 Results of Numerical Simulations

The possibility of minority ion overheating was addressed by first studying the dependence of the minority steady-state distribution function on wave parameters and then comparing the optimal parameters, for which ions are not yet overheated, with those necessary for efficient α-channeling. We say that minority ions are "overheated" when $\chi < 5$, where $\chi = \mathcal{E}_{\rm fuel}/\mathcal{E}_{\rm e}$ is a ratio of collisional energy flows to majority ions ($\mathcal{E}_{\rm fuel}$) and to electrons ($\mathcal{E}_{\rm e}$). To compare wave amplitudes necessary for efficient α-channeling with those at which minority ion overheating occurred, we introduced another parameter $\Gamma = I_\alpha/I_i$. Here I_α is the wave intensity sufficient to drive α particles out of the device on half of their characteristic collisional relaxation time τ_α^0 and I_i is the wave intensity for which minority ion overheating occurs, *i.e.,* for which $\chi = 5$. If $\Gamma > 1$, the wave amplitude necessary for efficient α-channeling would cause minority ion overheating and some additional measures would have to

be taken to avoid this. On the other hand, if $\Gamma \ll 1$, the wave with intensity I_α could be insufficient to implement the technique and higher wave amplitudes or higher minority injection energies would be necessary.

If the midplane magnetic field B is known, most of the wave parameters are determined by the choice of the minority ion species; indeed, the minority ion charge and mass define the wave frequency, which should satisfy $\omega \approx \Omega_i$, and thus both wave polarization and $k_\perp$ value (assuming $k_\parallel \approx 0$) can be determined for both fast Alfvén and ion Bernstein branches. Therefore, if B and the plasma parameters are fixed, one may address the feasibility of the technique by calculating Γ for each suitable minority ion species. In our simulations, however, we took a different approach by allowing B to vary; this additional degree of freedom can be used, for example, to optimize the α particle extraction time thus lowering the extracting wave amplitude. Therefore, such wave characteristics as wave amplitude, wave polarization and $k_\perp/B$ entering the quasilinear diffusion tensor can be chosen as independent variables. Recall, however, that the wave polarization depends on $|\omega - \Omega_\alpha|$ and hence on the minority ion gyrofrequency; specifically, for fast Alfvén waves, $f_+/f_- \approx |\Omega_i - \Omega_\alpha|/\Omega_\alpha$, where f_+ is the left- and f_- is the right-hand polarized wave components. In our simulations we considered only two distinct wave polarizations: $f_+/f_- \approx 0.1$ for ^{22}Ne ions and $f_+/f_- \approx 0.05$ for a more rare isotope ^{21}Ne. Furthermore, in all our simulations using both Eqs. (5.4) and (5.7), the background plasma parameters were fixed. In particular, we chose plasma density and temperature to be $n_e = 3 \cdot 10^{13}\,\mathrm{cm}^{-3}$, $n_D = 0.9n_e$, $n_T = 0.1n_e$ and $T_e = T_D = T_T = 10\,\mathrm{keV}$ correspondingly, where the subscripts e, D and T stand for electron, deuterium and tritium parameters respectively. The magnetic field B was allowed to vary, while the mirror ratio R was equal to 5.

Our calculations of the stationary minority distribution function were carried out by solving the 1D Fokker-Planck equation (5.7) for different values of wave intensity I, wave polarization and $k_\perp/B$. The fully ionized ^{22}Ne and ^{21}Ne atoms were injected at 1.1 keV and the loss boundary was at 300 eV. As expected, χ was shown to be monotonically decreasing with I (see Fig. 5.2) since hotter minority ions tend to collide more frequently with electrons, but not ions. The dependence of χ on $k_\perp/B$, on the other hand, turned out to be non-monotonic with a local minimum at $k_\perp \sim \rho_i^{-1}$ (see Fig. 5.2), where ρ_i is the characteristic gyroradius of the hot minority ions. This suggests that low-$k_\perp$ waves might be more advantageous for limiting minority ion heating by a strong α-channeling wave. Finally, comparing two polarizations $f_+/f_- \approx 0.05$ and $f_+/f_- \approx 0.1$, the former was shown to be characterized by larger I_i. This result, however, is not sufficient to claim that Γ is smaller for $f_+/f_- \approx 0.05$ since α particle extraction simulations are necessary to determine the values of I_α in both these cases.

To calculate I_α, we performed numerical simulations of the α particle diffusion by solving the 2D Fokker-Planck equation using the Monte-Carlo method. Since the α-channeling wave cannot interact with deeply-trapped α particles due to the finite $\omega - \Omega_\alpha$, we focused our attention on extraction of α particles with $v_\parallel > \xi_\alpha v_\alpha$, where v_α is a velocity of 3.5 MeV α particles. The source of α particles was thus chosen to be mono-energetic with $v_\parallel > \xi_\alpha v_\alpha$ and $\xi_\alpha = 1/2$. Fixing the same plasma parameters as we used for minority ions, I_α was calculated for both polarizations and different $k_\perp/B$ values by finding a wave amplitude sufficient to extract α particles on time $\tau_\alpha^0/2$ (the characteristic extraction time is equal to the total number of particles for the stationary solution divided by the particle injection rate). The obtained values of I_α were then compared to the corresponding values of I_i. For both wave polarizations,

the minimum of I_α and Γ was achieved for $k_\perp/B$ satisfying $f_+ J_0(k_\perp\rho_\alpha)+f_- J_2(k_\perp\rho_\alpha) \approx 0$, where $\rho_\alpha = v_\alpha/\Omega_\alpha$. Given the optimal $k_\perp/B$, we calculated the corresponding magnetic field magnitude to be $B \approx 0.9\,\mathrm{T}$ for both polarizations. Furthermore, for $f_+/f_- = 0.1$, Γ was found to be equal to 0.43, while for $f_+/f_- = 0.05$, $\Gamma \approx 0.2$. This means that the α-channeling wave is not expected to cause minority ion overheating in both scenarios; instead, for $f_+/f_- = 0.05$, the wave with $I = I_\alpha$ can be even insufficient to heat the minorities enough for the technique to work. In the following, we use 2D Fokker-Planck simulations to optimize the technique and find optimal wave amplitudes for both considered polarizations.

Let us now calculate energy flows $\mathcal{E}_{\mathrm{fuel}}$ and $\mathcal{E}_{\mathrm{e}}$ and compare their sum $\mathcal{E}$ to the energy loss $\mathcal{W}$ associated with escaping minority ions. Solving numerically the 2D Fokker-Planck equation (5.4) with $k_\perp\rho_\alpha \approx 5.6$, we obtained the following results (see Fig. 5.3). For $f_+/f_- = 0.05$, one has $\mathcal{E}/\mathcal{W} = 1$ for $I \approx 2.3 I_\alpha$, and $\mathcal{E}/\mathcal{W} \approx 3.5$ at $I \approx I_i$. For $f_+/f_- = 0.1$, $\mathcal{E}/\mathcal{W} = 1$ for much smaller wave intensity $I \approx 0.7 I_\alpha$, and, finally, $\mathcal{E}/\mathcal{W} \approx 5.5$ at $I \approx 2 I_\alpha$. Thus, the energy lost with minority ions can be made several times smaller than the total energy mediated by minorities by increasing the wave amplitude to a sufficiently high level.

5.2 Nonlocal Energy Transfer Through the Alpha-Channeling Mode Coupling

The minority ion heating mechanism discussed in Sec. 5.1 can, in principle, be used to redirect the energy extracted from α particles directly to the background fuel ions. Heating the fuel ions using the α particle energy not only reduces the need for external power, but can also make ions hotter than the plasma electrons, causing

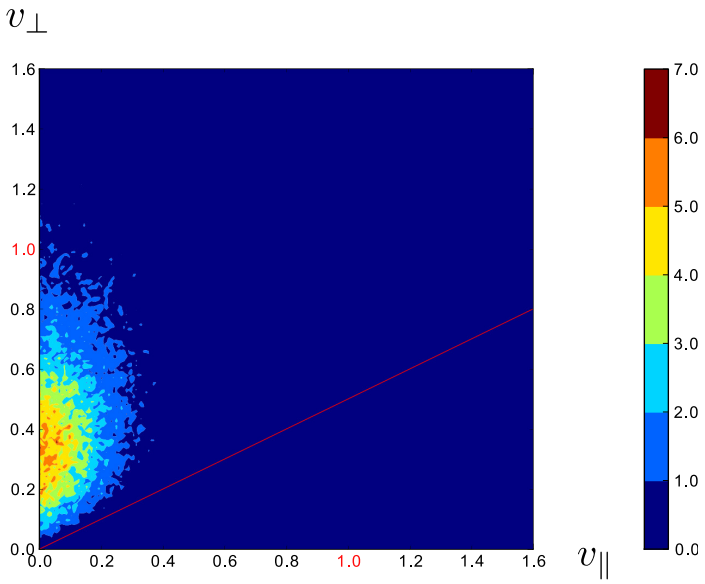

Figure 5.3: The steady state distribution of the mirror-trapped ^{22}Ne minority ions obtained by using Monte-Carlo method (with about 30000 particles) to solve the 2D Fokker-Plank equation (5.4). The wave is characterized by $\gamma = 1.0$ and $k_\perp \rho_\alpha \approx 5.6$ and the minority ions are injected with initial energy $\mathcal{E}_0 = 1.1\,\text{keV}$ and $v_\perp / v_\parallel = 2$. The solid red line shows the loss cone boundary and the particle velocities are normalized to the velocity of a 100 keV ion.

the device to operate in the so-called "hot-ion mode" Refs. [Clarke, 1980; Dawson et al., 1971; Furth and Jassby, 1974; Jassby, 1977; Post et al., 1973]. There are, however, other ways the α particle energy can be employed to lower the external power required for the operation of a mirror machine. In the following, a method of redirecting a fraction of the α particle energy to the plasma heating in the device plugs is considered.

As shown in Sec. 4.3, the α-channeling modes identified in mirror machines are localized near the minima of the magnetic field profile. Even if the parameters of the plasma in the device plugs are chosen in such a way that the α-channeling wave with a fixed frequency can propagate both in the centrall cell and in the plug, there is generally a large region between these two "cavities" where the wave propagation is

prohibited. Therefore, it is natural to expect that in this case of two localized modes separated by a large evanescent region, the energy coupling between the cavities is small. In other words, it would seem that the wave damping in the plug should be much greater than the wave growth rate in the centrall cell in order to balance the energy incoming from the α particles by the energy going to the heated species. In this section, however, we find conditions under which there exists a mode in the system, for which the amplitudes of the waves propagating in two isolated cavities are comparable despite of a large evanescent region between them. If these conditions are satisfied and such mode is excited, weak wave growth in one of the cavities can be balanced out by a weak wave damping in another cavity. As a result, the excited stationary wave transfers energy between two regions separated by a large "insulation" region, where the wave propagation is prohibited. Note here that there might exist other mechanisms of wave energy transfer. For example, in the presence of nonlinear effects, three-wave interaction can couple the α-channeling mode to other waves, which can later damp their energy on background plasma species. The detailed discussion of this energy transfer mechanism goes beyond the scope of this thesis.

5.2.1 Modes of the System with Two Cavities

In this section, we study a simplified model describing a spectrum of electromagnetic modes in a mirror machine with two magnetic field minima. A tractable one-dimensional wave equation can be obtained by first rewriting the general wave equation (4.14) in the (R, η) coordinates described in Sec. 4.2.1. Assuming that the variables R and η can be separated and fixing the transverse mode structure, one obtains a one-dimensional equation on the longitudinal wave profile. Instead of studying

the actual high-order vector wave equation, consider the following simplified model:

$$\frac{d^2\phi}{dx^2} + Q(x;\omega)\phi = 0, \tag{5.22}$$

where $\phi(x)$ is the one-dimensional scalar wave field and $Q(x;\omega) = \kappa^2(x;\omega)$ with $\kappa(x;\omega)$ being a solution of the dispersion relation $\mathcal{D}(\kappa, x, \omega) = 0$. Assume that $Q(x;\omega)$ has four zeros on the real axis at $x = x_i(\omega)$ such that $x_1 < x_2 < x_3 < x_4$ and that $Q(x;\omega)$ is negative (wave evanescent region) for $x < x_1$, $x > x_4$ and $x_2 < x < x_3$.

If κ^{-1} is much smaller than L being the characteristic scale of $Q(x)$, one can use the WKB approximation to find the solutions of Eq. (5.22). In the following, we use the phase-integral method [White, 2005] to find the consistent golbal solution on the whole real axis.

The Stokes diagram for the problem of interest is shown in Fig. 5.4. For simplicity, we assume that all four zeros of $Q(x;\omega)$ are located sufficiently far from each other and hence all Stokes constants are approximately equal to i [White, 2005]. Following the standard procedure, one can connect the coefficients of the dominant and subdominant solutions in the adjacent regions. Choosing the subdominant solutions $(x, x_4)_s$ and $(x_1, x)_s$ on the real axis for $x > x_4$ and $x < x_1$ correspondingly, *i.e.,* choosing

$$\phi_E(x) = \frac{a_4}{\sqrt{|\kappa(x)|}} \exp\left(-\int_{x_4}^{x} |\kappa(x')|\, dx'\right), \tag{5.23}$$

$$\phi_A(x) = \frac{a_1}{\sqrt{|\kappa(x)|}} \exp\left(-\int_{x}^{x_1} |\kappa(x')|\, dx'\right), \tag{5.24}$$

one can continue these solutions to the regions (3) and (8):

$$\phi_D(x) = \frac{2a_4}{\sqrt{\kappa(x)}} \cos\left(\int_{x_4}^{x} \kappa(x')\, dx' + \frac{\pi}{4}\right), \tag{5.25}$$

$$\phi_B(x) = \frac{2a_1}{\sqrt{\kappa(x)}} \cos\left(\int_{x}^{x_1} \kappa(x')\, dx' + \frac{\pi}{4}\right), \tag{5.26}$$

where $a_4 = 1$ and a_1 is an unknown constant. Similarly, solutions to the left and to the right of the points x_2 and x_3 can be connected to each other as follows:

$$\phi_B(x) = \frac{2a_2}{\sqrt{\kappa(x)}} \cos\left(\int_{x_2}^{x} \kappa(x')\,dx' + \frac{\pi}{4} + \varphi_2\right), \tag{5.27}$$

$$\phi_C(x) = \frac{a_2}{\sqrt{|\kappa(x)|}}\left[\cos\varphi_2 \exp\left(-\int_{x_2}^{x} |\kappa(x')|\,dx'\right) + 2\sin\varphi_2 \exp\left(\int_{x_2}^{x} |\kappa(x')|\,dx'\right)\right], \tag{5.28}$$

and

$$\phi_D(x) = \frac{2a_3}{\sqrt{\kappa(x)}} \cos\left(\int_{x}^{x_3} \kappa(x')\,dx' + \frac{\pi}{4} + \varphi_4\right), \tag{5.29}$$

$$\phi_C(x) = \frac{a_3}{\sqrt{|\kappa(x)|}}\left[\cos\varphi_4 \exp\left(-\int_{x}^{x_3} |\kappa(x')|\,dx'\right) + 2\sin\varphi_4 \exp\left(\int_{x}^{x_3} |\kappa(x')|\,dx'\right)\right], \tag{5.30}$$

where a_2, a_3, φ_2 and φ_4 are unknown constants. Noticing that $\phi(x)$ is described by two independent expressions in some of the regions, the relations between a_i and φ_i can be obtained:

$$a_2 = a_1 \cos\pi n, \qquad \varphi_2 = \pi n + \frac{\pi}{2} + \int_{x_1}^{x_2} \kappa(x')\,dx', \tag{5.31}$$

$$a_3 = a_4 \cos\pi m, \qquad \varphi_4 = \pi m + \frac{\pi}{2} + \int_{x_3}^{x_4} \kappa(x')\,dx', \tag{5.32}$$

for some integer numbers n and m, and

$$a_2 \cos\varphi_2 = 2a_3 \sin\varphi_4 \exp\left(\int_{x_2}^{x_3} |\kappa(x')|\,dx'\right), \tag{5.33}$$

$$2a_2 \sin\varphi_2 = a_3 \cos\varphi_4 \exp\left(-\int_{x_2}^{x_3} |\kappa(x')|\,dx'\right). \tag{5.34}$$

Combining Eqs. (5.33) and (5.34), one obtains the quantization condition for Eq. (5.22) with two potential wells [Delabaere, 1997; Berry, 1984; Şerban, 2008; Platt, 2008]:

$$\tan\varphi_2 \tan\varphi_4 = \Gamma^2. \tag{5.35}$$

where $\Gamma(\omega) = (1/2)\exp(-\int_{x_2}^{x_3} |\kappa(x';\omega)|\, dx')$.

In the limit of vanishing tunneling, when $\Gamma = 0$, the quantization condition (5.35) is factored to two expressions $\tan\varphi_2 = 0$ and $\tan\varphi_4 = 0$. Recalling the definitions of φ_2 and φ_4, these conditions can be rewritten as:

$$\delta_1(\omega) \equiv \int_{x_1}^{x_2} \kappa(x';\omega)\, dx' = \pi n + \frac{\pi}{2} \tag{5.36}$$

and

$$\delta_2(\omega) \equiv \int_{x_3}^{x_4} \kappa(x';\omega)\, dx' = \pi m + \frac{\pi}{2} \tag{5.37}$$

for some integer n and m. These are the usual quantization conditions for each isolated potential well. Therefore, in the limit $\Gamma = 0$, the spectrum of modes of Eq. (5.22) with two potential wells is composed of the modes of one well (with the corresponding frequency spectrum) and the modes of another well.

Consider another special case of two identical potential wells when $Q(x;\omega)$ is an even function. Since the set of the modes of Eq. (5.22) is invariant under the transformation $x \to -x$, one concludes that all exact solutions of Eq. (5.22) are symmetric, or antisymmetric. At the same time, for this potential profile, $\delta_1(\omega) = \delta_2(\omega)$ for all frequencies ω. Substituting this equality in Eq. (5.35) and then in Eqs. (5.33) and (5.34), one obtains that $|a_2| = |a_3|$, what means that all WKB solutions of Eq. (5.22) are either symmetric, or antisymmetric in agreement with the exact solutions.

Now consider the case of finite, but weak tunneling, when $\Gamma \ll 1$. Assume that both φ_2 and φ_4 satisfy $\varphi_i = \pi n_i + \alpha_i$ with $n_i \in \mathbb{Z}$ and $|\alpha_i| \ll 1$. The quantization condition (5.35) can then be rewritten as:

$$\alpha_2\alpha_4 \approx \Gamma^2 \tag{5.38}$$

and therefore, following Eq. (5.34), the amplitudes a_2 and a_3 are related through

$$|a_2| = |a_3|\frac{|\alpha_4|}{\Gamma} = \frac{|\alpha_4|}{\Gamma}. \tag{5.39}$$

This expression suggests that the wave amplitudes in the two cavities are comparable only if $|\alpha_2|$ and $|\alpha_4|$ are comparable. If $|\alpha_2| \ll |\alpha_4|$ or $|\alpha_4| \ll |\alpha_2|$, the mode will be localized mostly in one of the wells, showing only a very weak tunneling to another cavity.

The spectrum of modes of Eq. (5.22) can be analyzed as follows. Recalling that the phase differences δ_1 and δ_2 are functions of the wave frequency ω, one can study the spectrum geometrically by finding all intersections of the curve $[\delta_1(\omega), \delta_2(\omega)]$ with the level curves formed by the solutions of the quantization condition:

$$\cot\delta_1 \cot\delta_2 = \Gamma^2. \tag{5.40}$$

Note that if $\Gamma \ll 1$, even though the right-hand side of this equation depends on ω, this dependence does not affect the qualitative behaviour of the level curves. Figure 5.5 illustrates the bahvior of the curve $[\delta_1(\omega), \delta_2(\omega)]$ and the level curve (5.40). If an intersection between the curves occurs inside a small Γ-sized vicinity of a point $(\pi/2 + \pi n, \pi/2 + \pi m)$, the corresponding mode will be characterized by $|a_2| \sim |a_3|$, *i.e.,* the wave amplitudes in the cavities will be comparable. However, as Γ decreases, such intersections become less and less frequent. Therefore, for small Γ, in order for the mode with $|a_2| \sim |a_3|$ to exist, the parameters of the cavities must be chosen carefully.

5.2.2 Mode Damping

In the previous section, conditions under which a mode in a two-cavity system has comparable wave amplitudes in both cavities were derived. The effect of damping on

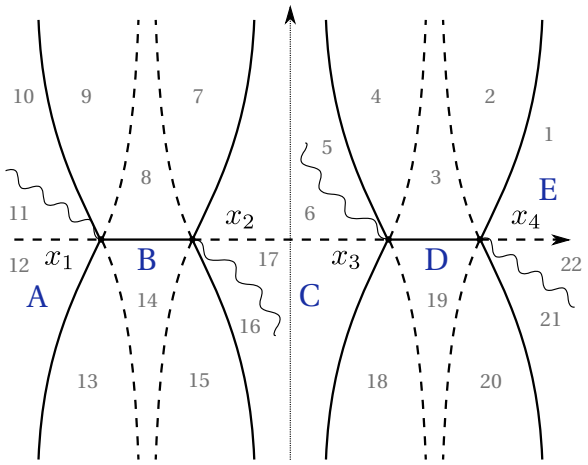

Figure 5.4: The Stokes diagram corresponding to Eq. (5.22). The anti-Stokes lines are shown with solid lines, the Stokes lines are shown with the dashed lines, and the cuts necessary to define the square root functions are shown with script lines.

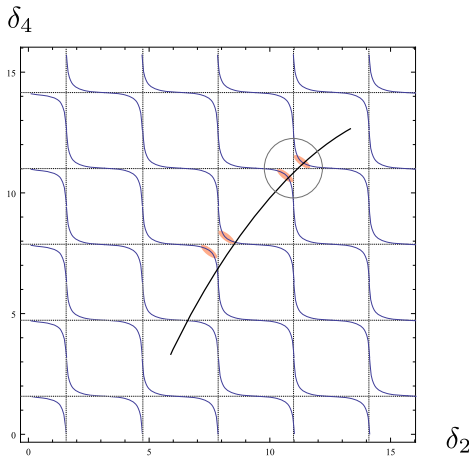

Figure 5.5: The curve $[\delta_1(\omega), \delta_2(\omega)]$ and the level curve solving Eq. (5.40). Some of the areas in small vicinities of the points $(\pi/2 + \pi n, \pi/2 + \pi m)$, where the modes are characterized by $|a_2| \sim |a_3|$ are shown with red. The intersection of the curves in one of such areas is shown with a circle.

these waves, however, was discussed only qualitatively. In this section, we calculate the damping of the identified modes and find conditions under which these modes are stationary, *i.e.,* the situation when all energy exctracted by the mode in one cavity is redirected to another, where it is damped.

Let $\hat{A}_\omega$ be a family of linear operators on a Hilbert space V with a scalar product $\langle \cdot, \cdot \rangle$ defining the modes in the system without wave damping and wave amplification. The modes $\varphi_i \in V$ and the corresponding frequencies ω_i solve $\hat{A}_{\omega_i}\varphi_i = 0$. Let $\hat{\Delta}_\omega$ be a small correction to the operator responsible for the wave-particle interactions leading to the mode dissipation or growth. The mode spectrum in the system with dissipations can then be found approximately by solving

$$\hat{A}_{\omega_i}\delta\varphi_i + \hat{\Delta}_{\omega_i}\varphi_i + \delta\omega_i \frac{\partial \hat{A}_{\omega_i}}{\partial \omega_i}\varphi_i \approx 0, \tag{5.41}$$

where the new frequencies are equal to $\omega_i + \delta\omega_i$ and the new modes are $\varphi_i + \delta\varphi_i$.

Let $\hat{A}^*_\omega$ be a Hermitian conjugate to $\hat{A}_\omega$, *i.e.,* $\langle \hat{A}^*_\omega x, y\rangle = \langle x, \hat{A}^*_\omega y\rangle$ for all $x, y \in V$. If ψ_ω is a solution of the equation $\hat{A}^*_\omega \psi_\omega = 0$ [2], then $\langle \psi_\omega, \hat{A}_\omega \phi\rangle = 0$ for all $\phi \in V$. Taking a scalar product of ψ_{ω_i} with Eq. (5.41), one therefore obtains:

$$\delta\omega_i = -\frac{\langle \psi_{\omega_i}, \hat{\Delta}_\omega \varphi_i\rangle}{\left\langle \psi_{\omega_i}, \partial \hat{A}_{\omega_i}/\partial\omega_i\, \varphi_i \right\rangle}. \tag{5.42}$$

If the operators $\hat{A}_{\omega_i}$ are Hermitian, Eq. (5.42) can be simplified by noticing that $\psi_{\omega_i} = \phi_i$. For real Q, the operator $d^2/dx^2 + Q(x;\omega)$ entering Eq. (5.22) is Hermitian for the scalar product defined by $\langle \psi, \phi\rangle = \int_{-\infty}^{+\infty} \psi^* \phi\, dx$ [3]. Therefore, one can transform Eq. (5.42) as follows:

$$\delta\omega_i = -\nu^{-1} \int \varphi_i^* \hat{\Delta}_\omega \varphi_i\, dx, \tag{5.43}$$

---

[2]The solution of this equation can be shown to exist by applying the Reisz representation theorem [Conway, 1985] to the operator $\hat{Q} = \hat{1} - \hat{P}$, where $\hat{P}$ is an operator of orthogonal projection to $\hat{A}_\omega V$.

[3]Utilization of this scalar product is justified if $V \subseteq L^2(\mathbb{R})$.

where $\nu = \int \varphi_i^* \varphi_i (\partial Q/\partial\omega)\, dx$.

Assume that $\hat{\Delta}_\omega$ vanishes outside of the potential wells located at $x_1 < x < x_2$ and $x_3 < x < x_4$. The mode $\varphi_i + \delta\varphi_i$ is then stationary if the following condition is satisfied:

$$-\nu \,\mathrm{Im}\, \delta\omega_i = \mathrm{Im} \int_{x_1}^{x_2} \varphi_i^* \hat{\Delta}_\omega \varphi_i \, dx + \mathrm{Im} \int_{x_3}^{x_4} \varphi_i^* \hat{\Delta}_\omega \varphi_i \, dx = 0. \tag{5.44}$$

Assume for simplicity that the operator $\hat{\Delta}_\omega$ acts on its argument by multiplying it by a complex function. In this case, if $|\varphi_i(x_1 < x < x_2)| \gg |\varphi_i(x_3 < x < x_4)|$, the condition (5.44) can be satisfied only if $|\mathrm{Im}\, \Delta_\omega(x_1 < x < x_2)| \ll |\mathrm{Im}\, \Delta_\omega(x_3 < x < x_4)|$. In terms of the original physical problem this means that the mode damping in the plug at $x_3 < x < x_4$ should be much greater than the wave growth in the centrall cell at $x_1 < x < x_2$. If such a strong damping of the α-channeling wave in the plug is impossible [4], excitation of a wave with $|a_2| \sim |a_3|$ discussed in detail in Sec. 5.2.1 is necessary.

5.2.3 Mode Energy Coupling with Plasma Waves

The analysis of Eq. (5.22) conducted in Sec. 5.2.1 predicted the existence of modes with comparable wave amplitudes in two potential wells separated by a large evanescent region. In this section, we consider an application of this effect to the α-channeling in mirror machines. Specifically, we find conditions on the device plug plasma necessary for achieving an efficient energy transfer between the α-channeling wave in the central cell and a similar wave in the device plug.

---

[4] Notice that the value of $\mathrm{Im}\, \Delta_\omega(x_3 < x < x_4)$ is also limited by the assumption that the operator $\hat{\Delta}_\omega$ acts as a small perturbation to the operator $\hat{A}_\omega$.

Assume that the α-channeling is implemented by exciting a fast Alfvén wave or an ion Bernstein wave with a low longitudinal mode number n_c in the device central cell. The phase difference δ_1 is then approximately equal to $\pi/2 + \pi n_c$. Following the derivation of the one-dimensional wave equation (5.22), assume that the variables R and η can be separated in the equation on the mode structure. Given the $k_R(R)$ dependence in the midplane cross-section of the central cell, one can then find the transverse mode structure in the device plug and given the plug parameters, calculate $k_\parallel(\eta)$ to find δ_2 in this part of the device.

The efficient energy coupling between the central cell and the device plug is possible if $\delta_2 \approx \pi/2 + \pi n_p$ for some integer n_p. In the following, we will focus on the plug modes with low longitudinal numbers n_p and $k_\parallel \ll \omega/v_{\mathrm{th}\,e}$. Recalling that $k_R(R)$ is fixed along the whole length of the device, one observes that a mode with $k_\parallel \approx 0$ in both the central cell and the plug may exist if the following condition derived from Eq. (4.52) is satisfied:

$$\frac{a_1 b_1 - d_1^2}{a_1 B_1} = \frac{a_2 b_2 - d_2^2}{a_2 B_2}, \tag{5.45}$$

where B_i are the magnetic field magnitudes, constants a_i, b_i and d_i are given by Eqs. (4.53), (4.54), (4.55) and the index 1 stands for the central cell, while the index 2 stands for the device plug. For fast Alfvén waves with $k_\perp \rho_i \ll 1$, Eq. (5.45) can be simplified as follows:

$$\frac{2R_1 L_1}{(R_1 + L_1)B_1} = \frac{2R_2 L_2}{(R_2 + L_2)B_2}, \tag{5.46}$$

where $R_i = S_i + D_i$, $L_i = S_i - D_i$ and S_i, D_i are given by Eqs. (4.57) and (4.58). This expression connects the plasma parameters and the magnetic field magnitudes in both cavities. If this condition is satisfied, making a small perturbation to the wave frequency and the geometrical characteristics of the device plug, one can find

the modes with comparable wave amplitudes in both cavities by finding solutions of Eq. (5.35) which satisfy $|\alpha_2| \sim |\alpha_4|$.

Chapter 6

Possible Future Experiments

In Chapter 4, plasma waves suitable for the α-channeling implementation in mirror machines were identified. Despite of having a numerical evidence for a possibility of α-channeling implementation with the identified waves (see Chapter 2), the experimental verification of the proposed technique is necessary to validate it's feasibility and to gain a knowledge of possible practical issues. The successful experimental implementation of the α-channeling technique requires that the waves with the advantageous parameters are excited in the device plasma and that the high-energetic particles behave in such wave fields as predicted by theory. Therefore, in the following, being limited by the capabilities of the presently available mirror machines, we propose to subdivide the experimental verification of the α-channeling technique into two separate stages. In the first stage, one can verify that the identified localized modes can be excited in a mirror confined plasmas by a proper choice of plasma and antenna parameters. Then, in the second stage, one can check that the high energetic particles are cooled down by the waves with properties similar to those proposed

in Chapters 2 and 4. Furthermore, it could be useful to verify that the radial displacement of the high-energetic particle is correlated to the particle energy change. This effect is particularly important for limiting particle heating by waves in some α-channeling scenarios discussed in Sec. 2.4.

This chapter is organized as follows. In Sec. 6.1, experiments which could verify existence of localized modes with parameters close to those necessary for efficient α-channeling are discussed. Among several existing mirror machines, which could potentially be used to demonstrated the core ideas of the α-channeling, the Large Plasma Device (LAPD) [Gekelman et al., 1991] located at the University of California, Los Angeles possesses a few advantageous properties such as the large device length and a customizable magnetic field profile. Even though excitation of a localized mode with the required properties in the LAPD can be challenging, an experiment demonstrating reflection of a fast Alfvén wave from the area with a large magnetic field, could be implemented in this device with only minor modifications of the experimental setup. Furthermore, the LAPD is also suitable for verifying the energy channeling effect. In Sec. 6.2, a modification of the experimental setup used in Refs. [Zhang et al., 2008, 2009], which could be employed to demonstrate cooling and an associated radial drift of particles interacting with a wave, is proposed.

6.1 Mode Excitation Experiments

In Chapter 4, three waves were identified as suitable for the α-channeling implementation: (a) the shear Alfvén wave, (b) the fast Alfvén wave and (c) the ion Bernstein wave. All of these waves are characterized by a large axial wavelength comparable to the length of the device. Therefore, one approach to exciting the

corresponding α-channeling modes would be to place rf antennas at the ends of the device even though the waves of interest do not propagate in that region. Another alternative is placing antennas at the radial periphery of the device. As discussed in Sec. 4.3, the ion Bernstein waves are expected to reach the device boundary (Fig. 4.3), where the plasma density can be several orders of magnitude smaller than that in the device center. Hence, despite of a small transverse wavelength, such waves can be excited by an externally-placed antenna. In contrast to the ion Bernstein wave, the radial reflection of the fast Alfvén wave identified in Sec. 4.3, occurs much closer to the device axis, where the plasma density is only several times smaller than in the center (Fig. 4.3). However, such wave is characterized by a much smaller k_R and hence a much larger wavelength. Therefore, even though there is a large region at the device periphery, where the fast wave is not expected to propagate, it might still be possible to excite such a mode with an externally-placed antenna.

The Large Plasma Device (LAPD) [Gekelman et al., 1991] located at the University of California, Los Angeles is an attractive experimental setup for verifying the alpha-channeling technique due to such attractive properties as the large device length, a customizable magnetic field profile and a wide range of available diagnostic tools. Numerous wave launching experiments conducted on this device were mainly concerned with the shear Alfven waves. In one of such experiments, contained shear Alfvén modes [Vincena et al., 2011] similar to those proposed in Chapter 4, were studied. Up until recently, no experiments involving fast Alfvén waves or ion Bernstein waves were conducted in the LAPD. At the present moment, however, one of the LAPD groups is involved in an ongoing fast wave launching research effort. This experimental campaign could be a perfect opportunity to verify the existence of the modes identified as suitable for alpha-channeling.

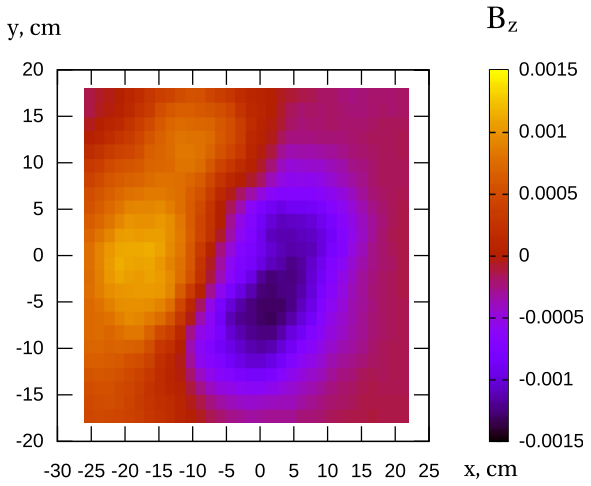

Figure 6.1: The perturbation $\delta B_z(x, y)$ of the z component (directed along the device axis) of the magnetic field $\boldsymbol{B}$ measured in the LAPD at the plane 37 at $t = 0.007963\,\mathrm{s}$ as a result of exciting a fast wave in the configuration with $B = 640\,\mathrm{G}$. The characteristic transverse scale between the maximum and the minimum of the magnetic field is approximately equal to 18 cm, what suggests $\lambda_\perp \approx 36\,\mathrm{cm}$.

In one of these recent fast wave launching experiments, the fast wave was excited by a specially designed antenna [Carter, 2011] with a characteristic scale of order of 10 cm, which was placed at the device periphery and driven with a frequency 2.8 MHz. The central cell magnetic field was equal to 640 G, the plasma density was approximately equal to $2 \cdot 10^{12}\,\mathrm{cm}^{-3}$ and the plasma temperature was equal to 5 keV for electrons and 1 keV for ions. The measured wave field profile in one of the device planes is shown in Fig. 6.1. According to this graph, the characteristic perpendicular wavelength in this experiment was approximately equal to 36 cm. Substituting the corresponding value of $k_\perp$ and other plasma and device parameters in the cold plasma dispersion relation, one obtains $k_\parallel \approx 0.0524\,\mathrm{cm}^{-1}$ or $\lambda_\parallel \approx 1.2\,\mathrm{m}$, what is sufficiently

close to the experimental estimate $\lambda_{\parallel} \approx 1.0\,\mathrm{m}$ [1]. This experimental result is thus in a good agreement with the cold wave theory and it can be interpreted as a confirmation of a possibility of launching fast waves from the device periphery into the device core.

In the following, we suggest several experiments involving only minor modifications of the fast wave launching setup, which could verify the possibility of exciting localized α-channeling modes in mirror machines. For example, it might be possible to launch fast waves with a fixed azimuthal wave number by arranging N rf antennas at the device periphery, placing them at the azimuthal angles $\psi_n = 2\pi n/N$. Measuring the wave radial profile, one could then compare the radial cutoff locations to those predicted by theory.

In another experiment, the fast wave reflection from the regions of strong magnetic field could be studied. This reflection is the main mechanism responsible for confinement of fast waves near the device midplane and leading to existence of the localized modes. The cold dispersion relation (4.56) suggests that the critical magnetic field corresponding to the fast wave cutoff in the discussed system is approximately equal to 1.4 kG. The fast wave reflection could, therefore, be studied by raising B at one side of the LAPD to approximately 1.5 kG or higher. If the characteristic scale of the magnetic field inhomogeneity is of order of 1 m or greater, the wave reflection from such a region will be nearly adiabatic. One could verify that the wave reflection occurs by measuring the magnetic field perturbation near the launching point and in the high-B region. It might also be interesting to measure the full structure of the excited wave showing the exponential decay of the wave amplitude inside the high-B

[1] The difference between the analytical estimate and the experimental value can be attributed to warm plasma effects (the electron thermal speed is comparable to the wave phase velocity) and possible inaccuracies in estimates for experimental values of $\lambda_{\perp}$ and $\lambda_{\parallel}$.

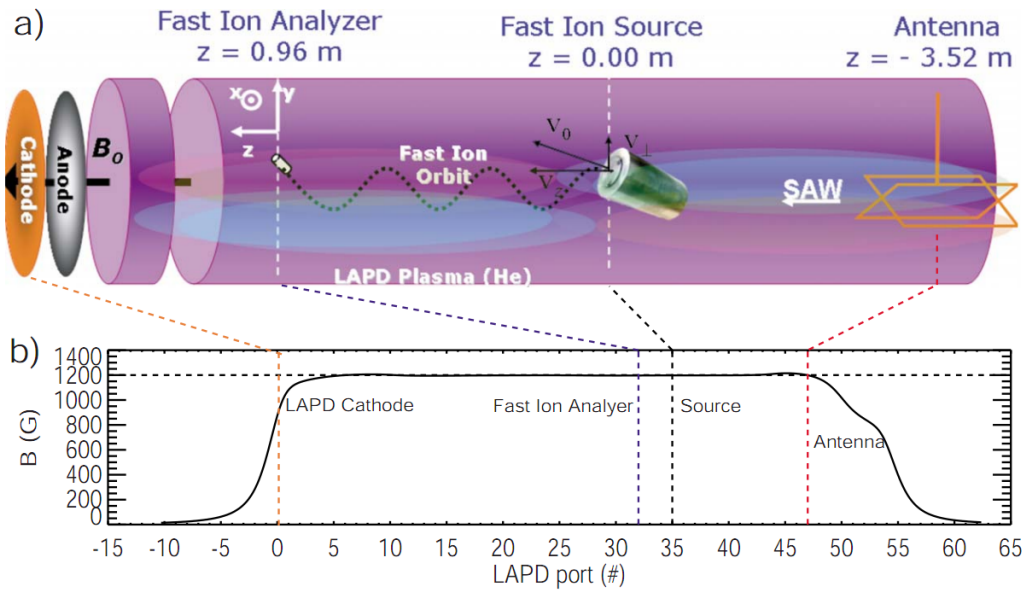

Figure 6.2: (Figure 2 from [Zhang et al., 2009]) Experimental setup at the LAPD. (a) Overview of instruments (not to scale, dotted helix is the fast ion orbit; white box denotes the fast ion-SAW interaction region). (b) Ambient magnetic field profile vs LAPD port number (black solid). The distance between two adjacent ports is 0.32 m. Instrument's typical locations are marked by dashed perpendicular lines.

region. Finally, limiting the wave propagation region with two high-B regions, one could attempt to excite the localized modes and then study the amplitude of these modes depending on the antenna location (moving it from the midplane to the wave evanescent region as necessary for one of the proposed wave launching schemes).

6.2 Alpha-Channeling Experiment

Due to a wide choice of diagnostic tools and a possibility of placing ion sources and rf antennas in the main device chamber, the LAPD is suitable for studying wave-particle interaction in plasmas. For example, in Refs. [Zhang et al., 2008, 2009], resonant interaction between 600 eV Lithium ions and a plain shear Alfvén waves

with frequencies ranging from $0.1\Omega_{He}$ to $1.0\Omega_{He}$ was considered, where Ω_{He} is the gyrofrequency of a singly ionized helium. In this experiment, the ion source and the rf antenna were placed in a homogeneous magnetic field with $B \approx 1.2\,\mathrm{kG}$ (Fig. 6.2). Exciting a shear Alfvén wave and injecting particles with a fixed pitch angle in it, the perturbation of the particle trajectory was studied by measuring the profile of the scattered beam using the particle detector. In the following, we show that by making a small modification to this experiment, one might be able to demonstrate the core ideas of the α-channeling (including both particle cooling with the wave and the correlation between the particle radial excursion and the particle energy change).

The perturbation of the particle energy observed in the wave-particle interaction experiment [Zhang et al., 2008, 2009] was relatively small since the particles passed the rf region only once. Injecting ions from within the region limited by two magnetic mirrors would, on the other hand, trap the particles causing them to interact with the wave on a each particle bounce. The magnetic mirror ratio necessary for such an experiment depends on the ion beam injection angle. For example, if $v_{\mathrm{beam}\,\perp}/v_{\mathrm{beam}\,\parallel} \sim 3$, the mirror ratio of 1.5 to 2 should be sufficient to show a loss of half of the initial beam ion energy upon leaving the mirror through the loss cone (and the mirror ratio should be even smaller if a smaller loss of the beam ion energy should prove sufficient).

The experiment design is chosen depending on the capabilities of the available particle detectors. If the particle detectors can measure both velocity distribution and spatial density of ions, the observation of the diffusion path in both velocity and configuration space might be possible. Specifically, placing the detectors outside of the region bounded by the magnetic mirrors, one could measure the particle state upon leaving the central cell through the loss cone. By changing the mirror ratio,

it would then be possible to study the diffusion path shape and dependence of the average particle exit time on the wave parameters.

If the particle detectors are capable of measuring the spatial beam profile only, some information about the diffusion path can still be obtained. Particularly, assuming that the velocity-space diffusion follows the theoretical predictions, one can compare the measured shift of the particle gyrocenter as the particle escapes the trap through the loss cone with the radial excursion obtained from Eq. (2.8). Besides showing the correlations between the radial excursion and particle energy change, the dependence of the extraction time on the wave parameteres (specifically on $k_\perp$) can be obtained. Indeed, the characteristic perpendicular wavelength for the waves launched in Refs. [Zhang et al., 2008, 2009] was approximately equal to 20 cm, which is only four times larger than the beam ion gyroradius, *i.e.,* $k_\perp \rho \approx 1.6$. The particle extraction time is therefore expected to depend on $k_\perp$ strongly, reaching the minimum for $k_\perp \sim \rho^{-1}$. Furthermore, during the interaction of the fast ions with the shear Alfvén wave, a significant radial drift (compared to $\rho_i \sim 5\,\mathrm{cm}$ when the ion loses half its energy) is expected to occur.

Unfortunately, there are several issues which can potentially prevent one from making reliable measurements of the resonant particle diffusion. The first issue is that since the particles are trapped in the central cell for many bounce periods, the distribution function of the escaping particles will be scattered over the gyro-angle. As a result, if the particle detector collects ions from a small area with a characteristic linear size a, the total flow of particles on this detector will be comparable to $n_{\mathrm{esc}} a/(2\pi\rho)$, where n_{esc} is the total flow of escaping particles. Furthermore, due to

the particle diffusion, some of the beam ions might hit the ion source [2] decreasing the total number of trapped ions over time. The characteristic time τ_{hit} of such a particle loss must, therefore, be larger than the characteristic time of particle extraction τ_{extr}. If for some configuration $\tau_{\text{extr}} \gtrsim \tau_{\text{hit}}$, the ion ejection time can be decreased by lowering the mirror ratio. Even though, in this case, the beam particles will loose only a small fraction of their energy, the characteristic change of their guiding-center position can still be of order of a centimeter, thus being easily detectable with a spatial beam profile analyzer.

[2] This could be simpler to avoid if the collisional and stochastic diffusion were negligible.

Chapter 7

Negative Mass Effect

One of the possible manifestations of the nonlinear wave-particle resonance is a modification of a particle response to external low-frequency perturbations (with time scales larger than the wave oscillation period). In this case, the slow particle dynamics can be described by introducing an effective particle mass, which depends not only on a particle rest mass, but also on the particle state and wave parameters. The conceptual possibility of the negative-mass effect (NME) was demonstrated in Ref. [Dodin and Fisch, 2008c], where the effective mass of a single charged magnetized particle in a field of a circularly-polarized "pump" wave was shown to become negative under certain conditions.

The particle dynamics in a field of a *vacuum wave* considered in Ref. [Dodin and Fisch, 2008c] was exactly integrable, allowing one to derive NME from the least action principle directly. This approach, however, cannot be easily generalized to waves with dispersion different from that in vacuum. In this chapter, we discuss [Zhmoginov et al., 2010] an alternative approach to NME based on a Hamiltonian perturbation

theory. First, the generalized wave-particle interaction model is considered and a concept of an effective mass defining the particle response to slow external perturbations is introduced. We then study a physical system containing a magnetized charged particle and a circularly-polarized wave propagating along the unperturbed magnetic field with a phase velocity c/n_0. We demonstrate that the particle effective mass can become negative and that this effect originally observed for $n_0 = 1$ [Dodin and Fisch, 2008c] is retained for the refraction index other than 1 [Zhmoginov et al., 2010]. Finally, considering a collective plasma behavior in which the particles resonant with the wave play a significant role, we show that the negative effective mass can destabilize the system, amplifying small plasma density fluctuations. Other manifestations of the negative effective particle mass are discussed later in Chapter 10.

7.1 Generalized Wave-Particle Interaction

In this section, we use a Hamiltonian perturbation theory to study a generalized model of resonant wave-particle interactions. Consider a general system governed by a Hamiltonian of the form

$$H = H_0(\boldsymbol{I}) + \varepsilon H_1(\boldsymbol{I}) \cos(\boldsymbol{\ell} \cdot \boldsymbol{\phi} - \omega_0 t), \tag{7.1}$$

where H_0 is the Hamiltonian of the unperturbed system, H_1 is the perturbation Hamiltonian describing the particle interaction with a wave [Lichtenberg and Lieberman, 1992, §2.2], $\varepsilon \ll 1$ is a small parameter, $\boldsymbol{I}$ is the n-dimensional action vector, ω_0 is the wave frequency, $\boldsymbol{\phi}$ is the conjugate angle vector, and $\boldsymbol{\ell} = (\ell_1, \ldots, \ell_n)$ is some constant integer vector. (Both H_0 and H_1 can also slowly depend on time t, but, since this dependence does not affect our considerations, we will omit it from our equations for brevity.) Without loss of generality, assume nonzero ℓ_n. Then,

performing a canonical transformation to the new actions $\boldsymbol{J}$ and the new angles $\boldsymbol{\theta}$ via the generating function

$$\Phi(\boldsymbol{J}, \boldsymbol{\phi}, t) = \phi_1 J_1 + \cdots + \phi_{n-1} J_{n-1} + (\boldsymbol{\ell} \cdot \boldsymbol{\phi} - \omega_0 t) J_n, \tag{7.2}$$

one can write the new Hamiltonian $\mathcal{H} \equiv H + \partial\Phi/\partial t$ as

$$\mathcal{H} = H_0(\boldsymbol{I}) - \omega_0 J_n + \varepsilon H_1(\boldsymbol{I}) \cos\theta_n, \tag{7.3}$$

where

$$J_i = I_i - \ell_i I_n/\ell_n \quad (i < n), \tag{7.4}$$

$$J_n = I_n/\ell_n. \tag{7.5}$$

Since $\mathcal{H}$ is independent of the $n-1$ new angles $\theta_i = \phi_i$ for $i < n$, the corresponding new actions J_i are conserved. Therefore, the perturbed system is integrable and can be described by just two equations:

$$\dot{J}_n = \varepsilon H_1(\boldsymbol{I}) \sin\theta_n, \tag{7.6}$$

$$\dot{\theta}_n = \omega_n(\boldsymbol{I}) - \omega_0 + \varepsilon \Omega_n(\boldsymbol{I}) \cos\theta_n, \tag{7.7}$$

where $\omega_n(\boldsymbol{I}) = \boldsymbol{\ell} \cdot \partial H_0/\partial \boldsymbol{I} = \partial H_0/\partial J_n$ and $\Omega_n(\boldsymbol{I}) = \boldsymbol{\ell} \cdot \partial H_1/\partial \boldsymbol{I} = \partial H_1/\partial J_n$.

The dynamics of the system described by Eqs. (7.6) and (7.7) is determined by the types of its stationary points in (θ_n, J_n) plane (or, more precisely, cylinder), which are found from

$$\dot{J}_n = 0, \quad \dot{\theta}_n = 0. \tag{7.8}$$

Those include

$$\omega_n(\boldsymbol{I}) - \omega_0 + \varepsilon \Omega_n(\boldsymbol{I}) = 0, \quad \theta_n = 0, \tag{7.9}$$

$$\omega_n(\boldsymbol{I}) - \omega_0 - \varepsilon \Omega_n(\boldsymbol{I}) = 0, \quad \theta_n = \pi, \tag{7.10}$$

and an additional family of stationary points found from

$$H_1(\boldsymbol{I}) = 0, \quad \omega_n(\boldsymbol{I}) - \omega_0 + \varepsilon\Omega_n(\boldsymbol{I})\cos\theta_n = 0. \tag{7.11}$$

In $\boldsymbol{J}$-space, the stationary points given by Eqs. (7.9)–(7.11) form a set of $(n-1)$-dimensional manifolds, which we will further call *stationary surfaces* (or *stationary curves*, if $n = 2$).

The stability of the stationary solutions with respect to small perturbations is determined by the eigenvalues $\boldsymbol{\lambda}$ of the Jacobian matrix calculated for the linearized Eqs. (7.6) and (7.7) in the vicinity of each stationary point s with $\boldsymbol{J} = \boldsymbol{J}^*$ and $\theta_n = \theta_n^*$. For the equilibrium described by Eqs. (7.9) and (7.10), one has

$$\lambda_{1,2}^2 = \varepsilon H_1 \left(\left.\frac{\partial\omega_n}{\partial J_n}\right|_s + \varepsilon \left.\frac{\partial\Omega_n}{\partial J_n}\right|_s \cos\theta_n^* \right) \cos\theta_n^*, \tag{7.12}$$

whereas for the other type of stationary points, described by Eq. (7.11), one has

$$\lambda_1 = \varepsilon\Omega_n(\boldsymbol{J}^*)\sin\theta_n^*, \tag{7.13}$$

$$\lambda_2 = -\varepsilon\Omega_n(\boldsymbol{J}^*)\sin\theta_n^*. \tag{7.14}$$

Since Eqs. (7.13) and (7.14) yield $\lambda_1 + \lambda_2 = 0$, the equilibrium solving $H_1 = 0$ always corresponds to a saddle. Of primary interest, however, are center-like equilibria, which can hold particles on larger time scales. Such stable points are only possible via Eq. (7.12), and if $\lambda_{1,2}^2 < 0$. The manifolds formed in $\boldsymbol{J}$-space by these points will be called *stable surfaces*.

Any point on any connected stable surface can be transformed into any other point on this surface, by applying additional forces, assuming that they are sufficiently weak (so the surface itself persists) and slow (so the perturbation is adiabatic). To illustrate this, consider a system described by the Hamiltonian (7.1) yet with an additional term of the form $-\boldsymbol{f}(t)\cdot\boldsymbol{\phi}$. In this case, the stationary points of Eqs. (7.6) and (7.7) are not

perturbed significantly, and the adiabatic invariant $\oint J_n \, d\theta_n$ associated with the rapid oscillations in (θ_n, J_n) space is conserved. Therefore, a particle located near the stable surface $J_n(J_1, \ldots, J_{n-1})$ will remain in its vicinity, even if the overall displacement in $\boldsymbol{J}$-space is substantial. The displacement itself is governed by $\dot{J}_i = g_i$, where $g_i = f_i - \ell_i f_n/\ell_n$ for $i < n$. However, in the original $\boldsymbol{I}$-space, the drift equations for the particle moving along the stable surface have an additional term, which originates from Eq. (7.4):

$$\dot{I}_i = g_i + l_i \sum_{k=1}^{n-1} g_k \frac{\partial J_n}{\partial J_k}. \tag{7.15}$$

Such a response to the external force is different from that of a system not subjected to the weak perturbation H_1.

In application to the wave-particle interaction problem, discussed in the following sections, this means that the response of an "oscillating" particle to an external force F can be different from that of a particle which is at rest or undergoes slow motion only. Specifically, an *effective mass* can be assigned to the particle [Dodin and Fisch, 2008c,b], according to

$$m_{\|}\dot{v} = F. \tag{7.16}$$

For simplicity, we only consider one-dimensional (1D) dynamics here; hence the index $\|$ reflecting that v is assumed parallel to F. In the sections to follow, we show that $m_{\|}$ can be very different from the particle rest mass m, even for weakly relativistic oscillations; thus, properties of "metaplasma" composed of such oscillation centers can be different from those of "normal" plasmas.

7.2 Magnetized Particle in a Wave

In this section, we apply the formalism developed in Sec. 7.1 to study the dynamics of a charged particle moving in a homogeneous magnetic field in a presence of a circularly polarized wave propagating along the magnetic field and characterized by the refraction index n_0. First, in Sec. 7.2.1, we derive the particle Hamiltonian, which is later used in Sec. 7.2.2 to determine the shape of the stationary curves. The stability of the stationary states is then analyzed in Sec. 7.2.3.

7.2.1 Basic Equations

Consider a particle moving in a homogeneous magnetic field $\boldsymbol{B}_0 = B_0\hat{\boldsymbol{z}}$, alternatively defined via the vector potential $\boldsymbol{A}_0 = -\hat{\boldsymbol{x}}By$, and the "pump" wave field with circular polarization, governed by $\boldsymbol{A}_w = (mc^2/q)(a_0/\sqrt{2})\,(\hat{\boldsymbol{x}}\cos\xi - \hat{\boldsymbol{y}}\sin\xi)$, where m and q are the particle mass and charge correspondingly, c is the speed of light, a_0 is the normalized wave field amplitude, $\hat{\boldsymbol{x}}$, $\hat{\boldsymbol{y}}$, and $\hat{\boldsymbol{z}}$ are unit vectors directed along x, y, and z correspondingly, and $\xi = \omega_0 t - kz$. The particle Hamiltonian reads as

$$H = \sqrt{m^2c^4 + c^2(\boldsymbol{P} - q\boldsymbol{A}/c)^2}, \tag{7.17}$$

where $\boldsymbol{A} = \boldsymbol{A}_0 + \boldsymbol{A}_w$, and $\boldsymbol{P}$ is the particle canonical momentum. We assume that the wave field is weak and hence treat $\boldsymbol{A}_w$ as a perturbation. Therefore, after a canonical transformation to the new actions

$$\widetilde{\mu} = (\boldsymbol{P} - q\boldsymbol{A}_0/c)^2/2m\Omega_0, \quad m\Omega_0 X = m\Omega_0 x + P_y \tag{7.18}$$

and the new angle variables

$$\widetilde{\theta} = \tan^{-1}[(P_x + m\Omega_0 y)/P_y] + \pi/2, \quad Y = -P_x/m\Omega_0, \tag{7.19}$$

similarly to Ref. [Smith and Pereira, 1978], $H \approx H_0 + \varepsilon H_1 \cos(\widetilde{\theta} - \omega_0 t + kz)$ can be approximated as

$$H = H_0 - \frac{\varepsilon \widetilde{\mu}^{1/2}}{H_0} \cos(\widetilde{\theta} - \omega_0 t + kz), \tag{7.20}$$

where $H_0 = c(m^2c^2 + 2m\Omega_0\widetilde{\mu} + p_\parallel^2)^{1/2}$ is the particle Hamiltonian without the wave, $p_\parallel \equiv P_z$ is the component of the kinetic momentum parallel to $\boldsymbol{B}_0$, $\varepsilon = mc^3\sqrt{m\Omega_0}a_0$ is the normalized amplitude playing the role of the small parameter, $\Omega_0 = qB_0/mc$ is the nonrelativistic Larmor frequency, and $\widetilde{\mu}$ is the canonical momentum, which is related to the particle magnetic moment $\mu \equiv p_\perp^2/(2m\Omega_0)$ (here $\boldsymbol{p}_\perp$ is the kinetic momentum transverse to $\boldsymbol{B}_0$) as

$$\mu = \widetilde{\mu} + \frac{mc^2a_0^2}{4\Omega_0} - a_0 c\sqrt{\frac{m\widetilde{\mu}}{\Omega_0}} \cos(\widetilde{\theta} - \omega_0 t + kz). \tag{7.21}$$

(Note that, unlike in Eq. (7.3), the small parameter ε is dimensional here.)

Following the general formalism of Sec. 7.1, we introduce the action and the angle variables of the unperturbed problem

$$I_1 = p_\parallel/k, \qquad \phi_1 = kz, \tag{7.22}$$

$$I_2 = \widetilde{\mu}, \qquad \phi_2 = \widetilde{\theta}. \tag{7.23}$$

Representing $\widetilde{\theta} - \omega_0 t + kz$ as $\boldsymbol{\ell} \cdot \boldsymbol{\phi} - \omega_0 t$, where $\boldsymbol{\ell} = (1, 1)$, we obtain then

$$J_1 = p_\parallel/k - \widetilde{\mu}, \qquad \theta_1 = kz, \tag{7.24}$$

$$J_2 = \widetilde{\mu}, \qquad \theta_2 = \widetilde{\theta} - \omega_0 t + kz. \tag{7.25}$$

Hence, we put Eq. (7.20) in the form (7.3), now reading as

$$\mathcal{H} = H_0 - \omega_0 J_2 - \frac{\varepsilon\sqrt{J_2}}{H_0} \cos\theta_2, \tag{7.26}$$

where

$$H_0 = c[m^2c^2 + 2m\Omega_0 J_2 + k^2(J_1 + J_2)^2]^{1/2}. \tag{7.27}$$

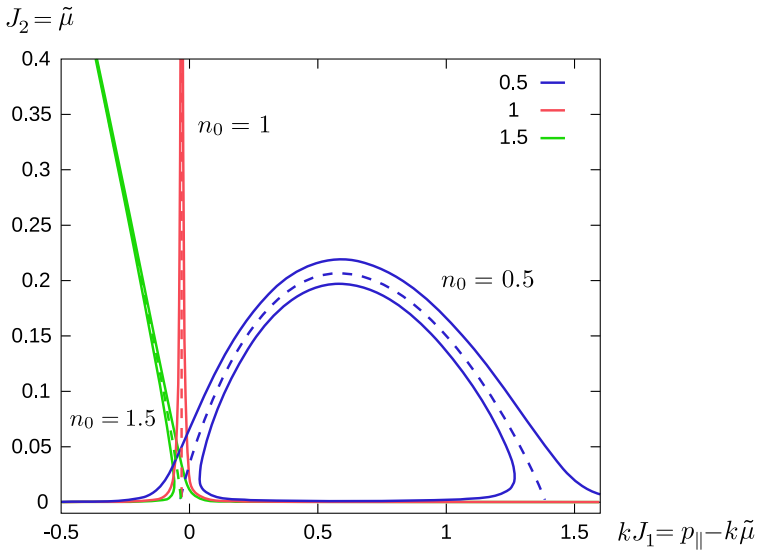

Figure 7.1: Stationary curves solving Eqs. (7.30) and (7.31) for $\varepsilon = 0$ (dashed) and $\varepsilon = 0.01$ (solid) for $n_0 = 0.5$, 1, 1.5 and $\omega_0 = 0.97\,\Omega_0$ (in units $m = q = c = 1$).

In the sections to follow, we discuss the stationary points of the Hamiltonian (7.26) and their stability, showing that unexpected dynamics can result in this seemingly well-studied problem.

7.2.2 Stationary Curves

The stationary points of the system governed by the Hamiltonian (7.26) form two distinct families. The first family contains system states that solve $H_1(J_1, J_2) = 0$ and $\cos\theta_2 = 0$ simultaneously:

$$\tilde{\mu} = 0, \qquad \theta_2 = \pi/2, \tag{7.28}$$

$$\tilde{\mu} = 0, \qquad \theta_2 = 3\pi/2. \tag{7.29}$$

The second family, which we will focus on, is obtained by solving Eqs. (7.9) and (7.10):

$$\frac{\Omega_0}{\widetilde{\gamma}} + \frac{kp_\parallel}{m\widetilde{\gamma}} - \omega_0 + \varepsilon Q = 0, \quad \theta_2 = 0, \tag{7.30}$$

$$\frac{\Omega_0}{\widetilde{\gamma}} + \frac{kp_\parallel}{m\widetilde{\gamma}} - \omega_0 - \varepsilon Q = 0, \quad \theta_2 = \pi, \tag{7.31}$$

where we introduced

$$Q = \frac{m^2c^2 + p_\parallel^2 - 2kp_\parallel\widetilde{\mu}}{2m^3c^4\widetilde{\gamma}^3\sqrt{\widetilde{\mu}}}, \tag{7.32}$$

and $\widetilde{\gamma} \equiv H_0/mc^2$ is the Lorentz factor of the unperturbed motion.

The shape of the stationary curves can be established for sufficiently small ε by neglecting the terms proportional to ε in Eqs. (7.30) and (7.31). Substituting $\varepsilon = 0$ in these equations, one obtains two asymptotic zeroth-order solutions:

$$\widetilde{\mu} = 0, \tag{7.33}$$

$$\widetilde{\mu} = \frac{(n_0^2 - 1)p_\parallel^2}{2m\Omega_0} + \frac{n_0 c p_\parallel}{\omega_0} + \frac{mc^2}{2\Omega_0}\left(\frac{\Omega_0^2}{\omega_0^2} - 1\right), \tag{7.34}$$

where $n_0 \equiv ck/\omega_0$ is the medium refraction index. In variables $(p_\parallel, \widetilde{\mu})$, Eq. (7.34) describes a parabola, concave for $n_0 < 1$ and convex for $n_0 > 1$. (One can show, however, that, in the latter case, only one of the branches of this parabola is physically realizable.) In (J_1, J_2) space, Eq. (7.34) rewrites as:

$$\frac{\Omega_0^2}{\omega_0^2} - 1 + \frac{n_0^2\omega_0^2(J_1 + J_2)^2(n_0^2 - 1)}{m^2c^4} + \frac{2\Omega_0[n_0^2 J_1 + (n_0^2 - 1)J_2]}{mc^2} = 0, \tag{7.35}$$

which can be shown to yield a single-valued dependence $J_2(J_1)$ (dashed curves in Fig. 7.1) in the upper half plane $J_2 \geq 0$.

For nonzero ε, multi-valued dependence is realized (solid curves in Fig. 7.1), which can be seen as follows. Rewrite Eqs. (7.30) and (7.31) as $\Lambda(\widetilde{\mu}, p_\parallel) = \pm\varepsilon$ where

$\Lambda = (\Omega_0 + kp_\parallel/m - \omega_0\widetilde{\gamma})/(\widetilde{\gamma}Q)$ is the normalized detuning from the (Doppler-shifted) cyclotron resonance. Since the derivative $\partial\Lambda/\partial\widetilde{\mu}$ does not generally vanish on the curve given by Eq. (7.34) and since $\Lambda(\widetilde{\mu}; p_\parallel) \sim \sqrt{\widetilde{\mu}}$, assuming that $p_\parallel$ avoids the vicinities of the zeros of Eq. (7.34), one can show that there will be a single perturbed solution $\widetilde{\mu}$ corresponding to the unperturbed solution (7.33) and two perturbed solutions corresponding to Eq. (7.34). The same property holds for the stationary curves in (J_1, J_2) space. Therefore, depending on $p_\parallel$ (or J_1) there are either one, or three solutions $\widetilde{\mu}$ (or J_2) of Eqs. (7.30) and (7.31).

The bifurcation, or critical points $\mathcal{F}$ are the points, at which the transition between one and three solutions in (J_1, J_2) plane occurs (Fig. 7.2). The critical point, which becomes weakly-relativistic for $n_0 \approx 1$ and $\omega_0 \approx \Omega_0$ as ε goes to zero, can be found as follows. Multiply Eqs. (7.30) and (7.31) by $\widetilde{\gamma}\sqrt{J_2}$ to rewrite them as

$$\sqrt{J_2}F_0(J_1, J_2, \chi) \pm \varepsilon F_1(J_1, J_2, \chi) = 0, \tag{7.36}$$

where $\chi \equiv n_0 - 1$,

$$F_0 = \Omega_0 + \frac{kp_\parallel}{m} - \omega_0\widetilde{\gamma}, \qquad F_1 = \widetilde{\gamma}Q\sqrt{J_2}. \tag{7.37}$$

Assuming $\chi \ll 1$, we solve Eq. (7.36) perturbatively in both ε and χ. To do so, consider first the unperturbed solution corresponding to $\varepsilon = 0$ and $\chi = 0$:

$$J_1 = J_1^0 = \frac{mc^2(\omega_0^2 - \Omega_0^2)}{2\omega_0^2\Omega_0}. \tag{7.38}$$

Hence, the perturbation $\delta J_1(J_2)$ can be expressed as:

$$\delta J_1 \approx -\chi\,\frac{\partial F_0/\partial\chi}{\partial F_0/\partial J_1} - \frac{\varepsilon F_1}{\sqrt{J_2}\,\partial F_0/\partial J_1}, \tag{7.39}$$

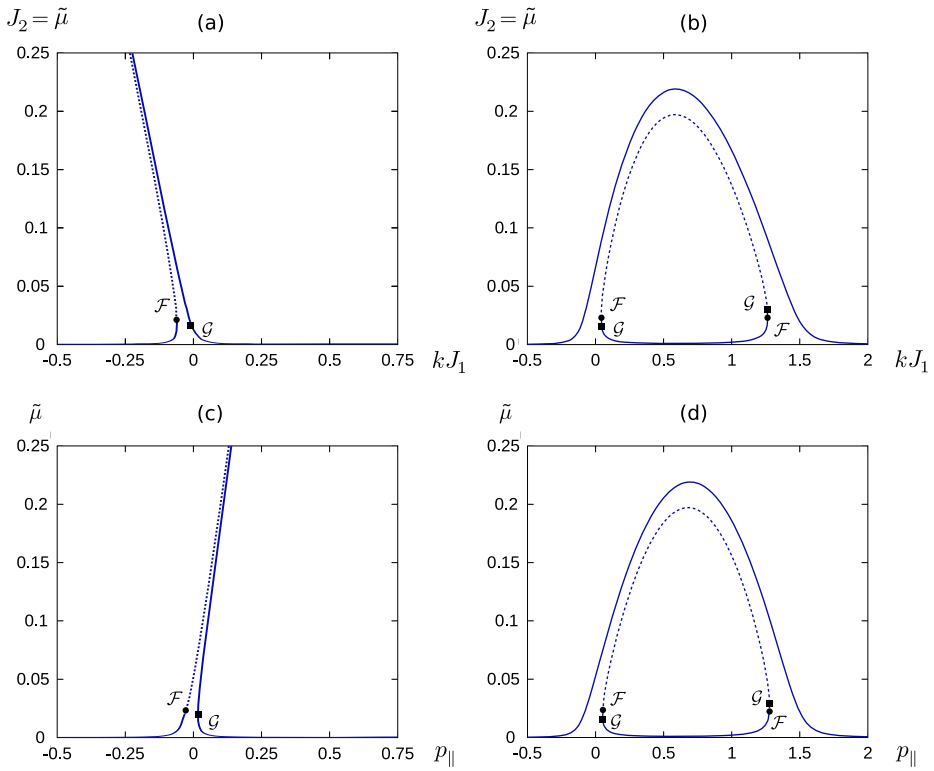

Figure 7.2: Stationary curves plotted for the same parameters as in Fig. 7.1 for $n_0 = 1.5$ [(a) and (c)] and $n_0 = 0.5$ [(b) and (d)] in coordinates $(kJ_1, J_2 = \widetilde{\mu})$ [(a) and (b)] and in coordinates $(p_\parallel, \widetilde{\mu})$ [(c) and (d)]. Unstable branches (dashed) lie above the critical points (dots), at which dJ_2/dJ_1 is infinite. Stable branches (solid) are those below the critical points and also those corresponding to single-valued $J_2(J_1)$. Here $\mathcal{F} = (J_1^c, J_2^c)$ is the critical point where dJ_2/dJ_1 is infinite; $\mathcal{G}$ is the critical point where $d\widetilde{\mu}/dp_\parallel$ is infinite; $J_1 = p_\parallel/k - \widetilde{\mu}$, $J_2 = \widetilde{\mu}$.

where the derivatives of F_0 are taken at $J_1 = J_1^0$ and $\chi = 0$. Substituting the expressions for F_0 and F_1 in Eq. (7.39), one finally obtains:

$$\delta J_1 = -\frac{\sqrt{J_2}(\varepsilon + 2J_2^{3/2}\chi\omega_0^2)}{2mc^2\Omega_0} + \frac{(1+\Omega_0^2/\omega_0^2)(\varepsilon - 4J_2^{3/2}\chi\omega_0^2)}{4\sqrt{J_2}\Omega_0^2} - \\ - \frac{mc^2\chi(\omega_0^2/\Omega_0^2 + 2 - 3\Omega_0^2/\omega_0^2)}{4\Omega_0}. \quad (7.40)$$

A tedious yet straightforward calculation yields that the critical point $\mathcal{F} = (J_1^c, J_2^c)$, where $d(\delta J_1)/dJ_2$ vanishes, is given by $J_1^c = J_1^0 + \delta J_1(J_2^c)$,

$$J_2^c = \left(\frac{\varepsilon}{8\chi\omega_0^2}\right)^{2/3}, \quad (7.41)$$

and resides within the validity domain of the perturbation theory developed here for small ε and χ. In other words, infinite dJ_2/dJ_1 corresponds to $\widetilde{\mu} = \mu_c$, where

$$\mu_c^{3/2} = \left(\frac{mc^2}{\omega_0}\right)^{3/2} \frac{a_0}{8|1-n_0|}\sqrt{\frac{\Omega_0}{\omega_0}}. \quad (7.42)$$

7.2.3 Stability of the Stationary Points

By definition, each of the points on the stationary curves $J_1(J_2)$ found in Sec. 7.2.2, corresponds to a stationary orbit characterized by fixed actions J_1 and J_2 (or, alternatively, fixed $\widetilde{\mu}$ and $p_\parallel$). While those corresponding to $H_1(J_2) = 0$ are always saddles (Sec. 7.1), the stability of the stationary trajectories corresponding to $\theta_2 = 0$ and $\theta_2 = \pi$ may vary and can be assessed as follows.

The Hamiltonian flow on the phase cylinder (θ_2, J_2) can exhibit only two types of equilibria: centers, which are stable stationary points with Poincaré index $\zeta = 1$, and saddles, which are unstable points with index $\zeta = -1$ [Ueno et al., 2003; Candel and Conlon, 2003]. It turns out that, for the Hamiltonian (7.20), this fact is sufficient to predict the type of stationary points without calculating the eigenvalues

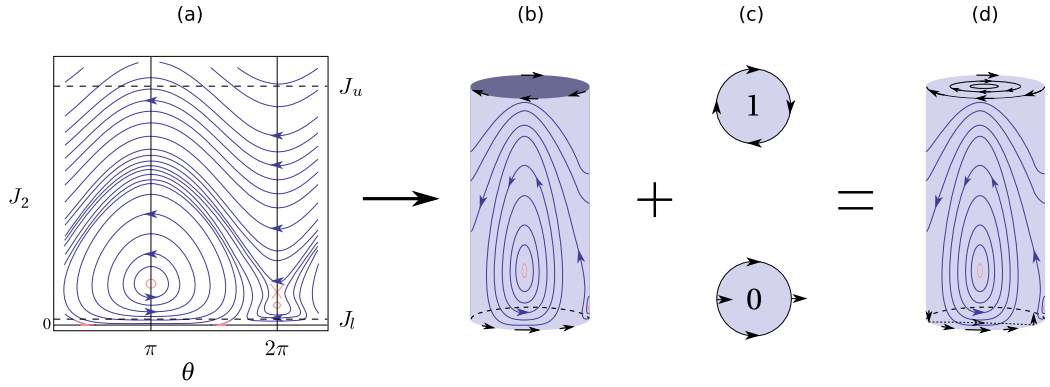

Figure 7.3: Construction of a compact manifold with a continuous vector field from a part ($\hat{J}_l < J_2 < \hat{J}_u$) of the original Hamiltonian vector field defined for $J_2 > 0$ [Fig. (a)]. The latter is considered on a cylinder [Fig. (b)], to which we add two "caps", one at the top and one at the bottom [Fig. (c)]. Using the asymptotic behavior of the original field at large and small J_2, the vector field is continued analytically to the caps, resulting in the upper cap Poincaré index $\zeta_u = 1$ and the lower cap index $\zeta_l = 0$, assuming n_0 is not equal to unity. The resulting manifold [Fig. (d)] is compact; hence the Poincaré-Hopf theorem can be applied, allowing to formally deduce the stability of the equilibria on the plot (a) without calculating the corresponding eigenvalues $\boldsymbol{\lambda}$, otherwise found from Eqs. (7.12)–(7.14).

$\boldsymbol{\lambda}$. Specifically, one can do this by using the Poincaré-Hopf theorem [Ueno et al., 2003; Candel and Conlon, 2003; Smith, 1984], for which to be applicable we will need to transform the phase cylinder into a compact orientable differentiable manifold. The latter is done as follows.

Using the asymptotic expansions of H_0 and H_1 and their derivatives near $J_2 = 0$ and at $J_2 \to \infty$, choose some $\hat{J}_l$ and $\hat{J}_u > \hat{J}_l$ for which the Hamiltonian vector field governed by Eq. (7.20) is continued smoothly to the cylinder "caps" at $J_2 = \hat{J}_l$ and $J_2 = \hat{J}_u$ (Fig. 7.3). Specifically, assuming that $\omega_0 \sim \Omega_0$, choose $\hat{J}_u$ such that $\hat{J}_u \gg J_1$, $\hat{J}_u \gg mc^2/\Omega_0$, and $\hat{J}_u^{3/2} \gg \varepsilon(2n_0|\chi|\omega_0^2)^{-1}$. In this case, the Hamiltonian equations

following from Eq. (7.20) can be approximated by

$$\dot{J}_2 \approx -\varepsilon(n_0^2\omega_0^2\hat{J}_u)^{-1/2}\sin\theta_2, \tag{7.43}$$

$$\dot{\theta}_2 \approx \omega_0(n_0-1) + \varepsilon(2n_0\omega_0\hat{J}_u^{3/2})^{-1}\cos\theta_2. \tag{7.44}$$

Hence, the flow on the upper rim of the cylinder is as shown in Fig. 7.3(b), meaning that the cap has the index $\zeta_u = 1$ [Fig. 7.3(c)].

Similarly, consider the vicinity of $J_2 = 0$. For $\hat{J}_l \ll mc^2/\Omega_0$, the canonical equations read

$$\dot{J}_2 \approx -\varepsilon\hat{J}_l^{1/2}(m^2c^4 + n_0^2\omega_0^2J_1^2)^{-1/2}\sin\theta_2, \tag{7.45}$$

$$\dot{\theta}_2 \approx -\varepsilon(4\hat{J}_l)^{-1/2}(m^2c^4 + n_0^2\omega_0^2J_1^2)^{-1/2}\cos\theta_2. \tag{7.46}$$

Hence, the flow on the lower rim is different from that on the upper rim [Fig. 7.3(b)], yielding the index $\zeta_l = 0$.

The cylinder considered together with the two caps forms a compact manifold [Fig. 7.3(d)] diffeomorphic to a sphere, to which the Poincaré-Hopf theorem can be applied. Specifically, the latter states that all the equilibrium indexes on the manifold sum up to 2. Subtracting the contribution from the caps ($\zeta_u + \zeta_l = 1$), one gets

$$\sum_s \zeta_s = 1, \tag{7.47}$$

for the stationary points with $J_2 > 0$ on the original cylinder without the caps. Recall now that there exist either one or three solutions for a stationary point at nonzero J_2 (Sec. 7.2.2; having two solutions is the intermediate degenerate case). In the former case, Eq. (7.47) yields that the only equilibrium is a center, whereas in the latter case there must exist two centers and one saddle [1].

[1] In the degenerate case $n_0 = 1$, there always exist two stationary points for given J_1. A similar application of the Poincaré-Hopf theorem shows that they are both stable, in agreement with Ref. [Dodin and Fisch, 2008c].

It now remains to figure out *which* of the points corresponds to the saddle. Since the latter appears only when $J_2(J_1)$ becomes double-valued at one of the branches (as we just showed), consider a pair of equilibria corresponding to the double-valued $J_2(J_1)$ at fixed J_1 (Fig. 7.2). The related eigenvalues $\boldsymbol{\lambda}$ are given by

$$\lambda^2 = \varepsilon H_1 \frac{dR}{dJ_2} \cos\theta_2, \tag{7.48}$$

where $R(J_2) = \omega_n(J_2) - \omega_0 + \varepsilon\Omega_0(J_2)\cos\theta_2$ is such that it equals zero at each of the equilibria. Due to the latter, dR/dJ_2 must have different signs at the two stationary points corresponding to a given J_1 and θ_2. And since $H_1 > 0$, the sign of λ^2 has to be different in these points as well. Therefore, the saddle *always* corresponds to one of the branches of the double-valued $J_2(J_1)$. Since at $\chi \to 0$ the critical point $\mathcal{F}$, which separates the two branches, goes to infinity, we further conclude that it must be the intermediate branch that is unstable [Figs. 7.2(a) and (b)].

7.3 Tristability

In Sec. 7.2, the stationary curves for the wave-particle interaction problem (7.20) were studied. Now consider the same stationary curves in coordinates $(p_\parallel, \widetilde{\mu})$ [Fig. 7.2(c) and (d)]. In this case, the curves look similar to those in coordinates (J_1, J_2) [Fig. 7.2(a) and (b)] in that they also exhibit a bifurcation point (one or two), further called $\mathcal{G}$, where $d\widetilde{\mu}/dp_\parallel$ is infinite. As follows from Eq. (7.24), this new point $\mathcal{G}$ corresponds to $dJ_2/dJ_1 = -1$, and therefore does *not* map to the bifurcation point $\mathcal{F}$ (corresponding to infinite dJ_2/dJ_1), where the stability is lost (Sec. 7.2.3). Particularly, for $n_0 > 1$, $\mathcal{G}$ falls below $\mathcal{F}$, *i.e.,* into the interior of the stability region, whereas for $n_0 < 1$, there are two points $\mathcal{G}$, exactly one of which falls into the stability region. Hence, in either case, there can be up to three different *stable* stationary points for a given $p_\parallel$.

In other words, unlike a "normal" 1D nonlinear oscillator undergoing near-resonant interaction with an external force, where only up to two stable stationary orbits are possible [Landau and Lifshitz, 1976, §29; Bogoliubov and Mitropolskii, 1961, §15], a wave-driven particle in a magnetic field is *tristable*. Previously, this tristability was demonstrated for the degenerate case $n_0 = 1$, by exact integration of the particle motion equations [Dodin and Fisch, 2008c]. The perturbative analysis offered above shows that the tristability is a robust effect, also holding for n_0 other than unity and therefore could be observed in real physical systems. In what follows, we show that this effect yields important implications regarding the particle response to fields *additional* to $\boldsymbol{B}_0$ and the wave; particularly, negative $m_\parallel$ can result.

7.4 Effective Parallel Mass

Suppose that an additional low-frequency perturbation force F directed along z is applied to the particle, so the Hamiltonian (7.26) can be written as

$$\mathcal{H} = H_0 - \omega_0 J_2 - \frac{\varepsilon\sqrt{J_2}}{H_0}\cos\theta_2 - F\theta_1/k, \tag{7.49}$$

where we used that $z = \theta_1/k$ [Eq. (7.24)]. Due to the oscillations in the high-frequency field and the static magnetic field, the particle mass is effectively modified, yielding that the parallel mass

$$m_\parallel \equiv F/\dot{v}, \tag{7.50}$$

which can further be rewritten as

$$m_\parallel \approx m\,F\left[\frac{d}{dt}\left(\frac{p_\parallel}{\widetilde{\gamma}}\right)\right]^{-1}, \tag{7.51}$$

no longer equals the rest mass m (Sec. 7.1). By analogy with the particle dynamics in a crystal [Kittel, 1996], the particle motion along z corresponding to Eq. (7.49),

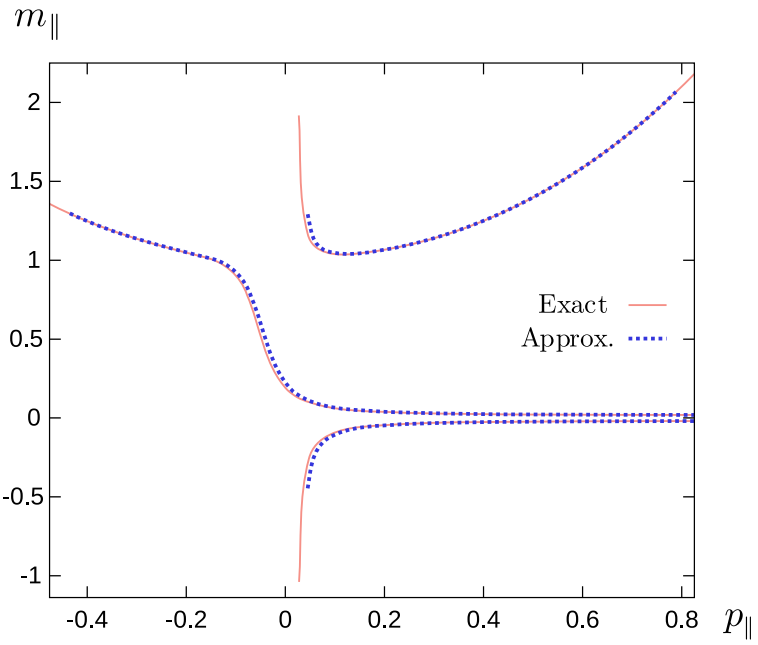

Figure 7.4: $m_\parallel(p_\parallel)$ calculated for $n_0 = 1$, $\omega_0 = 0.97\,\Omega_0$, and $\varepsilon = 0.02$ (in units $m = c = q = 1$): the exact expression from Ref. [Dodin and Fisch, 2008c] (solid) and the approximate expression (7.57) (dashed).

can then be described by the Hamiltonian

$$H_{\text{eff}}(p, z) = K(p) + U(z). \tag{7.52}$$

Here $U(z)$ is the potential energy satisfying $F = -U'(z)$; $K(p)$ is the effective kinetic energy, or "quasienergy", related to $m_\parallel$ through

$$m_\parallel^{-1} = d^2K/dp^2; \tag{7.53}$$

and p is the canonical momentum, or the "quasimomentum", related to $v = \dot{z}$ through $v = dK/dp$ (see also Sec. 7.5). Since $\dot{p} = k\dot{J}_1 = F$, one has $p = kJ_1$, not to be confused with $p_\parallel$.

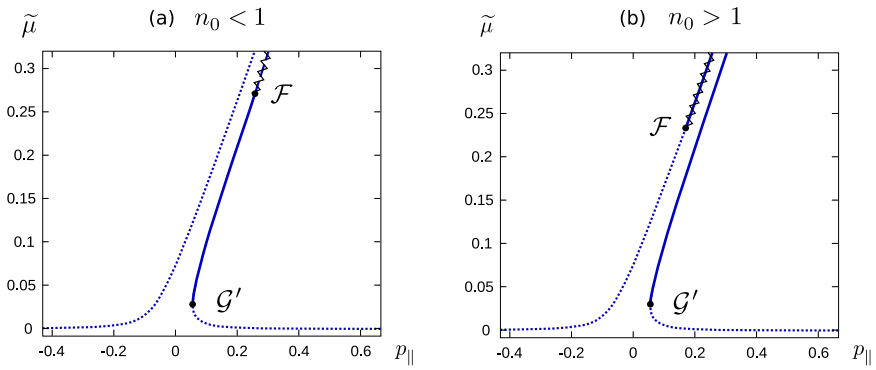

Figure 7.5: A schematic plot of the stationary curves in $(p_\parallel, \widetilde{\mu})$ coordinates with the regions of positive and negative parallel mass for (a) $n_0 < 1$ and (b) $n_0 > 1$. The parts of the curves with the negative parallel mass are shown with the solid lines, while the positive mass parts are shown with the dashed lines. The unstable parts of the plot are shown with the zig-zag lines. The points of zero and infinity $m_\parallel$ are denoted by $\mathcal{F}$ and $\mathcal{G}'$ correspondingly.

Using Eqs. (7.24) and (7.27) to represent $p_\parallel$ and $\widetilde{\gamma}$ as functions of J_1 and J_2, Eq. (7.51) can be written as

$$\frac{m_\parallel}{m} = F\left[\frac{d}{dt}\left(\sqrt{\frac{m^2c^2k^2(J_1+J_2)^2}{m^2c^2+2m\Omega_0 J_2+k^2(J_1+J_2)^2}}\right)\right]^{-1}. \tag{7.54}$$

From Eq. (7.49), one has $\dot{J}_1 = F/k$. To find $\dot{J}_2$, for simplicity, suppose a particle in the vicinity of a stationary state and recall (Sec. 7.1) that it will remain in this vicinity as long as the perturbation force F is adiabatic. As the stationary state itself evolves in response to F, the particle will follow the stationary curve $J_2(J_1)$; thus,

$$\dot{J}_2 = (dJ_2/dJ_1)\dot{J}_1. \tag{7.55}$$

Using these, we now rewrite Eq. (7.54) as

$$\frac{m_\parallel}{m} = \left[\frac{1+dJ_2/dJ_1}{\widetilde{\gamma}}\left(1-\frac{p_\parallel}{\widetilde{\gamma}}\frac{\partial\widetilde{\gamma}}{\partial p_\parallel}\right) - \frac{p_\parallel}{k\widetilde{\gamma}^2}\frac{\partial\widetilde{\gamma}}{\partial\widetilde{\mu}}\frac{dJ_2}{dJ_1}\right]^{-1}. \tag{7.56}$$

After simplification, one finally obtains:

$$m_\parallel = m\widetilde{\gamma}^3\left[1+\frac{2\widetilde{\mu}\Omega_0}{mc^2}+\left(1-\frac{p_\parallel\Omega_0}{mc^2k}+\frac{2\widetilde{\mu}\Omega_0}{mc^2}\right)\frac{dJ_2}{dJ_1}\right]^{-1}. \tag{7.57}$$

As seen in Fig. 7.4, Eq. (7.57) agrees with the results of Ref. [Dodin and Fisch, 2008c], where a different derivation for $m_\parallel$ was proposed, limited to $n_0 = 1$.

From Fig. 7.4 (and Ref. [Dodin and Fisch, 2008c]), one can conclude that $m_\parallel$ exhibits multiple branches and *can* become negative; we now explore more generally *when* this happens. The sign of $m_\parallel$ changes where $m_\parallel$ becomes zero or infinite. The first case is realized when $dJ_1/dJ_2 = 0$, which is exactly the bifurcation point $\mathcal{F}$ (Sec. 7.2.2). The second one corresponds to the zero of the denominator in Eq. (7.57). Assuming that the particle is weakly relativistic, or $p_\parallel \ll mc$ and $\widetilde{\mu} \ll mc^2/\Omega_0$, one concludes that $dJ_2/dJ_1 \approx -1$. Therefore, $m_\parallel$ is singular at the point $\mathcal{G}'$, which is close to the point $\mathcal{G}$, where $d\widetilde{\mu}/dp_\parallel$ is infinite. Hence, the negative-mass region is located on the stationary curves between the points with zero and infinite $m_\parallel$, corresponding to $\mathcal{F}$ and $\mathcal{G}' \approx \mathcal{G}$, respectively.

If $n_0 < 1$, the points $\mathcal{F}$ and $\mathcal{G}'$ belong to the same branch of the stationary curve with $\theta_n = 0$; then, $m_\parallel$ can be observed for $\widetilde{\mu} < \mu_c$, where μ_c is given by

$$\mu_c^{3/2} = \left(\frac{mc^2}{\omega_0}\right)^{3/2} \frac{a_0}{8(1-n_0)}\sqrt{\frac{\Omega_0}{\omega_0}}. \tag{7.58}$$

On the other hand, if $n_0 > 1$, the points $\mathcal{F}$ and $\mathcal{G}'$ belong to different branches of the stationary curve; then, the negative-mass region is not limited at high energies (Fig. 7.5). In either case, NME is due to particle sticking to the resonance curve, which makes the pump wave (with the help of B_0) produce an average ponderomotive force overcompensating the perturbation F.

Finally, notice that Eq. (7.57) was derived under the assumption that the particle is initially in a stationary state and, hence, remains restricted to the stationary curve $J_2(J_1)$. If, however, the particle is initially displaced from this curve, it will undergo oscillations in (J_2, θ_2) space (rather than remain at a fixed location). However, the corresponding oscillation orbit will still remain centered around a stationary point

mapping to the stationary curve $J_2(J_1)$. Assuming the oscillations are almost linear, the *average* $J_2(J_1)$ would be the same in this case, meaning that the above derivation for $m_\parallel$ holds also for particles that were not necessarily at a stationary state initially. Hence, away from the bifurcation points $\mathcal{F}$, corrections to Eq. (7.57) can result only from *large*-amplitude oscillations in (J_2, θ_2) space, *i.e.,* at essentially relativistic transverse energies. [This conclusion also agrees with Eq. (38) of Ref. [Dodin and Fisch, 2008c], from where it follows that $m_\parallel$ is not affected by the displacement from the stationary point, unless the parameter s introduced there is comparable to or larger than unity.]

7.5 Parallel Mass Instability

At negative $m_\parallel$, particles are accelerated in the direction opposite to the external force F. Should F be the electrostatic force qE due to space charge fluctuations in plasma, the charge will not be compensated by the induced motion of the oscillation centers but rather amplified. As a result, a collective plasma instability further called *parallel mass instability* develops.

The instability growth rate is found from the longitudinal wave dispersion relation. Assuming $E \sim \exp(-i\omega_e t + ik_e z)$, this dispersion relation may be written as [Lifshitz and Pitaevskii, 1981]

$$1 + \sum_s \frac{4\pi n_s q_s^2}{k_e} \int_{-\infty}^{+\infty} \frac{dp}{\omega_e - k_e v} \frac{\partial f_s}{\partial p} = 0, \tag{7.59}$$

where n_s is the plasma density, and $f_s(p)$ is the unperturbed distribution function of species s. Further assuming that the plasma is cold [*i.e.,* the the characteristic width

of each $f_s(p)$ is much smaller than ω_e/k_e], Eq. (7.59) can be rewritten as

$$1 + \sum_s \frac{4\pi n_s q_s^2}{\omega_e^2} \int_{-\infty}^{+\infty} dp\, v \frac{\partial f_s}{\partial p} = 0. \tag{7.60}$$

Using that $dv = dp/m_\parallel$ and $v(p = 0) = 0$, one can also express Eq. (7.60) as

$$1 + \sum_s \frac{4\pi n_s q_s^2}{\omega_e^2} \int_{-\infty}^{+\infty} dp \left(\int_0^p \frac{dp_0}{m_{\parallel s}(p_0)} \right) \frac{\partial f_s}{\partial p} = 0. \tag{7.61}$$

where $m_{\parallel s}$ is the parallel mass of the species s. Hence, Eq. (7.61) can be put in the form

$$\omega_e^2 = \sum_s \frac{4\pi n_s q_s^2}{\bar{m}_{\parallel s}}, \tag{7.62}$$

where we introduced the parallel mass $\bar{m}_{\parallel s}$ averaged over the particle distribution:

$$\bar{m}_{\parallel s}^{-1} = \int_{-\infty}^{+\infty} dp\, m_{\parallel s}^{-1}(p)\, f_s(p). \tag{7.63}$$

Depending on $f_s(p)$, the frequency ω_e can be either real or imaginary. In the former case, when particles with positive $m_{\parallel s}$ dominate, one recovers the electrostatic Langmuir oscillations, with the energy density given by $|E|^2/(8\pi)$ as usual. However, when dominant are particles with $m_{\parallel s} < 0$, the field E will not oscillate but rather grow exponentially. The energy that supports the instability is the quasienergy ΔK that is released when negative-mass particles leave the vicinity of the unstable equilibrium at the local maximum of $K(p)$ (Fig. 7.6). On the other hand, one can equivalently say that ΔK is drawn from the pump wave [which is what shapes $K(p)$], whereas negative-mass particles act as mediators connecting the pump energy reservoir with the wave field E. Correspondingly, for $n_0 < 1$, the instability can occur only when $\widetilde{\mu} < \mu_c$ [Eq. (7.42)], which is the condition under which $m_\parallel < 0$ is possible. (For $n_0 > 1$, there is no such condition for negative-mass particles; however, at $\widetilde{\mu} > \mu_c$, one of the positive-mass branches becomes unstable; see Sec. 7.4.)

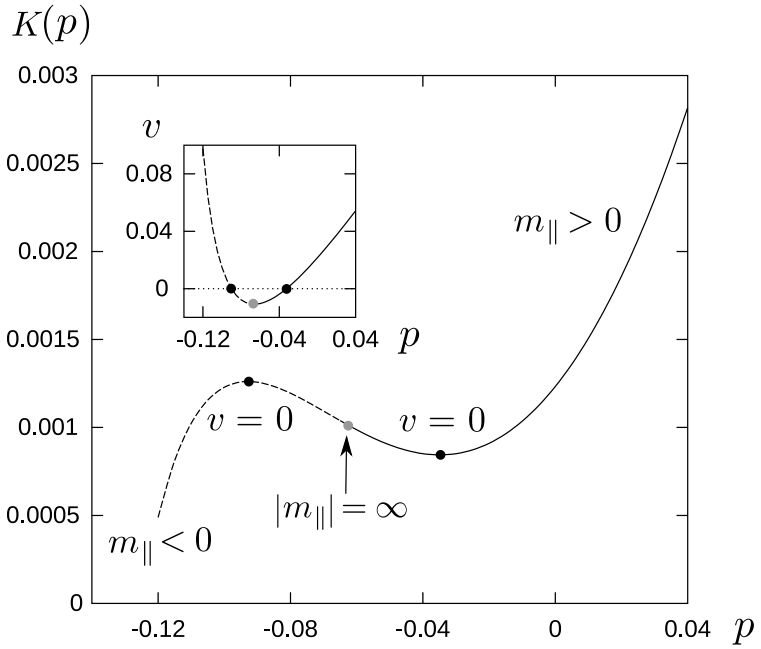

Figure 7.6: The quasienergy K vs the quasimomentum p for $n = 0.98$, $\omega_0 = 0.85\Omega_0$ and $\varepsilon = 0.05$ (in units $m = c = q = 1$), exhibiting regions of positive (solid) and negative (dashed) parallel mass $m_\parallel$. The inset also demonstrates that the velocity v is nonmonotonic as a function of p; hence, there are two distinct values of p corresponding to $v = 0$ (black disks). The plot $K(p)$ shown here corresponds to the singular branches of $m_\parallel(v)$ in Fig. 7.5a, merging at $|m_\parallel| = \infty$ (gray disk). The continuous branch from Fig. 7.5a, corresponding to $m_\parallel$ with a fixed sign, is not shown here.

Chapter 8

Negative Mass Effect in the Presence of Dissipations

The feasibility of the NME studied in Chapter 7 can be influenced by various non-ideal effects unaccounted in our original model (7.1); for example, by particle collisions, cyclotron radiation, or electromagnetic instabilities driven by unstable particle distributions. In this chapter, we study [Zhmoginov et al., 2011b] how NME is modified in the presence of the radiation friction [Landau and Lifshitz, 1971] or friction forces of a different nature. Specifically, introducing a dissipative force in the nonlinear system (7.1), we identify conditions of the dissipation-induced instability and estimate the characteristic time scale on which it develops. To provide an example of an instability caused by the NME, consider a one-dimensional motion of a stationary particle exhibiting NME, *i.e.,* a particle, for which $v \equiv \partial K/\partial p \approx 0$ and $m_{\|}^{-1} \equiv \partial^2 K/\partial p^2 < 0$, where $K(p)$ entering the effective Hamiltonian (7.52) is the particle kinetic energy. Introducing a friction force $F_{\text{frix}} = -\alpha v$, where α is a small

constant, one can write the particle equation of motion as:

$$m_{\|}\dot{v} = -\alpha v. \tag{8.1}$$

If $m_{\|} < 0$, the solution of this equation reads $v(t) = v(0)\exp(\alpha t/m_{\|})$. Therefore, one observes that the friction-induced instability is developed in this example.

In this section, we first consider a behavior of the generalized wave-particle system in the presence of dissipations. Specifically, in Sec. 8.1, the conditions of the dissipation-induced instability are derived and the evolution of the background wave is analyzed. The results of Sec. 8.1 are then applied in Sec. 8.2 to a specific physical system, namely a magnetized radiating charged particle moving in a field of a circularly-polarized wave. The effect of the radiation friction on the particle motion and NME are considered.

8.1 General Formalism

In this section, the dynamics of a particle, treated as a generalized nonlinear dynamical system, under the action of a weak resonant wave in the presence of an even weaker dissipative force is considered. First, in Sec. 8.1.1, we study the effect of dissipations on the particle motion. Then, in Sec. 8.1.2, we show how the evolution of the wave itself can be predicted.

8.1.1 Driven System

Consider a general wave-particle interaction model given by the Hamiltonian (7.3). Assume that the system is perturbed by a weak dissipative force $\boldsymbol{\xi}(\boldsymbol{J}, \boldsymbol{\phi}) = (\boldsymbol{\mathcal{J}}, \boldsymbol{\Theta})$,

i.e.,

$$\dot{J}_i = \varepsilon \delta_{in} H_1(\boldsymbol{J}) \sin\theta_n + \mathcal{J}_i, \tag{8.2}$$

$$\dot{\theta}_i = \omega_i(\boldsymbol{J}) - \delta_{in}\omega_0 + \varepsilon \frac{\partial H_1}{\partial J_i} \cos\theta_n + \Theta_i, \tag{8.3}$$

where δ_{ij} is the Kronecker symbol, and $\omega_i = \partial H_0/\partial J_i$. Assume initial conditions such that the system is close to an unperturbed stable surface S, that $\boldsymbol{\xi}(\boldsymbol{J}, \boldsymbol{\phi})$ is not resonant to the oscillations at frequencies $\varpi_i = \partial H_0/\partial I_i$, and that the period of oscillations T_* around the stable surface S is much larger than all $2\pi/\varpi_i$ (and the corresponding beat frequencies). Then, for $i < n$, one can average Eqs. (8.2) and (8.3) over the fast oscillations in $\boldsymbol{\phi}$ to get

$$\dot{J}_{i<n} = \bar{\mathcal{J}}_i, \quad \dot{\theta}_{i<n} = \tilde{\omega}_i, \tag{8.4}$$

where $\tilde{\omega}_i = \omega_i + \varepsilon\,(\partial H_1/\partial J_i)\cos\theta_n + \bar{\Theta}_i$, and $\bar{\mathcal{J}}_i$, $\bar{\Theta}_i$ denote averages of $\mathcal{J}_i$ and Θ_i over the phases ϕ_i. Therefore, the effect of friction on the degrees of freedom corresponding to $i < n$ consists in adding a slow drift in J_i and slightly modifying the frequencies to $\tilde{\omega}_i$.

Now let us consider the remaining degree of freedom, (J_n, θ_n). Recalling that the dynamics in these variables is slow compared to the dynamics in $\boldsymbol{\phi}$, average Eqs. (8.2) and (8.3) for $i = n$ over the fast oscillations in $\boldsymbol{\phi}$:

$$\dot{J}_n = \varepsilon H_1(\boldsymbol{J}) \sin\theta_n + \bar{\mathcal{J}}_n, \tag{8.5}$$

$$\dot{\theta}_n = \omega_n(\boldsymbol{J}) - \omega_0 + \varepsilon \frac{\partial H_1}{\partial J_n} \cos\theta_n + \bar{\Theta}_n. \tag{8.6}$$

Unlike for $i < n$ [Eqs. (8.4)], the average friction force can now be compensated by Hamiltonian forces. This means that the dissipation does not destroy the equilibrium

in (J_n, θ_n) plane but rather shifts it to a new location $(\bar{J}_n^*, \bar{\theta}_n^*)$ given by

$$\varepsilon H_1(J_{i<n}, \bar{J}_n^*) \sin \bar{\theta}_n^* = -\bar{\mathcal{J}}_n, \tag{8.7}$$

$$\omega_n(J_{i<n}, \bar{J}_n^*) - \omega_0 + \varepsilon \frac{\partial H_1}{\partial J_n} \cos \bar{\theta}_n^* = -\bar{\Theta}_n, \tag{8.8}$$

which drifts slowly due to $J_{i<n}$ following Eqs. (8.4). Hence, we consider this (quasi-) equilibrium as a *local* stationary point of the system. The surface formed by the local stationary points $\bar{J}_n^*(J_1, \ldots, J_{n-1})$ will be further called a *local stationary surface* $\bar{S}$.

From expanding Eqs. (8.5) and (8.6) in the vicinity of the new stable stationary point $(\bar{J}_n^*, \bar{\theta}_n^*)$, it follows that the effect of friction is determined by derivatives of $\bar{\mathcal{J}}_n$ (and $\bar{\Theta}_n$) rather than $\bar{\mathcal{J}}_i$ itself [unlike in Eq. (8.4)]. To see this, consider the normalized phase space area that the particle orbit encircles in (J_n, θ_n) plane:

$$\Lambda = \frac{1}{2\pi} \oint J_n \, d\theta_n. \tag{8.9}$$

Without friction, Λ would be an adiabatic invariant [1], *i.e.,* $\dot{\Lambda} \approx 0$, as shown in Ref. [Landau and Lifshitz, 1976]. The conservation of Λ causes the autoresonant phase-locking effect [Fajans and Frièdland, 2001; Polomarov and Shvets, 2007] when the system state "sticks" to the the local stationary surface $\bar{S}$. With the friction, however, an argument similar to that in Ref. [Landau and Lifshitz, 1976] yields (see Sec. 9.1 for a more detailed derivation)

$$2\pi\dot{\Lambda} \approx \oint_l \bar{\mathcal{J}}_n \, d\theta_n - \oint_l \bar{\Theta}_n \, dJ_n + \frac{2\pi}{T_*} \sum_{k<n} \int_0^{T_*} \frac{\partial \Lambda}{\partial J_k} \bar{\mathcal{J}}_k \, dt, \tag{8.10}$$

where l is the periodic orbit of the Hamiltonian system (7.3). Using the Stokes theorem and approximating $\Lambda \approx \alpha \, \delta J_n^2/2 + \beta \, \delta\theta_n^2/2$, Eq. (8.10) can then be transformed

[1] Note that Λ is *not* the same as the average J_n, because $d\theta_n$ changes its sign along the orbit.

as

$$2\pi\dot{\Lambda} \approx \int\limits_{M} \left(\frac{\partial \bar{\mathcal{J}}_n}{\partial J_n} + \frac{\partial \bar{\Theta}_n}{\partial \theta_n} \right) dJ_n \, d\theta_n - \frac{2\pi}{T_*} \sum_{k<n} \int\limits_{0}^{T_*} \frac{\partial \bar{J}_n^*}{\partial J_k} \frac{\partial \bar{\mathcal{J}}_k}{\partial J_n} \alpha \delta J_n^2 \, dt, \tag{8.11}$$

where M is the oriented area of the phase space (J_n, θ_n) encircled by l [2], $\delta J_n = J_n - \bar{J}_n^*$ and $\delta\theta_n = \theta_n - \bar{\theta}_n^*$. Considering system oscillations in a small vicinity of the stable point $(\bar{J}_n^*, \bar{\theta}_n^*)$, and neglecting the variations of $\partial\bar{\mathcal{J}}_n/\partial J_n$ on this scale, one can approximate:

$$\mathfrak{I} = \frac{\dot{\Lambda}}{\Lambda} \approx \frac{\partial \bar{\mathcal{J}}_n}{\partial J_n} - \sum_{k<n} \frac{\partial \bar{\mathcal{J}}_k}{\partial J_n} \frac{\partial \bar{J}_n^*}{\partial J_k}, \tag{8.12}$$

where we used $\Lambda = (2\pi)^{-1} \int_M dJ_n \, d\theta_n$. This shows that the phase space within the (J_n, θ_n) orbit grows or shrinks depending on the signs of $\partial\bar{\mathcal{J}}_i/\partial J_n$. Then, if $\mathfrak{I} > 0$, a particle perturbation from the stable stationary surface grows exponentially, thus indicating *dissipative instability* as introduced in the general theory of dynamical systems [Krechetnikov and Marsden, 2007].

The subset of the local stationary surface $\bar{S}$ close to the stationary surface S of the original Hamiltonian system, for which $\mathfrak{I} < 0$, is an *attractor* of the system with friction. Specifically, trajectories are pulled toward this surface due to friction, and further motion along $\bar{S}$ is determined by the properties of the dissipation function $\boldsymbol{\xi}$. Notice also that the attracting part of $\bar{S}$ is generally characterized by a specific value of θ_n^*, therefore indicating the *phase bunching* occuring in the system. At intersections of $\bar{S}$ with $\bar{\mathcal{J}}_{i<n} = 0$ (which is, generally, a set of one-dimensional (1D) curves in n-dimensional space $\boldsymbol{J}$), the attractor has stationary points. The stability of these points in the $J_{i<n}$ subspace can be determined by calculating the eigenvalues of the matrix $D_{ij} \equiv \partial\bar{\mathcal{J}}_i/\partial J_j$. Specifically, if there is at least one eigenvalue of D_{ij} with a positive real part, the corresponding stationary point is unstable.

---

[2] The area sign is positive for clockwise-rotating orbits and negative otherwise.

8.1.2 Extended System

Suppose now that the generalized dynamical system that we introduced above actually describes the interaction between a particle and a wave, with ω_0 being the wave frequency; hence, one may ask what happens to the wave action I_w as the friction force $\boldsymbol{\xi}$ is applied to a particle. Despite the total action in the particle-field system decays (by definition of $\boldsymbol{\xi}$), I_w may, in fact, grow, meaning that the wave is amplified through dissipation. Below, we derive the general conditions under which such a dissipative amplification of the wave is possible.

Consider an extended system, where the wave is treated as a single independent degree of freedom. The corresponding Hamiltonian then reads as

$$H' = H_0(\boldsymbol{I}) + \varepsilon H_1(\boldsymbol{I}, \mathcal{E}) \cos(\boldsymbol{\ell} \cdot \boldsymbol{\phi} - \psi) + \omega_0 I_w, \tag{8.13}$$

where $\psi = \omega_0 t$ is the wave canonical phase, and I_w is the action variable conjugate to ψ [Dodin and Fisch, 2008a]. Instead of the generating function (7.2), take

$$\Phi = J_1\phi_1 + \cdots + J_{n-1}\phi_{n-1} + J_n(\boldsymbol{\ell} \cdot \boldsymbol{\phi} - \psi) + \mathcal{I}\psi, \tag{8.14}$$

so $\mathcal{I} = I_w + J_n$ is the new action representing the total number of quanta in the two resonant degrees of freedom, θ_n and ψ. Then, (J_i, θ_i) are the new actions and angles correspondingly, defined through

$$\theta_{i<n} = \phi_i, \qquad \theta_n = \boldsymbol{\ell} \cdot \boldsymbol{\phi} - \psi, \tag{8.15}$$

$$J_{i<n} = I_i - \ell_i I_n/\ell_n, \qquad J_n = I_n/\ell_n. \tag{8.16}$$

Since the new Hamiltonian, $\mathcal{H}' = H'$, or

$$\mathcal{H}' = H_0(\boldsymbol{J}) + \varepsilon H_1(\boldsymbol{J}, \mathcal{I}) \cos\theta_n + \omega_0(\mathcal{I} - J_n), \tag{8.17}$$

does not depend on ψ or $\theta_{i<n}$, one concludes that $J_{i<n}$ and $\mathcal{I}$ are constants of motion.

In the presence of a dissipative force $\boldsymbol{\xi}$ on the particle, one then obtains like in Sec. 8.1.1:

$$\langle \dot{\mathcal{H}}' \rangle = \sum_{i<n} \left\langle \frac{\partial \mathcal{H}'}{\partial J_i} \mathcal{J}_i \right\rangle + \left\langle \frac{\partial \mathcal{H}'}{\partial J_n} \mathcal{J}_n \right\rangle + \left\langle \frac{\partial \mathcal{H}'}{\partial \theta_n} \Theta_n \right\rangle + \left\langle \frac{\partial \mathcal{H}'}{\partial \mathcal{I}} \mathcal{J}_{\mathcal{I}} \right\rangle, \tag{8.18}$$

where the effective dissipative force $\mathcal{J}_{\mathcal{I}}$ corresponding to $\mathcal{I}$ [in the sense of Eq. (8.2)] satisfies $\mathcal{J}_{\mathcal{I}} = \mathcal{J}_n$. (Remember that, without interacting with the particle, the wave is assumed undamped.) Close to $\bar{S}$, the second and the third terms are negligible; then, $\langle \dot{H}' \rangle \approx \boldsymbol{\Omega} \cdot \bar{\boldsymbol{\mathcal{J}}}$, where $\boldsymbol{\Omega} = (\omega_1, \ldots, \omega_{n-1}, \omega_0)$. Therefore, the force $\boldsymbol{\xi}$ dissipates energy if [3]

$$\boldsymbol{\Omega} \cdot \bar{\boldsymbol{\mathcal{J}}} < 0. \tag{8.19}$$

Even when the latter is satisfied, though, the wave energy does not necessarily decay. Indeed, consider the evolution of the wave action I_w:

$$\dot{I}_w = \bar{\mathcal{J}}_n - \dot{J}_n. \tag{8.20}$$

Assuming, as before, that the system operates near $\bar{S}$, one obtains:

$$\dot{I}_w = \bar{\mathcal{J}}_n - \sum_{i<n} \frac{\partial \bar{J}_n^*}{\partial J_i} \bar{\mathcal{J}}_i. \tag{8.21}$$

Note that this expression can be related to Eq. (8.12), which defines $\mathfrak{I}$ characterizing the stability of the local stationary surface:

$$\mathfrak{I} = \frac{\partial \dot{I}_w}{\partial J_n}. \tag{8.22}$$

Equation (8.21) can be rewritten as

$$\dot{I}_w = \sum_{i \leq n} \bar{\mathcal{J}}_i \frac{\partial R}{\partial J_i}, \tag{8.23}$$

[3] Strictly speaking, $\langle \dot{\mathcal{H}}' \rangle < 0$ is not a sufficient condition for $\boldsymbol{\xi}$ to be dissipative (due to possible energy increase on smaller time scales), but it is a necessary condition.

where $R(J_1, \ldots, J_n) = J_n - \bar{J}_n^*(J_1, \ldots, J_{n-1})$. Hence, $\dot{I}_w$ equals the derivative of R along $\bar{\boldsymbol{\mathcal{J}}}$ in $\boldsymbol{J}$ space:

$$\dot{I}_w = \bar{\boldsymbol{\mathcal{J}}} \cdot \nabla_{\boldsymbol{J}} R. \tag{8.24}$$

On the other hand, since R is constant (zero) on the local stationary surface, the gradient of R in $\boldsymbol{J}$ space, $\nabla_{\boldsymbol{J}} R$, is orthogonal to $\bar{S}$. Particularly, since $\partial R/\partial J_n > 0$, the vector $\nabla_{\boldsymbol{J}} R$ points toward larger J_n. Thus, the dissipation causes the wave energy to decrease ($\dot{I}_w < 0$) only if $\bar{\boldsymbol{\mathcal{J}}}$ at $\bar{S}$ points toward the lower one of the two halves of the J_n space separated by $\bar{S}$.

In principle, though, $\bar{\boldsymbol{\mathcal{J}}}$ can also point in the opposite direction, causing wave amplification; that is, I_w increases in this case through dissipation, apparently, at the expense of the particle internal energy. (Notice that this effect is different from the conventional dissipative instabilities [Birdsall and Whinnery, 1953; Laslett et al., 1965; Neil and Sessler, 1965; Timofeev and Shvilkin, 1976]; in particular, the wave energy growth may not be exponential.) In Sec. 8.2, we illustrate how this effect is possible in a specific physical system.

8.2 Radiation Friction

Consider a physical system introduced in Sec. 7.2, namely a magnetized charged particle moving in a field of a circularly-polarized electromagnetic wave with the refraction index n_0. In this section, we study the influence of the radiation friction on particle motion and wave dynamics. First, we introduce the radiation friction force in Sec. 8.2.1. The particle dynamics under the influence of this force is then studied in Sec. 8.2.2. Finally, in Sec. 8.2.3, the implications of the obtained results for the NME are discussed.

8.2.1 Radiation Friction Force

The radiation reaction four-force on a particle reads as [Landau and Lifshitz, 1971]:

$$g^i = \frac{2q^3}{3mc^3}\frac{\partial F^{ik}}{\partial x^l}u_k u^l - \frac{2q^4}{3m^2c^5}F^{il}F_{kl}u^k + \frac{2q^4}{3m^2c^5}\left(F_{kl}u^l\right)\left(F^{km}u_m\right)u^i, \tag{8.25}$$

where F_{ik} is the electromagnetic four-tensor, and u^i is the particle four-velocity. Since the dominant motion in our case is assumed [Zhmoginov et al., 2010] to be the cyclotron motion (rather than the wave-driven oscillations), keep only the terms due to the static field B_0; then,

$$g^x = -\frac{2q^4}{3m^2c^5}B_0^2[(u^x)^2 + (u^y)^2 + 1]u^x, \tag{8.26}$$

$$g^y = -\frac{2q^4}{3m^2c^5}B_0^2[(u^x)^2 + (u^y)^2 + 1]u^y, \tag{8.27}$$

$$g^z = -\frac{2q^4}{3m^2c^5}B_0^2[(u^x)^2 + (u^y)^2]u^z. \tag{8.28}$$

Using an approximate relation $\widetilde{\mu} \approx (p_x^2 + p_y^2)(2m\Omega_0)^{-1}$ and Eqs. (8.26) and (8.27), one obtains

$$\bar{\mathcal{J}}_2 \approx -\frac{\kappa J_2}{\widetilde{\gamma}}\left(2J_2 + \frac{mc^2}{\Omega_0}\right), \tag{8.29}$$

where $\kappa = (4q^2\Omega_0^3)(3m^2c^5)^{-1}$, and $\widetilde{\gamma} = H_0/(mc^2)$. To find $\bar{\mathcal{J}}_1$, recall that $J_1 = p_z/k - J_2$, and therefore $\mathcal{J}_1 = \dot{p}_z/k - \mathcal{J}_2$, where $\dot{p}_z$ can be taken from Eq. (8.28):

$$\dot{p}_z \approx \frac{cg^z}{\widetilde{\gamma}} = -\frac{4q^2\Omega_0^3}{3m^2c^5\widetilde{\gamma}}\,k(J_1 + J_2)J_2. \tag{8.30}$$

Therefore,

$$\bar{\mathcal{J}}_1 = -\frac{\kappa J_2}{\widetilde{\gamma}}\left(J_1 - J_2 - \frac{mc^2}{\Omega_0}\right). \tag{8.31}$$

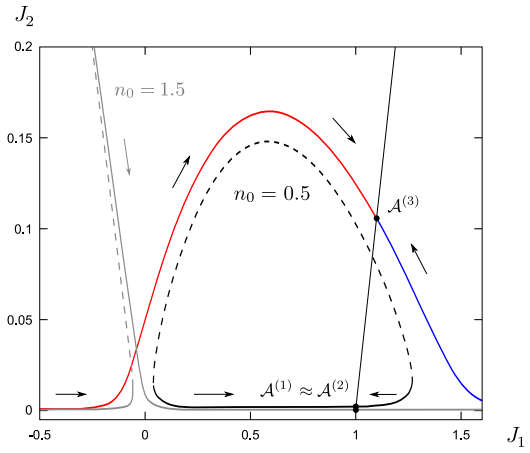

Figure 8.1: Two stationary curves plotted for $n_0 = 0.5$ and $n_0 = 1.5$ for $\varepsilon = 0.01$, $\omega = 0.98\,\Omega_0$ (in units $m = q = c = 1$). The stable parts of the curves are solid and the unstable parts are dashed. The curve $\mathcal{J}_1(J_1, J_2) = 0$, which is a straight line here, intersects the stationary curves for $n_0 = 1.5$ and $n_0 = 0.5$ in one and two points correspondingly. The direction of the dissipation-driven drift along the stationary curves is shown with arrows.

8.2.2 Stationary Points and Dissipative Dynamics

Consider now how the dissipative force $\boldsymbol{\mathcal{J}}$ affects the average dynamics, taking into account that the particle remains attached to the stationary curve $\bar{S}$, or $\bar{J}_2^*(J_1)$, that we found in Sec. 7.2 (Fig. 8.1). As discussed previously, the dissipative force $\boldsymbol{\mathcal{J}}$ can lead to an exponential decay or exponential growth of the adiabatic invariant Λ. Using Eq. (8.12), one can find those parts of $\bar{S}$ that attract the nearby trajectories by solving:

$$\frac{\partial \bar{J}_2^*}{\partial J_1} > \frac{\partial \bar{\mathcal{J}}_2/\partial J_2}{\partial \bar{\mathcal{J}}_1/\partial J_2}. \tag{8.32}$$

Assuming that $J_2 \ll mc^2/\Omega_0$, one can approximate this expression as:

$$\frac{\partial \bar{J}_2^*}{\partial J_1} > \frac{1}{J_1\Omega_0/mc^2 - 1}. \tag{8.33}$$

It is easy to see that this condition is satisfied for both "branches" of $\bar{S}$ with $|J_1| \to \infty$ (see Fig. 8.1). However, the condition (8.33) is violated in the negative-parallel-mass

region. Indeed, Eq. (8.33) is equivalent to $m_{\|} > 0$ with $m_{\|}$ given by Eq. (7.57) for $J_2 \ll mc^2/\Omega_0$. One therefore concludes that the radiation friction makes the negative-mass region of the stable stionary curve unstable. Specifically, any trajectory localized near this part of the curve, would eventually leave its vicinity even if the particle action J_1 did not change considerably.

The dynamics on the attracting part of the stable stationary curve is governed by the properties of the dissipative force $\mathcal{J}_1$. The stationary points $\mathcal{A}^{(j)} \equiv (J_1^{(j)}, J_2^{(j)})$ of this dynamics can be found by indentifying intersections of $\bar{S}$ with the curve $\bar{\mathcal{J}}_1 = 0$, which, according to Eq. (8.31), represents a straight line in (J_1, J_2) space, given by

$$J_1 - J_2 = mc^2/\Omega_0. \tag{8.34}$$

Depending on the wave refraction index, $n_0 \equiv kc/\omega_0$, there can be one or two stable stationary points, as seen in Fig. 8.1. Using Eqs. (8.34), (7.30) and (7.31), one can find $\mathcal{A}^{(j)}$ explicitly to the leading order in ε, at least for ω_0 close to Ω_0 and $|n_0 - 1| \ll 1$. Specifically, at $n_0 > 1$, there is only one stationary point, $\mathcal{A}^{(1)} = (J_1^{(1)}, J_2^{(1)})$, with

$$J_1^{(1)} \approx mc^2/\Omega_0, \tag{8.35}$$

$$J_2^{(1)} \approx \frac{\varepsilon^2(3+2\sqrt{2})}{8m^2c^4\Omega_0^2}. \tag{8.36}$$

whereas at $n_0 < 1$, there exist two such points, $\mathcal{A}^{(2)} \approx \mathcal{A}^{(1)}$ and $\mathcal{A}^{(3)} = (J_1^{(3)}, J_2^{(3)})$, with:

$$J_1^{(3)} \approx \frac{mc^2\Omega_0}{4\omega^2(1-n_0)}, \tag{8.37}$$

$$J_2^{(3)} \approx \frac{mc^2}{\Omega_0}\left[\frac{\Omega_0^2}{4\omega^2(1-n_0)} - 1\right]. \tag{8.38}$$

Both stationary points $\mathcal{A}^{(1)}$ and $\mathcal{A}^{(2)}$ are generally characterized by $\mathfrak{I} < 0$. However, the stationary point $\mathcal{A}^{(3)}$ can, in principle, belong to the part of $\bar{S}$ repelling

nearby trajectories. The sign of $\mathfrak{I}$ at $\mathcal{A}^{(3)}$ can be calculated by substituting Eqs. (8.37) and (8.38) in Eq. (8.12). Assuming that $|n_0-1| \ll 1$, one obtains that $\mathfrak{I} < 0$, *i.e.,* the stationary point $\mathcal{A}^{(3)}$ belongs to the attracting part of $\bar{S}$, if

$$\frac{d\bar{J}_2^*}{dJ_1} > -3. \tag{8.39}$$

The stability of the stationary points in J_1-space can be determined by calculating the derivative $\partial\bar{\mathcal{J}}_1/\partial J_1$. Since

$$\partial\bar{\mathcal{J}}_1/\partial J_1 < 0, \tag{8.40}$$

each of the stationary points $\mathcal{A}^{(j)}$ ($j = 1, 2, 3$) is stable, *i.e.,* attracts trajectories lying in its vicinity (Fig. 8.2). Hence, the particle response to the radiation friction in the system considered here can be summarized as follows: First, assuming that $\bar{S}$ is characterized by $\mathfrak{I} < 0$ almost everywhere, the particle is picked up by the wave and is accelerated by the light pressure. Yet, the altered longitudinal velocity affects the detuning from the cyclotron resonance and, thus, also the energy of wave-driven oscillations. On the other hand, the latter energy can either decrease or increase, depending on the initial conditions, because the stationary curve $\bar{J}_2^*(J_1)$ is a multi-valued function (Fig. 8.1). Specifically, if a particle is originally closer to the branch connected to $\mathcal{A}^{(1)}$ (at $n_0 > 1$) or $\mathcal{A}^{(2)}$ (at $n_0 < 1$), then it will be further attracted to this branch and follow it toward the equilibrium, *losing* the transverse energy. On the other hand, if a particle is instead closer to the branch connected to $\mathcal{A}^{(3)}$ (this is only possible at $n_0 < 1$), it will follow the branch toward higher J_2, thereby *increasing* the transverse energy (Figs. 8.1 and 8.2).

The time scale for these processes can be estimated as follows. To the stationary curve, a particle is attracted on the time scale δt_Λ derived from Eq. (8.12), with $\bar{\mathcal{J}}_2 \approx -\kappa J_2 mc^2/\Omega_0$ [Eq. (8.29)], where we assumed, for simplicity, that the particle

motion is nonrelativistic. Then,

$$\delta t_\Lambda \sim \frac{\Omega_0}{mc^2\kappa} \approx 2.6\,\mathrm{s} \times \frac{M^3}{Z^4 B_0[\mathrm{T}]^2}, \tag{8.41}$$

where M is the particle mass in the units of the electron mass, Z is the particle charge in the units of the electron charge, and $B_0[\mathrm{T}]$ is the static magnetic field measured in Teslas. For the motion along the curve, the time scale δt is found from:

$$\frac{\dot{J}_2}{J_2} = \frac{d\bar{J}_2^*}{dJ_1}\frac{\dot{J}_1}{J_2} = -\frac{\kappa}{\widetilde{\gamma}}\frac{d\bar{J}_2^*}{dJ_1}\left(J_1 - J_2 - \frac{mc^2}{\Omega_0}\right) \approx \frac{d\bar{J}_2^*}{dJ_1}\frac{mc^2\kappa}{\Omega_0\widetilde{\gamma}}. \tag{8.42}$$

When $|d\bar{J}_2^*/dJ_1| \sim 1$ (on the negative-mass branch), one has $\delta t \sim \delta t_\Lambda$. This suggests that motion along $\bar{S}$ resulting in particles leaving the negative-mass region occurs on the time scale of the adiabatic invariant evolution [4]. However, on the low-energy, quasi-flat branch $\bar{J}_2^*(J_1)$, δt can be much larger.

8.2.3 Negative Mass Effect with Radiation Friction

Now let us study whether the wave-particle interaction leads to wave damping or amplification. As shown in Sec. 8.1.2, the wave-particle interaction in the presence of friction can lead to wave damping ($\dot{I}_w < 0$) or wave amplification ($\dot{I}_w > 0$). Assuming that the particle is nonrelativistic (or weakly relativistic), one can rewrite the condition for amplification, $\dot{I}_w > 0$ using Eq. (8.21) as $d\bar{J}_2^*/dJ_1 < \bar{\mathcal{J}}_2/\bar{\mathcal{J}}_1$. Using Eqs. (8.29) and (8.31), this also rewrites approximately as

$$\frac{d\bar{J}_2^*}{dJ_1} < \frac{2J_2 + mc^2/\Omega_0}{J_1 - J_2 - mc^2/\Omega_0}. \tag{8.43}$$

Interestingly, Eq. (8.43) coincides with the necessary and sufficient condition for the particle "effective parallel mass" $m_\parallel$ given by Eq. (7.57) to be negative. Hence, we

[4] The adiabatic invariant Λ is growing since $\mathfrak{I} > 0$ in the negative-mass region.

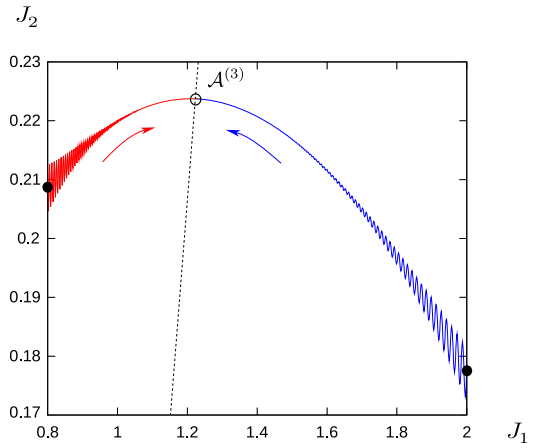

Figure 8.2: Two trajectories of a particle in (J_1, J_2) space obtained by numerical integration of the motion equations corresponding to the Hamiltonian H [Eq. (7.26)] and added radiation friction g [Eqs. (8.26)-(8.28)]. In this example, $n_0 = 0.5$, $\omega = 0.97\,\Omega_0$, $\varepsilon = 0.01$, and $m = c = q = 1$. Two initial particle states are shown with solid disks at $J_1 = 0.8$ and $J_1 = 2.0$. Both particle trajectories asymptotically converge (see the arrows) to the intersection (circle) of the stationary curve and the curve given by $\mathcal{J}_1 = 0$ (dashed), yielding a stationary point $\mathcal{A}^{(3)}$ [cf. Fig. 8.1].

can summarize the results of this section also as follows. All particles with negative parallel mass exhibit slow drift along the stable stationary curve, driven by the light pressure and accompanied by the wave amplification and an increase of particle deviation from $\bar{S}$. The corresponding dynamics turns out to be "stable", in respect that the particle transverse energy is monotonically decreasing due to cyclotron cooling. On the other hand, some of particles with positive parallel mass exhibit "unstable" dynamics, *i.e.,* while the particles are accelerated by the light pressure, their transverse energy also grows due to cyclotron heating. The characteristic time of the particle drift along the local stationary surface $\bar{S}$ is given by Eq. (8.42). At $B \sim 1\,\mathrm{T}$, it is of order of seconds for electrons and $10^9\,\mathrm{s}$ for ions. Hence, we can conclude that the NME predicted in Refs. [Dodin and Fisch, 2008c; Zhmoginov et al., 2010] persists through dissipation and thereby represents a robust physical effect, potentially observable in a feasible experiment.

Chapter 9

Negative Effective Mass in the Presence of Stochastic External Forces

In this chapter, we propose [Zhmoginov et al., 2011c] how stochastic perturbations can be included in the canonical formalism for a broad class of resonant Hamiltonian systems similar to those yielding NME. Particularly, we model the stochastic system evolution with the Fokker-Planck equation, which coefficients are expressed through the statistical properties of the external noise. The general formalism is discussed in Sec. 9.1. In application to the wave-particle interaction problem, in Sec. 9.2, we consider a charged particle interacting with a pump wave in a static magnetic field and find the diffusion coefficient and the drag terms caused by the particle collisions with the cold background plasmas. Instead of performing the numerical study of the Fokker-Planck equation, we then analytically estimate slow averaged particle motion and the characteristics of the stationary distribution function. Reverting to

the negative mass effect, we then show that the collisional force can be used to localize particles on the negative mass branch only if the particle mass is much larger than the masses of all plasma species.

9.1 General Formalism

9.1.1 Basic equations

Consider a generalized nonlinear wave-particle Hamiltonian introduced in Sec. 7.1:

$$H = H_0(\boldsymbol{I}) + \varepsilon H_1(\boldsymbol{I}) \cos(\boldsymbol{\ell} \cdot \boldsymbol{\phi} - \omega_0 t). \tag{9.1}$$

Recall that $(\boldsymbol{I}, \boldsymbol{\phi})$ are the action-angle variables of the unperturbed Hamiltonian $H_0(\boldsymbol{I})$, $\varepsilon \ll 1$ is a small parameter, ω_0 is a "wave" frequency, $\boldsymbol{\ell} = (\ell_1, \ldots, \ell_n)$ is an n-dimensional integer vector, and $n \equiv \dim \boldsymbol{I} = \dim \boldsymbol{\phi}$. Let $\varpi_i = \partial H_0 / \partial I_i$ be the unperturbed frequencies. Assuming nonzero ℓ_n, one can make a canonical transformation defined by the generating function (7.2) to obtain the following new Hamiltonian:

$$\mathcal{H}(\boldsymbol{J}, \boldsymbol{\theta}) = H_0(\boldsymbol{J}) - \omega_0 J_n + \varepsilon H_1(\boldsymbol{J}) \cos \theta_n \tag{9.2}$$

independent of $n - 1$ new canonical coordinates $\theta_{i<n}$. The new canonical variables $(\boldsymbol{J}, \boldsymbol{\theta})$ are related to the unperturbed action-angle variables $(\boldsymbol{I}, \boldsymbol{\phi})$ through Eqs. (7.4) and (7.5).

In the following, along with the canonical variables $(\boldsymbol{J}, \boldsymbol{\theta})$ we will also use the action-angle variables of the perturbed Hamiltonian (9.2). The actions $\boldsymbol{K}$ and angles

$\boldsymbol{\psi}$ reading

$$\boldsymbol{K} = (J_1, J_2, \ldots, J_{n-1}, \Lambda), \tag{9.3}$$

$$\psi_{i<n} = \theta_i + \int \frac{\partial J_n(\boldsymbol{K}, \theta_n)}{\partial K_i}\, d\theta_n, \tag{9.4}$$

$$\psi_n = \int \frac{\partial J_n(\boldsymbol{K}, \theta_n)}{\partial K_n}\, d\theta_n, \tag{9.5}$$

can be derived using the following generating function [Landau and Lifshitz, 1976]:

$$\Phi(\boldsymbol{K}, \boldsymbol{\theta}) = \sum_{k<n} K_k \theta_k + \int J_n(\boldsymbol{K}, \theta_n)\, d\theta_n, \tag{9.6}$$

where the integral is taken along the system trajectory in a clockwise direction, $\Lambda = (2\pi)^{-1} \oint J_n\, d\theta_n$ is calculated over the closed system orbit (unlike in Chapter 8, Λ is positively-defined here). Since $\Lambda \geq 0$, the frequency $\omega_* = \dot{\zeta}$ with which the system oscillates around the equilibrium may be negative. The absolute value of ω_* is given by:

$$\omega_*^2 \approx -\varepsilon H_1 \frac{\partial \Omega}{\partial J_n} \cos\theta_n^*, \tag{9.7}$$

where $\Omega = \partial H_0/\partial J_n - \omega_0 + \varepsilon\,(\partial H_1/\partial J_n)\cos\theta_n^*$, and all functions of $\boldsymbol{J}$ are evaluated at $(J_{i<n}, J_n^*)$.

Consider a perturbation of the system (9.1) by a weak *stochastic non-resonant* force $\boldsymbol{\xi}(\boldsymbol{I}, \boldsymbol{\phi}, t)$. The dependence of force $\boldsymbol{\xi}$ on parameters $\boldsymbol{I}$, $\boldsymbol{\phi}$ and t is assumed to be characterized by two distinct scales: slow and fast. The small scales in $\boldsymbol{\phi}$ and t correspond to the "stochastic part" of the force $\boldsymbol{\xi}$. They introduce a high-frequency noise and a very strong dependence of $\boldsymbol{\xi}$ on the system state resulting in a rapid loss of correlations between two systems with almost identical initial states. The slow scales, on the other hand, appear in $\boldsymbol{\xi}$ as slow dependencies on time t (much slower compared to the T_*) and actions $\boldsymbol{I}$. The "slow" dependence of $\boldsymbol{\xi}$ on $\boldsymbol{\phi}$ is assumed to be not in resonance with the frequency ω_* of slow system oscillations, *i.e.,* the

amplitudes of all harmonics of $\boldsymbol{\xi}$ characterized by frequencies comparable to ω_* are thought to be vanishingly small.

The evolution of the action-angle variables in the presence of the stochastic force is given by:

$$\dot{K}_i = \mathcal{K}_i, \tag{9.8}$$

$$\dot{\psi}_i = \frac{\partial \mathcal{H}}{\partial K_i} + \Psi_i, \tag{9.9}$$

where $\mathcal{H}$ is treated as a function of $\boldsymbol{K}$ and $(\mathcal{K}_i, \Psi_i)$ are the K- and ψ-projections of $\boldsymbol{\xi}$ correspondingly. For convenience, in the following, the stochastic force $\boldsymbol{\xi}$ is also described by two vector fields $(\boldsymbol{\mathcal{J}}, \boldsymbol{\Theta})$, which enter the equations of motion in (J, θ) variables:

$$\dot{J}_i = -\frac{\partial \mathcal{H}}{\partial \theta_i} + \mathcal{J}_i, \tag{9.10}$$

$$\dot{\theta}_i = \frac{\partial \mathcal{H}}{\partial J_i} + \Theta_i. \tag{9.11}$$

In the abscence of stochastic fluctuations, as discussed in Chapter 8, the weak external force $\boldsymbol{\xi}$ causes a slow drift along local stationary surface $\bar{S}$. If the system is initialized near $\bar{S}$, it will remain "locked" to this surface while moving along it. However, recall that depending on the properties of the force $\boldsymbol{\xi}$, different regions of the local stationary surface $\bar{S}$ can be stable or unstable. If $\bar{S}$ is stable, the adiabatic invariant associated with slow oscillations in a vicinity of the stationary point in the (J_n, θ_n) plane is decreasing with time, what causes system trajectories to attract towards $\bar{S}$. In the opposite case, however, the system trajectory is repelled from $\bar{S}$ and the system eventually leaves the vicinity of the stationary point.

9.1.2 Fokker-Planck equation

Consider now how the dynamics near $\bar{S}$ is affected by stochastic forces. Specifically, let us derive the Fokker-Planck equation for the "reduced" distribution $\bar{f}(\boldsymbol{K},t) = (2\pi)^{-n}\int f(\boldsymbol{K},\boldsymbol{\psi},t)\,d^n\psi$, where $f(\boldsymbol{K},\boldsymbol{\psi},t)$ is the full distribution of the system states. In contrast to Ref. [Budker and Belyaev, 1958], we derive the Fokker-Planck coefficients for the phase-locked system starting with the $(\boldsymbol{\mathcal{J}},\boldsymbol{\Theta})$ representation of the stochastic force $\boldsymbol{\xi}$.

Assuming that the characteristic time scale of the reduced distribution dynamics is very slow compared to all periods $T_i \equiv 2\pi/\dot{\psi}_i$, the evolution of $\bar{f}$ can be approximately described by the Fokker-Planck equation [Budker and Belyaev, 1958]:

$$\frac{\partial \bar{f}}{\partial t} = -\sum_{i=1}^{n}\frac{\partial}{\partial K_i}\left(\mathcal{F}_i\bar{f}\right) + \sum_{i,j=1}^{n}\frac{\partial^2}{\partial K_i \partial K_j}\left(\mathcal{D}_{i,j}\bar{f}\right), \tag{9.12}$$

where the coefficients $\mathcal{F}_i$ and $\mathcal{D}_{i,j}$ are calculated by averaging the increments ΔK_i accumulated over a time Δt much larger than all T_i (yet sufficiently small so that the system trajectories are perturbed only weakly) over the initial angles $\boldsymbol{\psi}^0$:

$$\mathcal{F}_i = \frac{\langle \Delta K_i\rangle_\psi}{\Delta t}, \qquad \mathcal{D}_{i,j} = \frac{\langle \Delta\widetilde{K}_i \Delta\widetilde{K}_j\rangle_\psi}{2\Delta t}, \tag{9.13}$$

where $\Delta\widetilde{K}_i = \Delta K_i - \langle \Delta K_i\rangle_\psi$.

9.1.3 Calculation of $\mathcal{F}_i$

To proceed with the calculation of $\mathcal{F}_i$ and $\mathcal{D}_{i,j}$ given $\boldsymbol{\mathcal{J}}$ and $\boldsymbol{\Theta}$, consider a period of time $[\tau, \tau+\Delta t]$ with Δt much larger than all T_i. Representing $\boldsymbol{\xi}$ as a function of the initial actions $\boldsymbol{K}^0$, the initial angles $\boldsymbol{\psi}^0$ and time, one obtains:

$$\langle \Delta K_{i<n}\rangle_\psi = \left\langle \int_\tau^{\tau+\Delta t} \mathcal{J}_i\,dt \right\rangle_\psi, \tag{9.14}$$

$$\langle \Delta K_n \rangle_\psi = \left\langle \int_\tau^{\tau+\Delta t} \left(\frac{\partial K_n}{\partial J_n} \mathcal{J}_n + \frac{\partial K_n}{\partial \theta_n} \Theta_n + \sum_{k<n} \frac{\partial K_n}{\partial K_k} \mathcal{J}_k \right) dt \right\rangle_\psi . \tag{9.15}$$

Assume that the stochastic force $\boldsymbol{\xi}(\boldsymbol{K}^0, \boldsymbol{\psi}^0, t)$ has a small-scale noise in both time and the initial angle. More specifically, assume that it is characterized by an autocorrelation time $\tau_{\rm ac}$ much smaller than all of the periods T_i and the characteristic autocorrelation scale $\Delta\boldsymbol{\psi}^0_{\rm ac}$ such that $|\Delta\boldsymbol{\psi}^0_{\rm ac}| \ll 2\pi$. In this case, the integrals over the time and the initial angle in Eqs. (9.14) and (9.15) can be approximated by the integrals over the "slow" time and "slow" angles of the fast-time and small-angle average $\langle\boldsymbol{\xi}\rangle_\circ$ of the stochastic force. This averaging operation stands for the average over the time much larger than $\tau_{\rm ac}$, but much smaller than all T_i and over the range of angles much larger than $\Delta\boldsymbol{\psi}^0_{\rm ac}$, but much smaller than 2π. In the following, we consider $\langle\boldsymbol{\xi}\rangle_\circ$ as a function of the local momenta $\boldsymbol{J}$, coordinates $\boldsymbol{\phi}$ (on the unperturbed trajectory) and time and assume that $\langle\boldsymbol{\xi}\rangle_\circ(\boldsymbol{J}, \boldsymbol{\phi}, t)$ is a slow function of time with a characteristic time scale much larger than all T_i. Making a Fourier decomposition of $\langle\boldsymbol{\xi}\rangle_\circ$:

$$\langle\boldsymbol{\xi}\rangle_\circ = \sum_{\boldsymbol{m}} \boldsymbol{\Xi}^{\boldsymbol{m}}(\boldsymbol{J}, t) e^{i\boldsymbol{m}\cdot\boldsymbol{\phi}}, \tag{9.16}$$

where $\boldsymbol{m}$ are the integer vectors, one obtains:

$$\langle\boldsymbol{\xi}\rangle_\circ = \sum_{\boldsymbol{m}} \boldsymbol{\Xi}^{\boldsymbol{m}}[J_{i<n}, J_n(\boldsymbol{K}, \psi_n), t] \exp(i\Phi^{\boldsymbol{m}}), \tag{9.17}$$

where

$$\Phi^{\boldsymbol{m}} = \sum_{k<n} m_k \theta_k + \frac{m_n}{\ell_n} \left[\theta_n(\boldsymbol{K}, \psi_n) + \omega_0 t - \sum_{k<n} \ell_k \theta_k \right] \tag{9.18}$$

and $\theta_{k<n} = \psi_k - \int \partial J_n(\boldsymbol{K}, \theta_n)/\partial K_i \, d\theta_n$. Since $\theta_{k<n} \approx \psi_k$, only the resonant terms, for which:

$$\sum_{k<n} \varpi_k (\ell_k m_n - \ell_n m_k) - m_n \omega_0 \sim O(\omega_*) \tag{9.19}$$

may contribute to the integral over the time Δt. In the following, we assume that $\boldsymbol{\Xi}^{\boldsymbol{m}} = 0$ for all such resonant terms except for $\boldsymbol{\Xi}^0 = \langle\langle\boldsymbol{\xi}\rangle_\circ\rangle_\phi$. Therefore, the time

integrals in Eqs. (9.14) and (9.15) are independent of $\psi^0_{k<n}$ and the averaging over these angles can be avoided.

Denoting $\langle\langle \boldsymbol{\xi} \rangle_\circ \rangle_\phi$ by $\bar{\boldsymbol{\xi}}$, recalling that the particle state is localized near $\bar{S}$ and that the dependence of $\boldsymbol{\Xi}^{\boldsymbol{m}}$ on time is slow, one obtains:

$$\mathcal{F}_{i<n} \approx \bar{\mathcal{J}}_i(J_{i<n}, J^*_n, t), \tag{9.20}$$

$$2\pi\mathcal{F}_n \approx \oint \bar{\mathcal{J}}_n \, d\theta_n - \oint \bar{\Theta}_n \, dJ_n + \sum_{k<n} \int_0^{2\pi} \frac{\partial K_n}{\partial J_k} \bar{\mathcal{J}}_k d\psi_n, \tag{9.21}$$

where we used $\partial K_n/\partial J_n = \omega_*^{-1}\partial\mathcal{H}/\partial J_n$, $\partial K_n/\partial\theta_n = \omega_*^{-1}\partial\mathcal{H}/\partial\theta_n$ and the integrals are taken over the unperturbed trajectory.

The derivative $\partial K_n/\partial J_k$ can be calculated as follows. The action $K_n(J_n, \theta_n, J_{k<n})$ is equal to the area of the closed system trajectory passing through (J_n, θ_n). Consider some unperturbed action K_n and the corresponding system trajectory calculated for certain $J_{k<n} = J^0_{k<n}$. Fixing some (J^0_n, θ^0_n) on the unperturbed trajectory, the perturbed orbit passing through (J^0_n, θ^0_n) for $J_k = J^0_k + \delta J_k$ can be found by noticing that it should satisfy the following equation:

$$\begin{aligned}\mathcal{H}(J_n + \delta J_n, \theta_n + \delta\theta_n, J_{k<n}) + \sum_{i<n} \frac{\partial\mathcal{H}(J_n, \theta_n, J_{k<n})}{\partial J_i}\delta J_i \approx \\ \approx \mathcal{H}(J^0_n, \theta^0_n, J_{k<n}) + \sum_{i<n} \frac{\partial\mathcal{H}(J^0_n, \theta^0_n, J_{k<n})}{\partial J_i}\delta J_i,\end{aligned} \tag{9.22}$$

or after simple transformations:

$$\frac{\partial\mathcal{H}}{\partial J_n}\delta J_n + \frac{\partial\mathcal{H}}{\partial\theta_n}\delta\theta_n + \sum_{i<n} \frac{\partial\mathcal{H}(J_n, \theta_n, J_{k<n})}{\partial J_i}\delta J_i \approx \sum_{i<n} \frac{\partial\mathcal{H}(J^0_n, \theta^0_n, J_{k<n})}{\partial J_i}\delta J_i. \tag{9.23}$$

For simplicity, consider a perturbation with $\delta\theta_n = 0$ [1], the change of the area enclosed by the curve can then be calculated as:

$$\delta K_n = \frac{1}{2\pi} \oint \delta J_n \, d\theta_n, \tag{9.24}$$

[1] Strictly speaking, $\delta\theta_n$ must be non-vanishing on some small part of the unperturbed orbit.

or after using Eq. (9.23):

$$\delta K_n(J_n^0,\theta_n^0) = \frac{1}{2\pi}\sum_{i<n}\oint\left[\frac{\partial\mathcal{H}}{\partial J_i}(J_n^0,\theta_n^0) - \frac{\partial\mathcal{H}}{\partial J_i}(J_n,\theta_n)\right]\frac{\delta J_i d\theta_n}{\partial\mathcal{H}/\partial J_n}. \tag{9.25}$$

Note here that only the first term in Eq. (9.25) depends on the position (J_n^0,θ_n^0) on the system orbit. Rewriting Eq. (9.25) as:

$$\frac{\partial K_n}{\partial J_k}(J_n,\theta_n) = \frac{1}{2\pi\omega_*}\int_0^{2\pi}\left[\frac{\partial\mathcal{H}}{\partial J_k}(J_n,\theta_n) - \frac{\partial\mathcal{H}}{\partial J_k}(J_n',\theta_n')\right]d\psi_n', \tag{9.26}$$

and using the Green's theorem, one obtains:

$$\mathcal{F}_n \approx \frac{\partial\bar{\mathcal{J}}_n}{\partial J_n}K_n + \frac{1}{2\pi\omega_*}\sum_{k<n}\frac{\partial\bar{\mathcal{J}}_k}{\partial J_n}(J_n^*)\int_0^{2\pi}\frac{\partial\mathcal{H}}{\partial J_k}\delta J_n d\psi_n, \tag{9.27}$$

where $\delta J_n = J_n - J_n^*$, we approximated $\bar{\mathcal{J}}_k$ as $\bar{\mathcal{J}}_k(J_n^*) + (\partial\bar{\mathcal{J}}_k/\partial J_n)\delta J_n$ and used $\oint \delta J_n\, d\psi_n = 0$. The last term in Eq. (9.27) is simplified if we assume that $\mathcal{H}$ can be decomposed as follows in a vicinity of a stationary point (J_n^*,θ_n^*):

$$\mathcal{H} \approx \mathcal{H}_0(J_{i<n}) + \frac{\gamma_{11}(J_n - J_n^*)^2}{2} + \frac{\gamma_{22}(\theta_n - \theta_n^*)^2}{2}. \tag{9.28}$$

Substituting this expression in Eq. (9.27), one finally obtains:

$$\mathcal{F}_n \approx \left(\frac{\partial\bar{\mathcal{J}}_n}{\partial J_n} - \sum_{k<n}\frac{\partial\bar{\mathcal{J}}_k}{\partial J_n}\frac{\partial J_n^*}{\partial J_k}\right)K_n. \tag{9.29}$$

For some problems, like the effect of radiation friction on the particle with the negative mass, the last term in Eq. (9.29) can play a crucial role in determining the stability of the system.

9.1.4 Calculation of $\mathcal{D}_{ij}$

Following the definition of $\mathcal{D}_{i,j}$ given by Eq. (9.13), one can show that:

$$\mathcal{D}_{i<n,j<n} = \frac{1}{2\Delta t}\left\langle \int_\tau^{\tau+\Delta t}\widetilde{\mathcal{J}_i}\,dt \int_\tau^{\tau+\Delta t}\widetilde{\mathcal{J}_j}(t')\,dt' \right\rangle_\psi, \tag{9.30}$$

where:

$$\widetilde{\boldsymbol{\mathcal{J}}} = \boldsymbol{\mathcal{J}} - \langle\langle \boldsymbol{\mathcal{J}} \rangle_\circ \rangle_\phi, \tag{9.31}$$

$$\widetilde{\boldsymbol{\Theta}} = \boldsymbol{\Theta} - \langle\langle \boldsymbol{\Theta} \rangle_\circ \rangle_\phi. \tag{9.32}$$

Introducing new variables $T = (t + t')/2$ and $\varrho = t - t'$ and recalling that the autocorrelation time $\tau_{\rm ac}$ is much smaller than all periods T_i, one can approximate:

$$\mathcal{D}_{i<n,j<n} \approx \frac{1}{\Delta t} \left\langle \int_\tau^{\tau+\Delta t} \langle \mathfrak{P}_{i,j} \rangle_\circ \, dT \right\rangle_\psi , \tag{9.33}$$

where

$$\mathfrak{P}_{i,j}(\boldsymbol{K}^0, \boldsymbol{\psi}^0, T) = \frac{1}{2} \int_{-t_*}^{t_*} \widetilde{\mathcal{J}}_i(T + \varrho/2) \widetilde{\mathcal{J}}_j(T - \varrho/2) \, d\varrho \tag{9.34}$$

and $t_* = \min\{T - \tau, \tau + \Delta t - T\}$. Assuming that $\langle \mathfrak{P}_{i,j} \rangle_\circ$ is independent of Δt and that the resonant harmonics of $\langle \mathfrak{P}_{i,j} \rangle_\circ(\boldsymbol{J}, \boldsymbol{\phi}, t)$ can be neglected following the same argument we used in Sec. 9.1.3, one can introduce $\bar{\mathfrak{P}}_{i,j} = \langle\langle \mathfrak{P}_{i,j} \rangle_\circ \rangle_\phi$ and obtain:

$$\mathcal{D}_{i<n,j<n} \approx \bar{\mathfrak{P}}_{i,j}. \tag{9.35}$$

The calculation of $\mathcal{D}_{i<n,n}$ can be performed by combining Eq. (9.15) with Eq. (9.13):

$$\mathcal{D}_{n,j<n} \approx \frac{1}{2\Delta t} \left\langle \int_\tau^{\tau+\Delta t} \left(\frac{\partial K_n}{\partial J_n} \widetilde{\mathcal{J}}_n + \frac{\partial K_n}{\partial \theta_n} \widetilde{\Theta}_n + \sum_{k<n} \frac{\partial K_n}{\partial K_k} \widetilde{\mathcal{J}}_k \right) dt \int_\tau^{\tau+\Delta t} \widetilde{\mathcal{J}}_j \, dt \right\rangle. \tag{9.36}$$

Using $(\omega_* \Delta t)^{-1} \int_\tau^{\tau+\Delta t} \delta J_n^2 \, dt \sim K_n/\gamma_{11}$ and $\partial \mathcal{H}/\partial J_n \approx \gamma_{11} \delta J_n$, one obtains:

$$\mathcal{D}_{n,j<n} \approx \left(\frac{\partial \bar{\mathfrak{P}}_{n,j}}{\partial J_n} - \sum_{k<n} \frac{\partial \bar{\mathfrak{P}}_{k,j}}{\partial J_n} \frac{\partial J_n^*}{\partial J_k} \right) K_n. \tag{9.37}$$

The final diffusion coefficient $\mathcal{D}_{n,n}$ is most tedious to calculate. After straightforward transformations of Eq. (9.13), the final expression can be written as:

$$\mathcal{D}_{n,n} \approx \left[\gamma_{11} \bar{\mathfrak{P}}_{n,n} + \gamma_{22} \bar{\mathfrak{Q}}_{n,n} - 2\gamma_{11} \sum_{k<n} \bar{\mathfrak{P}}_{n,k} \frac{\partial J_n^*}{\partial J_k} + \gamma_{11} \sum_{k<n} \sum_{j<n} \bar{\mathfrak{P}}_{j,k} \frac{\partial J_n^*}{\partial J_j} \frac{\partial J_n^*}{\partial J_k} \right] \frac{K_n}{\omega_*}, \tag{9.38}$$

where

$$\mathfrak{Q}_{i,j}(\boldsymbol{K}^0, \boldsymbol{\psi}^0, T) = \frac{1}{2} \int_{-t_*}^{t_*} \widetilde{\Theta}_i(T + \varrho/2) \widetilde{\Theta}_j(T - \varrho/2) \, d\varrho. \tag{9.39}$$

9.1.5 Stationary distribution function

Consider a stationary solution of the Fokker-Planck equation (9.12) localized near a stable stationary point with $J_{k<n} = J_k^0$ and $J_n = J_n^*(J_{k<n}^0)$. Introducing a small parameter ε_ξ proportional to the stochastic force $\boldsymbol{\xi}$, one can rescale all Fokker-Planck coefficients and actions by introducing: $\bar{\mathcal{F}}_i = \mathcal{F}_i/\varepsilon_\xi$, $\bar{\mathcal{D}}_{i,j} = \mathcal{D}_{i,j}/\varepsilon_\xi^2$, $\bar{K}_i = K_i/\varepsilon_\xi$. The Fokker-Planck equation rewritten in these new variables retains its original form (9.12).

In the following, we identify a stationary distribution function $\bar{f}$ solving Eq. (9.12) assuming that the widths of $\bar{f}$ in $\bar{K}_{i\leq n}$ are of order of one, *i.e.,* scale as ε_ξ^0. Noticing that $\bar{\mathcal{F}}_n$ and $\bar{\mathcal{D}}_{i\leq n,n}$ are proportional to ε_ξ, we look for the distribution function by decomposing it as

$$\bar{f} = \sum_{k\geq 0} \varepsilon_\xi^k \bar{f}_k. \tag{9.40}$$

Consider first the zeroth-order terms of the Fokker-Planck equation:

$$-\sum_{j<n} \frac{\partial}{\partial \bar{J}_j}\left(\bar{\mathcal{F}}_j \bar{f}_0\right) + \sum_{j<n}\sum_{k<n} \frac{\partial^2}{\partial J_j \partial J_k}\left(\bar{\mathcal{D}}_{j,k}\bar{f}_0\right) = 0. \tag{9.41}$$

Neglecting the dependence of the Fokker-Planck coefficients $\bar{\mathcal{F}}_j$ and $\bar{\mathcal{D}}_{j,k}$ on $\bar{K}_n$, the solution of this equation defines the $\bar{K}_{i<n}$-profile of $\bar{f}_0$ leaving the $\bar{K}_n$ dependence of $\bar{f}$ to be determined by the first-order equation, which in turn reads

$$-\sum_{j<n} \frac{\partial}{\partial \bar{J}_j}\left(\bar{\mathcal{F}}_j \bar{f}_1\right) - \frac{\partial}{\partial \bar{K}_n}\left(\bar{\mathcal{F}}_n \bar{f}_0\right) + \sum_{j<n}\sum_{k<n} \frac{\partial^2}{\partial \bar{J}_j \partial \bar{J}_k}\left(\bar{\mathcal{D}}_{j,k}\bar{f}_1\right) + \\ + \sum_{j<n} \frac{\partial^2}{\partial \bar{J}_j \partial \bar{K}_n}\left(\bar{\mathcal{D}}_{j,n}\bar{f}_0\right) + \frac{\partial^2}{\partial \bar{K}_n^2}\left(\bar{\mathcal{D}}_{n,n}\bar{f}_0\right) = 0. \tag{9.42}$$

Neglecting the dependence of $\bar{\mathcal{F}}_n$ and $\bar{\mathcal{D}}_{n,n}$ on $\bar{J}_{i<n}$, one can first solve the equation on the $\bar{K}_n$-profile of $\bar{f}_0$:

$$-\frac{\partial}{\partial \bar{K}_n}\left(\bar{\mathcal{F}}_n \bar{f}_0\right) + \frac{\partial^2}{\partial \bar{K}_n^2}\left(\bar{\mathcal{D}}_{n,n}\bar{f}_0\right) = 0 \tag{9.43}$$

and then use the obtained solution to find $\bar{f}_1$:

$$-\sum_{j<n}\frac{\partial}{\partial\bar{J}_j}\left(\bar{\mathcal{F}}_j\bar{f}_1\right)+\sum_{j<n}\sum_{k<n}\frac{\partial^2}{\partial\bar{J}_j\partial\bar{J}_k}\left(\bar{\mathcal{D}}_{j,k}\bar{f}_1\right)=-\sum_{j<n}\frac{\partial^2}{\partial\bar{J}_j\partial\bar{K}_n}\left(\bar{\mathcal{D}}_{j,n}\bar{f}_0\right). \tag{9.44}$$

In the following, we use Eqs. (9.41) and (9.43) to estimate the characteristic width of the distribution function $\bar{f}$.

9.1.6 Second-order corrections to $\mathcal{F}_n$

As seen from Eq. (9.43), the stationary solution of the Fokker-Planck equation (9.12) with coefficients $\mathcal{F}_n$ and $\mathcal{D}_{n,n}$ proportional to K_n has a characteristic width scaling as a magnitude of the stochastic force $\boldsymbol{\xi}$. Therefore, for particles in such distribution, $\mathcal{F}_n$ calculated using the first-order perturbation theory and given by Eq. (9.29) is proportional to ξ^2 rather than ξ. On the other hand, the second-order contribution to $\mathcal{F}_n$ would also be proportional to ξ^2. In the following, we calculate the second-order contribution and discuss the implications of this additional term.

Assume for simplicity that H_0, H_1, $\bar{\mathcal{J}}_n$ and $\bar{\Theta}_n$ are time-independent. Let $\bar{\boldsymbol{\mathcal{J}}}^*$ and $\bar{\boldsymbol{\Theta}}^*$ be J_n-independent components of the average force $\bar{\boldsymbol{\xi}}$ [2] on the local stationary surface $\bar{S}$ defined as follows:

$$\bar{\boldsymbol{\mathcal{J}}}^*=\bar{\boldsymbol{\mathcal{J}}}[J_{k<n},\bar{J}_n^*(J_{k<n})],\quad \bar{\boldsymbol{\Theta}}^*=\bar{\boldsymbol{\Theta}}[J_{k<n},\bar{J}_n^*(J_{k<n})]. \tag{9.45}$$

The J_n- and θ_n-projections of this force can then be embedded in the Hamiltonian (9.2) by introducing two additional terms:

$$H=H_0(\boldsymbol{J})-\omega_0 J_n+\varepsilon H_1(\boldsymbol{J})\cos\theta_n-\bar{\mathcal{J}}_n^*\theta_n+\bar{\Theta}_n^*J_n. \tag{9.46}$$

---

[2] Recall that $\bar{\boldsymbol{\xi}}=\langle\langle\boldsymbol{\xi}\rangle_\circ\rangle_\phi$.

All stationary points $(\bar{J}_n^*, \bar{\theta}_n^*)$ of this Hamiltonian form the local stationary surface $\bar{S}$. Expand the Hamiltonian H in a vicinity of a local stationary point $(\bar{J}_n^*, \bar{\theta}_n^*)$ as:

$$H \approx H_*(J_{k<n}) + \frac{\gamma_{11}(J_n - \bar{J}_n^*)^2}{2} + \frac{\gamma_{22}(\theta_n - \bar{\theta}_n^*)^2}{2} + \gamma_{12}(J_n - \bar{J}_n^*)(\theta_n - \bar{\theta}_n^*), \quad (9.47)$$

where γ_{ij}, $\bar{J}_n^*$ and $\bar{\theta}_n^*$ are functions of $J_{k<n}$. Making a canonical transformation defined by the following generating function

$$\Phi(\boldsymbol{J}, \hat{\boldsymbol{\theta}}) = \left[(\gamma_{11}/\gamma_{22})^{1/4}\hat{\theta}_n + \bar{\theta}_n^*\right]\left[J_n - \bar{J}_n^*\right] + \sum_{k<n}\hat{\theta}_k J_k, \quad (9.48)$$

one can rewrite the Hamiltonian in the new canonical variables $(\hat{\boldsymbol{J}}, \hat{\boldsymbol{\theta}})$ as:

$$H \approx H_*\left(\hat{J}_{k<n}\right) + \sqrt{\gamma_{11}\gamma_{22}}\,\frac{\hat{J}_n^2 + \hat{\theta}_n^2}{2} + \gamma_{12}\hat{J}_n\hat{\theta}_n. \quad (9.49)$$

Assume for simplicity that $\gamma_{12} = 0$. In the presence of friction $\boldsymbol{\xi}$, the equations of motion derived from Eq. (9.49) are modified as follows:

$$\dot{\hat{J}}_{k<n} = \mathcal{J}_k, \quad (9.50)$$

$$\dot{\hat{J}}_n = -\sqrt{\gamma_{11}\gamma_{22}}\hat{\theta}_n + \hat{\mathcal{J}}_n, \quad (9.51)$$

$$\dot{\hat{\theta}}_n = \sqrt{\gamma_{11}\gamma_{22}}\hat{J}_n + \hat{\Theta}_n, \quad (9.52)$$

where $\Gamma = \gamma_{11}/\gamma_{22}$, $\grave{\mathcal{J}}_n = \mathcal{J}_n - \bar{\mathcal{J}}_n^*$, $\grave{\Theta}_n = \Theta_n - \bar{\Theta}_n^*$ and

$$\hat{\mathcal{J}}_n = \left(\grave{\mathcal{J}}_n - \sum_{k<n}\frac{\partial \bar{J}_n^*}{\partial J_k}\mathcal{J}_k\right)\Gamma^{1/4} + \sum_{k<n}\frac{\hat{J}_n}{4\Gamma}\frac{\partial\Gamma}{\partial J_k}\mathcal{J}_k, \quad (9.53)$$

$$\hat{\Theta}_n = \left(\grave{\Theta}_n - \sum_{k<n}\frac{\partial \bar{\theta}_n^*}{\partial J_k}\mathcal{J}_k\right)\Gamma^{-1/4} - \sum_{k<n}\frac{\hat{\theta}_n}{4\Gamma}\frac{\partial\Gamma}{\partial J_k}\mathcal{J}_k. \quad (9.54)$$

The action K_n of the oscillations in $(\hat{J}_n, \hat{\theta}_n)$ reads $K_n = \hat{J}_n^2/2 + \hat{\theta}_n^2/2$. The evolution of this action due to the friction force $\boldsymbol{\xi}$ is then given by the following equation:

$$\omega_* \dot{K}_n = \hat{\mathcal{J}}_n\dot{\hat{\theta}}_n - \hat{\Theta}_n\dot{\hat{J}}_n. \quad (9.55)$$

Integration of this equation can then be performed over the unperturbed trajectory, *i.e.,* over a circle in $(\hat{J}_n, \hat{\theta}_n)$ space. Using this relation one can immediately derive the first-order expressions for $\mathcal{F}_n$ and $\mathcal{D}_{n,n}$. Indeed, recalling that $\hat{\mathcal{J}}_n$ and $\hat{\Theta}_n$ are functions of $\hat{J}_n$, one obtains:

$$\mathcal{F}_n \approx \frac{\partial \langle \langle \hat{\mathcal{J}}_n \rangle_\circ \rangle_\phi}{\partial \hat{J}_n} K_n \approx \left(\frac{\partial \bar{\mathcal{J}}_n}{\partial J_n} - \sum_{k<n} \frac{\partial \bar{J}_n^*}{\partial J_k} \frac{\partial \bar{\mathcal{J}}_k}{\partial J_n} \right) K_n \tag{9.56}$$

in full agreement with Eq. (9.29). Notice that in this derivation of $\mathcal{F}_n$, the contributions from last terms in Eqs. (9.53) and (9.54) canceled each other.

The second-order contribution to $\mathcal{F}_n$ can be obtained by performing the integration of

$$\dot{K}_n = \frac{\partial K_n}{\partial \hat{J}_n} \hat{\mathcal{J}}_n + \frac{\partial K_n}{\partial \hat{\theta}_n} \hat{\Theta}_n \tag{9.57}$$

over a trajectory calculated using the first-order perturbation theory. Let δK_n, $\delta \psi_n$ and $\delta J_{k<n}$ denote the first-order corrections to the unperturbed particle trajectory characterized by $K_n = K^0$, $\psi_n = \psi^0 = \psi_n^0 + \omega_* t$ and $J_{k<n} = J_{k<n}^0$. The change of the action K_n over a time interval Δt can then be approximated as:

$$\Delta K_n \approx \underbrace{\int_t^{t+\Delta t} \left(\frac{\partial \hat{J}_n}{\partial K_n} \delta K_n + \frac{\partial \hat{J}_n}{\partial \psi_n} \delta \psi_n \right) \hat{\mathcal{J}}_n \, dt}_{C_1} + \underbrace{\int_t^{t+\Delta t} \left(\frac{\partial \hat{\theta}_n}{\partial K_n} \delta K_n + \frac{\partial \hat{\theta}_n}{\partial \psi_n} \delta \psi_n \right) \hat{\Theta}_n \, dt}_{C_2} + \\ + \underbrace{\int_t^{t+\Delta t} \hat{J}_n \delta \hat{\mathcal{J}}_n \, dt}_{C_3} + \underbrace{\int_t^{t+\Delta t} \hat{\theta}_n \delta \hat{\Theta}_n \, dt}_{C_4}, \tag{9.58}$$

Introduce $\langle \hat{\boldsymbol{\mathcal{J}}} \rangle = \langle \langle \hat{\boldsymbol{\mathcal{J}}} \rangle_\circ \rangle_\phi$, $\langle \hat{\boldsymbol{\Theta}} \rangle = \langle \langle \hat{\boldsymbol{\Theta}} \rangle_\circ \rangle_\phi$, $\hat{\boldsymbol{\mathcal{J}}}^{\sim} = \hat{\boldsymbol{\mathcal{J}}} - \langle \hat{\boldsymbol{\mathcal{J}}} \rangle$ and $\hat{\boldsymbol{\Theta}}^{\sim} = \hat{\boldsymbol{\Theta}} - \langle \hat{\boldsymbol{\Theta}} \rangle$. The perturbations $\delta \hat{\mathcal{J}}_n$ and $\delta \hat{\Theta}_n$ can then be represented as:

$$\delta \hat{\mathcal{J}}_n = \langle \hat{\mathcal{J}}_n \rangle (K^0 + \delta K, \psi^0 + \delta \psi) - \langle \hat{\mathcal{J}}_n \rangle (K^0, \psi^0) + \\ + \hat{\mathcal{J}}_n^{\sim} (K^0 + \delta K, \psi^0 + \delta \psi, t) - \hat{\mathcal{J}}_n^{\sim} (K^0, \psi^0, t). \tag{9.59}$$

$$\delta\hat{\Theta}_n = \langle\hat{\Theta}_n\rangle(K^0+\delta K,\psi^0+\delta\psi) - \langle\hat{\Theta}_n\rangle(K^0,\psi^0)+ \\ + \hat{\Theta}_n^{\sim}(K^0+\delta K,\psi^0+\delta\psi,t) - \hat{\Theta}_n^{\sim}(K^0,\psi^0,t). \quad (9.60)$$

Assuming that the two last terms in Eqs. (9.59) and (9.60) vanish in the calculation of $\mathcal{F}_n$, one can approximate:

$$\delta\langle\hat{\mathcal{J}}_n\rangle \approx \frac{\partial\langle\hat{\mathcal{J}}_n\rangle}{\partial K_n}\delta K_n + \frac{\partial\langle\hat{\mathcal{J}}_n\rangle}{\partial\psi_n}\delta\psi_n + \sum_{k<n}\frac{\partial\langle\hat{\mathcal{J}}_n\rangle}{\partial J_k}\delta J_k, \quad (9.61)$$

$$\delta\langle\hat{\Theta}_n\rangle \approx \frac{\partial\langle\hat{\Theta}_n\rangle}{\partial K_n}\delta K_n + \frac{\partial\langle\hat{\Theta}_n\rangle}{\partial\psi_n}\delta\psi_n + \sum_{k<n}\frac{\partial\langle\hat{\Theta}_n\rangle}{\partial J_k}\delta J_k. \quad (9.62)$$

To proceed, notice that

$$\frac{\partial\langle\hat{\mathcal{J}}_n\rangle}{\partial K_n} = \frac{\partial\langle\hat{\mathcal{J}}_n\rangle}{\partial\hat{J}_n}\frac{\hat{J}_n}{2K_n}, \qquad \frac{\partial\langle\hat{\Theta}_n\rangle}{\partial K_n} = \frac{\partial\langle\hat{\theta}_n\rangle}{\partial\hat{J}_n}\frac{\hat{J}_n}{2K_n}, \quad (9.63)$$

$$\frac{\partial\langle\hat{\mathcal{J}}_n\rangle}{\partial\psi_n} = \frac{\partial\langle\hat{\mathcal{J}}_n\rangle}{\partial\hat{J}_n}\hat{\theta}_n, \qquad \frac{\partial\langle\hat{\Theta}_n\rangle}{\partial\psi_n} = \frac{\partial\langle\hat{\theta}_n\rangle}{\partial\hat{J}_n}\hat{\theta}_n, \quad (9.64)$$

where we employed $\hat{J}_n = \sqrt{2K_n}\sin\psi_n$ and $\hat{\theta}_n = \sqrt{2K_n}\cos\psi_n$. The first-order perturbation of K_n, ψ_n and J_k, in turn, read

$$\delta K_n \approx \int \hat{J}_n\hat{\mathcal{J}}_n\,dt + \int \hat{\theta}_n\hat{\Theta}_n\,dt, \quad (9.65)$$

$$\delta\psi_n \approx \int \frac{\hat{\theta}_n}{2K_n}\hat{\mathcal{J}}_n\,dt - \int \frac{\hat{J}_n}{2K_n}\hat{\Theta}_n\,dt, \quad (9.66)$$

$$\delta J_{k<n} \approx \int \mathcal{J}_k\,dt. \quad (9.67)$$

Now one can combine Eqs. (9.58), (9.61)-(9.67) to calculate the average of ΔK. For example, the term C_1 can be rewritten as follows:

$$\int_t^{t+\Delta t}\left[\frac{\hat{J}_n'}{2K_n}\int_t^{t'}\left(\hat{J}_n''\hat{\mathcal{J}}_n'' + \hat{\theta}_n''\hat{\Theta}_n''\right)dt'' + \frac{\hat{\theta}_n'}{2K_n}\int_t^{t'}\left(\hat{\theta}_n''\hat{\mathcal{J}}_n'' - \hat{J}_n''\hat{\Theta}_n''\right)dt''\right]\hat{\mathcal{J}}_n'\,dt', \quad (9.68)$$

where $X' \equiv X(t')$ and $X'' \equiv X(t'')$. Using expressions for $\hat{J}_n$ and $\hat{\theta}_n$, one obtains:

$$\langle C_1 \rangle = \int\limits_t^{t+\Delta t} dt' \int\limits_t^{t'} dt'' \left[\sin\psi'_n \sin\psi''_n \Big(\langle \hat{\mathcal{J}}_n'^{\sim} \hat{\mathcal{J}}_n''^{\sim} \rangle + \langle \hat{\mathcal{J}}'_n \rangle \langle \hat{\mathcal{J}}''_n \rangle \Big) + \right.$$
$$\sin\psi'_n \cos\psi''_n \Big(\langle \hat{\mathcal{J}}_n'^{\sim} \hat{\Theta}_n''^{\sim} \rangle + \langle \hat{\mathcal{J}}'_n \rangle \langle \hat{\Theta}''_n \rangle \Big) + \cos\psi'_n \cos\psi''_n \Big(\langle \hat{\mathcal{J}}_n'^{\sim} \hat{\mathcal{J}}_n''^{\sim} \rangle + \langle \hat{\mathcal{J}}'_n \rangle \langle \hat{\mathcal{J}}''_n \rangle \Big) -$$
$$\left. \cos\psi'_n \sin\psi''_n \Big(\langle \hat{\mathcal{J}}_n'^{\sim} \hat{\Theta}_n''^{\sim} \rangle + \langle \hat{\mathcal{J}}'_n \rangle \langle \hat{\Theta}''_n \rangle \Big) \right]. \quad (9.69)$$

Performing the integration by time and recalling that averages like $\langle \hat{\mathcal{J}}_n'^{\sim} \hat{\mathcal{J}}_n''^{\sim} \rangle$ are localized in a small vicinity of $t' = t''$, one obtains (for $\Delta t \gg T_*$):

$$\langle C_1 \rangle \approx \Big(\hat{\mathfrak{P}}_{n,n} + \langle \hat{\mathcal{J}}_n \rangle \langle \hat{\Theta}_n \rangle \Big) \Delta t, \quad (9.70)$$

where $\hat{\mathfrak{P}}_{n,n}$ is defined by Eq. (9.34) for $\hat{\mathcal{J}}_n$ instead of $\mathcal{J}_n$. Similarly, one can calculate the average of the term C_2:

$$\langle C_2 \rangle \approx \Big(\hat{\mathfrak{Q}}_{n,n} - \langle \hat{\mathcal{J}}_n \rangle \langle \hat{\Theta}_n \rangle \Big) \Delta t. \quad (9.71)$$

Now let us calculate $\langle C_3 \rangle$:

$$\int\limits_t^{t+\Delta t} \hat{J}'_n \left[\frac{\partial \langle \hat{\mathcal{J}}_n \rangle}{\partial \hat{J}_n} \frac{\hat{J}'_n}{2K_n} \int\limits_t^{t'} \Big(\hat{J}''_n \hat{\mathcal{J}}''_n + \hat{\theta}''_n \hat{\Theta}''_n \Big)\, dt'' + \frac{\partial \langle \hat{\mathcal{J}}_n \rangle}{\partial \hat{J}_n} \frac{\hat{\theta}'_n}{2K_n} \int\limits_t^{t'} \Big(\hat{\theta}''_n \hat{\mathcal{J}}''_n - \hat{J}''_n \hat{\Theta}''_n \Big)\, dt'' + \right.$$
$$\left. + \sum_{k<n} \frac{\partial \langle \hat{\mathcal{J}}_n \rangle}{\partial J_k} \int\limits_t^{t'} \langle \mathcal{J}_k \rangle\, dt'' \right] dt'. \quad (9.72)$$

Recalling that $\hat{J}_n$ and $\hat{\theta}_n$ are proportional to K_n, one can see that this expression is much smaller than $\langle C \rangle_1$ and $\langle C \rangle_2$ for particles localized near $\bar{S}$, *i.e.,* particles with small K_n.

Adding $\langle C_1 \rangle$ and $\langle C_2 \rangle$, one therefore obtains a final result for the second-order correction to $\mathcal{F}_n$:

$$\mathcal{F}_n \approx \frac{\partial \langle \langle \hat{\mathcal{J}}_n \rangle_\circ \rangle_\phi}{\partial \hat{J}_n} K_n + \hat{\mathfrak{P}}_{n,n} + \hat{\mathfrak{Q}}_{n,n}. \quad (9.73)$$

Note that the last two terms in the previous equation can also be represented as:

$$\hat{\mathfrak{P}}_{n,n} + \hat{\Omega}_{n,n} \approx \frac{\partial \hat{\mathcal{D}}_{n,n}}{\partial K_n}. \tag{9.74}$$

Once the second-order correction to $\mathcal{F}_n$ is calculated, the width of the stationary distribution function localized near $\bar{S}$ can be estimated. Substituting $\mathcal{F}_n \approx AK_n + B$ and $\mathcal{D}_{n,n} \approx BK_n$ in Eq. (9.43), where A and B are treated as constants, one obtains:

$$f(K_{i<n}, K_n) \approx f_0(K_{i<n}) \exp\left(\frac{AK_n}{B}\right) = f_0 \exp\left[\frac{(\partial\langle\langle \hat{\mathcal{J}}_n\rangle_\circ\rangle_\phi/\partial \hat{J}_n)K_n}{\hat{\mathfrak{P}}_{n,n} + \hat{\Omega}_{n,n}}\right]. \tag{9.75}$$

This expression can also be rewritten in coordinates (J_n, θ_n) by noticing that $A/B \approx \mathcal{F}_n^{(1)}/\mathcal{D}_{n,n}^{(1)}$:

$$f(K_{i<n}, K_n) \approx f_0(K_{i<n}) \exp\left(\frac{\mathcal{F}_n^{(1)} K_n}{\mathcal{D}_{n,n}^{(1)}}\right), \tag{9.76}$$

where $\mathcal{F}_n^{(1)}$ and $\mathcal{D}_{n,n}^{(1)}$ denote the first-order expressions given by Eqs. (9.29) and (9.38) correspondingly.

Notice here that the second-order correction to $\mathcal{F}_n$ is critical for calculating the stationary distribution function. Indeed, without this term, the equation on f reads

$$\frac{\partial f/\partial K_n}{f} = \frac{A}{B} - \frac{1}{K_n}. \tag{9.77}$$

The solution $f(K_{i<n}, K_n) = f_0(K_{i<n}) K_n^{-1} \exp(AK_n/B)$ of this equation is singular in $K_n = 0$ [3]. However, when the second-order correction to $\mathcal{F}_n$ is introduced, the last term in Eq. (9.77) vanishes and the stationary solution becomes a regular function.

---

[3] The $1/K_n$ singularity makes the integral $\int f\, dK_n$ divergent.

9.2 Effect of Collisions on Magnetized Particle in a Wave Field

In this section, we study the effect of collisions on the wave-particle system first introduced in Sec. 7.2, namely, on a charged particle moving in a homogeneous magnetic field in a presence of a circularly polarized wave propagating along the magnetic field and characterized by the refraction index n_0. Considering a single test particle moving through a background plasma, we derive the statistical properties of the collisional force in Sec. 9.2.1. Using the results of Sec. 7.1, we then study the particle dynamics induced by collisions and the stability of stationary points in Sec. 9.2.2.

9.2.1 Calculation of the collisional forces $\boldsymbol{\mathcal{J}}$ and $\boldsymbol{\Theta}$ for cold plasmas

In this section, we calculate forces $\boldsymbol{\mathcal{J}}$ and $\boldsymbol{\Theta}$ entering the particle equations of motion (9.10) and (9.11) and attributed to collisions with a cold background plasma. Consider a magnetized test particle travelling through a low-density homogeneous cold non-relativistic plasma. Assuming that the test and plasma particle gyroradia are much larger than the plasma Debye length λ_D, a single small-angle scattering event of the test particle on one of the plasma particles can be approximated as a binary collision of two free-moving particles.

The Hamiltonian describing scattering of two relativistic charged particles reads

$$H(\boldsymbol{p}_1, \boldsymbol{p}_2, \boldsymbol{r}_1, \boldsymbol{r}_2) = c\sqrt{m_1^2 c^2 + \boldsymbol{p}_1^2} + c\sqrt{m_2^2 c^2 + \boldsymbol{p}_2^2} + \frac{q_1 q_2}{|\boldsymbol{r}_1 - \boldsymbol{r}_2|}, \qquad (9.78)$$

where $\boldsymbol{p}_1$, $\boldsymbol{p}_2$, $\boldsymbol{r}_1$ and $\boldsymbol{r}_2$ are kinetic particle momenta and particle positions and m_1, m_2, q_1, q_2 are the particle masses and charges correspondingly. The equations describing relative particle motion can be obtained by making a canonical transformation with the following generating function:

$$\Phi(\boldsymbol{p}, \boldsymbol{P}, \boldsymbol{r}_1, \boldsymbol{r}_2) = \boldsymbol{p} \cdot (\boldsymbol{r}_1 - \boldsymbol{r}_2) + \boldsymbol{P} \cdot \frac{m_1 \boldsymbol{r}_1 + m_2 \boldsymbol{r}_2}{m_1 + m_2}, \tag{9.79}$$

where $\boldsymbol{p}$, $\boldsymbol{P}$ are the new canonical momenta corresponding to the new canonical coordinates $\boldsymbol{\rho}$ and $\boldsymbol{R}$ related to the old canonical variables through:

$$\boldsymbol{\rho} = \boldsymbol{r}_1 - \boldsymbol{r}_2, \qquad \boldsymbol{R} = \frac{m_1 \boldsymbol{r}_1 + m_2 \boldsymbol{r}_2}{m_1 + m_2}, \tag{9.80}$$

$$\boldsymbol{p} = \frac{m_2 \boldsymbol{p}_1 - m_1 \boldsymbol{p}_2}{m_1 + m_2}, \qquad \boldsymbol{P} = \boldsymbol{p}_1 + \boldsymbol{p}_2. \tag{9.81}$$

Rewriting the Hamiltonian in the new variables

$$H(\boldsymbol{p}, \boldsymbol{P}, \boldsymbol{\rho}) = c\sqrt{m_1^2 c^2 + \left(\boldsymbol{p} + \frac{m_1 \boldsymbol{P}}{m_1 + m_2}\right)^2} + \\ + c\sqrt{m_2^2 c^2 + \left(-\boldsymbol{p} + \frac{m_2 \boldsymbol{P}}{m_1 + m_2}\right)^2} + \frac{q_1 q_2}{|\boldsymbol{\rho}|}, \tag{9.82}$$

and noticing that the total momentum $\boldsymbol{P} = \boldsymbol{p}_1 + \boldsymbol{p}_2$ is conserved, one reduces the problem to the analysis of the relative particle dynamics in coordinates $\boldsymbol{p}$ and $\boldsymbol{\rho}$.

Assuming that the particle scattering angle is small, the perturbation theory can be applied to find the change of the relative particle momentum $\boldsymbol{p}$. The zeroth-order particle motion is charterized by constant $\boldsymbol{p} = \boldsymbol{p}^{(0)}$ and

$$\dot{\boldsymbol{\rho}}^{(0)}(t) = \boldsymbol{v}_0 = \boldsymbol{v}(\boldsymbol{p}^{(0)}) = \left[\frac{\boldsymbol{p}_1}{m_1 \gamma_1} - \frac{\boldsymbol{p}_2}{m_2 \gamma_2}\right]_{\boldsymbol{p}^{(0)}}, \tag{9.83}$$

where $\boldsymbol{p}_1(\boldsymbol{p}) = \boldsymbol{p} + m_1 \boldsymbol{P}(m_1 + m_2)^{-1}$, $\boldsymbol{p}_2(\boldsymbol{p}) = -\boldsymbol{p} + m_2 \boldsymbol{P}(m_1 + m_2)^{-1}$ and $\gamma_i^2(\boldsymbol{p}) = 1 + \boldsymbol{p}_i^2/(m_i c)^2$. The equation on the first-order perturbation of $\boldsymbol{p}$ then reads

$$\dot{\boldsymbol{p}}^{(1)} \approx \frac{q_1 q_2 \boldsymbol{\rho}^{(0)}(t)}{|\boldsymbol{\rho}^{(0)}(t)|^3}. \tag{9.84}$$

Noticing that Eq. (9.84) is identical to the equation on the relative particle momentum perturbation in the non-relativistic case, one can approximate:

$$\Delta \boldsymbol{p}^{(1)} \approx \frac{\boldsymbol{\rho}_0}{\rho_0} \frac{2 q_1 q_2}{\rho_0 v_0}, \tag{9.85}$$

where $\boldsymbol{\rho}_0$ is the impact parameter defined as:

$$\boldsymbol{\rho}_0 = \boldsymbol{\rho}^{(0)}(t) - \frac{\boldsymbol{\rho}^{(0)}(t) \cdot \boldsymbol{v}_0}{v_0}. \tag{9.86}$$

The first-order momentum perturbation given by Eq. (9.85) describes the change of the direction of motion, but not the particle slowing-down. This effect can be accounted for by considering the second-order momentum perturbation calculated as follows. Rewriting Eq. (9.82) before and after the collision as $\rho \to \infty$:

$$H(\boldsymbol{p}, \boldsymbol{\rho}; \boldsymbol{P}) \approx E_\infty(\boldsymbol{p}; \boldsymbol{P}) = m_1 c^2 \gamma_1 + m_2 c^2 \gamma_2. \tag{9.87}$$

one obtains:

$$\Delta E_\infty(\boldsymbol{p}; \boldsymbol{P}) \approx \left. \frac{\partial E_\infty}{\partial \boldsymbol{p}} \right|_{\boldsymbol{p}^{(0)}} \cdot \Delta \boldsymbol{p} + \frac{1}{2} \left. \frac{\partial E_\infty}{\partial \boldsymbol{p} \, \partial \boldsymbol{p}} \right|_{\boldsymbol{p}^{(0)}} : \Delta \boldsymbol{p} \, \Delta \boldsymbol{p} \approx 0. \tag{9.88}$$

Recalling that $\partial E_\infty / \partial \boldsymbol{p} = \boldsymbol{v}$, this equation can further be rewritten as:

$$\boldsymbol{v}_0 \cdot \Delta \boldsymbol{p}^{(2)} + \frac{1}{2} \left. \frac{\partial \boldsymbol{v}}{\partial \boldsymbol{p}} \right|_{\boldsymbol{p}^{(0)}} : \Delta \boldsymbol{p}^{(1)} \, \Delta \boldsymbol{p}^{(1)} \approx 0. \tag{9.89}$$

The parallel momentum perturbation $\Delta \boldsymbol{p}_\parallel^{(2)}$ is then given by:

$$\Delta p_\parallel = -\frac{1}{2 v_0} \left. \frac{\partial \boldsymbol{v}}{\partial \boldsymbol{p}} \right|_{\boldsymbol{p}^{(0)}} : \Delta \boldsymbol{p}_\perp \, \Delta \boldsymbol{p}_\perp, \tag{9.90}$$

where we omitted the superscripts and denoted the first-order momentum perturbation as $\Delta \boldsymbol{p}_\perp \equiv \Delta \boldsymbol{p}^{(1)}$. Substituting Eq. (9.83) in Eq. (9.90), one finally obtains:

$$\Delta p_\parallel = -\frac{1}{2 v_0} \left[|\Delta \boldsymbol{p}_\perp|^2 \left(\frac{1}{m_1 \gamma_1} + \frac{1}{m_2 \gamma_2} \right) - \frac{(\Delta \boldsymbol{p}_\perp \cdot \boldsymbol{p}_1)^2}{m_1^3 c^2 \gamma_1^3} - \frac{(\Delta \boldsymbol{p}_\perp \cdot \boldsymbol{p}_2)^2}{m_2^3 c^2 \gamma_2^3} \right]. \tag{9.91}$$

This expression can be simplified for cold non-relativistic plasmas with $|\boldsymbol{p}_2| \ll mc$ as:

$$\Delta p_{\parallel} \approx -\frac{|\Delta \boldsymbol{p}_{\perp}|^2}{2v_0}\left(\frac{1}{m_1\gamma_1}+\frac{1}{m_2}\right). \tag{9.92}$$

Assume for simplicity that thermal velocities of all plasma species are much smaller than v_1. If the plasma is homogeneous, so is the probability distribution of impact parameters $\boldsymbol{\rho}_0$. Therefore, the average of the momentum perturbation $\Delta\boldsymbol{p}_1$ accumulated over a time period Δt [4] and the averages of $\Delta\widetilde{\boldsymbol{p}}_1\Delta\widetilde{\boldsymbol{p}}_1$ can be expressed as follows:

$$\langle \Delta p_{1\,\alpha}\rangle = 0, \qquad \langle \Delta p_{1\,\beta}\rangle = 0, \tag{9.93}$$

$$\langle \Delta \widetilde{p}^{\,2}_{1\,\alpha}\rangle = C^2\Delta t, \qquad \langle \Delta \widetilde{p}^{\,2}_{1\,\beta}\rangle = C^2\Delta t, \tag{9.94}$$

$$\langle \Delta \widetilde{p}_{1\,\alpha}\Delta \widetilde{p}_{1\,\beta}\rangle = 0, \tag{9.95}$$

$$\langle \Delta p_{1\,\gamma}\rangle \approx -\frac{C^2}{v_0}\left(\frac{1}{m_1\gamma_1}+\frac{1}{m_2\gamma_2}\right), \tag{9.96}$$

$$\langle \Delta \widetilde{p}_{1\,\gamma}\Delta \widetilde{p}_{1\,i}\rangle \approx 0 \quad \text{for} \quad i=\alpha,\beta,\gamma, \tag{9.97}$$

where $\Delta\widetilde{\boldsymbol{p}} \equiv \Delta\boldsymbol{p} - \langle\Delta\boldsymbol{p}\rangle$ and (α,β,γ) is a local orthogonal coordinate system with the axis γ directed along $\boldsymbol{p}_1$.

To calculate C, average Eq. (9.85) over the impact parameters distributed homogeneously within a section of a Debye sphere:

$$\left\langle (\Delta\boldsymbol{p}^{(1)})^2\right\rangle \approx \frac{4q_1^2q_2^2}{\pi\lambda_D^2v_0^2}\int\limits_{b_0}^{\lambda_D}\frac{2\pi\rho_0\,d\rho_0}{\rho_0^2} = \frac{8q_1^2q_2^2}{\lambda_D^2v_0^2}\ln\frac{\lambda_D}{b_0}, \tag{9.98}$$

where $b_0 = q_1q_2/(p^{(0)}v_0)$ is the impact parameter for a finite-angle scattering. Since $v_2 \ll v_1$, Eq. (9.98) will retain its form after averaging over the background plasma

[4] The time period Δt should be much larger than $\lambda_D/|\boldsymbol{v}_1-\boldsymbol{v}_2|$, but much smaller than the time on which $|\Delta\boldsymbol{p}_1| \sim p_1$.

velocity distribution and hence:

$$C^2 = \frac{1}{2}\frac{\left\langle (\Delta \boldsymbol{p}^{(1)})^2 \right\rangle}{\Delta\tau_c} = \frac{4q_1^2 q_2^2}{\lambda_D^2 v_0^2}\frac{1}{\Delta\tau_c}\ln\frac{\lambda_D}{b_0}, \tag{9.99}$$

where $\Delta\tau_c \approx (n_p \pi \lambda_D^2 v_0)^{-1}$ is a collisional time and n_p is a plasma density.

The perturbations of the canonical momenta J_i and canonical coordinates θ_i by the collisional force can be calculated given the perturbation of the momentum $\boldsymbol{p}$:

$$\Delta J_i = \frac{\partial J_i}{\partial \boldsymbol{p}}\hat{\boldsymbol{U}}\begin{pmatrix}\Delta p_{1\,\alpha}\\ \Delta p_{1\,\beta}\\ \Delta p_{1\,\gamma}\end{pmatrix}, \qquad \Delta\theta_i = \frac{\partial \theta_i}{\partial \boldsymbol{p}}\hat{\boldsymbol{U}}\begin{pmatrix}\Delta p_{1\,\alpha}\\ \Delta p_{1\,\beta}\\ \Delta p_{1\,\gamma}\end{pmatrix}, \tag{9.100}$$

where $\hat{\boldsymbol{U}} = \hat{\boldsymbol{R}}_{z,\psi}\hat{\boldsymbol{R}}_{x,\kappa}$ is the matrix transforming vectors in the local coordinate system (α, β, γ) to the (x, y, z) coordinates, $\hat{\boldsymbol{R}}_{a,b}$ is a rotation matrix corresponding to the rotation around axis a by an angle b, ψ is the particle gyro-angle and $\kappa = \tan^{-1}(p_\perp/p_\parallel)$. Substituting

$$\hat{\boldsymbol{U}} = \begin{pmatrix}\cos\psi & \cos\kappa\sin\psi & -\sin\psi\sin\kappa\\ -\sin\psi & \cos\kappa\cos\psi & -\cos\psi\sin\kappa\\ 0 & \sin\kappa & \cos\kappa\end{pmatrix} \tag{9.101}$$

one can calculate the perturbations of the canonical variables $\boldsymbol{J}$ and $\boldsymbol{\theta}$ and find their averages:

$$\bar{\mathcal{J}}_1 = -\frac{C^2}{p^2}\left(\frac{p_\parallel}{k} - \frac{p_\perp^2}{m\Omega}\right)S \qquad \bar{\mathcal{J}}_2 = -\frac{C^2}{p^2}\frac{p_\perp^2}{m\Omega}S, \tag{9.102}$$

$$\bar{\Theta}_1 = 0, \qquad \bar{\Theta}_2 = 0, \tag{9.103}$$

$$\mathfrak{P}_{1,1} = \frac{C^2 p_\perp^2}{p^2 k^2}T^2, \qquad \mathfrak{P}_{1,2} = -\frac{C^2 p_\parallel}{kp^2}\frac{p_\perp^2}{m\Omega}T, \qquad \mathfrak{P}_{2,2} = \frac{C^2 p_\perp^2 p_\parallel^2}{m^2\Omega^2 p^2}, \tag{9.104}$$

$$\mathfrak{Q}_{1,1} = 0, \qquad \mathfrak{Q}_{1,2} = 0, \qquad \mathfrak{Q}_{2,2} = \frac{C^2}{p_\perp^2}. \tag{9.105}$$

Here $S = 1 + m\gamma/M$, $T = 1 + kp_\parallel/(m\Omega)$, $m = m_1$, $M = m_2$, $p^2 = p_\perp^2 + p_\parallel^2$, $p_\parallel = k(J_1 + J_2)$, $p_\perp^2 = 2m\Omega J_2$ and $\gamma = \sqrt{1 + p^2/(m^2c^2)}$.

9.2.2 Diffusion due to collisional force

Given the expressions for $\bar{\boldsymbol{\xi}}$, $\hat{\mathfrak{P}}$ and $\hat{\mathfrak{Q}}$, one can use the results of Sec. 9.1 to derive the Fokker-Planck equation coefficients. First, using Eqs. (9.20) and (9.29), one obtains:

$$\mathcal{F}_1 \approx -\frac{C^2(J_1 - J_2)}{p^2}\left(1 + \frac{m\widetilde{\gamma}}{M}\right). \tag{9.106}$$

The stationary points on $\bar{S}$ attracting or repelling particle trajectories are identified by solving $\mathcal{F}_1 = 0$. This can be done graphically by finding intersections of the line $J_1 = J_2$ with the stationary curve. As suggested by Fig. 8.1, for $n_0 < 1$ there might be up to three stationary points; in the following, however, we will consider the point with the lowest energy only.

First notice that since $\partial\mathcal{F}_1/\partial J_1 < 0$, the low-energy stationary point is stable with respect to the motion along $\bar{S}$ (with respect to J_1). The stability of the point with respect to Λ can then be studied by calculating $\mathcal{F}_2$. Again, using Eqs. (9.20) and (9.29), substituting $J_1 = J_2$ and assuming $J_2 \ll mc^2/\Omega$, one obtains:

$$\mathcal{F}_2 \approx -\frac{C^2\Lambda(1 + M/m)(-dJ_2^*/dJ_1)}{2M\Omega_0 J_2}. \tag{9.107}$$

The derivative dJ_2^*/dJ_1 on the low-energy branch of the stationary curve $\bar{S}$ laying to the right of the resonance (*i.e.,* at $J_1 > J_1^0 = mc^2(\omega_0^2 - \Omega_0^2)/(2\omega_0^2\Omega_0)$) is negative, becoming smaller than -1 in the negative-mass region. Therefore, the particle dynamics in the vicinity of $\bar{S}$ is unstable and the adiabatic moment Λ is exponentially increasing.

The collisional relaxation could, in principle, be used to bring a particle to the state with the negative parallel mass if $dJ_2^*/dJ_1 < -1$ at the intersection of the line $J_1 = J_2$ and $\bar{S}$. Unfortunately, the instability in Λ is expected to repell the particle trajectories from $\bar{S}$ over time. To avoid this, introduce an additional constant parallel

force acting in the z direction. By a proper choice of the force, the new solutions of $\mathcal{F}_1 = 0$ can occur at arbitrary J_1 including $J_1 < 0$. At the same time, performing calculation of $\mathcal{F}_2$ for $J_1 \neq J_2$ (both J_1 and J_2 are assumed to be much smaller than mc^2/Ω), one obtains:

$$\mathcal{F}_2 \approx -\frac{C^2 J_1 \Lambda (1 + M/m)(-dJ_2^*/dJ_1)}{2M\Omega J_2^2} \tag{9.108}$$

and therefore, the new stationary point with $J_1 < 0$ solving $\mathcal{F}_1 = 0$ will be stable with respect to Λ as well with respect to J_1.

The feasibility of the proposed method for bringing the particles inside ther negative-mass region can be limited by collisional stochastization of particle trajectories. Specifically, for this technique to be practical, the expected distribution function widths should be small compared to J_2 and the characteristic negative-mass region size. To estimate the characteristic widths of the distribution function, we calculated $\mathcal{D}_{1,1}$ and $\mathcal{D}_{2,2}$ under the assumption that $\varepsilon \ll \chi \ll \delta$, where $\delta = (\Omega_0 - \omega_0)/\Omega_0$. Taking $J_1 \sim -mc^2\delta/\Omega_0$, $J_2 \sim (\varepsilon/\chi)^{2/3} \sim J_2^*$ and assuming that $\delta \ll (\varepsilon/\chi)^{2/3}$, after a tedious yet straighforward calculations, the following estimate for the characteristic distribution function width w_1 along J_1 was obtained:

$$w_1 \approx \frac{J_2 M}{2(m + M)\Omega_0}. \tag{9.109}$$

The expression for w_2 being the characteristic width along J_2 was also shown to be proportional to $M/(m + M)$, but also inversely proportional to $\sqrt{\varepsilon}$. One therefore concludes that for $m \sim M$, the collisional stochastization of particle trajectories will prohibit particle localization near $\bar{S}$. In order for particles to remain attached to the stable stationary curves, most of collisions should involve light particles with $M \ll m$.

Chapter 10

Applications of the Negative Mass Effect

The NME, manifesting itself as an acceleration of a particle in an opposite direction to that of the applied force, can lead to unconventional collective effects in plasmas containing large fractions of resonant particles. For example, in Sec. 7.5, we showed that the NME can result in a collective electrostatic plasma instability. In this chapter, we study other phenomena emerging in plasmas with negative-mass particles. Specifically, in Sec. 10.1, we discuss the "frequency-doubling" effect observed when an incident plasma wave with a frequency ω_p leads to particle oscillations with the frequency $2\omega_p$. Next, in Sec. 10.2, we discuss how the NME makes it possible to control propagation of plasma waves. in the presence of large fractions of resonan

10.1 Frequency Doubling

In the following, we show how the NME can be used to double the frequency of the low-frequency wave[1]. Consider a particle localized in a vicinity of a stable stationary surface S. As discussed in Sec. 7.4, particle response to some weak external fields can be described using the effective Hamiltonian

$$H_{\text{eff}} = K(p) + U(z), \tag{10.1}$$

where z is a coordinate along the magnetic field, $U(z)$ is the potential energy, $K(p)$ is the particle kinetic energy, p is the canonical momentum, or the "quasimomentum" related to the particle velocity $v_\parallel = \dot{z}$ through $v_\parallel = dK/dp$. The kinetic energy K defines the particle response to the external force $F = -dU/dz$. In particular, one can see that the parallel effective mass $m_\parallel$ introduced as $m_\parallel \dot{v}_\parallel = F$ is given by

$$m_\parallel^{-1} = \frac{d^2K}{dp^2}. \tag{10.2}$$

Consider a case when the dependence of the particle parallel velocity $v_\parallel$ on the canonical momentum p has extrema, *i.e.,* $dv_\parallel/dp = 0$. Noticing that $dv_\parallel/dp$ can be rewritten as:

$$\frac{dv_\parallel}{dp} = \frac{d^2K}{dp^2} = m_\parallel^{-1}, \tag{10.3}$$

one concludes that $m_\parallel^{-1} = 0$ in all extrema of $v_\parallel(p)$. These states and states with $m_\parallel = 0$ limit the regions of the negative parallel mass. An example of a $v_\parallel(p)$ dependence with an extremum is shown on Fig. 7.6.

Consider a particle localized near some extremum p_0 of $v_\parallel(p)$ (Fig. 10.1). The dynamics of such a particle in the field of a monochromatic external force $F\cos\omega_p t$

[1]The wave frequency should be much smaller than the frequency of the laser wave.

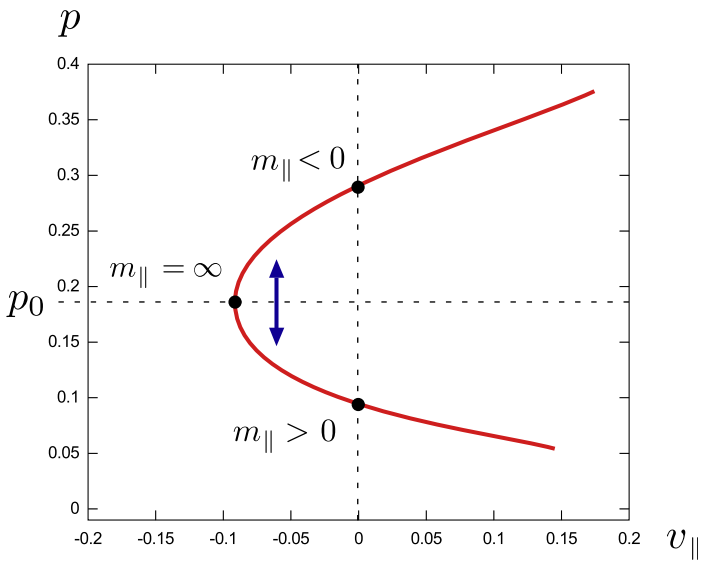

Figure 10.1: The conceptual plot of the dependence $p(v_\|)$ near the point with $dv_\|/dp = 0$. Being perturbed by a wave with frequency $\omega_p \ll \omega_0$ with ω_0 being the laser frequency, the particle responds by oscillating with a frequency $2\omega_p$. The regions of the positive and negative parallel mass and the states with $v_\| = 0$ are also shown.

is governed by the equation

$$\dot{p} = F \cos \omega_p t, \tag{10.4}$$

the solution of which reads

$$p(t) = p_0 + \frac{F}{\omega_p} \sin \omega_p t. \tag{10.5}$$

The evolution of the particle velocity can then be obtained by substituting this solution in $v_\|(p)$. In particular, approximating $v_\|(p)$ as $v_\|(p_0) + \alpha \Delta p^2$, where $\Delta p = p - p_0$ and α is some constant, one obtains:

$$v_\|(t) = v_\|(p_0) + \frac{\alpha F^2}{\omega_p^2} \sin^2 \omega_p t. \tag{10.6}$$

Therefore, experiencing a monochromatic force with a frequency ω_p, the particle is oscillating with a double frequency. As any charged particle moving with an acceleration, it will radiate electromagnetic waves with a frequency $2\omega_p$ equal to that of the particle oscillations.

10.2 NME and the Group Velocity of Plasma Waves

In Sec. 7.5, the dispersion relation for Langmuir waves in media with negative-mass particles was derived. Considering a cold plasma, general dispersion relation (7.59) was approximated by Eq. (7.62), which showed that plasma with negative-mass particles can exhibit an absolute instability with respect to electrostatic perturbations. In this section, we focus our attention on another interesting effect associated with the dispersion relation (7.59), namely on the fact that the group velocity of the Langmuir waves in NME plasmas can be affected by collectively manipulating plasma particles or by adiabatically changing the electromagnetic wave properties: its amplitude and frequency.

The group velocity $v_{\rm gr}$ of the Langmuir waves in NME plasmas is derived as follows. Assuming that the plasma is cold, *i.e.,* that $\omega/k \gg v_{{\rm c}\,s}$ for all s, where $v_{{\rm c}\,s}$ is the characteristic velocity of particles of species s, the integral in Eq. (7.59) can be expanded in powers of k:

$$\omega^2 - \sum_{\ell \geq 0} A_\ell \frac{k^\ell}{\omega^\ell} = 0, \tag{10.7}$$

where

$$A_\ell = -\sum_s 4\pi n_s q_s^2 \int_{-\infty}^{+\infty} v^{\ell+1} \frac{\partial f_s}{\partial p}\, dp. \tag{10.8}$$

Equation (10.7) can then be solved for ω iteratively. The lowest-order solution reading $\omega^{(0)} = \sqrt{A_0}$ is substituted in Eq. (10.7) to provide the first-order solution $\omega^{(1)}$.

Substituting the obtained expression for $\omega^{(1)}$ in Eq. (10.7), one can then calculate the second-order solution, and so on. As a result, an approximate expression for ω up to the second order terms in $kv_{\mathrm{c}\,s}/\omega$ is found:

$$\omega^2 \approx A_0 + k\frac{A_1}{A_0^{1/2}} + k^2\left[\frac{A_2}{A_0} - \frac{A_1^2}{2A_0^2}\right] + o(k^2 v_{\mathrm{c}\,s}^2/\omega^2). \tag{10.9}$$

The coefficients A_ℓ can be expressed as the averages over the distribution function, namely:

$$A_\ell = \sum_s 4\pi n_s q_s^2 \int_{-\infty}^{+\infty} \frac{v^\ell f_s}{m_\parallel}\, dp, \tag{10.10}$$

where we used $dv/dp = m_{\parallel\,s}^{-1}$. The coefficient A_0 is calculated using the definition of $\bar{m}_{\parallel\,s}$ in Eq. (7.63):

$$A_0 = \sum_s \bar{\omega}_{p\,s}^2, \tag{10.11}$$

where $\bar{\omega}_{p\,s}^2 = 4\pi n_s q_s^2/\bar{m}_{\parallel\,s}$. The remaining coefficients A_ℓ are expressed as follows:

$$A_\ell = (1+\ell)\sum_s \bar{\omega}_{p\,s}^2 \left\langle v^\ell \bar{m}_{\parallel\,s}/m_{\parallel\,s}\right\rangle_f, \tag{10.12}$$

where $\langle \ldots \rangle_f$ denotes the average over the particle distribution.

Assume that for all plasma species, f_s are localized functions with such a small charactersitc width that $m_{\parallel\,s}$ is nearly constant on this scale. The expressions for A_ℓ can then be rewritten as:

$$A_1 = 2\sum_s \bar{\omega}_{p\,s}^2 \langle v\rangle_s, \tag{10.13}$$

$$A_2 = 3\sum_s \bar{\omega}_{p\,s}^2 \left(\langle v\rangle_s^2 + v_{\mathrm{th}\,s}^2\right), \tag{10.14}$$

where $\langle v\rangle_s = \langle v_s\rangle_f$ and $v_{\mathrm{th}\,s}^2 = \langle (v_s - \langle v\rangle_s)^2\rangle_f$ is the thermal velocity of particles of species s squared. Substituting Eqs. (10.13) and (10.14) in Eq. (10.9), one finally obtains:

$$\omega^2 \approx \omega_p^2 + 2\sum_s \bar{\omega}_{p\,s}^2 \frac{k\langle v\rangle_s}{\omega_p} + \frac{k^2}{\omega_p^2}\left[3\sum_s \bar{\omega}_{p\,s}^2\left(\langle v\rangle_s^2 + v_{\mathrm{th}\,s}^2\right) - \frac{2}{\omega_p^2}\left(\sum_s \bar{\omega}_{p\,s}^2\langle v\rangle_s\right)^2\right]. \tag{10.15}$$

where $\omega_p^2 = \sum_s \bar{\omega}_{p\,s}^2$. The group velocity of the Langmuir waves can then be calculated by taking a derivative of Eq. (10.15) by k:

$$v_{\rm gr} = \sum_s \frac{\bar{\omega}_{p\,s}^2}{\omega_p^2}\langle v\rangle_s + \frac{3k}{\omega_p}\left[\sum_s \frac{\bar{\omega}_{p\,s}^2}{\omega_p^2}\left(\langle v\rangle_s^2 + v_{{\rm th}\,s}^2\right) - \left(\sum_s \frac{\bar{\omega}_{p\,s}^2}{\omega_p^2}\langle v\rangle_s\right)^2\right]. \tag{10.16}$$

Consider a special case, in which all particle currents are zero, *i.e.*, $\langle v\rangle_s = 0$ for all plasma species s. The wave dispersion relation can then be simplified as follows:

$$\omega^2 \approx \omega_p^2 + 3\sum_s \bar{\omega}_{p\,s}^2 \frac{k^2 v_{{\rm th}\,s}^2}{\omega_p^2}. \tag{10.17}$$

Taking a derivative of this expression by k, one recovers the group velocity of the Langmuir waves:

$$v_{\rm gr} = \frac{3k}{\omega_p}\sum_s \frac{\bar{\omega}_{p\,s}^2}{\omega_p^2} v_{{\rm th}\,s}^2. \tag{10.18}$$

In the following, we show that under a slow adiabatic change of the system parameters which keep $\langle v\rangle_s = 0$ for all s, the wave group velocity can be changed considerably. Specifically, we demonstrate that changing the properties of the electromagnetic wave resonant with particles, the Langmuir wave packets can be slowed down.

Let the circularly-polarized electromagnetic wave interacting resonantly with one of the plasma species adiabatically change its amplitude a_0 and wave frequency ω_0. As wave parameters evolve, so do the states of the particles resonant with it. However, as discussed in Sec. 7.1, if the wave evolution is sufficiently slow, the system posesses two adiabatic invariants: $J_1 = p_\parallel/k - \widetilde{\mu}$ and Λ being the action of the one-dimensional dynamics in (J_2, θ_2) variables. The particle is therefore attached to the stable stationary curve S and the change of $p_\parallel$ is equal to the change of $k\widetilde{\mu}$. Therefore, if both time dependencies $a_0(t)$ and $\omega_0(t)$ are chosen in such a way that $J_2(J_1) = \widetilde{\mu}$ is constant, the parallel particle momentum $p_\parallel$ is also fixed and hence $\langle v\rangle_s$ remain equal to 0 for all s, what allows one to use Eq. (10.18) for calculating the wave group velocity at all times.

Unlike $\widetilde{\mu}$ and $p_{\|}$, the effective parallel mass $m_{\|}$ of the particles is evolving along with the wave parameters. One can therefore manipulate the group velocity of the Langmuir waves propagating in plasmas by adjusting the background laser radiation. For instance, it might be possible to slow down Langmuir wave packets without affecting the background particle distributions directly. This can be done by either substantially decreasing the effective parallel mass $m_{\|}$, or making terms in the sum in Eq. (10.18) cancel each other. The first approach is limited by the fact that as $m_{\|}$ goes to zero, the Langmuir wave frequency approaches infinity, potentially violating the requirement that $\omega_p \ll \omega_0$, *i.e.,* becoming comparable to the laser frequency. Another limitation of this method is that for $n_0 < 1$, the zero of $m_{\|}$ can be approached from the negative-mass branch only (see Fig. 7.5) and before this point is reached, ω_p^2 becomes negative, *i.e.,* plasma becomes unstable with respect to electrostatic perturbations.

The second approach can be implemented by choosing such wave parameters that $\sum_s \bar{\omega}_{p\,s}^2 v_{\mathrm{th}\,s}^2 \approx 0$. Assuming that there are only two species with comparable $v_{\mathrm{th}\,s}^2$, one concludes that $\bar{\omega}_{p\,s}$ should also be comparable to each other, but have the opposite signs. This condition can, for example, be satisfied in quasineutral electron-positron plasmas by choosing such wave characteristics that:

$$m_{\|\,1} = -\frac{v_{\mathrm{th}\,1}^2}{v_{\mathrm{th}\,2}^2} m_e, \tag{10.19}$$

where the particles of species 1 are assumed to be in resonance with the laser wave. Another alternative could be to use electron-ion plasmas with two fractions of electrons, one of which is resonant with the wave. Since the electron mass is much smaller than the ion mass, both electron contributions to v_{gr} (coming from resonant and non-resonant particles) will have to nearly cancel each other. At the same time, if the thermal velocities of two electron species are not equal, the plasma frequency ω_p will remain finite. Assuming that the thermal velocities of resonant and non-resonant

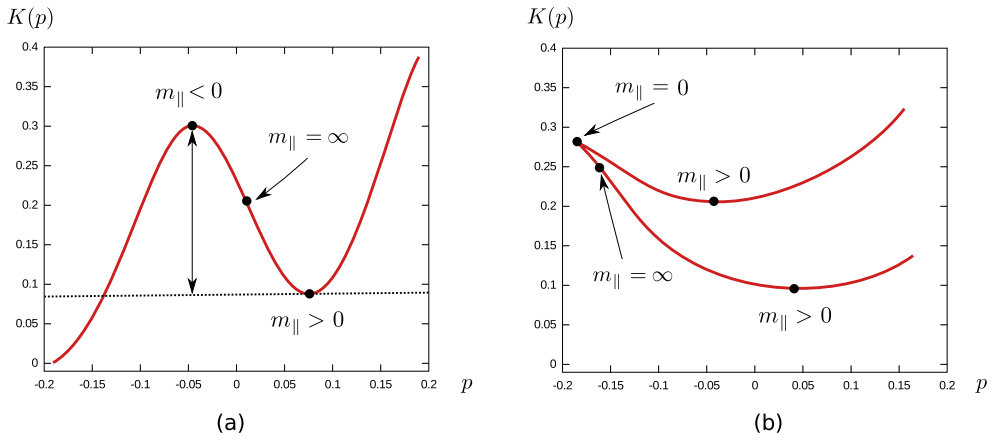

Figure 10.2: Dependencies $K(p)$ showing two possible arrangements of the stationary states with $v = \partial K/\partial p = 0$: (a) two states with $v = 0$ are separated by a single point, where the sign of $m_\parallel$ changes, (b) two states with $v = 0$ are separated by two points, where the sign of $m_\parallel$ changes. In the case (a), two states with $v = 0$ have different signs of $m_\parallel$, while in the case (b), the signs are the same. As suggested by Fig. 7.5, one of the states with $v = 0$ in the case (b) is unstable.

electrons are comparable, the parallel mass of resonant particles required to observe the vanishing of $v_{\rm gr}$ would have to be comparable to $-m_e$. Such a parallel mass is then expected to be reached for particles sufficiently far away from the point with $dJ_2/dJ_1 = \infty$, *i.e.,* from the point $\mathcal{F}$ in Fig. 7.2, where the particle stability is lost. The proposed approach is therefore expected to be practical for slowing down plasma waves and possibly even demonstrating the change of the group velocity sign.

10.3 Interaction of the Wave Packet with Negative-Mass Particles

Analyzing resonant interaction of a magnetized charged particle with a circularly-polarized electromagnetic wave, we showed in Sec. 7.2, that up to three different stationary particle states characterized by $v_\parallel = 0$, but different values of μ can be

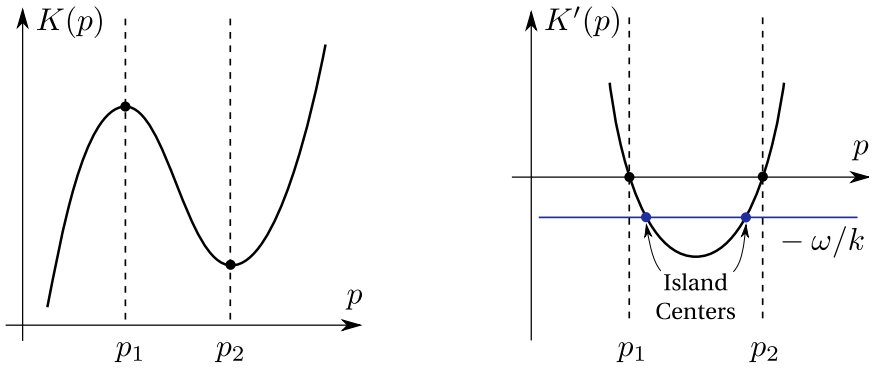

Figure 10.3: Dependencies $K(p)$ and $v = K'(p) \equiv dK/dp$ for the negative-mass particle. The wave phase velocity shown with a blue solid line intersects $K'(p)$ in two points (where the centers of the island chains are formed).

realized for a proper choice of wave parameters. Consider a single branch[2] of the stationary surface S containing two such particle states $\hat{h}$ and $\hat{l}$, with $\hat{h}$ having larger energy than $\hat{l}$ (Fig. 7.6). Unlike $\hat{l}$, the state $\hat{h}$ is generally characterized by a negative parallel mass (Fig. 10.2) and can thus be unstable with respect to the radiation friction. Noticing an analogy between the states $\hat{h}$, $\hat{l}$ and the excited and ground states of a stationary atom [Feynman et al., 1977], one could be interested in wave-particle interaction techniques capable of transfering particles between $\hat{h}$ and $\hat{l}$ and depositing the extracted energy to the wave, thus amplifying it. In this section, we propose such a technique and study its efficiency.

The interaction of a wave with a particle having an effective parallel mass $m_\parallel \neq$ const is described by the following Hamiltonian (see Sec. 7.4):

$$H_{\text{eff}} = K(p) + \varphi(z,t)\cos(\omega t - kz + \psi_0), \tag{10.20}$$

where $K(p)$ is the particle kinetic energy, $m_\parallel^{-1} = \partial^2 K/\partial p^2$, $\psi_0(z,t)$ is the slowly-changing phase-shift, and ω, k and φ are the wave frequency, wavenumber and wave

[2]All stable states on a branch are accessible from any other stable state on the same branch by applying weak adiabatic external forces.

profile (chosen to be real and positive) correspondingly. The characteristic spatial and temporal scales of the wave envelope reading $\varphi/(\partial\varphi/\partial z)$ and $\varphi/(\partial\varphi/\partial t)$ are assumed to be much larger than k^{-1} and ω^{-1} respectively. Make a canonical transformation from (z, p) to the new canonical variables $\psi = \omega t - kz$ and $I = -p/k$ defined via the following generating function:

$$\Phi(I, z, t) = (\omega t - kz)I. \tag{10.21}$$

The new Hamiltonian $\mathcal{H}$ reading

$$\mathcal{H} = K(-kI) + \varphi(\psi, t)\cos(\psi + \psi_0) + \omega I \tag{10.22}$$

depends on time through $\varphi(\psi, t)$ and $\psi_0(\psi, t)$. For simplicity, assume that the wave group velocity is much greater than the particle velocity and the wave phase velocity and thus, φ and ψ_0 can be approximated as functions of time only.

First let us analyze the phase portrait of the dynamical system governed by $\mathcal{H}$. Instead of using the canonical variables (I, ψ), we will consider the phase space in coordinates I and $\theta = \psi + \psi_0$. The stationary points of this system correspond to the wave-particle resonances and read

$$\theta = \pi n, \qquad \partial\mathcal{H}/\partial I = \omega - kv(I) = 0, \tag{10.23}$$

where $v = \partial K/\partial p$ and n is an integer number. Assuming that $K(p)$ behaves like p^3, the dependence $\partial K/\partial p(p)$ is expected to behave like p^2 (Fig. 10.3). Let v_* be the minimum of $K(p)$ in the region of interest. Then, as illustrated in Fig. 10.3, for all waves with phase velocities in the range $v_* < v_{\rm ph} < v_* + \delta v$ for some $\delta v > 0$, there exist exactly two resonances I_1 and I_2 solving Eq. (10.23). Therefore, if the wave amplitude is sufficiently small, two chains of islands in vicinities of I_1 and I_2 are formed as shown in Fig. 10.4a. As the wave amplitude grows, the widths of the

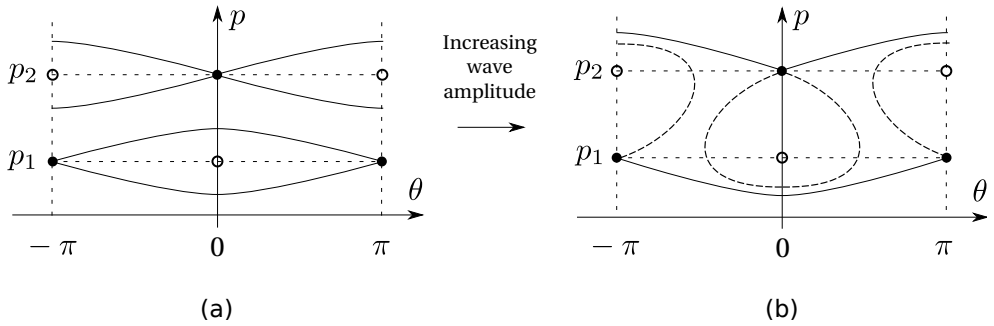

Figure 10.4: Two different topologies of the phase space for the wave-particle interaction problem. Stable stationary points (circles), unstable stationary points (solid disks) and system separatrices (lines) are shown: (a) $\varphi < \varphi_*$, (b) $\varphi > \varphi_*$.

islands increase until two chains merge together (Fig. 10.4b). The transition between two different topologies of the system phase portrait occurs when the values of $\mathcal{H}$ calculated for both separatrices become equal. The corresponding wave amplitude $\varphi = \varphi_*$ is then given by

$$2\varphi_* = K(p_2) - K(p_1) + (p_2 - p_1)\omega/k, \tag{10.24}$$

where $p_i = -kI_i$.

Before proceeding to the analysis of the particle dynamics, let us introduce a function $\alpha_i(\varphi) = \langle I \rangle$ to each separatrix s_i, where $\langle x \rangle = \int_0^{2\pi} x\, d\theta$. The separatrices are assigned indicies as follows. If $\varphi < \varphi_*$, the four separatrices are assigned numbers 1 through 4 in such a way that $\alpha_i(\varphi) < \alpha_j(\varphi)$ for all $i < j$ (Fig. 10.4a). For $\varphi > \varphi_*$, the separatrices are assigned indices 1 and 4 with $\alpha_1(\varphi) < \alpha_4(\varphi)$ (Fig. 10.4b). Note that the integration in the case $\varphi > \varphi_*$ should be performed along the parts of the separatraix shown in Fig. 10.4b with solid lines, avoiding the loops shown with dashed lines.

Now consider the dynamics of a particle interacting with a finite-width wave packet, *i.e.,* assume that $\varphi(t) \to 0$ for $|t| \to \infty$. In the following, we will also

assume that $\varphi(t)$ is "bell-shaped", *i.e.,* $\dot{\varphi} > 0$ for $t < t_m$ and $\dot{\varphi} < 0$ for $t > t_m$, where $t_m = \mathrm{argmax}_t\, \varphi(t)$. The single particle trajectory at $t = -\infty$ is then characterized by $I = I_0 = \mathrm{const}$. As the wave amplitude experienced by the particle grows, the particle momentum starts oscillating. However, if the wave packet is sufficiently smooth, the adiabatic invariant $J = \int_0^{2\pi} I\, d\theta$ is approximately conserved. Therefore, before the particle trajectory crosses one of the separatices, $\langle p \rangle = -kI_0$ is satisfied.

Choosing $I_0 < I_1$, we say that the particle is initialized in the state 1, meaning that the particle is expected to cross the separatrix s_1 first. If $\min_t \alpha_1[\varphi(t)] > I_0$, the particle will never cross the first separatrix (or any other) and the final state of the particle will be characterized by $I = I_0$. We then say that in this case, the particle ends up in the same state 1, undergoing transition $1 \to 1$. In the following, we will consider the case $\min_t \alpha_1[\varphi(t)] < I_0$, when the particle trajectory crosses at least one separatrix. To avoid confusion, we will enumerate all possible scenarios.

1. Let t_a be the smallest value of t, for which $\alpha_1[\varphi(t)] = I_0$ and let $\varphi_a = \varphi(t_a)$. Assume first that $\varphi_a < \varphi_*$, *i.e.,* that the particle becomes trapped by the lower island before it is merged with the upper island. In this case, two scenarios are possible.

   (a) In the first scenario, $\varphi_m = \max_t \varphi(t) < \varphi_*$, what means that the island chains remain separated at all times. While being trapped, the adiabatic invariant $J = \int I\, d\theta$ of the particle calculated over the *closed trajectory* is conserved. Noticing that J is identical to the phase space volume encircled by the trajectory, one concludes that the particle will remain trapped in the wave until the volume of the island[3] V_1^i shrinks to its initial value

[3]The volume of the island is defined as the volume contained between two separatrices.

observed upon the particle trapping. Then, by analogy with Refs. [Cary et al., 1986; Bruhwiler and Cary, 1992], one expects that the particle can detrap from the island crossing either s_1 (final state 1) or s_2 (final state 2). In the former case of the $1 \to 1$ transition, the final particle state is $I = I_0 = \alpha_1(\varphi_a)$ and in the latter case of the $1 \to 2$ transition, the final state is $I = \alpha_2(\varphi_a)$ because after the particle detraps, $\langle I \rangle$ stays constant. If the wave profile is sufficiently long, the probabilities of finding a particle in one of the final states are approximately 1/2 and 1/2. The described sequence of transitions is shown in Fig. 10.5a.

(b) Now consider the second scenario, in which $\varphi_m = \max_t \varphi(t) > \varphi_*$, *i.e.,* the islands merge while the particle is trapped in one of the islands. In this case, the particle trajectory behaves exactly like in the previous scenario 1a up until the moment of time, when $\varphi(t) = \varphi_*$. After two island chains are merged, the particle trajectory ends up inside the upper loop shown with dashed lines in Fig. 10.4. While the wave amplitude increases further, the loop volume decreases and the phase space volume of the trajectory J is conserved. There are two possibilities of the particle trajectory evolution at this point:

i. In the first case, the particle trajectory does not detrap from the loop until the islands merge again, *i.e.,* the loop volume V_1^l is larger[4] than J even at φ_m. After the islands separate when $\varphi(t)$ falls back to φ_*, the particle trajectory becomes trapped between separatrices s_1 and s_2 again (Fig. 10.5b). This means that like in the previous scenario,

[4]The phase space volume of the loop decreases with φ.

two possible transitions are $1 \to 1$ (with the final $I = I_0$) and $1 \to 2$ (with the final $I = \alpha_2(\varphi_a)$). This scenario is illustrated in Fig. 10.5b.

ii. Now consider the scenario, in which the particle detraps from the loop at $\varphi > \varphi_*$ (Fig. 10.5c). After the particle detraps at $\varphi = \varphi_x$, it becomes passing and it remains confined in the resonance region until the wave amplitude starts decreasing. Then, once the wave amplitude falls to φ_x, the particle can either become trapped in the loop again, or intersect the separatrix s_4. The probabilities of these transitions can be determined by comparing times that the particle spends on the separatrix (shown with a solid line in Fig. 10.5c) and on the loop (shown with a dashed line). Here we consider the former case. After becoming trapped in the loop, the particle follows the same path as in the previous scenario (after φ falls down to φ_*, the particle becomes trapped in the lower island, eventually detrapping from it), ending up in one of two final states: 1 and 2 (with roughly the same probabilities). This scenario is illustrated in Fig. 10.5c.

iii. Just like in the previous scenario, assume that the particle detraps from the loop at $\varphi > \varphi_*$, but then, as the wave amplitude falls down to φ_x, it crosses the separatrix s_4 (Fig. 10.6a). In this case, the final state of the particle is 4 and the final $I = \alpha_4(\varphi_x)$. This scenario is illustrated in Fig. 10.6a.

2. Now consider the case, in which the particle becomes trapped by the wave after two island chains merge together, *i.e.,* $\alpha_1(\varphi) = I_0$ is satisfied for $\varphi > \varphi_*$. After becoming trapped, the particle follows a periodic trajectory, conserving the adiabatic invariant $J = \langle I \rangle$ (Fig. 10.6b). As the wave amplitude increases,

Table 10.1: Possible scenarios of the negative-mass particle dynamics in the wave field.

scenario	conditions	figures	transitions
(A)	$\max_t \varphi(t) < \varphi_*$	Fig. 10.5a	$1 \to 1, 2$
(B)	$\varphi_a < \varphi_*$, $V_1^i(\varphi_a) > \min_t V_1^l[\varphi(t)]$	Fig. 10.5b	$1 \to 1, 2$
(C)	$\varphi_a < \varphi_*$, $V_1^i(\varphi_a) < \min_t V_1^l[\varphi(t)]$	Figs. 10.5c, 10.6a	$1 \to 1, 2, 4$
(D)	$\varphi_a > \varphi_*$	Figs. 10.6b, 10.6c	$1 \to 1, 3, 4$

the particle becomes more deeply trapped, eventually detrapping only when φ falls down to φ_a. At this moment, two scenarios are possible:

(a) In the first scenario, the particle detraps crossing the separatrix s_1. The probability of this outcome is proportional to the ratio of times spent on the separatrix to the total time spent on the seperatrix and the loop. In this case, the final state of the particle is 1 with $I = I_0$. This scenario is illustrated in Fig. 10.6b.

(b) In the second scenario, after φ falls down to φ_a, the particle becomes trapped in the lower loop (Fig. 10.6c). As the wave amplitude decreases, the particle remains trapped in this loop and once φ falls down to φ_*, the trajectory is confined within the higher island. Therefore, in the end, the particle detraps from the wave through one of the two separatrices: s_3 or s_4 (again, with equal probabilities). In the former case, we say that the final state is 3 with $I = \alpha_3(\varphi_b)$, while in the latter case, the final state is 4 with $I = \alpha_4(\varphi_b)$, where φ_b solves $V_2^i(\varphi_b) = V_2^l(\varphi_a)$ with $V_2^i(\varphi)$ being the phase space volume of the upper island and $V_2^l(\varphi)$ is the volume of the lower loop.

All possible particle trajectories discussed above are outlined in Table 10.1. Assuming that the low-energy state with $v = 0$ corresponds to the state 4, one could be interested in identifying the scenrio with the largest probability of the transition $1 \to 4$. Two scenarios, in which this transition can be observed are the cases (C) and (D) (see Table 10.1). The rough estimate for the probability of the transition $1 \to 4$ in the case (C) is $T_2^s/(T_2^s + T_2^l)$, where T_2^s is the time particle spends near the upper separatrix shown with a solid line in Fig. 10.6a and T_2^l is the time particle spends near the upper loop when the particle detraps, *i.e.,* at $\varphi = \varphi_b$ solving $V_1^l(\varphi_b) = V_1^i(\varphi_a)$. Note that the probability of the transition $1 \to 4$ can be increased in this case by decreasing T_2^l, *i.e.,* by decreasing the amplitude φ_a, for which the particle becomes trapped by the wave[5].

The probability of the transition $1 \to 4$ in the scenario (D) is given by $(1/2)T_1^s/(T_1^s + T_1^l)$, where T_1^s is the time particle spends near the lower separatrix shown with a solid line in Fig. 10.6c and T_1^l is the time particle spends near the lower loop when the particle detraps, *i.e.,* at $\varphi = \varphi_b$ solving $V_2^l(\varphi_b) = V_2^i(\varphi_a)$. Note that this probability is expected to be smaller than the porbability of the transition $1 \to 4$ in the previous case (C).

[5]Lower φ_a means lower V_1^i and higher φ_b solving $V_1^l(\varphi_b) = V_1^i(\varphi_a)$.

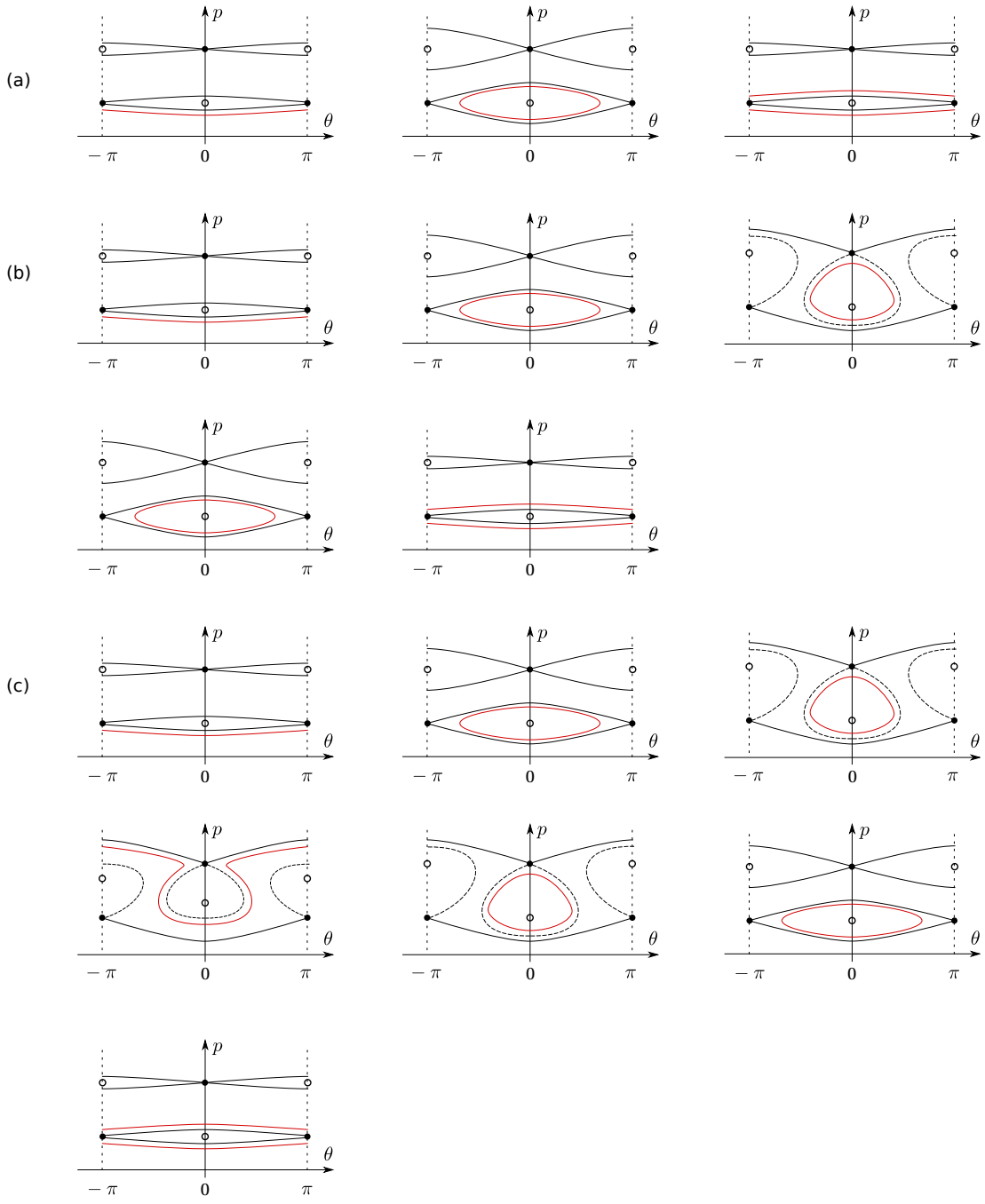

Figure 10.5: Possible scenarios of the negative-mass particle dynamics in the wave fields: (a) scenario (A) in Table 10.1; (b) scenario (B) and (c) one of the possibilies for the trajectory dynamics in scenario (C).

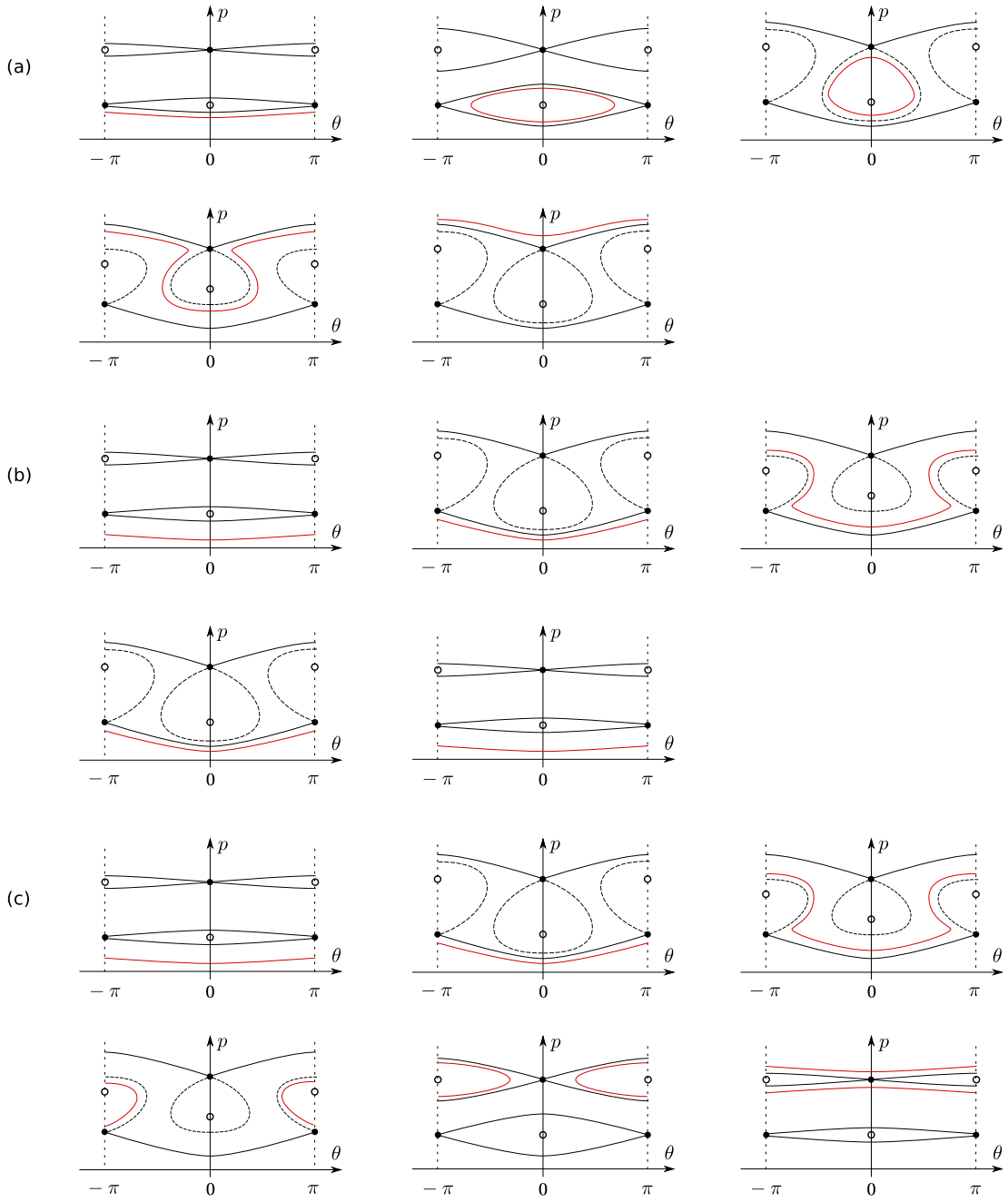

Figure 10.6: Possible scenarios of the negative-mass particle dynamics in the wave field: (a) one of the possibilities for the trajectory dynamics in scenario (C) in Table 10.1; (b) and (c) depict the scenario (D).

Chapter 11

Conclusions and Future Work

In this chapter, the main results of the thesis are summarized, and possible directions of further research in the course of the thesis topic are presented.

11.1 Conclusions

This thesis is dedicated to two different manifestations of resonant wave-particle interaction, occuring in systems with resonances located close (α-channeling) or far (negative-mass effect) from each other. The research described in this thesis deepens the knowledge of the phenomena themselves and also the possibilities and difficulties in applying these effects in real-life physical systems. Below, the list of main results of the dissertation grouped by the chapter in which they are obtained is presented.

Chapter 2

- Analytical treatment of the wave-particle interaction in the presence of the inhomogeneous background magnetic field is presented. Relations between diffusion path characteristics and rf region parameters are established. As a result, the

systems of rf regions suitable for the α-channeling implementation in two mirror machine designs are proposed.

- The possibility of extracting more than 60% of the total trapped α particle energy on a time much smaller than the characteristic collisional time is simulated in one of the optimized device designs.

- It is demonstrated that the waves proposed for α-channeling are not expected to perturb the background plasma significantly. The possibility of using α-channeling waves for injecting and heating the fuel ions is shown.

Chapter 3

- An optimization problem of flux rearrangement in a rectangular network of intersecting diffusion paths is formulated. A system of algebraic equations describing the stationary particle distribution in a rectangular network of thin diffusion paths is derived.

- An analogy between the diffusion flux rearrangement problem and a similar problem of current rearrangement in an electrical network of one-dimensional conductors is demonstrated.

- The formulated optimization problem is solved by showing that the minimum of the optimized functional is reached asymptotically in a system of paths with diffusion coefficients equal to 1, β, β^2, β^3 and β^4 as β goes to infinity.

- Numerical methods capable of identifying the minima of more general optimization functionals in the presence of limitations on system parameters are proposed. Supplementary calculations necessary for implementing such methods are presented.

Chapter 4

- A dynamical system describing the evolution of the α-channeling mode in the presence of wave damping is presented. It is shown that excitation of localized weakly-damped modes can be more advantageous (particularly if the device fusion reactivity is not sufficiently high) for α-channeling implementation compared to the excitation of waves fully damped in a resonance region.

- An algorithm for searching the parameter space for weakly-damped modes localized in the device interior is proposed. After applying this algorithm to two mirror machine designs, three waves suitable for α-channeling implementation in mirror machines, namely the fast Alfvén wave (propagating across the magnetic field), the shear Alfvén wave and the ion Bernstein wave (propagating along the magnetic field), are identified in both device designs.

Chapter 5

- It is demonstrated that by injecting minority ions resonant with the α-channeling wave, a significant fraction of the wave energy can be redirected to heating of the minority ions, which acting as a catalyst, eventually forward their energy to colder fuel ions through collisions.

- It is shown that a fraction of the energy extracted from α particles in the central cell can be used to heat plasmas in the device plugs. Specifically, the α-channeling mode gaining energy in the central cell is predicted to be stabilizied by only weak wave damping in the plug (with properly chosen parameters).

Chapter 6

- A possibility of using currently available experimental devices for studying the α-channeling modes and demonstrating the α-channeling effect is demonstrated. Specifically, modifications of the recent experiments on the Large Plasma Device (LAPD) [Gekelman et al., 1991] capable of showing the existance of the localized fast Alfvén waves and demonstrating the core principles of the α-channeling technique, are proposed.

Chapter 7

- For a classical particle undergoing nonlinear interaction with a wave in dielectric medium, a perturbation theory is developed, showing that the particle motion can be described in terms of an effective parallel mass which can become negative.

- A relativistic particle interacting with a circularly polarized wave and a static magnetic field is studied as an example. For the three stationary orbits corresponding to the same velocity parallel to the magnetic field, the conditions are found under which all these equilibria are centerlike, or neutrally stable.

- It is shown that a negative parallel mass is realized in the vicinity of the intermedate-energy equilibrium, and a plasma collective instability of a new type is identified.

Chapter 8

- It is shown that the effect of radiation friction can be included in the Hamiltonian treatment of wave-particle interactions with autoresonant phase-locking, yielding a generalized canonical approach to the problem of dissipative dynamics near a nonlinear resonance.

- As an example, equations governing the dynamics of a charged particle in a pump wave and a static magnetic field in the presence of the friction force due to cyclotron radiation are derived. Particles with negative parallel masses $m_{\parallel}$ are shown to transfer their kinetic energy to the pump wave, thus amplifying it. Counterintuitively, such particles are also predicted to undergo "stable" dynamics, decreasing their transverse energy monotonically due to cyclotron cooling, whereas some of those with positive $m_{\parallel}$ are predicted to undergo cyclotron heating instead, extracting energy from the pump wave.

Chapter 9

- The approach to including stochastic perturbations in the canonical formalism for a broad class of resonant Hamiltonian systems similar to those yielding NME is proposed. Specifically, the stochastic system evolution is modelled with the Fokker-Planck equation, the coefficients of which are expressed through the statistical properties of the external noise.

- Considering a charged particle interacting with a pump wave in a static magnetic field, the diffusion coefficient and the drag terms caused by the particle collisions with the cold background plasmas are derived.

Chapter 10

- The response of a particle initialized near the extremum of the $v(p)$ dependence to the external wave with frequency ω_p is shown to occur at the second harmonic of the wave frequency.

- It is predicted that by slowly changing the laser wave frequency and amplitude, one can control the group velocity of electrostatic waves propagating in plasmas

with negative-mass particles. A conceptual possibility of making this group velocity vanish is demonstrated.

- Considering a negative-mass particle in the field of a resonant low-frequency adiabatic electrostatic wave, it is demonstrated that depending on the peak wave amplitude and wave phase velocity, four different scenarios, each characterized by different final particle states, are possible. It is shown that two of these scenarios can be used to transport particles between the states with $v = 0$ and the one scenario with the largest probability of such a transition is identified.

11.2 Future Work

Our studies of the α-channeling technique implementaion and the negative-mass effect deepend our understanding of the resonant wave-particle interaction and the ways this physical phenomenon can be used for phase-space engineering. However, at the same time, a number of new research directions are suggested. The analysis of the α-channeling technique, performed in this thesis, outlines numerous approaches to the possible practical implementaions of this method. On the other hand, our studies of the negative-mass effect provide a ground for finding similar phenomena in other physical systems and suggest numerous unusual manifestations of this effect, which could have a significant practical value. Several objectives following from our research immediately are indicated:

1. Identify new analytical and numerical approaches to the calculation of the α-channeling mode structure. Simulate α particle dynamics in the full three-dimensional wave field and propose specific mirror machine designs, which could benefit from the α-channeling implementation.

2. Design physical experiments for the LAPD device and possibly other existing mirror machines, which could demonstrate the possibility of exciting the α-channeling waves as well as the α-channeling effect itself.

3. Propose experiments, which could verify the possibility of using minority ion injection for redirecting energy from the α-channeling wave to the background fuel ions. Identify ways of applying the minority ion injection technique in tokamaks, potentially extending the choice of waves, which could be used for α-channeling in toroidal devices. Using numerical codes capable of calculating mode structure, show that the efficient energy transfer between two localized modes is indeed possible by a careful choice of the wave and plasma parameters.

4. Apply the formalism developed in Chapters 7, 8 and 9 to studying the nonlinear resonance in various dynamical systems of physical interest. Identify phenomena similar to the negative-mass effect in other physical systems.

5. Design physical experiments, which could potentially demonstrate various manifestations of the NME, including such effects as negative-mass instability, frequency-doubling, group velocity manipulation and maser-like wave amplification in the excited medium. Develop new numerical codes and use them to simulate these physical phenomena, studying their practical usability and identifying possible parasitic effects.

Appendix A

Perturbation Theory Approach to Nonlinear Resonance

The resonance between different degrees of freedom of a physical system can be understood using the Hamiltonian perturbation theory. The unperturbed integrable dynamical system (with non-interacting degrees of freedom) is generally described by a Hamiltonian $H_0(\boldsymbol{J})$, where $\boldsymbol{J}$ are the action variables canonically conjugate to the cyclic coordinates θ called the system angles. Examples of such unperturbed systems include a classical nonlinear oscillator, a charged particle moving in a homogeneous or inhomogeneous magnetic field or a molecule with internal degrees of freedom. Along with the particle coordinates and momenta, the unperturbed Hamiltonian may also include degrees of freedom corresponding to the wave fields, namely the wave actions measuring the number of quanta in different modes and angles corresponding to the wave phase. Now consider a weak perturbation to the system Hamiltonian depending on angles $\boldsymbol{\theta}$ and thus leading to the coupling of different degrees of freedom. Let

$\boldsymbol{\Omega}(\boldsymbol{J}) = \dot{\boldsymbol{\theta}} = \partial H/\partial \boldsymbol{J}$ be the unperturbed frequencies. According to the KAM theory [Lichtenberg and Lieberman, 1992], for sufficiently small perturbation amplitude, most particle trajectories remain regular and periodic. However, in a small vicinity of each resonance satisfying $\boldsymbol{\ell} \cdot \boldsymbol{\Omega} = 0$ for some integer vector $\boldsymbol{\ell}$, the stochastic regions within which the particles exhibit chaotic behavior are formed.

Depending on the regularity of particle trajectories, all wave-particle manipulation techniques discussed above can be roughly divided to two large classes. In the physical systems belonging to the first class, the resonance islands formed in a vicinity of each resonance [Lichtenberg and Lieberman, 1992] are located sufficiently far from each other and do not overlap. In this case, the particle motion within the resonance island is regular, becoming chaotic only when approaching the island separatrix. Considering dynamics of a particle trapped near the center of an island, one observes that the adiabatic invariant associated with this motion is conserved if the system parameters are allowed to vary slowly. As a result, the system "sticks" to the resonance and even if the parameters are changed substantially, the particle remains deeply-trapped within the island. This effect is called an "autoresonance" [Kolomenskii and Lebedev, 1963] and it is employed in a wide variety of practical techniques including particle acceleration and current drive and plasma control.

The second class of phenomena emerges in dynamical systems, in which the resonance surfaces are so close to each other that a single stochastic volume is formed. Therefore, instead of being trapped in a single resonance for a long time, the resonant particle now exhibits a random walk within the whole stochastic region. Assuming that there are no regions of regular motion within the volume, the particle distribution dynamics can generally be approximated by the Fokker-Planck equation, which is shown to take a form of a quasilinear diffusion equation [Kaufman and Nakayama,

1970; Kaufman, 1971]. The quasilinear diffusion is generally employed to describe particle heating in fusion devices [Stix, 1958; Kesner, 1978; Bernstein and Baxter, 1981]. However, only recently it was realized that this phenomenon can also be used for phase-space engineering. The selective nature of the wave-particle interaction allows one to arrange localized diffusion regions within the problem phase space. As a result, in the presence of the particle population inversion across such a region, the diffusive particle flows emerge, which by a careful choice of wave parameters can be highly beneficial [Fisch and Rax, 1992].

Appendix B

Analytical Estimates for Diffusion Path Characteristics

In this appendix, we derive Eqs. (2.5)-(2.8) and discuss higher-order terms appearing in these equations due to magnetic field inhomogeneity. Consider a charged particle in an inhomogeneous magnetic field with $\boldsymbol{B} = \boldsymbol{r}B_z'(z)/2 + B_z(z)\hat{\boldsymbol{z}}$, which interacts with an electrostatic wave defined by the scalar potential φ reading

$$\varphi \approx f_0(r,z)\mathrm{Re}\, e^{-i\phi} \tag{B.1}$$

where the wave phase ϕ satisfies $\partial\phi/\partial\tau = \omega$, $\partial\phi/\partial\psi = -m$, $\partial\phi/\partial z = -k_z$ and $\partial\phi/\partial r = -k_r$. In the following, we will omit the operator Re. Introducing the particle gyro-center position $\boldsymbol{R} = \boldsymbol{r} + \boldsymbol{u}\times\boldsymbol{b}/b^2$, one can use equations of particle motion (2.4) to derive the equation on $\boldsymbol{R}$:

$$\dot{\boldsymbol{R}} = \dot{\boldsymbol{r}} + \dot{\boldsymbol{u}}\times\boldsymbol{b}/b^2 + \boldsymbol{u}\times\Big((\boldsymbol{u}\nabla)(\boldsymbol{b}/b^2)\Big) = \\ = u_\parallel\hat{\boldsymbol{b}} - \frac{\nabla f_0\times\boldsymbol{b}}{b^2}e^{-i\phi} - \frac{i(\boldsymbol{k}\times\boldsymbol{b})f_0}{b^2}e^{-i\phi} + \boldsymbol{u}\times\Big((\boldsymbol{u}\nabla)(\boldsymbol{b}/b^2)\Big), \tag{B.2}$$

where $\boldsymbol{r}$ is the particle position and ϕ is the wave phase. The last term in Eq. (B.2) describes the curvature and the gradient drifts in an inhomogeneous magnetic field, while the second term is responsible for particle drifts due to the wave-particle interaction.

Choosing a local Cartesian coordinate system (x, y, z) in such a way that $\hat{\boldsymbol{z}}$ is directed along the device axis and $\hat{\boldsymbol{y}}$ is directed along the radius and introducing α as an angle between the magnetic field lines and $\hat{\boldsymbol{z}}$, one can express the local particle coordinates as:

$$x = \rho \cos\theta, \tag{B.3}$$

$$y = r_{\mathrm{gc}} - \rho \sin\theta \cos\alpha, \tag{B.4}$$

$$z = z_{\mathrm{gc}} + \rho \sin\theta \sin\alpha, \tag{B.5}$$

where θ is the gyrophase, ρ is the gyroradius and $(r_{\mathrm{gc}}, z_{\mathrm{gc}}, \psi_{\mathrm{gc}})$ are the gyrocenter coordinates in the cylindrical coordinate system. Noticing that $\hat{\boldsymbol{b}} = (-\sin\alpha, \cos\alpha, 0)$ and using $\boldsymbol{k} = (k_r, k_z, -m/r)$, one can then project Eq. (B.2) on the axes $\hat{\boldsymbol{r}} = \hat{\boldsymbol{y}}$, $\hat{\boldsymbol{z}}$ and $\hat{\boldsymbol{\psi}} = \hat{\boldsymbol{x}}$:

$$\dot{r}_{\mathrm{gc}} = -u_{\parallel} \sin\alpha - \frac{imf_0 e^{-i\phi} \cos\alpha}{rb} + O(\varepsilon^2, \chi\varepsilon), \tag{B.6}$$

$$\dot{z}_{\mathrm{gc}} = u_{\parallel} \cos\alpha + \frac{imf_0 e^{-i\phi} \sin\alpha}{rb} + O(\varepsilon^2, \chi\varepsilon), \tag{B.7}$$

$$\dot{\psi}_{\mathrm{gc}} = \frac{u_d}{r} - \frac{if_0 k_z \sin\alpha e^{-i\phi}}{rb} + \frac{if_0 k_r \cos\alpha e^{-i\phi}}{rb} - \frac{(\nabla f_0 \times \hat{\boldsymbol{b}})_{\psi} e^{-i\phi}}{rb} + O(\varepsilon^2, \chi\varepsilon), \tag{B.8}$$

where $u_d = (u_{\perp}^2/2 + u_{\parallel}^2)(\boldsymbol{b} \times \nabla b)_{\psi}/b^3$ is the magnetic drift velocity and $\chi = f_0/E$ together with $\varepsilon = \rho/L$ are small parameters. Given the guiding-center position, the particle coordinates can also be expressed in the cylindrical coordinate system rather

than the local Cartesian system as in Eqs. (B.3)-(B.5):

$$r = \sqrt{(r_{\rm gc} - \rho\cos\alpha\sin\theta)^2 + \rho^2\cos^2\theta}, \tag{B.9}$$

$$z = z_{gc} + \rho\sin\alpha\sin\theta, \tag{B.10}$$

$$\psi = \psi_{gc} - \arctan\left(\frac{\rho\cos\theta}{r_{\rm gc} - \rho\cos\alpha\sin\theta}\right). \tag{B.11}$$

The equation describing particle parallel velocity evolution can be obtained by projecting Eq. (2.4) on $\hat{\boldsymbol{b}}$:

$$\dot{u}_\parallel = -\frac{u_\perp^2}{2}\frac{b'}{b} - i(k_z\cos\alpha + k_r\sin\alpha)f_0 e^{-i\phi} - (\nabla f_0\cdot\hat{\boldsymbol{b}})e^{-i\phi} + O(\varepsilon^2,\chi^2). \tag{B.12}$$

For sufficiently weak waves, the change of the magnetic moment μ and the radial position R can be neglected while solving Eq. (B.12) inside the rf region. However, the first-order corrections to the evolution of the wave phase ϕ can be crucial if the rf region is thick and the magnetic field is nearly homogeneous. Using Eqs. (B.6)-(B.8), one can first find the equation on $\phi_{\rm gc} \equiv \phi[\boldsymbol{r}_{\rm gc}(\tau),\tau]$:

$$\dot{\phi}_{gc} \approx \omega - k_z u_\parallel\cos\alpha - k_r u_\parallel\sin\alpha - k_\psi u_d + \frac{k_\psi(\nabla f_0\times\hat{\boldsymbol{b}})_\psi e^{-i\phi}}{b} + O(\varepsilon^2,\chi^2). \tag{B.13}$$

where $k_\psi = m/r_{\rm gc}$. The equation on ϕ can then be obtained using Eqs. (B.9)-(B.11):

$$\phi \approx \phi_{\rm gc} - k_z\rho\sin\alpha\sin\theta + k_r r_{\rm gc} - k_r\sqrt{(r_{\rm gc} + \rho\cos\alpha\sin\theta)^2 + \rho^2\cos^2\theta} + \\ + m\arctan\left(\frac{\rho\cos\theta}{r_{\rm gc} + \rho\cos\alpha\sin\theta}\right), \tag{B.14}$$

or after expanding it in a small parameter $\rho/r_{\rm gc}$:

$$\phi = \phi_{\rm gc} + \delta\phi \approx \phi_{\rm gc} - k_z\rho\sin\alpha\sin\theta - k_r\rho\cos\alpha\sin\theta + k_\psi\rho\cos\theta, \tag{B.15}$$

where $\delta\phi$ is a a purely-oscillating function. Higher order terms in $\rho/r_{\rm gc}$ will introduce just small corrections to the particle motion.

Assuming that $\rho \ll r_{\rm gc} \ll L$, one can transform Eqs. (B.6), (B.12) and (B.13) by approximating $\sin\alpha \approx \alpha \approx rb'/2b$ and $\cos\alpha \approx 1$:

$$\dot{\mathfrak{r}}_{\rm gc} \approx -\frac{imf_0 e^{-i(\phi_{\rm gc}+\delta\phi)}}{r_{\rm gc} b}, \tag{B.16}$$

$$\dot{u}_\parallel \approx -\frac{u_\perp^2}{2}\frac{b'}{b} - \left(if_0 k_z - \frac{\partial f_0}{\partial z} - \frac{\partial f_0}{\partial r}\frac{r_{\rm gc} b'}{2b} \right) e^{-i(\phi_{\rm gc}+\delta\phi)}, \tag{B.17}$$

$$\dot{\phi}_{\rm gc} \approx \omega - k_z u_\parallel - k_r u_\parallel \frac{r_{\rm gc} b'}{2b} - k_\psi u_d + \frac{k_\psi}{b}\left(\frac{\partial f_0}{\partial r} - \frac{r_{\rm gc} b'}{2b}\frac{\partial f_0}{\partial z} \right) e^{-i(\phi_{\rm gc}+\delta\phi)}, \tag{B.18}$$

where $\mathfrak{r}_{\rm gc} = r_{\rm gc}/\sqrt{b}$ is an approximate constant of motion in the abscence of the wave, when a particle moves along the magnetic field line solving $dr/dz \approx -rb'/2b$. Finally, multiplying Eq. (2.4) by $\boldsymbol{u}$ and introducing $E = u^2/2$, one obtains:

$$\dot{E} = -i(\boldsymbol{u}\cdot\boldsymbol{k}) f_0 e^{-i\phi} + (\boldsymbol{u}\cdot\nabla f_0) e^{-i\phi}. \tag{B.19}$$

Near the resonance, $\phi_{\rm gc}$ does not contain rapidly-oscillating harmonics. The perturbation $\delta\phi$, on the other hand is oscillating with frequency Ω, what allows one to rewrite $e^{-i\phi}$ as:

$$\sum_{l\in\mathbb{Z}} e^{-i\phi_{\rm gc}} i^l J_l(\bar{k}\rho) e^{-il(\theta+\varkappa)}, \tag{B.20}$$

where J_l is the Bessel function of the first kind, $\bar{k} = \sqrt{k_\psi^2 + (\alpha k_z + k_r)^2}$ and $\varkappa = \arctan[(\alpha k_z + k_r)/k_\psi]$. Noticing that $\dot{\phi}_{\rm gc} \approx \omega - k_z u_\parallel$, one then concludes that $e^{-i\phi}$ contains harmonics with frequencies $\omega - k_z u_\parallel - l\Omega$. Since the resonance occurs near $\dot{\phi} = 0$, instead of considering all these harmonics, one can focus on the resonant terms only:

$$\dot{\mathfrak{r}}_{\rm gc} \approx -\frac{i^{\ell+1} m f_0 J_\ell(\bar{k}\rho) e^{-i\phi_\ell - i\ell\varkappa}}{r_{\rm gc} b}, \tag{B.21}$$

$$\dot{u}_\parallel \approx -\frac{u_\perp^2}{2}\frac{b'}{b} - \left(if_0 k_z - \frac{\partial f_0}{\partial z} - \frac{\partial f_0}{\partial r}\frac{r_{\rm gc} b'}{2b} \right) i^\ell J_\ell(\bar{k}\rho) e^{-i\phi_\ell - i\ell\varkappa}, \tag{B.22}$$

$$\tag{B.23}$$

$$\dot{\phi}_\ell \approx \omega - k_z u_\parallel - \ell\Omega - k_r u_\parallel \frac{r_{\rm gc} b'}{2b} - k_\psi u_d + \\ + \frac{k_\psi}{b}\left(\frac{\partial f_0}{\partial r} - \frac{r_{\rm gc} b'}{2b}\frac{\partial f_0}{\partial z}\right) i^\ell J_\ell(\bar{k}\rho) e^{-i\phi_\ell - i\ell\varkappa}, \quad \text{(B.24)}$$

$$\dot{E} \approx -f_0 \Bigg[i\left(k_\parallel u_\parallel - k_r u_\parallel \frac{r_{\rm gc} b' 2}{2b}\right) i^\ell J_\ell(\bar{k}\rho) + \\ + \frac{i^{\ell+1} Z}{2}\left(J_{\ell+1} e^{i\nu} + J_{\ell-1} e^{-i\nu}\right)\Bigg] e^{-i\phi_\ell - i\ell\varkappa}, \quad \text{(B.25)}$$

where ℓ is the resonance number, for which $\omega - k_z u_\parallel - \ell\Omega \approx 0$, $\nu = \arctan[(k_r + \alpha k_\parallel)/k_\psi]$, and $Z^2 = k_\psi^2 u_\perp^2 + (k_r u_\perp + \alpha k_\parallel u_\perp)^2$.

The system of equations (B.21)-(B.25) can be solved numerically to find the particle state dynamics. However, we will simplify this system further neglecting some higher-order terms and assuming that $k_r \ll k_\psi$:

$$\dot{\mathfrak{r}}_{\rm gc} \approx -\frac{i^{\ell+1} k_\psi f_0 J_\ell(k_\psi\rho) e^{-i\phi_\ell}}{b}, \quad \text{(B.26)}$$

$$\dot{u}_\parallel \approx -\frac{u_\perp^2}{2}\frac{b'}{b} - \left(i f_0 k_z - \frac{\partial f_0}{\partial z}\right) i^\ell J_\ell(k_\psi\rho) e^{-i\phi_\ell}, \quad \text{(B.27)}$$

$$\dot{\phi}_\ell \approx \omega - k_z u_\parallel - \ell\Omega - k_\psi u_d, \quad \text{(B.28)}$$

$$\dot{E} \approx -i^{\ell+1}\left(k_\parallel u_\parallel + \ell\Omega\right) f_0 J_\ell(k_\psi\rho) e^{-i\phi_\ell}. \quad \text{(B.29)}$$

Finally, introducing the unperturbed parallel velocity $u_{\parallel\,0}$ and $\delta \equiv u_\parallel - u_{\parallel\,0}$, one can rewrite these equations with respect to a new "times" z:

$$\delta' \approx -i^\ell J_\ell(k_\psi\rho)\frac{i f_0 k_z - \partial f_0/\partial z}{u_{\parallel\,0}} e^{-i\phi_\ell}, \quad \text{(B.30)}$$

$$\phi_\ell' \approx \frac{\omega - k_z u_{\parallel\,0} - \ell\Omega - k_\psi u_d}{u_{\parallel\,0}} - \frac{(\omega - \ell\Omega - k_\psi u_d)\delta}{u_{\parallel\,0}^2}, \quad \text{(B.31)}$$

$$\frac{d\mathfrak{r}}{dE} \approx \frac{m}{r_{\rm gc}\omega\Omega}, \quad \text{(B.32)}$$

$$\frac{dE}{d\delta} \approx \frac{\omega}{k_z}. \quad \text{(B.33)}$$

where X' denotes dX/dz.

Appendix C

One-Dimensional Model of the Particle Distribution Function

In this Appendix we show that a spatial scale of the particle density distribution in a rectangular network of thin diffusion paths greatly exceeds a characteristic diffusion path width. This fact allows us to employ a one-dimensional model for the distribution function, considering dependence only in the path direction.

Consider first the simplest network formed of two straight effectively one-dimensional diffusion paths intersecting at a right angle (Fig. C.1a). In steady state Eq. (3.1) reads

$$D_{xx}(x,y)\frac{\partial^2 f}{\partial x^2} + D_{yy}(x,y)\frac{\partial^2 f}{\partial y^2} = 0. \tag{C.1}$$

It is solved for the distribution function f in the domain comprised of two, horizontal and vertical narrow stripes, with widths w_h and w_v correspondingly. At one exit of each path (distances r_h and r_v apart from the intersection region) the particles are absorbed and $f = 0$, at the other two exits input particle flux densities are given, and since the problem is linear, one of the two can be taken equal to zero.

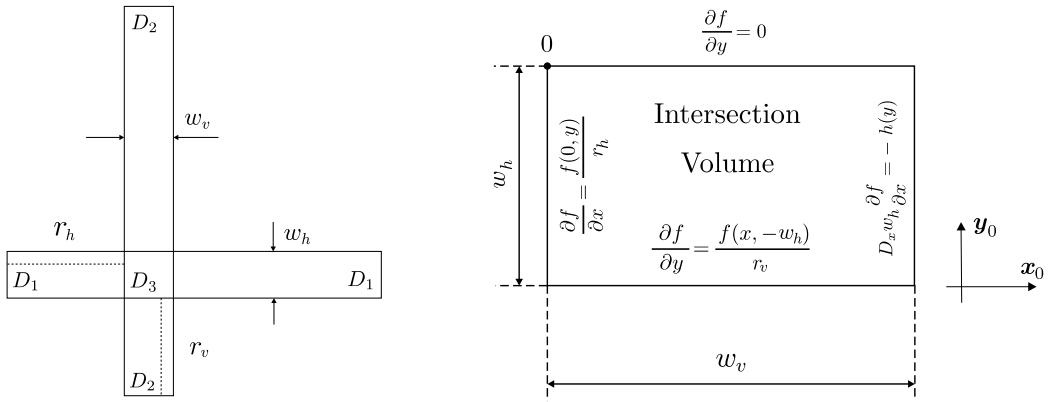

Figure C.1: (a) Two intersecting diffusion paths and their geometrical sizes; (b) intersection volume and the boundary conditions.

When the parameter μ, which is responsible for a weak transverse diffusion, is negligible, an approximate solution outside of intersection region reads: $f(x,y) = h_1(y) + h_2(y)x - \mu h_1''(y)x^2/(2D_x) - \mu h_2''(y)x^3/(6D_x) + O(\mu^2)$ for horizontal path, or $f(x,y) = h_1(x) + h_2(x)y - \mu h_1''(x)y^2/(2D_y) - \mu h_2''(x)y^3/(6D_y) + O(\mu^2)$ for vertical path, where h_1 and h_2 are arbitrary smooth functions with characteristic spatial scales $L_i = (h_i''/h_i)^{-1/2}$. Furthermore, when condition $(\mu/\min D_i)(\max l_i^2/\min L_i^2) \ll 1$, with l_i being a path length, is satisfied, the solution outside of the intersection region can be approximated by the leading order terms. Thus, the solution in the original domain might be obtained by solving the diffusion equation in the intersection volume with a new set of boundary conditions (see Fig. C.1b):

$$\left.\frac{\partial f}{\partial y}\right|_{y=0} \approx 0, \qquad D_x w_h \left.\frac{\partial f}{\partial x}\right|_{x=w_v} \approx -h(y), \tag{C.2}$$

$$\left.\frac{\partial f}{\partial y}\right|_{y=-w_h} \approx \frac{f(x,-w_h)}{r_v}, \qquad \left.\frac{\partial f}{\partial x}\right|_{x=0} \approx \frac{f(0,y)}{r_h}. \tag{C.3}$$

where $h(y)$ is the horizontal input flux density.

Equation (C.1) with boundary conditions (C.2) can be solved by separating variables:

$$f \approx \sum_{k=0}^{\infty} c_k \left[\left(1 + \frac{2}{\lambda_{xk} r_h - 1} \right) \exp(\lambda_{xk} x) + \exp(-\lambda_{xk} x) \right] \cos \lambda_{yk} y, \tag{C.4}$$

where c_k are constant coefficients, $\lambda_{xk} = \sqrt{\lambda_k / D_x}$, $\lambda_{yk} = \sqrt{\lambda_k / D_y}$, and λ_k is found from the equation:

$$\tan^{-1} \left(w_h \sqrt{\lambda_k / D_y} \right) = r_v \sqrt{\lambda_k / D_y}. \tag{C.5}$$

Assuming that the width of the horizontal path w_h is much smaller than the distance from the intersection volume to the particle sink r_v, Eq. (C.5) can be solved approximately:

$$\lambda_{y0} \approx \frac{1}{(r_v w_h)^{1/2}} \ll \frac{1}{w_h}, \tag{C.6}$$

$$\lambda_{yk} \approx \frac{\pi k}{w_h} + \frac{1}{r_v \pi k} \approx \frac{\pi k}{w_h}, \quad \text{for } k > 0. \tag{C.7}$$

The relation $\lambda_{y0} \ll \lambda_{yk}$ for $k > 0$ suggests that if the input flux density $h(y)$ is quasi-homogeneous, $c_k \ll c_0$. Neglecting the terms of order w_h / r_v, the fraction of the input particle flux absorbed at the left loss boundary is then given by:

$$\frac{J_{x=0}}{J_{x=w_v}} \approx \frac{1}{1 + \lambda_{x0}^2 w_v r_h} = \left(1 + \frac{D_y w_v r_h}{D_x w_h r_v} \right)^{-1} = \left(1 + \frac{D_y w_v r_h}{D_x w_h r_v} \right)^{-1}. \tag{C.8}$$

Thus, in a steady state regime, the net particle flux J incoming by the horizontal diffusion path divides into two outgoing fluxes J_h and J_v:

$$J_h \approx J \cdot \left(1 + \frac{D_y w_v r_h}{D_x w_h r_v} \right)^{-1}, \qquad J_v = J - J_h. \tag{C.9}$$

Particularly, when $D_y w_v r_h$ is much smaller or much larger than $D_x w_h r_v$, the major part of the input flux will be absorbed at the, whereas in a symmetric system with $D_y w_v r_h = D_x w_x r_v$, the input flux is divided into two equal fluxes.

Consider a network comprised of $\bar{n}$ horizontal and $\bar{m}$ vertical paths, and denote by $\boldsymbol{D}_x$ and $\boldsymbol{D}_y$ vectors of diffusion coefficients of horizontal and vertical diffusion paths correspondingly. The flux distribution in a such network is a sum of distributions in two simpler systems: (i) the system with zero vertical input fluxes and the horizontal input flux densities equal to $\boldsymbol{j}_x^i(y)$ and (ii) the system with zero horizontal input fluxes and the vertical input flux densities equal to $\boldsymbol{j}_x^i(y)$. The solution f_{ijk} in the intersection region formed by horizontal and vertical diffusion paths with indices i and j can be found in the form $f_{ijk} = X_{ijk}(x)Y_{ijk}(y)$, where X_{ijk} and Y_{ijk} satisfy

$$\frac{X''_{ijk}}{X_{ijk}} = \frac{\lambda_{ijk}}{D_{xi}}, \qquad \frac{Y''_{ijk}}{Y_{ijk}} = -\frac{\lambda_{ijk}}{D_{yj}}, \tag{C.10}$$

with k enumerating eigenfunctions and eigenvalues λ_{ijk}. For convenience, we assign the origin to the volume's left bottom corner.

Considering, for example, a system with zero vertical input fluxes, the vertical eigenfunctions $Y_{ijk}(y)$ can be found independently in each column as follows. Noticing that the intersection volumes on a vertical path are restricted to have the same horizontal structure, one concludes that λ_{ijk} for different values of i are connected through $\lambda_{ijk} = \lambda_{jk}D_{xi}$. Values of λ_{jk} can then be found using vertical boundary conditions simplified when μ is negligible: (a) boundary condition at the bottom intersection region:

$$Y'_{1jk}(0) = Y_{1jk}/b_j, \tag{C.11}$$

where b_j is the distance to the particle sink on the vertical path with index j; (b) zero input flux density condition at the top intersection region $Y'_{njk}(y_n) = 0$, and (c) conditions necessary to connect adjacent intersection volumes:

$$Y'_{i,j,k}(y_i) = Y'_{i+1,j,k}(0), \tag{C.12}$$

$$Y_{i+1,j,k}(0) - Y_{i,j,k}(y_i) = Y'_{i,j,k}(y_i)\Delta y_i = Y'_{i+1,j,k}(0)\Delta y_i, \tag{C.13}$$

where y_i is the width of the horizontal path with index i, and Δy_i is the distance between horizontal paths with indices i and $i+1$. These equations can be solved approximately when the vertical and the horizontal diffusion path widths x_i and y_j are much smaller than all distances between paths Δx_j, Δy_i and distances to the sinks a_i and b_j, by considering the leading zeroth-order terms in the expansion by small parameters $\varepsilon_i = \max\{x_i/\Delta x_j, x_i/a_j, y_i/\Delta y_j, y_i/b_j\}$. Assuming $\lambda_j y_i^2 D_{xi}/D_{yj} \ll 1$ and $\lambda_j > 0$ (which we later show to be consistent with our final result), we can use small-value expansions, as we did solving Eq. (C.5), to obtain a simplified equation for the zeroth eigenvalue λ_{j0}:

$$s_{i+1} = \frac{s_i}{1-s_i}\frac{D_{x,i+1}}{D_{x,i}}\frac{y_{i+1}}{y_i} + \frac{\Delta y_i}{b_j}\,\tau_{i+1}, \tag{C.14}$$

$$s_n = 1, \quad s_1 = \tau_1. \tag{C.15}$$

where $\tau_i = \lambda_{j0} D_{x,i} y_i b_j / D_{y,j}$. For any k, the solution for τ_k of this recursive scheme is of order of one when all equation parameters are of order of one, which suggests that all possible solutions for λ_{j0} are of order of $(yb)^{-1}$ and assumption used above holds. It can be proved that, in the general case, Eq. (C.14) has exactly n nonnegative and no negative solutions, which justifies the assumption $\lambda_j > 0$.

Once the eigenvalues λ_{j0} and corresponding eigenfunctions are calculated, the horizontal quasi-homogeneous input flux density can be decomposed by eigenfunctions of the rightmost vertical path. Quasi-homogeneity of the input flux density suggests that its decomposition is dominated by the zeroth eigenfunctions corresponding to eigenvalues λ_{j0}, because all other eigenfunctions oscillate a few times on a width of at least one of diffusion paths. Noticing that the decomposition of zeroth eigenfunction of one vertical diffusion path by eigenfunctions of the adjacent path contains just zeroth eigenfunctions to the zeroth order term in a small parameter $\varepsilon = \max \varepsilon_i$, one

can couple zeroth-order eigenfunctions of adjacent vertical diffusion paths and find an approximate solution everywhere in the system. Obtained solution is a linear combination of just zeroth eigenvalues (to the zeroth order in small parameters), which suggests that the spatial scale of the particle distribution function is much larger than the characteristic path width.

Appendix D

Time-Dependent Flow Separation

The flux rearrangement problem introduced and solved in Chapter 3 is formulated as a minimization of a linear combination of the outgoing fluxes for a *steady-state* solution of the diffusion equation (3.1). This problem was approached by showing that in the limit of thin diffusion paths, the solution in the original two-dimensional domain can be approximated by a solution of the diffusion equation on a system of intersecting one-dimensional paths. In Appendix C, this approximation was explained by considering first a system of two intersecting thin diffusion paths. Given the ingoing fluxes, the steady-state solution of the diffusion equation was obtained and the outgoing particles fluxes were calculated. In this appendix, we extend this analysis to the non-steady-state regime. Assuming arbitrary initial conditions "above" the intersection point (no particles are placed in between the intersection point and the particle sinks), the fraction of particles escaping horizontal and vertical sinks (over an infinite time) is calculated.

Consider a system of two semi-infinite diffusion paths intersecting at the right angle (see Fig. D.1). The geometrical notation for this system is taken identical to

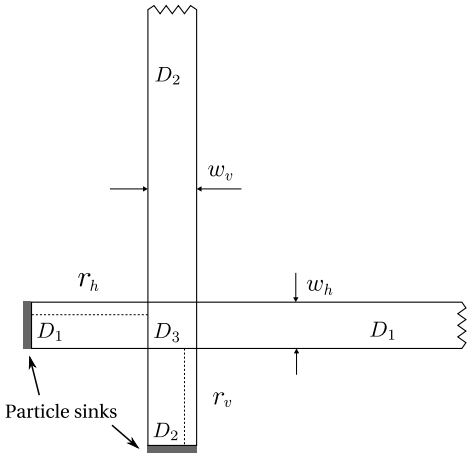

Figure D.1: The system of two intersecting semi-infinite diffusion paths. The geometrical notations is equivalent to the notation used in Appendix C. At $t = 0$, there are no particles in the intersection volume and between the volume and the particle sinks.

the notation used in Appendix C. Let f_1 and f_2 be the particle distributions on the horizontal and the vertical diffusion paths (outside of the intersection region) correspondingly. Following Appendix C, one can study particle diffusion in the limit $\tilde{w}_h \equiv w_h/r_v \ll 1$ and $\tilde{w}_v \equiv w_v/r_h \ll 1$. Replacing both paths with one-dimensional rays intersecting at the single point, one obtains the following diffusion equations for $f_1(x,t)$ and $f_2(y,t)$:

$$\frac{\partial f_1}{\partial t} = \frac{\partial}{\partial x}\left(D_1 \frac{\partial f_1}{\partial x}\right) = \frac{\partial J_1}{\partial x}, \tag{D.1}$$

$$\frac{\partial f_2}{\partial t} = \frac{\partial}{\partial y}\left(D_2 \frac{\partial f_2}{\partial y}\right) = \frac{\partial J_2}{\partial y}, \tag{D.2}$$

where J_1 and J_2 are particle flows along the diffusion paths. The boundary conditions imposed by the path intersection and the presence of sinks read

$$f_1(-r_h, t) = f_2(-r_v, t) = 0, \tag{D.3}$$

$$f_1(0,t) \approx f_2(0,t), \tag{D.4}$$

$$w_h\left[J_1(-0,t) - J_1(+0,t)\right] + w_v\left[J_2(-0,t) - J_2(+0,t)\right] \approx 0, \tag{D.5}$$

where the origin is chosen to be at the intersection point and we assume that both f_1 and f_2 vanish at infinity.

Consider diffusion in a system initialized with no particles between the intersection volume and the sinks, *i.e.,* let $f_1(x, t = 0) = 0$ for $x \leq 0$ and $f_2(y, t = 0) = 0$ for $y \leq 0$. Let $f(t)$ be the particle density at the intersection region. Since two segments $-r_h \leq x \leq 0$ and $-r_v \leq y \leq 0$ have the sinks and the intersection point as their boundaries, one can find particle distribution function on them at any moment of time if $f(t)$ is supplied. For convenience, the diffusion equation on both segments can be brought to a universal dimensionless form reading

$$\frac{\partial f_i}{\partial \tau_i} - \frac{\partial^2 f_i}{\partial z_i^2} = 0, \tag{D.6}$$

where $z_1 = x/r_h + 1$, $z_2 = y/r_v + 1$, $\tau_1 = tD_1/r_h^2$ and $\tau_2 = tD_2/r_v^2$. The total number of particles N_i escaping through each sink is then proportional to

$$w_h D_1 \int \frac{\partial f_1}{\partial x}(0, t)\, dt = w_h r_h \int_0^\infty \frac{\partial f_1}{\partial z_1}(0, \tau_1)\, d\tau_1 \tag{D.7}$$

for the horizontal path and

$$w_v D_2 \int \frac{\partial f_2}{\partial y}(0, t)\, dt = w_v r_v \int_0^\infty \frac{\partial f_2}{\partial z_2}(0, \tau_2)\, d\tau_2 \tag{D.8}$$

for the vertical path.

To proceed, make a Laplace transform of the dimensionless diffusion equation (D.6) [Cranck, 1975]:

$$p\bar{f}_i(z, p) = \frac{\partial^2 \bar{f}_i(z, p)}{\partial z^2}. \tag{D.9}$$

where

$$\bar{f}_i(z, p) \equiv \int_0^\infty e^{-p\tau_i} f_i(z, \tau_i)\, d\tau_i, \tag{D.10}$$

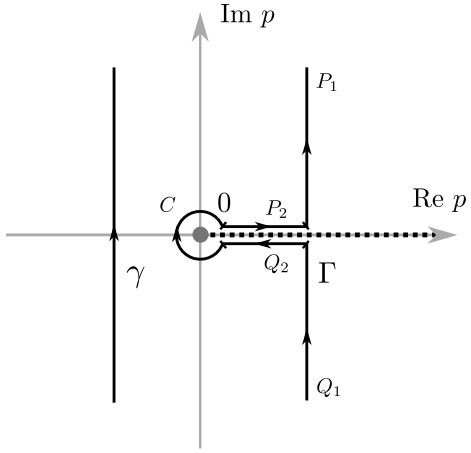

Figure D.2: Transformation of the contour of integration.

and p is a complex number. Solving Eq. (D.9) with the imposed boundary conditions reading $\bar{f}_i(0,p) = 0$ and $\bar{f}_i(1,p) = \bar{g}_i(p)$, one obtains

$$\bar{f}_i(z,p) = \frac{\bar{g}_i(p)(e^{\sqrt{p}z} - e^{-\sqrt{p}z})}{e^{\sqrt{p}} - e^{-\sqrt{p}}}, \tag{D.11}$$

where the square root is defined unambiguously by making a cut along the positive real axis (by saying that $\sqrt{x+i0} = \sqrt{x}$ and $\sqrt{x-i0} = -\sqrt{x}$ for real x). Substituting Eq. (D.11) in the expression for I_i, one obtains:

$$I_i = \frac{1}{2\pi i} \int_0^\infty \int_{\gamma-i\infty}^{\gamma+i\infty} \frac{2\bar{g}_i(p)\sqrt{p}}{e^{\sqrt{p}} - e^{-\sqrt{p}}} e^{p\tau_i}\, dp\, d\tau_i, \tag{D.12}$$

or after performing integration by τ_i:

$$I_i = -\frac{1}{2\pi i} \int_{\gamma-i\infty}^{\gamma+i\infty} \frac{2\bar{g}_i(p)}{\sqrt{p}(e^{\sqrt{p}} - e^{-\sqrt{p}})}\, dp, \tag{D.13}$$

where γ is an arbitrary negative real number.

If $\bar{f}(p)$ is analytic for Re $p \geq 0$, the integrand in Eq. (D.13) does not have singularities for Re $p > 0$ and goes to zero as Re p goes to infinity. Transforming the contour of integration as shown in Fig. D.2, one can therefore show that

$$I_i = -\frac{1}{2\pi i} \int_C \frac{2\bar{g}_i(p)}{\sqrt{p}(e^{\sqrt{p}} - e^{-\sqrt{p}})}\, dp, \tag{D.14}$$

where we noticed that the integrals over the paths P_1 and Q_1 vanish as Γ goes to infinity and that the integral over P_2 cancels with the integral over Q_2. Expanding the integrand near $p = 0$, one finally obtains:

$$I_i = -\frac{1}{2\pi i} \int_C \frac{\bar{g}_i(0)}{p}\, dp = \int g_i(\tau_i)\, d\tau_i, \tag{D.15}$$

where we recalled that $\bar{g}_i(0) = \int g_i(\tau_i)\, d\tau_i$. Substituting this expression in Eqs. (D.7) and (D.8), one finally obtains:

$$N_1 = \frac{D_1 w_h}{r_h} F, \qquad N_2 = \frac{D_2 w_v}{r_v} F, \tag{D.16}$$

where $F = \int f(t)\, dt$.

In conclusion, for any initial conditions non-zero "above" the intersection point, the particle flows are separated between two paths as:

$$\frac{N_1}{N_2} = \frac{D_1 w_h r_v}{D_2 w_v r_h}. \tag{D.17}$$

This expression can be verified by considering possible extreme regimes. For example, if D_1 or w_h go to zero, particles do not diffuse along the horizontal path in agreement with Eq. (D.17). Furthermore, Eq. (D.17) suggests that increasing r_h results in more particles escaping through the sink on the vertical path.

Bibliography

Aamodt, R. E. (1971). Particle containment in mirror traps in presence of fluctuating electric fields. *Phys. Rev. Lett.* **27**, 135.

Albert, J. M. (1993). Cyclotron resonance in an inhomogeneous magnetic field. *Phys. Fluids B* **5**, 2744.

Amagishi, Y., A. Tsushima, and M. Inutake (1982). Conversion of compressional Alfvén waves into ion-cyclotron waves in inhomogeneous magnetic-fields. *Phys. Rev. Lett.* **48**, 1183.

amd S. C. Chapman, J. W. S. C. and R. O. Dendy (2010). Electron current drive by fusion-product-excited lower hybrid drift instability. *Phys. Rev. Lett.* **105**, 255003.

Andresen, G. B., M. D. Ashkezari, M. Baquero-Ruiz, W. Bertsche, P. D. Bowe, E. Butler, P. T. Carpenter, C. L. Cesar, et al. (2011). Autoresonant excitation of antiproton plasmas. *Phys. Rev. Lett.* **106**, 025002.

Andreson, D. (1983). Distortion of the distribution function of weakly RF heated minority ions in a tokamak plasma. *J. Plasma Phys.* **29**, 317.

Arunasalam, V. (1976). Quasilinear theory of ion-cyclotron-resonance heating of plasmas and associated longitudinal cooling. *Phys. Rev. Lett.* **37**, 746.

Baldwin, D. E. (1977). End-loss processes from mirror machines. *Rev. Mod. Phys.* **49**, 317.

Baldwin, D. E., H. L. Berk, and L. D. Pearlstein (1976). Turbulent lifetimes in mirror machines. *Phys. Rev. Lett.* **36**, 1051.

Baldwin, D. E. and B. G. Logan (1979). Improved tandem mirror fusion reactor. *Phys. Rev. Lett.* **43**, 1318.

Barth, I., L. Friedland, E. Sarid, and A. G. Shagalov (2009). Autoresonant transition in the presence of noise and self-fields. *Phys. Rev. Lett.* **103**, 155001.

Bauer, D., P. Mulser, and W. H. Steeb (1995). Relativistic ponderomotive force, uphill acceleration, and transition to chaos. *Phys. Rev. Lett.* **75**, 4622.

Bellman, R. (2003). *Dynamic Programming.* Mineola, New York: Courier Dover Publications.

Berk, H. L., B. N. Breizman, and N. V. Petviashvili (1997). Spontaneous hole-clump pair creation in weakly unstable plasmas. *Phys. Lett. A* **234**, 213.

Bernstein, I. B. and D. C. Baxter (1981). Relativistic theory of electron cyclotron resonance heating. *Phys. Fluids* **24**, 108.

Berry, M. V. (1984). The adiabatic limit and the semiclassical limit. *J. Phys. A: Math. Gen.* **17**, 1225.

Birdsall, C. K. and J. R. Whinnery (1953). Waves in an electron stream with general admittance walls. *J. Appl. Phys.* **24**, 314.

Bogoliubov, N. N. and Y. A. Mitropolskii (1961). *Asymptotic Methods in the Theory of Nonlinear Oscillations.* New York: Gordon and Breach.

Bratman, V. L., N. S. Ginzburg, G. S. Nusinovich, M. I. Petelin, and V. K. Yulpatov (1979). Cyclotron and synchrotron masers. In A. V. Gaponov-Grekhov (Ed.), *Relativistic HF Electronics*, Volume 1, pp. 157. Gorky, U.S.S.R.: Institute of Applied Physics.

Brau, C. A. (1990). *Free-electron lasers*. Boston: Academic Press.

Breun, R., S. N. Golovato, L. Yujiri, B. McVey, A. Molvik, D. Smatlak, R. S. Post, D. K. Smith, and N. Hershkowitz (1981). Experiments in a tandem mirror sustained and heated solely by RF. *Phys. Rev. Lett.* **47**, 1833.

Brizard, A. J. and T. S. Hahm (2007). Foundations of nonlinear gyrokinetic theory. *Rev. Mod. Phys.* **79**, 421.

Bruhwiler, D. L. and J. R. Cary (1992). Particle dynamics in a large-amplitude wave packet. *Phys. Rev. Lett.* **68**, 255.

Bruhwiler, D. L. and J. R. Cary (1994a). Adiabatic particle motion in spatially-varying wave structures. *Part. Accel.* **43**, 195.

Bruhwiler, D. L. and J. R. Cary (1994b). Dynamics of particles trapping and detrapping in coherent wave-packets. *Phys. Rev. E* **50**, 3949.

Budker, G. I. and S. T. Belyaev (1958). Kineticheskoe uravnenie dlya elektronnogo gaza pri redkih stolknoveniyah. In M. A. Leontovich (Ed.), *Fizika Plazmy i Problema Upravlyaemykh Termoyadernykh Reaktsiĭ (Plasma Physics and the Problem of Controlled Thermonuclear Reactions)*, Volume 2, pp. 330. Moscow: Izd. ANSSSR. Translated into English (New York: Pergamon Press, 1959).

Burkhart, G. R., P. N. Guzdar, and M. E. Koepke (1989). Theoretical modeling of drift cyclotron loss-cone instability mode structures. *Phys. Plasmas* **1**, 570.

Burkhart, G. R., P. N. Guzdar, and R. G. Littlejohn (1988). Radial localization of drift cone and ion cyclotron loss cone modes. *Phys. Fluids* **31**, 2928.

Busnardo-Neto, J., J. Dawson, T. Kamimura, and A. T. Lin (1976). Ion-cyclotron resonance heating of plasmas and associated longitudinal cooling. *Phys. Rev. Lett.* **36**, 28.

Candel, A. and L. Conlon (2003). *Foliations II*. Providence, Rhode Island: American Mathematical Society.

Carter, T. A. (2011). The basic plasma science facility at UCLA: studies of the fundamental physics of plasma waves. In *Proceedings of the 19 Topical Conference on Radio Frequency Power in Plasmas*.

Cary, J. R., D. F. Escande, and J. L. Tennyson (1986). Adiabatic-invariant change due to separatrix crossing. *Phys. Rev. A* **34**, 4256.

Cary, J. R. and R. T. Skodje (1989). Phase-change between separatrix crossings. *Physica D* **36**, 287.

Cho, T., J. Kohagura, T. Numakura, M. Hirata, H. Higaki, H. Hojo, M. Ichimura, et al. (2006). Observation and control of transverse energy-transport barrier due to the formation of an energetic-electron layer with sheared $E \times B$ flow. *Phys. Rev. Lett.* **97**, 055001.

Clark, D. S. and N. J. Fisch (2000). The possibility of high amplitude driven contained modes during ion Bernstein wave experiments in the tokamak fusion test reactor. *Phys. Plasmas* **7**, 2923.

Clarke, J. F. (1980). Hot-ion-mode ignition in a tokamak reactor. *Nucl. Fusion* **20**, 563.

Conway, J. B. (1985). *A Course in Functional Analysis*. New York: Springer-Verlag.

Costa, L. F. and G. Travieso (2007). Exploring complex networks through random walks. *Phys. Rev. E* **75**, 016102.

Cranck, J. (1975). *The Mathematics of Diffusion*. Oxford: Clarendon Press.

Davydovskii, V. Y. (1963). Possibility of resonance acceleration of charged particles by electromagnetic waves in a constant magnetic field. *Sov. Phys. JETP* **16**, 629.

Dawson, J. M., H. P. Furth, and F. H. Tenney (1971). Production of thermonuclear power by non-maxwellian ions in a closed magnetic field configuration. *Phys. Rev. Lett.* **26**, 1156.

Delabaere, E. (1997). Unfolding the quartic oscillator. *Annals of Physics* **261**, 180.

Dewar, R. L. (1973). Oscillation center quasilinear theory. *Phys. Fluids* **16**, 1102.

Dodin, I. Y. and N. J. Fisch (2008a). Diffusion paths in resonantly driven Hamiltonian systems. *Phys. Lett. A* **372**, 6111.

Dodin, I. Y. and N. J. Fisch (2008b). Non-newtonian mechanics of oscillation centers. In P. K. Shukla, B. Eliasson, and L. Stenflo (Eds.), *Frontiers in Modern Plasma Physics: 2008 ICTP International Workshop on the Frontiers of Modern Plasma Physics*, Volume 1061 of *AIP Conference Proceedings*, Melville, NY, pp. 263. AIP.

Dodin, I. Y. and N. J. Fisch (2008c). Positive and negative effective mass of classical particles in oscillatory and static fields. *Phys. Rev. E* **77**, 036402.

Dodin, I. Y., A. I. Zhmoginov, and N. J. Fisch (2008). Manley-Rowe relations for an arbitrary discrete system. *Phys. Lett. A* **372**, 6094.

Dunn, K. and D. Bergman (1995). Self diffusion of nuclear spins in a porous medium with a periodic microstructure. *J. Chem. Phys.* **102**, 3041.

Emmert, G. A., L. A. El-Guebaly, G. L. Kulcinski, J. F. Santarius, I. N. Sviatoslavsky, and D. M. Meade (1994). Improvement in fusion reactor performance due to ion channeling. *Fusion Technol.* **26**, 1158.

Eriksen, K., I. Simonsen, S. Maslov, and K. Sneppen (2003). Modularity and extreme edges of the internet. *Phys. Rev. Lett.* **90**, 148701.

Fajans, J. and L. Frièdland (2001). Autoresonant (nonstationary) excitation of pendulums, plutinos, plasmas, and other nonlinear oscillators. *Am. J. Phys.* **69**, 1096.

Ferraro, R. D., R. G. Littlejohn, H. Sanuki, and B. D. Fried (1987). Nonlocal effects on the drift cyclotron loss cone dispersion relation in cylindrical geometry. *Phys. Fluids* **30**, 1115.

Fetterman, A. J. and N. J. Fisch (2008). Alpha channeling in a rotating plasma. *Phys. Rev. Lett.* **101**, 205003.

Fetterman, A. J. and N. J. Fisch (2010a). Alpha channeling in rotating plasma with stationary waves. *Phys. Plasmas* **17**, 042112.

Fetterman, A. J. and N. J. Fisch (2010b). Contained modes in mirrors with sheared rotation. *Phys. Plasmas* **17**, 112508.

Fetterman, A. J. and N. J. Fisch (2010c). Wave-driven rotation in supersonically rotating mirrors. *Fusion Sci. Technol.* **57**, 343.

Fetterman, A. J. and N. J. Fisch (2011a). The magnetic centrifugal mass filter. *Phys. Plasmas* **18**, 094503.

Fetterman, A. J. and N. J. Fisch (2011b). Wave-particle interactions in rotating mirrors. *Phys. Plasmas* **18**, 055704.

Feynman, R. P., R. B. Leighton, and M. Sands (1977). *The Feynman Lectures on Physics: Quantum Mechanics. Volume 1.* Reading, MA: Addison Wesley.

Fisch, N. J. (1987). Theory of current drive in plasmas. *Rev. Mod. Phys.* **59**, 175.

Fisch, N. J. (1997). Prospects for alpha channeling: Initial results from TFTR. In *Fusion Energy 1996 (Proc. 16th Int. Conf. Montreal, 1996)*, Volume 1, pp. 271. IAEA.

Fisch, N. J. (2000). Physics of alpha channelling and related TFTR experiments. *Nucl. Fusion* **40**, 1095.

Fisch, N. J. (2006). Alpha channeling in mirror machines. *Phys. Rev. Lett.* **97**, 225001.

Fisch, N. J. (2007). Alpha channeling in mirror machines and in tokamaks. *Fusion Sci. Technol. 51*(2T), 1.

Fisch, N. J. and M. C. Herrmann (1994). Utility of extracting alpha-particle energy by waves. *Nucl. Fusion* **34**, 1541.

Fisch, N. J. and M. C. Herrmann (1995). Alpha power channelling with two waves. *Nucl. Fusion* **35**, 1753.

Fisch, N. J. and J. M. Rax (1992). Interaction of energetic alpha-particles with intense lower hybrid waves. *Phys. Rev. Lett.* **69**, 612.

Fisch, N. J. and J. M. Rax (1993). Free energy in plasmas under wave-induced diffusion. *Phys. Fluids B* **5**, 1754.

Fowler, T. K. and M. Rankin (1966). Fusion energy balance in mirror machines. *J. Nucl. Energy* **C8**, 121.

Friedland, L. (1994). Spatial autoresonance cyclotron accelerator. *Phys. Plasmas* **1**, 421.

Friedland, L., P. Khain, and A. G. Shagalov (2006). Autoresonant phase-space holes in plasmas. *Phys. Rev. Lett.* **96**, 225001.

Furth, H. P. and D. L. Jassby (1974). Power amplification conditions for fusion-reactor plasmas heated by reacting ion-beams. *Phys. Rev. Lett.* **32**, 1176.

Gardiner, C. W. (2004). *Handbook of Stochastic Methods for Physics, Chemistry, and the Natural Sciences* (Third ed.). Berlin: Springer-Verlag.

Gekelman, W., H. Pfister, Z. Lucky, J. Bamber, D. Leneman, and J. E. Maggs (1991). Design, construction, and properties of the large plasma research device – the LAPD at UCLA. *Rev. Sci. Instr.* **62**, 2875.

Gorelenkov, N. N., N. J. Fisch, and E. Fredrickson (2010). On the anomalous fast ion energy diffusion in toroidal plasmas due to cavity modes. *Plasma Phys. Control. Fusion* **52**, 055014.

Goto, T., K. Ishii, Y. Goi, N. Kikuno, Y. Katsuki, M. Yamanashi, M. Nakamura, M. Ichimura, T. Tamano, and K. Yatsu (2000). Ion diffusion in a velocity space induced by Alfvén ion cyclotron mode observed in a mirror plasma. *Phys. Plasmas* **7**, 2485.

Grawe, H. (1969). A stochastic model of electron cyclotron heating. *Plasma Physics* **11**, 151.

Hanson, J. D. and E. Ott (1984). An alpha-particle-driven Alfvén wave instability in a tandem mirror reactor. *Phys. Fluids* **27**, 150.

Hellén, E., J. Ketoja, K. Niskanen, and M. Alava (2002). Diffusion through fibre networks. *J. Pulp and Paper Sci.* **28**, 55.

Hizi, U. and D. Bergman (2000). Molecular diffusion in periodic porous media. *J. Appl. Phys.* **87**, 1704.

Intrator, T., S. Meassick, J. Browning, R. Majeski, J. R. Ferron, and N. Hershkowitz (1989). Measurements of electromagnetic waves in Phaedrus-B: Bench-mark test of ANTENA wave field calculations. *Nucl. Fusion* **29**, 377.

Jassby, D. L. (1977). Neutral-beam-driven tokamak fusion reactors. *Nucl. Fusion* **17**, 309.

Karimabadi, H., K. Akimoto, N. Omidi, and C. R. Menyuk (1990). Particle acceleration by a wave in a strong magnetic field: Regular and stochastic motion. *Phys. Fluids B* **2**, 606.

Karney, C. F. F. (1979). Stochastic ion heating by a lower hybrid wave: II. *Phys. Fluids* **22**, 2188.

Karney, C. F. F. (1986). Fokker-planck and quasi-linear codes. *Comp. Phys. Rep.* **4**, 183.

Katanuma, I., Y. Tatematsu, K. Ishii, T. Tamano, and K. Yatsu (2000). Ideal ballooning modes in the GAMMA10 tandem mirror. *J. Phys. Soc. Jap.* **69**, 3244.

Kaufman, A. N. (1971). Resonant interactions between particles and normal modes in a cylindrical plasma. *Phys. Fluids* **14**, 387.

Kaufman, A. N. and T. Nakayama (1970). Interactions of waves and particles in an inhomogeneous one-dimensional plasma. *Phys. Fluids* **13**, 956.

Kennel, C. F. and F. Engelmann (1966). Velocity space diffusion from weak plasma turbulence in a magnetic field. *Phys. Fluids* **9**, 2377.

Kesner, J. (1978). Quasi-linear model for ion cyclotron heating of tokamaks and mirrors. *Nucl. Fusion* **18**, 781.

Kesner, J. (1979). ICRF fueling of tandem mirror end plugs. *Nucl. Fusion* **19**, 108.

Kittel, C. (1996). *Introduction to Solid State Physics* (7th ed.). New York: Wiley.

Kleinberg, J. (1998). Authoritative sources in a hyperlinked environment. in *Proceedings of the 9th ACM-SIAM Symposium on Discrete Algorithms* (Association for Computing Machinery, New York, 1998); D. Gibson, J. Kleinberg, and P. Raghavan, in *Proceedings of the 9th ACM Conference on Hypertext and Hypermedia* (ACM Press, New York, 1998).

Koch, R. and D. Vaneester (1993). Enhancement of reactivity by RF. *Plasma Phys. Control. Fus.* **35**, A211.

Kolomenskii, A. A. and A. N. Lebedev (1963). Resonance effects associated with particle motion in a plane electromagnetic wave. *Sov. Phys. JETP* **17**, 179.

Krechetnikov, R. and J. E. Marsden (2007). Dissipation-induced instabilities in finite dimensions. *Rev. Mod. Phys.* **79**, 519.

Kuley, A., C. S. Liu, and V. K. Tripathi (2011). Energy channeling due to energetic-ion-driven instabilities in tokamak. *Phys. Plasmas* **18**, 032503.

Landau, L. D. and E. M. Lifshitz (1971). *The Classical Theory of Fields* (3rd ed.). New York: Pergamon Press.

Landau, L. D. and E. M. Lifshitz (1976). *Mechanics*. Oxford: Butterworth-Heinemann.

Laslett, L. J., V. K. Neil, and A. M. Sessler (1965). Transverse resistive instabilities of intense coasting beams in particle accelerators. *Rev. Sci. Instr.* **36**, 436.

Lichtenberg, A. J. and M. A. Lieberman (1992). *Regular and Chaotic Dynamics* (Second ed.). New York: Springer-Verlag.

Lichtenberg, A. J., M. J. Schwartz, and D. T. Tuma (1969). Non-adiabatic and stochastic mechanisms for cyclotron resonance trapping and heating in mirror geometries. *Plasma Phys.* **11**, 101.

Lifshitz, E. M. and L. P. Pitaevskii (1981). *Physical kinetics*. Oxford: Butterworth-Heinemann.

Litvak, A. G., A. M. Sergeev, E. V. Suvorov, M. D. Tokman, and I. V. Khazanov (1993). On nonlinear effects in electron-cyclotron resonance plasma heating by microwave radiation. *Phys. Fluids B* **5**, 4347.

Litwin, C. and N. Hershkowitz (1987). Eigenmode electric field profiles in cylindrical plasmas. *Phys. Fluids* **30**, 1323.

Luenberger, D. G. (1984). *Linear and Nonlinear Programming* (2nd ed.). Amsterdam: Addison-Wesley.

Majeski, R., J. J. Browning, S. Meassick, N. Hershkowitz, T. Intrator, and J. R. Ferron (1987). Effect of variable eigenmode excitation on RF stabilization of a mirror plasma. *Phys. Rev. Lett.* **59**, 206.

Moiseenko, V. E. and O. Ågren (2005). Radio-frequency heating of sloshing ions in a straight field line mirror. *Phys. Plasmas* **12**, 102504.

Moore, J. E. and N. J. Fisch (1994). Guiding-center equations for electrons in ultraintense laser fields. *Phys. Plasmas* **1**, 1105.

Mora, P. and T. A. Antonsen (1997). Kinetic modeling of intense, short laser pulses propagating in tenuous plasmas. *Phys. Plasmas* **4**, 217.

Neil, V. K. and A. M. Sessler (1965). Longitudinal resistive instabilities of intense coasting beams in particle accelerators. *Rev. Sci. Instr.* **36**, 429.

Northrop, T. G. (1963). *The Adiabatic Motion of Charged Particles.* New York: Interscience.

Petelin, M. I. (1974). On the theory of ultrarelativistic cyclotron self-resonance masers. *Radiophysics and Quantum Electronics* **17**, 686.

Platt, E. L. (2008). *WKB Analysis of Tunnel Coupling in a Simple Model of a Double Quantum Dot.* Ph. D. thesis, University of Waterloo, Ontario, Canada.

Polomarov, O. and G. Shvets (2007). Relativistic dynamical bistability and adiabatic excitation of strong plasma waves. *Phys. Plasmas* **14**, 055908.

Post, R. F. (1962). Critical conditions for self-sustaining reactions in the mirror machine. *Nucl. Fusion Suppl.* **1**, 99.

Post, R. F. (2007). The kinetic stabilizer axisymmetric tandem mirror: A review of approaches to its implementation. *Fusion Sci. Technol. 51*(2T), 112.

Post, R. F., T. K. Fowler, J. Killeen, and A. A. Mirin (1973). Concept for a high power-density mirror fusion reactor. *Phys. Rev. Lett.* **31**, 280.

Poupon, C., C. A. Clark, V. Frouin, J. Reǵis, I. Bloch, D. L. Bihan, and J.-F. Mangin (2000). Regularization of diffusion-based direction maps for the tracking of brain white matter fascicles. *NeuroImage* **12**, 184.

Pratt, J. and W. Horton (2006). Global energy confinement scaling predictions for the kinetically stabilized tandem mirror. *Phys. Plasmas* **13**, 042513.

Pratt, J., W. Horton, and H. L. Berk (2008). Energy confinement scaling predictions for the stabilized tandem mirror. *Journal of Fusion Energy* **27**, 91–95.

Rax, J. M. (1992). Compton harmonic resonances, stochastic instabilities, quasi-linear diffusion, and collisionless damping with ultra-high-intensity laser waves. *Phys. Fluids B* **4**, 3692.

Rax, J.-M., J. Robiche, and N. J. Fisch (2007). Autoresonant ion cyclotron isotope separation. *Phys. Plasmas* **14**, 043102.

Riccitellia, M., G. Vecchia, R. Maggioraa, C. K. Phillips, R. P. Majeski, J. R. Wilson, and D. N. Smithe (1999). ICRF heating scenarios for the IGNITOR machine. *Fusion Eng. Des.* **45**, 1.

Rosenbluth, M. N. (1972). Superadiabaticity in mirror machines. *Phys. Rev. Lett.* **29**, 408.

Scheidegger, A. E. (1974). *The Physics of Flow Through Porous Media* (3rd ed.). Toronto: University of Toronto Press.

Şerban, I. (2008). *Nonlinearities in the quantum measurement process of superconducting qubits*. Ph. D. thesis, Ludwig-Maximilians-Universität München, Munich.

Shklyar, D. R. (2011). Wave-particle interactions in marginally unstable plasma as a means of energy transfer between energetic particle populations. *Phys. Lett. A* **375**, 1583.

Shklyar, R. (1986). Particle interaction with an electrostatic VLF wave in the magnetosphere with an application to proton precipitation. *Planet. Space Sci.* **34**, 1091.

Simonsen, I. (2005). Diffusion and networks: A powerful combination! *Physica A* **357**, 317.

Smith, G. R., J. A. Byers, and L. L. Lodestro (1980). Superadiabatic and stochastic ion motion in the presence of a wave in a mirror-machine plasma. *Phys. Fluids* **23**, 278.

Smith, G. R. and A. N. Kaufman (1978). Stochastic acceleration by an obliquely propagating wave – an example of overlapping resonances. *Phys. Fluids* **21**, 2230.

Smith, G. R. and N. R. Pereira (1978). Phase-locked particle motion in a large-amplitude plasma wave. *Phys. Fluids* **21**, 2253.

Smith, R. A. (1984). Poincare index theorem concerning periodic-orbits of differential-equations. *Proc. London Math. Soc.* **s3-48**, 341.

Stix, T. H. (1958). Generation and thermalization of plasma waves. *Phys. Fluids* **1**, 308.

Stix, T. H. (1975). Fast-wave heating of a two-component plasma. *Nucl. Fusion* **15**, 737.

Stix, T. H. (1992). *Waves in Plasmas.* New York: Springer-Verlag.

Suchomel, B. J., B. M. Chen, and M. B. Allen (1998). Network model of flow, transport and biofilm effects in porous media. *Transport in Porous Media* **30**, 1.

Suvorov, E. V. and M. D. Tokman (1983). Quasilinear theory of cyclotron heating of plasma in toroidal systems by monochromatic radiation. *Plasma Phys.* **25**, 723.

Timofeev, A. V. (1974). Confinement of charged particles in adiabatic traps in the presence of monochromatic cyclotron oscillations. *Nucl. Fusion* **14**, 165.

Timofeev, A. V. and B. N. Shvilkin (1976). Drift-dissipative instability of an inhomogeneous plasma in a magnetic-field. *Sov. Phys. Usp.* **19**, 149.

Tokman, M. D. (1999). Effect of the ponderomotive force of a relativistically strong wave field on charged particles. *Plasma Phys. Rep.* **25**, 140.

Tumanian, R. V. (2003). Resonant laser coolind of relativistic charged-particle beams. *J. Opt. Soc. Am. B* **20**, 1033.

Turner, W. C., E. J. Powers, and T. C. Simonen (1977). Properties of electrostatic ion-cyclotron waves in a mirror machine. *Phys. Rev. Lett.* **39**, 1087.

Ueno, K., K. Shiga, and S. Morita (2003). *A Mathematical Gift: The Interplay Between Topology, Functions, Geometry, and Algebra*, Volume 1. Providence, Rhode Island: American Mathematical Society.

Uleysky, M. Y., E. V. Sosedko, and D. V. Makarov (2010). Autoresonant cooling of particles in spatially periodic potentials. *Tech. Phys. Lett.* **36**, 1082.

Valeo, E. J. and N. J. Fisch (1994). Excitation of large-k_θ ion-Bernstein waves in tokamaks. *Phys. Rev. Lett.* **73**, 3536.

Vincena, S. T., W. A. Farmer, J. E. Maggs, and G. J. Morales (2011). Laboratory realization of an ion-ion hybrid alfvén wave resonator. *Geophys. Res. Lett.* **38**, L11101.

Volchenkov, D. and P. Blanchard (2007). Random walks along the streets and canals in compact cities: Spectral analysis, dynamical modularity, information, and statistical mechanics. *Phys. Rev. E* **75**, 026104.

Wasserman, S. and K. Faust (1994). *Social Network Analysis: Methods and Applications*. Cambridge: Cambridge University Press.

White, R. B. (2005). *Asymptotic Analysis of Differential Equations*. London: Imperial College Press.

Yamagiwa, M. and T. Takizuka (1988). Icrf wave absorption by alpha-particles. *Nucl. Fusion* **28**, 2241.

Yamaguchi, Y., M. Ichimura, H. Higaki, S. Kakimoto, K. Horinouchi, K. Ide, D. Inoue, K. Nakagome, H. Nagai, A. Fukuyama, and T. Cho (2004). High harmonic fast wave propagation in the GAMMA10 tandem mirror. *J. Plasma Fusion Research* **6**, 665.

Yamaguchi, Y., M. Ichimura, H. Higaki, S. Kakimoto, K. Nakagome, K. Nemoto, M. Katano, H. Nakajima, A. Fukuyama, and T. Cho (2006). Eigenmode formations of $m = 1$ fast Alfvén waves in the ion-cyclotron frequency range in the GAMMA 10 central cell. *Plasma Phys. Control. Fusion* **48**, 1155.

Yasaka, Y., H. Takeno, A. Fukuyama, T. Toyoda, M. Miyakita, and R. Itatani (1992). Observation of ion-cyclotron heating due to mode conversion of fast waves in a simple mirror. *Phys. Fluids B* **4**, 1486.

Yatsu, K., T. D. Akhmetov, T. Cho, M. Hirata, H. Hojo, M. Ichimura, K. Ishii, A. Itakura, Y. Ishimoto, I. Katanuma, J. Kohagura, Y. Nakashima, T. Saito, Y. Tatematsu, and M. Yoshikawa (2001). High density experiment in the GAMMA 10 tandem mirror. In *Proc. of the 28th EPS Conference on Contr. Fusion and Plasma Phys., Funchal, June 2001*, Volume 25A of *ECA*, Geneva, pp. 1549. The European Physical Society.

Yoshikawa, S., M. A. Rothman, and R. M. Sinclair (1965). Absorption of ion cyclotron waves by one component of a two-ion plasma. *Phys. Rev. Lett.* **14**, 214.

Zhang, Y., W. W. H. amd S. Zhou, H. Boehmer, R. McWilliams, T. A. Carter, S. Vincena, and M. K. Lilley (2009). Doppler-shifted cyclotron resonance of fast ions with circularly polarized shear alfvén waves. *Phys. Plasmas* **16**, 055706.

Zhang, Y., M. Blattner, and Y. Yu (2007). Heat conduction process on community networks as a recommendation model. *Phys. Rev. Lett.* **99**, 154301.

Zhang, Y., W. W. Heidbrink, H. Boehmer, R. McWilliams, S. Vincena, T. A. Carter, W. Gekelman, D. Leneman, and P. Pribyl (2008). Observation of fast-ion doppler-shifted cyclotron resonance with shear alfvén waves. *Phys. Plasmas* **15**, 102112.

Zhmoginov, A. I., I. Y. Dodin, and N. J. Fisch (2010). Negative effective mass of wave-driven classical particles in dielectric media. *Phys. Rev. E* **81**, 036404.

Zhmoginov, A. I., I. Y. Dodin, and N. J. Fisch (2011a). Alpha-channeling in mirror machines. Prepared for submission to Phys. Plasmas.

Zhmoginov, A. I., I. Y. Dodin, and N. J. Fisch (2011b). A Hamiltonian model of dissipative wave-particle interactions and the negative-mass effect. *Phys. Lett. A* **375**, 1236.

Zhmoginov, A. I., I. Y. Dodin, and N. J. Fisch (2011c). Negative-mass effect in the presence of collisions. Prepared for submission to Phys. Lett. A.

Zhmoginov, A. I. and N. J. Fisch (2008a). Flux control in networks of diffusion paths. *Phys. Lett. A* **372**, 5534.

Zhmoginov, A. I. and N. J. Fisch (2008b). Simulation of α-channeling in mirror machines. *Phys. Plasmas* **15**, 042506.

Zhmoginov, A. I. and N. J. Fisch (2009). Waves for alpha channeling in mirror machines. *Phys. Plasmas* **16**, 112511.

Zhmoginov, A. I. and N. J. Fisch (2010). Feasibility studies of alpha-particle channeling in mirror machines. *Fusion Sci. Technol. 57*(4), 361.

Zhmoginov, A. I. and N. J. Fisch (2011a). Alpha-channeling mode structure and particle diffusion. To be submitted to ArXiv.

Zhmoginov, A. I. and N. J. Fisch (2011b). Channeling of fusion alpha-particle power using minority ion catalysis. *Phys. Rev. Lett.* **107**, 175001.